

ABSTRACT BOOK

SMRA 2022

34th Annual International Conference

*Solving Clinical Problems
with Human Creativity & Machine Learning*

All oral and poster abstracts are included in this Abstract Book.



Impacts of the COVID-19 Pandemic on the Use of Non-invasive Angiography

R Burgul, G Roditi

NHS Forth Valley, NHS Greater Glasgow and Clyde, Scotland, UK

Purpose: Non-invasive angiography was increasing year-on-year until the COVID-19 pandemic. We sought to evaluate the impact of the pandemic on the relative uses of MRA and CTA across different body systems and between different patient groups.

Methods: Governance permission was obtained for data collection from the local Radiology Information Systems (RIS) of two Health Boards representative of city/university teaching hospital versus district general hospital-based practise. Data were collated for all non-invasive angiographic studies performed by CT and MRI from 2019 to May 2022 regarding examination modality, examination type (body area), date and site of performance plus age, gender, patient type (in-patient versus out-patient versus ED etc.), time and day of performance.

Results: Highlights of the results are -

- Pulmonary angiographic studies have shown ~100% increase on pre-pandemic levels, exclusively performed by CT with now a rate of 1,095 scans per 100,000 population. This has largely been driven by concerns regarding pulmonary vascular thrombosis in association with COVID-19.
- Lower limb angiographic studies overall have returned to at least pre-pandemic levels but the share for MRA has reduced from 57% to 29% now – attributed to a reduction in out-patient elective studies, especially for claudicants who are not being intervened upon, hence not imaged (figure 1).
- Carotid studies overall increased by up to 55% over the period driven by a move away from carotid ultrasound during first pandemic waves with CTA particularly increasing to cover this need while MRA use has remained at ~11% of overall scans (figure 2).
- A 50% increase in venographic examinations has been driven by an increase in cerebral venographic studies related to concerns regarding vaccine associated thrombosis & thrombocytopenia, the overall share of total MRV use has fallen from 51% to 42%.
- Emergency department recourse to non-invasive angiographic imaging across all body systems has increased from 12% in 2019 to now 16% of studies performed, exclusively by CTA.

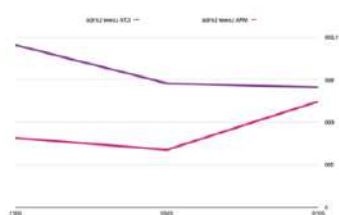


Figure 1

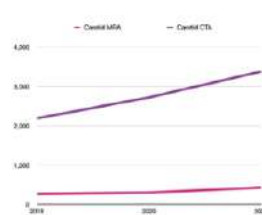


Figure 2

Discussion: The COVID-19 pandemic has not reduced non-invasive angiographic imaging, indeed the volume has increased across the pandemic period. However, this has not led to increased MRA activity levels but rather been driven by an increase in CTA use, especially in the ED.

Risk of Recurrent Cerebral Infarction in Stroke Patients with Intracranial Atherosclerotic Disease

Yi-Pei Liu¹, Bruce Wasserman^{1,2}, Richard Leigh³, Di Zhao⁴, Zhongqing Huang², Jarunee Intrapiromkul¹, and Ye Qiao¹

¹Department of Radiology, the Johns Hopkins University; ²Department of Radiology, the University of Maryland School of Medicine; ³Department of Neurology, the Johns Hopkins University; ⁴Department of Epidemiology, The Johns Hopkins Bloomberg School of Public Health

Objective: To reveal the associations between imaging characteristics of intracranial atherosclerotic plaques and new infarction in the downstream vascular territory in stroke patients using high-resolution intracranial vessel wall MRI (VWMRI).

Methods: 86 stroke patients (mean age 55 years old, 57% male, 49% white) who were clinically diagnosed as intracranial atherosclerotic disease (ICAD) and underwent contrast-enhanced VWMRI (3D, 0.5 mm isotropic) were included. Those who had ipsilateral extracranial cervical artery stenosis > 50%, cardiogenic emboli, atrial fibrillation were excluded. Plaque number and qualitative features (vascular segment, enhancement, stenosis, eccentricity) were documented. The cerebral infarcts were determined using DWI, and the corresponding responsible lesions were adjudicated as culprit (or probably-culprit) based on the previous established criteria¹. Patients were followed until the date of recurrent stroke, the date of new silent infarcts, death from any cause or 1 year after baseline VWMR scan, whichever came first. Multilevel survival analysis with Cox regression models were used to estimate the hazard ratios and 95% confidence intervals (CIs) of risk of new infarcts.

Results: A total of 459 plaques were identified in the 86 patients (mean, 5.33 per patient), 332 (72.3%) showed enhancement and 127 (27.7%) were classified as culprit plaques. Culprit plaques were associated with a higher grade of plaque enhancement (OR =3.58, 95% confidence interval (CI) =2.30 - 5.57). Of the 86 patients, 18 (9 male, 7 whites) had new infarcts within 12 months of follow-up (mean follow-up, 293.8 ± 132 days). Among these 18 patients, 40 new brain infarcts were recorded, and 20 were distributed in the same vascular territories, corresponding to the culprit plaques at the baseline. Culprit plaques, plaque stenosis and plaque enhancement are significantly associated with the new infarcts in univariate models. In the final multi-variable model, plaque enhancement remained significant (HR of grade 2 vs grade 0 = 4.68, 95% CI 1.44 -15.21), whereas stenosis degree was insignificant (HR 1.14, 95% CI 0.79 - 1.65, p-value=0.47) (**Table 1**). Sub-analysis in non-culprit plaques showed similar result that plaque enhancement was positively associated with new infarcts (HR of grade 2 vs grade 0 = 5.08, 95% CI 1.02 - 25.4, p-value=0.05).

Table 1: Cox regression for new brain infarction

	Univariate Model ¹	Multivariable Model ²
	Hazard Ratio (95% CI)	Hazard Ratio (95% CI)
Patient-specific variables		
Age (years)	1.02 (0.96 -1.08)	1.03 (0.96 - 1.09)
Gender (women vs men)	0.83 (0.18 - 3.80)	0.69 (0.13 - 3.70)
Race (white vs non-whites)	0.51 (0.10 - 2.48)	0.44 (0.08 - 2.39)
Smoking (yes vs no)	0.28 (0.04 - 2.00)	0.25 (0.04 - 1.76)
Hypertension (yes vs no)	6.43*e ¹⁰ (8.41e ⁹ - 4.93e ¹¹)	NA
Hyperlipidemia (yes vs no)	0.46 (0.06 - 3.33)	NA
Diabetes mellitus (yes vs no)	0.90 (0.18 - 4.42)	NA
Plaque-specific variables		
Culprit (yes vs no)	3.03 (1.52 - 6.03)	NA
Ordinal degree of stenosis, % per higher category	1.53 (1.12 - 2.07)	1.14 (0.79 - 1.65)
Grade of plaque enhancement (per grade)	2.30 (1.44 - 3.66)	NA
Grade of plaque enhancement		
grade 0	1.00 (Ref)	1.00 (Ref)
grade 1	2.41 (0.87 - 6.65)	2.32 (0.81 - 6.64)
grade 2	5.38 (1.96 - 14.79)	4.68 (1.44 - 15.21)
	p-trend< 0.001	p-trend= 0.009
Eccentricity (yes vs no)	1.05 (0.90 - 1.24)	NA
Number of plaques	1.02 (0.83 - 1.25)	NA

Mixed-effect conditional Hazard Ratio (HR) and 95% confidence intervals (95% CIs) estimated from Cox PH model using 1 univariate and 2 multivariate, adjusted for age, gender, race, cigarette smoking, ordinal degrees of stenosis (per higher category), and grade of plaque enhancement (grade 0 - 2). In the multivariate model, the LR test p-value<0.0001, ICC =0.88

Discussion and Conclusion: Culprit lesions were strongly associated with recurrent cerebral infarction in stroke patients, indicating increased risk for stroke in symptomatic arterial territories, likely caused by recurrent plaque rupture. Plaque enhancement was significantly associated with new cerebral infarction, after adjusting for stenosis degree and baseline demographics, highlighting its potential importance in future studies.

References: [1] Qiao Y, et al., Radiology 2014 May;271(2):534-42. [2] Kwee RM, Qiao Y et al., Neuroradiology 2019 Jun;61(6):651-657.

MRA/I of Morphology and Function in Intracranial Aneurysms of the Posterior Circulation

David Saloner¹, Alireza Sojoudi¹, Evan Kao¹, Yan Wang¹, Kazim Narsinh¹, Steven Hetts¹, Matt Amans¹, Chengcheng Zhu², Megan Ballweber¹, Keerthi Valluru¹, and Daniel Cooke¹

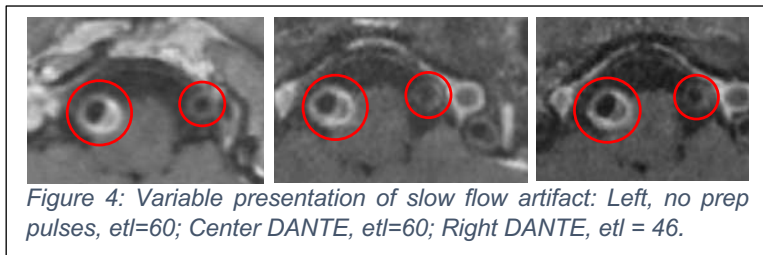
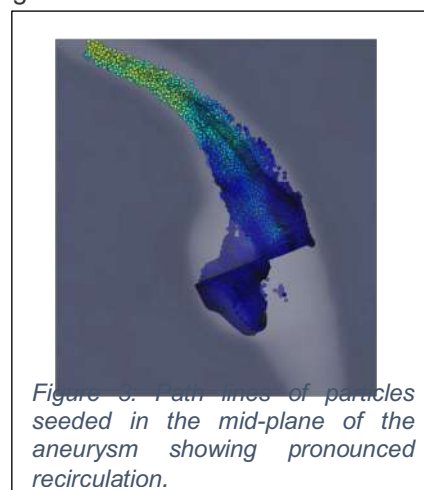
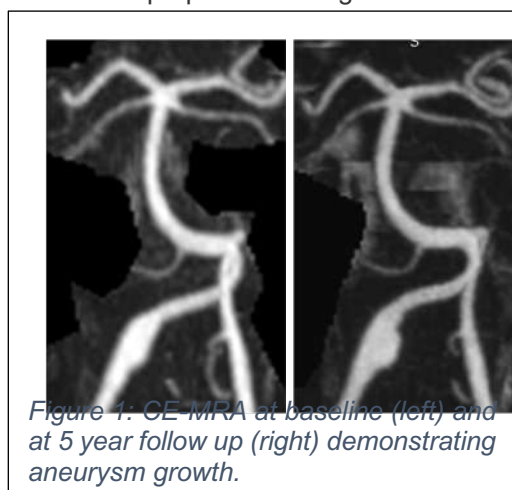
¹Department of Radiology and Biomedical Imaging, University of California, San Francisco, USA

²Department of Radiology, University of Washington, Seattle, USA

Purpose: The clinical management of fusiform aneurysms of the posterior circulation is a major challenge. Unlike saccular aneurysms these lesions are not amenable to clipping, stenting or coiling. They represent a major risk of debilitating symptoms from mass effect as they often impinge on the brain stem; from steno-occlusive impact on the pontine perforators; and, in the event of rupture, of a devastating stroke. In conditions with significant clinical symptoms, drastic interventions may be considered such as take-down of a diseased artery or surgical bypass. We report here on the investigation of a series of patients with vertebro-basilar disease who were imaged with a comprehensive suite of non-invasive MR imaging, and who have been followed serially over time – in many cases over many years. The aim of these investigations was to identify structural and functional features of the disease that might be predictive of the associated risk of deleterious outcomes.

Methods: 23 patients with fusiform aneurysms of the vertebro-basilar vasculature were enrolled for serial imaging on a 3T Skyra (Siemens Healthineers). All studies were performed using IRB approved protocols. Imaging sequences used included: T1-weighted 3D SPACE black blood VWI (0.6mm isotropic) pre and post Gd; CE-MRA (0.7mm isotropic); and 4D Flow MRI (1.0mm isotropic, VENC=80 cm/sec). The use of DANTE preparation pulses to suppress slow flow artifact was also investigated. In addition, Computation Fluid Dynamics calculations of the velocity field were performed based on the CE-MRA geometric boundary conditions, and using inlet velocity waveforms as determined from the 4D Flow measurements. Streamlines and particle paths were generated from the velocity maps, and other hemodynamic metrics, such as wss and pressure maps were evaluated. A semi-automated tool was used to segment the inner and outer walls of the lumen. The following metrics were measured: aneurysm volume change over time; categorization of degree of vessel wall enhancement; and fraction of recirculating flow. Velocity fields measured by 4D Flow were compared to those estimated by CFD to evaluate inter-modality consistency given variable resolution and inherent simulation assumptions such as Newtonian fluids, and non-compliant walls.

Results: The Coefficient of Variance of measurement of aneurysm volume was 5.5% and subjects showed an annualized growth rate of 1.32%/yr¹. Fig.1 displays a comparison of a CE-MRA on a patient with a fusiform aneurysm at baseline and at follow-up 5 years later showing significant aneurysm growth. Figure 2 shows a coronal SPACE VWI post Gd study showing substantial enhancement of the wall of the ipsilateral vertebral (arrow) but no enhancement of the contralateral vertebral. Figure 3 shows particle paths derived from the 4D Flow study showing pronounced flow recirculation in the aneurysm. Figure 4 shows SPACE studies without any flow suppression pulses compared to those with DANTE preparation using CAIPI acceleration with various echo train lengths.



Discussion: Multi-contrast MRI provides important insights into progression of disease of the intracranial vasculature. DANTE flow suppression reduces the manifestation of slow flow related signal which can mimic wall enhancement. Reduced etl sequences provide sharper images, further confining signal enhancement to the location of the wall. Co-localization of wall enhancement with sites of increased growth could

be indicative that this measure is predictive of likely future growth and aneurysm instability. Furthermore, CFD-validated 4D Flow measures provide insights into putative mechanisms for adverse physiological response as regions of low wall shear stress are noted at regions of enhancement and growth. The 4D Flow data also defines regions of slow recirculation which have been linked, in other territories, to thrombus layering and potential thrombo-embolic events.

References:

1. Liu X, Haraldsson H, Wang Y, Kao E, Ballweber M, Martin AJ, McCulloch CE, Faraji F, Saloner D; UCSF Intracranial Aneurysm Monitoring Group. A Volumetric Metric for Monitoring Intracranial Aneurysms: Repeatability and Growth Criteria in a Longitudinal MR Imaging Study. *AJNR Am J Neuroradiol.* 2021 42:1591-1597

Deep Learning Intracranial Aneurysm Detection on 3D TOF-MRA

Sinéad Culleton MB BCh BAO, FRCR, FFR(RCSI)¹, Clement Vachet MS², John Roberts PhD¹, Akihiko Sakata MD¹, Dennis Parker PhD¹, Edward Quigley MD PhD¹, Matthew Alexander MD¹, J. Scott McNally MD PhD¹

¹Utah Center for Advanced Imaging (UCAIR), Department of Radiology, University of Utah, Salt Lake, Utah, USA, ²Scientific Computing and Imaging Institute, University of Utah, Salt Lake Utah, USA

Purpose: Aneurysm detection is a clinically significant role for radiologists with known blind spots including the internal carotid and posterior communicating arteries. Misinterpretation or misses are frequent in the emergency or trainee setting. Aneurysm rupture carries high morbidity and mortality. There is a critical need to determine the ability and limitations of deep learning (DL) tools for aneurysm detection. This study aimed to assess a DL algorithm for intracranial aneurysm detection on 3D TOF-MRA and assess what effect size and location had on sensitivity.

Methods: In this IRB-approved retrospective study, 3D TOF-MRA sequences acquired at 3T between 2015-21 were reviewed for the presence of aneurysms. Thrombosed and fully treated aneurysms were excluded. Positive cases were confirmed by two neuroradiologists using consensus and additional CTA and DSA imaging when available. Aneurysms were manually segmented using ITK-SNAP to generate the ground truth dataset (Figure: A-B). DeepMedic was the 3D CNN used. The dataset was randomly divided into training (69%), validation (11%) and test (20%) cases and 5-fold-cross-validation was used. Four models were generated: the 3D-TOF volume, skull stripped, arterial segmentations and dilated arterial segmentations (dilated 3 voxels). Output predictions were post-processed, using a detection threshold of 5mm³. The Dice Similarity Coefficient (DSC), Hausdorff distance (HD), sensitivity, and precision were assessed.

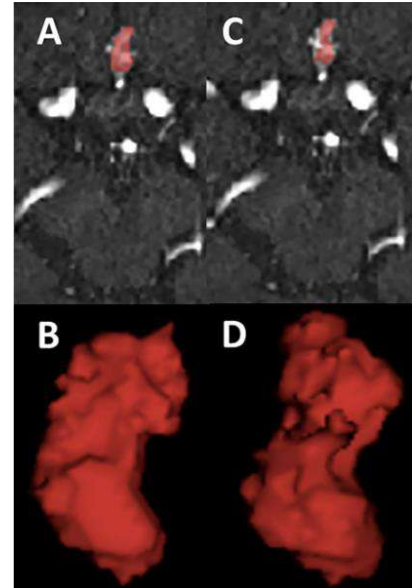


Figure: A-B is an example of a manually segmented anterior circulation aneurysm. C-D is the corresponding DL prediction made by DeepMedic.

Results: There were 122 subjects with 135 aneurysms (1.11 aneurysms/subject), with 128 (94.8%) saccular and 7 (5.2%) fusiform. By size, there were 40 (29.6%) small ≤ 3 mm, 69 (51.1%) medium >3 mm and ≤ 7 mm, and 26 (19.3%) large >7 mm aneurysms. Mean max diameter was 5.6 ± 3.5 mm. The majority were in the anterior circulation 113 (83.7%): ICA 50 (37.0%), ACOMM 30 (22.2%), MCA 30 (22.2%), ACA 3 (2.2%). Posterior aneurysms accounted for 22 (16.3%): Basilar 9 (6.8%), Vertebral 7 (5.2%), PCOMM 6 (4.4%). Optimum results were achieved using automated, dilated arterial segmentations of the circle of Willis and 5mm³ thresholding. The DSC was 0.417 ± 0.33 , HD 34.46 ± 43.19 , with 1.10 ± 0.54 predictions/subject. Overall sensitivity of detection was 63% (95%CI:54.9,71.2). Sensitivity was greatest for large aneurysms 92.3% (95%CI:82.1,100.0), moderate for medium 73.9% (95%CI:63.6,84.3), and poor for small 25% (95%CI:11.6,38.4). By location, the overall anterior circulation sensitivity was 63.7% (95%CI:54.9,72.6) as follows: ACOMM 76.7% (95%CI:61.5,91.8), ICA 68.0% (95%CI:55.1,80.9), MCA 60.0% (95%CI:42.5,77.5), ACA 66.7% (95%CI:13.3,100.0). Posterior circulation aneurysm sensitivity was 54.6% (95%CI:33.7,75.4) with: Basilar 66.7% (95%CI:35.9,97.5), Vertebral 42.9% (95%CI:6.2,79.5), and PCOMM 50.0% (95%CI:10.0,90.0).

Conclusion: DL aneurysm detection was highly size-dependent and detected aneurysms larger than 3 mm with moderate-to-high sensitivity. Location was less impactful than size, with moderate sensitivity for anterior and posterior circulation aneurysms.

Association of Combining Characteristics of Intracranial Atherosclerotic Disease and Cerebral Small Vessel Disease with Acute Ischemic Stroke in Symptomatic Patients: A Magnetic Resonance Imaging Study

Miaoxin Yu, MD¹; Qian Li, MD²; Gaifen Liu, PhD¹; Cheng Li, MD²; Xihai Zhao, MD, PhD³

¹ Department of Neurology, Beijing Tiantan Hospital, Capital Medical University, Beijing, China

² Department of Radiology, Zhongda Hospital, Medical School of Southeast University, Nanjing, China

³ Center for Biomedical Imaging Research, Department of Biomedical Engineering, Tsinghua University, Beijing, China

Purpose:

It has been shown that intracranial atherosclerosis disease (ICAD) and cerebral small vessel disease (CSVD) are respectively associated with ischemic stroke.^{1, 2} This study aimed to investigate the association of combining the characteristics of ICAD and CSVD with acute cerebral infarct (ACI) in symptomatic patients using magnetic resonance (MR) imaging.

Methods:

Patients with ICAD and anterior circulation ischemic stroke or transient ischemic attack were recruited from a multicenter study during March 2017 to March 2021. All patients underwent intracranial artery vessel wall and brain MR imaging at 3.0T. Two experienced radiologists reviewed all MR images with consensus blinded to clinical information. The MR imaging characteristics of location, length, maximal wall thickness, T1 hyperintense, plaque enhancement, and luminal stenosis of the intracranial plaque were assessed. The CSVD characteristics, including enlarged perivascular space (EPVS), white matter hyperintensity (WMH) and lacune were analyzed. The ACI at anterior circulation territory on diffusion weighted imaging was identified. Univariate and multivariable logistic regressions were used to evaluate the association of the MR imaging characteristics of ICAD and CSVD with ACI. The receiver operating characteristic (ROC) curve analysis was performed to assess the predictive value of MR imaging characteristics for ACI. The study protocol was approved by institutional review board and consent form was obtained from each subject.

Results:

Of 148 recruited patients (mean age: 57.04±11.00 years; 85 males), 71 (47.97%) had ACI. Plaque enhancement (grade=2, odds ratio [OR], 4.266; 95% confidence interval [CI], 1.608-11.319; P=0.004), EPVS (OR, 4.149; 95% CI, 2.017-8.532; P<0.001), WMH (OR, 8.053; 95% CI, 2.638-24.580; P<0.001) and lacune (OR, 2.593; 95% CI, 1.308-5.138; P=0.006) were associated with ACI in univariate analysis. After full adjustment, plaque enhancement (grade=2, OR, 5.623; 95% CI, 1.602-19.743; P=0.007), EPVS (OR, 4.200; 95% CI, 1.656-10.650; P=0.003), and WMH (OR, 9.036; 95% CI, 1.844-44.268; P=0.007) were still significantly associated with ACI. ROC curve analysis showed that area under the curve of plaque enhancement, EPVS and WMH was 0.640 (95% CI, 0.544–0.735), 0.670 (95% CI, 0.575-0.766) and 0.652 (95% CI, 0.558-0.746), and the combination of age, sex, BMI, plaque enhancement, EPVS, and WMH in the diagnosis of ACI was 0.807 (95% CI, 0.733-0.881), respectively.

Discussion and Conclusion:

Our study suggested that the combination of age, sex, BMI, plaque enhancement, EPVS, and WMH had higher strength than each characteristic of ICAD and CSVD alone, indicating that combining the measurements of MR imaging characteristics of cerebral large artery and small artery disease may have a stronger predictive value for the risk of acute cerebral infarction.

References:

1) Wang Y, et al. Stroke, 2014; 45:663-669. 2) Chen H, et al. Stroke Vasc Neurol, 2020; 5:128-137.

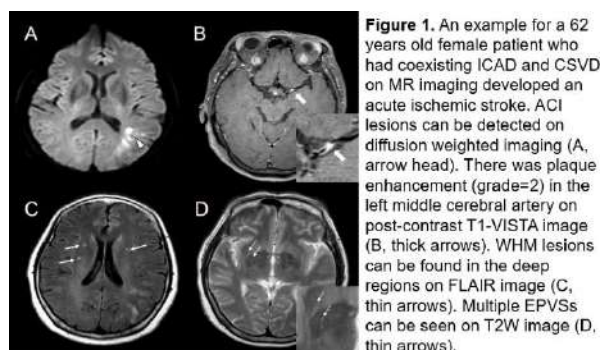


Figure 1. An example for a 62 years old female patient who had coexisting ICAD and CSVD on MR imaging developed an acute ischemic stroke. ACI lesions can be detected on diffusion weighted imaging (A, arrow head). There was plaque enhancement (grade=2) in the left middle cerebral artery on post-contrast T1-VISTA image (B, thick arrows). WMH lesions can be found in the deep regions on FLAIR image (C, thin arrows). Multiple EPVSs can be seen on T2W image (D, thin arrows).

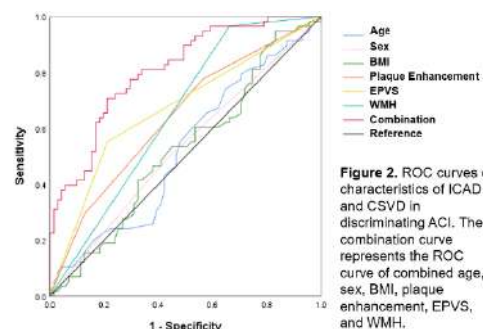


Figure 2. ROC curves of characteristics of ICAD and CSVD in discriminating ACI. The combination curve represents the ROC curve of combined age, sex, BMI, plaque enhancement, EPVS, and WMH.

A software platform for the combined analysis of intracranial blood flow, diffusion and perfusion

Patrick Winter¹, Jackson Moore², Maria Aristova², Neil Chatterjee², Jared Narvid³, David Saloner³, Sameer Ansari², Michael Markl², Susanne Schnell¹

¹Department of MR Physics, University of Greifswald, Greifswald, Germany, ²Department of Radiology, Northwestern University, Chicago, Illinois, USA,

³Department of Radiology and Biomedical Imaging, University of California, San Francisco, USA

Purpose: Intracranial atherosclerotic disease (ICAD) is a major cause of death in the western world. For clinical evaluation of the vascular mechanisms attributed to ICAD, a large range of non-invasive magnetic resonance imaging (MRI) techniques such as cerebral 4D flow MRI, diffusion- as well as perfusion measurements are utilized. In this context, several analysis tools have been developed for semi-automatic quantification of several functional parameters across the Circle of Willis (CoW) [1,2]. The ultimate goal of these analysis tools is the development of better prediction models for the assessment of stroke risk in ICAD patients. To date, however, most analysis tools evaluate cerebral MRI data separately, which can make a direct comparison between different imaging modalities laborious. Here, we present an advanced analysis platform that integrates different evaluation routines into a single software graphical user interface (GUI), in order to facilitate the development of improved multi-parametric ICAD prediction models.

Methods: Experiments were performed on a series of ICAD patients (n=4) on a 3T MRI system (Siemens). All protocols were in accordance with the Northwestern University Institutional Review Board. Perfusion measurements were conducted using bolus tracking with a single-dose (0.1mmol/kg) of Gd-based contrast agent (Magnevist). For both diffusion and perfusion, a 2D multi-slice echo planar imaging (EPI) technique was used. For measuring intracranial blood flow, a 4D flow dual-VENC sequence was utilized [1,3]. After post-processing [3] the 4D velocity data was imported to an in-house built semi-automatic MATLAB analysis tool. First, a threshold-based segmentation of the CoW was performed. Subsequently, centerlines were calculated for each individual vessel. Flow and cross-sectional areas were afterwards determined in several automatically positioned analysis planes perpendicular to the centerlines. The perfusion analysis was performed with a set of tools integrated into the same GUI. First, the perfusion datasets were co-registered to Montreal Neurological Institute (MNI) space and segmented according to the respective brain matter using the open-source statistical parametric (SPM) software package [2,4]. A vascular territory analysis of the brain regions was performed [2] and then the segmented perfusion and diffusion data were transformed back to original space. The regional blood flow (RBF), regional blood volume (RBV), mean transit time (MTT) and apparent diffusion coefficient (ADC) as well as the respective average values across the vascular territories are displayed in the GUI. For vessel visualization, an additional high-resolution TOF measurement was co-registered to the 4D flow data using SPM and displayed in the same GUI.

Results: Fig.1 displays a screenshot of the analysis tool combining different cerebral MRI techniques. A cut plane view of the processed CBF map (for colormap of exemplary slice see top left) and the corresponding vascular territories (white lines) are shown. In addition, a rendering of the vessel segmentation based on the TOF measurement is shown in red. Fig.2 shows a schematic overview of an MRI exam result for a representative ICAD patient, displaying the results of flow-measurement and vessel cross-sectional areas (median \pm interquartile values) fully integrated with CBF, CBV, MTT and ADC (mean \pm STD) for the main CoW vessels.

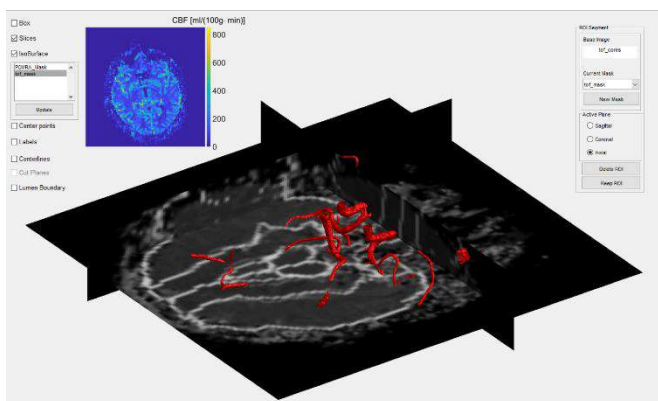


Figure 1: Screenshot of the analysis tool:

Cut planes of the CBF measurement and TOF segmentation.

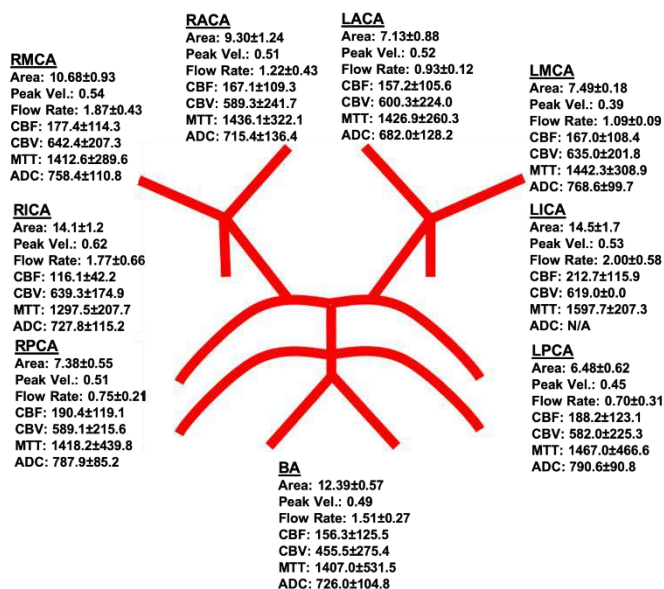


Figure 2: Exemplary MRI test result.

Discussion: We presented a new software tool that enables combined analysis of perfusion, diffusion and 4D flow MRI data. A direct comparison between different imaging modalities is now possible within the same software GUI environment. The software provides an easier reading of MRI exam results and sets the ground for developing prediction models of patient outcome. In the future, a larger cohort of patients will be assessed in a feasibility study to determine potential multi-parametric imaging biomarkers for ICAD disease progression.

Funding: NIH 1R01HL149787, NIH 1R21NS122511, NIH F30HL140910 and T32GM815229.

References

1. Vali et al, MRM 82(2):749-762, 2019
2. Chatterjee et al, MRM 33(5): 618-623, 2015
3. Schnell et al, JMIR 46 (1), 102-114, 2017
4. Unified Segmentation, Neuroimage 26(3), 839-851, 2005

Intracranial Aneurysm Segmentation from Highly Imbalanced 3D TOF-MRA Images using Evolving Hybrid Focal loss-based Deep Learning

Maysam Orouskhani, Dandan Chang, Mahmud Mossa-Basha, Chengcheng Zhu
Department of Radiology, University of Washington, Seattle, WA, USA

Purpose: Accurate segmentation of intracranial aneurysms plays an important role in the quantitative analysis and monitoring of intracranial aneurysm disease. However, working with imbalanced datasets is one of the most challenging issues in aneurysm segmentation. Since lesions often occupy a very smaller volume relative to the background, the model's prediction is biased towards low sensitivity. While traditionally deep learning segmentation models used cross-entropy and Dice as loss functions, the Hybrid Focal loss has been recently developed to tackle the imbalanced data [1]. However, it suffers from the number of hyperparameters. Therefore, we intend to tune the hyperparameters of the Hybrid Focal loss within the training process of deep neural network to handle the imbalanced data more efficiently.

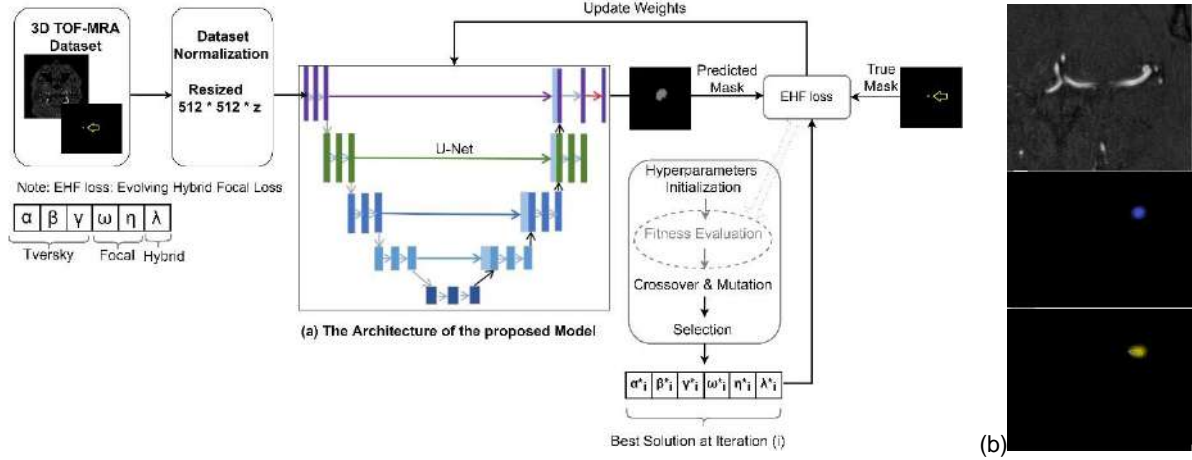


Fig. 1 (a): The architecture of the proposed model. (b): up: TOF, middle: True mask, down: Predicted mask

Methods: In this study, we used the Hybrid Focal loss as the basic loss function for training U-Net model. The Hybrid Focal loss is the summation of Focal loss and Focal Tversky loss. The Focal Tversky loss is derived from Tversky index (TI): $TI = \frac{\sum_{i=1}^N p_{oi} g_{oi}}{\sum_{i=1}^N p_{oi} g_{oi} + \alpha \sum_{i=1}^N p_{oi} g_{oi} + \beta \sum_{i=1}^N p_{1i} g_{oi}}$ where 'poi' is the probability of pixel 'i' belonging to the foreground class and 'p_{1i}' is the probability of pixel belonging to the background class. Also, the 'g_{oi}' value is 1 for foreground class and is 0 for background. Conversely, 'g_{1i}' takes values of 1 for background and 0 for foreground. Then, the Focal Tversky loss is $\mathcal{L}_{FT} = \sum_{c=1}^C (1 - TI)^{\frac{1}{\gamma}}$. In addition, the Focal loss is formulated as: $\mathcal{L}_F = \omega(1 - p)^{\eta} \cdot -1 * \log(p)$. Finally, the Hybrid Focal loss is presented as: $\mathcal{L}_{HF} = \lambda \mathcal{L}_F + (1 - \lambda) \mathcal{L}_{FT}$. In this work, we considered \mathcal{L}_{HF} as the objective function including six hyperparameters $\{\alpha, \beta, \gamma, \omega, \eta, \lambda\}$. We tried to find the optimal values of hyperparameters so that they minimize the Hybrid Focal loss. To solve the minimization problem within the training process of U-Net, we utilized the genetic algorithm (GA). During an iterative process, the GA executes multimodal search by evolutionary operators to produce diverse solutions to yield near-optimal solutions. To test the generalization, we conducted the model on ADAM dataset including 113 3D TOF-MRA images. We used 75% as training and 25% for testing. We normalized dataset using z-score normalization and resized to 512*512*z. The code was written in Python, and the model was trained and tested on a V100 GPU, 32 GB RAM.

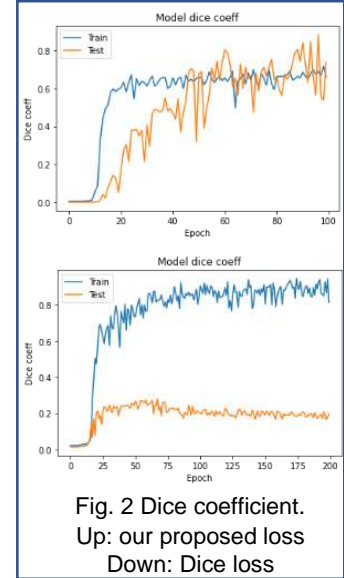


Fig. 2 Dice coefficient.
Up: our proposed loss
Down: Dice loss

Results: The Dice coefficient was calculated to evaluate the performance of the model. The simulation results illustrated that the model achieved segmentation accuracy of 68.5% (Dice coefficient) by using evolving Hybrid Focal loss. However, this metric dropped to 23.6% when the model used Dice loss function which was not suitable for segmenting aneurysm-containing images. Fig. 2 shows the obtained Dice coefficient of running both evolving Hybrid Focal loss and Dice loss for training and test at each epoch.

Discussion: This study proposed a deep learning model based on a new evolving loss function for handling the imbalanced data in the segmentation of intracranial aneurysm. The proposed model employed the GA to evolve the hyperparameters of Hybrid Focal loss in U-Net. The proposed evolving Hybrid Focal loss outperformed the Dice loss in the terms of Dice coefficient.

References: [1] Yeung, M., et.al, (2022). Unified focal loss, CMIG.

Acknowledgement: NIH grant (R00HL136883)

Associations Between Cerebral Blood Flow and Progression of White Matter Hyperintensity in Community-dwelling Adults: A Longitudinal Cohort Study

Hualu Han¹, Zihan Ning¹, Dandan Yang¹, Miaoxin Yu², Huiyu Qiao¹, Runhua Zhang², Gaifen Liu², Xihai Zhao¹

1.Center for Biomedical Imaging Research, Tsinghua University, Beijing, China;

2. Department of Neurology, Beijing Tiantan Hospital, Capital Medical University, Beijing, China

Purpose: White matter hyperintensity (WMH) is prevalent in elderly populations.¹ Ischemia is characterized by a decline in cerebral blood flow (CBF) and may play a key role in the pathogenesis of WMH.² However, the associations of CBF reductions and WMH progression remain controversial.³ **This study aimed to investigate the associations between CBF reduction and progression of WMH in community-based asymptomatic adults across the lifespan during 2 years' follow-up.**

Methods: Study sample: The participants were recruited from an ongoing community-based longitudinal and observational cohort study during April 2016 and July 2019. All participants underwent anatomical and pCASL perfusion imaging for brain at baseline. Brain MR imaging was also conducted at the 24th month during the follow-up study. The study protocol was approved by institutional review board and consent form was obtained from each participant. **MR imaging and image analysis:** The MR imaging was performed on a 3T Philips MR scanner with a 32-channel head coil. MR imaging sequences included T1w, T2-FLAIR and pCASL. CBF was measured on pCASL images and WMH was evaluated on T2-FLAIR images, respectively (Figure 1). Tissue segmentation was conducted on T1w images to derive binary masks of gray matter (GM) and normal appearing white matter (NAWM). **Statistical analysis:** Linear regressions were conducted to analyze the cross-sectional and longitudinal associations between CBF and WMH.

Results: A total of 229 adults (mean age 57.3±12.6 years, 94 males) were enrolled at baseline, of whom 84 participants (mean age 54.1 ± 11.9 years, 41 males) completed follow-up visit with a mean time interval of 2.77 ± 0.44 years. At baseline, there was a decreasing trend in GM CBF with the increase of WMH burden (P = 0.063), but this association was attenuated after adjusting for confounding factors (P = 0.271) (Table 1). In longitudinal analysis, both changes of CBF in GM and NAWM showed no significant associations with changes of WMH volumes (all P > 0.05). Baseline WMH volume was significantly associated with the reduction of perfusion in GM (P = 0.004) and NAWM (P = 0.005) during follow-up. On the contrary, neither baseline CBF in GM (P = 0.888) nor NAWM (P = 0.850) was associated with WMH progression. In addition, CBF changes within WMH were significantly associated with both baseline (P = 0.017) and progression (P = 0.015) of WMH volume.

Discussion: WMH burden was not directly associated with cerebral perfusion at baseline. Our longitudinal data analyses showed no direct associations between WMH progression and CBF reductions, regardless of GM or WM. We found that more severe WMH at baseline could predict faster decline of cerebral perfusion, but not vice versa. Additionally, blood flow changes within WMH were potential indicators for the occurrence and progression of WMH volume.

References: [1] Pantoni L., Lancet Neurol 2010;9:689-701. [2] Crane DE., Front Aging Neurosci 2015;7:131. [3] Shi Y., J Cereb Blood Flow Metab 2016;36:1653-67.

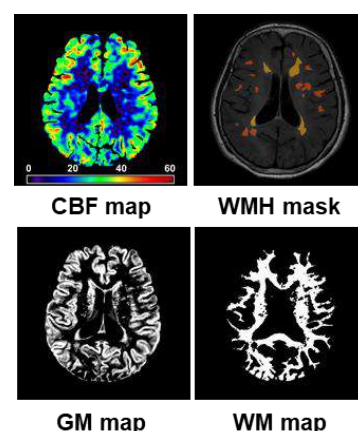


Figure 1. Typical MR images.

Table 1. Linear regressions between CBF and volume of WMH with log transformation at baseline after partial volume correction.

Outcome	Predictor	Univariate Model			Multivariate Model*		
		B	95% CI	P value	B	95% CI	P value
Cross-sectional analysis: baseline CBF and WMH volumes							
log(WMH) ₁	GM CBF ₁	-0.010	-0.020, 0.001	0.063	-0.006	-0.016, 0.005	0.271
log(WMH) ₁	NAWM CBF ₁	0.004	-0.012, 0.021	0.598	0.003	-0.012, 0.019	0.677
log(WMH) ₁	WMH CBF ₁	-0.016	-0.031, -0.001	0.032	-0.019	-0.033, -0.005	0.009
Longitudinal analysis: changes of CBF and WMH volumes							
Δlog(WMH)	ΔGM CBF	-0.005	-0.012, 0.002	0.136	-0.005	-0.012, 0.002	0.139
Δlog(WMH)	ΔNAWM CBF	-0.007	-0.017, 0.004	0.217	-0.008	-0.019, 0.003	0.164
Δlog(WMH)	ΔWMH CBF	-0.014	-0.025, -0.003	0.017	-0.019	-0.031, -0.007	0.002
Longitudinal analysis: baseline CBF predict changes of WMH volumes							
ΔGM CBF	log(WMH) ₁	-1.96	-3.25, -0.67	0.004	-2.14	-3.60, -0.67	0.005
ΔNAWM CBF	log(WMH) ₁	-0.99	-1.66, -0.31	0.005	-1.31	-2.18, -0.45	0.004
ΔWMH CBF	log(WMH) ₁	-1.01	-1.81, -0.20	0.015	-1.19	-2.07, -0.32	0.008
Longitudinal analysis: baseline WMH volumes predict changes of CBF							
Δlog(WMH)	GM CBF ₁	0.001	-0.003, 0.003	0.888	-0.002	-0.005, 0.002	0.339
Δlog(WMH)	NAWM CBF ₁	0.001	-0.004, 0.004	0.850	-0.001	-0.005, 0.004	0.758
Δlog(WMH)	WMH CBF ₁	0.002	-0.002, 0.005	0.317	0.002	-0.002, 0.006	0.271

^{*} Multivariate Model was additional adjusted for age, sex, vascular risk factors (i.e., obesity, smoking, history of hypertension, hypercholesterolemia and diabetes) and history of cardiovascular diseases.

Discrimination of Dolichoectasia and Atherosclerosis by MRA Tortuosity Metric Measurements in a Population-based Study

Shang Zhou¹, Melissa Caughey², Xinwei Zhou¹, Bruce Wasserman^{1,3} and Ye Qiao¹

¹ Department of Radiology, the Johns Hopkins University; ²Department of Biomedical Engineering, University of North Carolina & North Carolina State University; ³Department of Radiology, the University of Maryland School of Medicine

Purpose: Vessel tortuosity is an important geometric parameter reflecting vascular aging and medial degeneration. Tortuosity manifests in intracranial arteries, both with atherosclerotic and non-atherosclerotic diseases (e.g., dolichoectasia). Here, we compared the vessel tortuosity calculated by the angle metric (AM) and distance metric (DM), and its performance as a discriminator of radiologist-confirmed dolichoectasia and atherosclerosis, in 1906 older individuals from the general population.

Methods: An image-processing pipeline was developed to measure tortuosity of intracranial vessel segments by MRA in the Atherosclerosis Risk in Communities (ARIC) study [1]. Quantitative measurements (e.g., lumen area, diameter) were obtained at designated vessel segments using automated centerline segmentation in LAVA software (Figure 1A). The total, local, and change rate of AM- and DM-calculated tortuosity were computed using coordinates of the three-dimensional (3D) points from the segment centerline [2] (Figure 1B & 1C). Model performance was compared between AM- and DM-calculated tortuosity, using standardized, qualitative assessments of basilar dolichoectasia [3], and atherosclerosis (identified as eccentric wall thickening) as the outcomes.

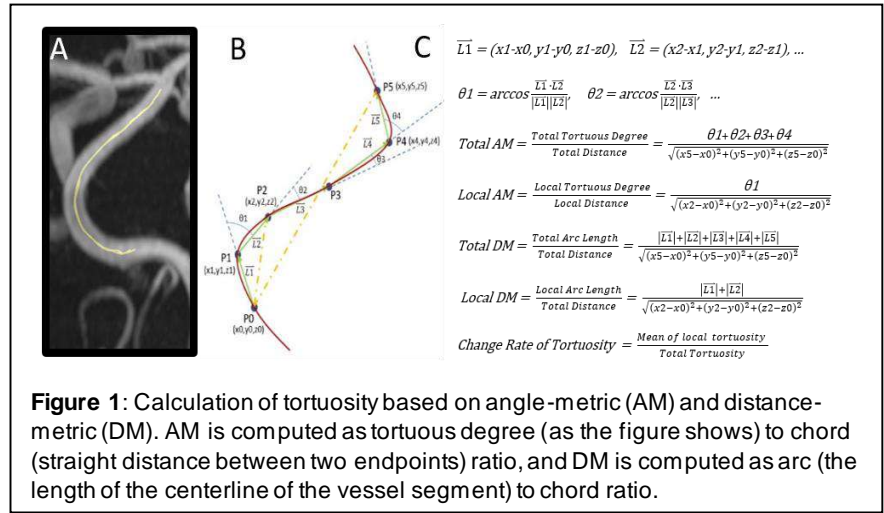


Figure 1: Calculation of tortuosity based on angle-metric (AM) and distance-metric (DM). AM is computed as tortuous degree (as the figure shows) to chord (straight distance between two endpoints) ratio, and DM is computed as arc (the length of the centerline of the vessel segment) to chord ratio.

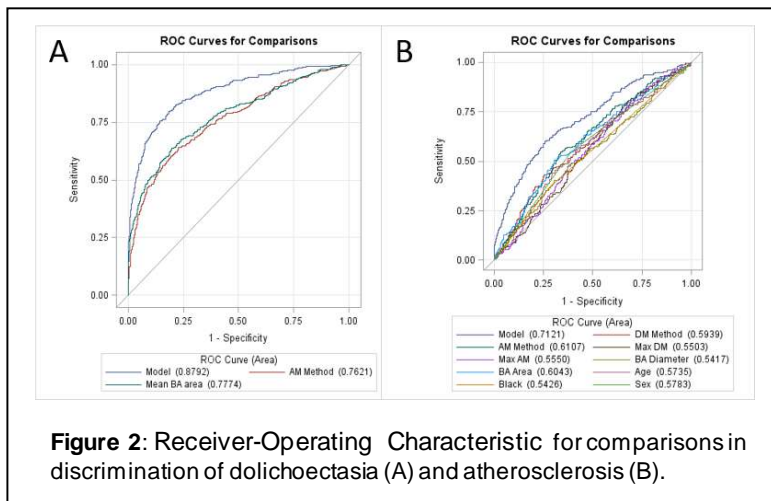


Figure 2: Receiver-Operating Characteristic for comparisons in discrimination of dolichoectasia (A) and atherosclerosis (B).

Results: AM- and DM-calculated total tortuosity were good individual discriminators of dolichoectasia (receiver-operating characteristic area under the curve [AUC] >0.70 for each), with model performance improving with the addition of lumen area (AM model: AUC = 0.88 (Figure 2A), DM model: AUC = 0.87). Individual discrimination of plaque was moderate for both tortuosity metrics but improved when combined with the addition of multiple geometric measures (maximum local tortuosity, lumen area, and diameter) and demographics (full model: AUC = 0.71, Figure 2B). When stratified by “S”, “C”, or “Line” shaped arterial presentation, the change rate of tortuosity improved model performance for discrimination of plaque (“S” shape: AUC = 0.75, “C” shape: AUC = 0.67, “Line” shape: AUC: 0.73).

Discussion and Conclusion: Tortuosity can discriminate intracranial atherosclerosis and dolichoectasia. AM-calculated tortuosity reflects more on the curvature, with DM-calculated tortuosity reflecting more on the vessel extension, both of which impose hemodynamic changes on the vessel wall which may lead to plaque formation. Therefore, the AM and DM methods may be considered complementary tortuosity measures, which discriminate atherosclerosis better in combination than as individual metrics. The change rate of tortuosity may have a larger effect on local hemodynamics and discriminate plaques better in “S” shaped vessels than other presentations. Future prospective studies are needed to test whether the tortuosity metrics can be predictors for the plaque formation.

References: [1] Zhou X et al. ISMRM 2022. [2] Telischak N et al. Clinical Anatomy 2020. [3] Smoker W et al. AJNR 1986.

Automatic centerline extraction of vessel branch based on point detection model

Wei Qiu¹, Hanyu Wei¹, Zhongsen Li¹, Rui Li¹

¹Center for Biomedical Imaging Research, Department of Biomedical Engineering, School of Medicine, Tsinghua University, Beijing 100084, China

Purpose: To purpose a method based on point detection depth learning model to detect seed points, so as to quickly and automatically extract the centerline of the target artery branch (CCA+ICA).

Methods: A total of 139 neck TOF MRA images were selected from the Cardiovascular Risk of Old Population (CROP) study. The central points of the left and right common carotid artery lumens on the 3rd axis slice and Internal carotid artery on the 3rd to last axis slice of the TOF MRA were marked as the starting and ending points of the centerline respectively (seed points). Four Gaussian heatmaps were generated as labels of the CNN model according to the seed points. The dataset was divided into training and test dataset according to a ratio of 4 : 1. The proposed CNN (Figure 1) was improved in the Hourglass model. The number of input image channels was changed from 1 to 5, and the number of convolution channels was optimized. The 1st to 5th axial slices of original image were randomly cut to 512×512×5 size image as the input of the starting point prediction CNN model. And the same was true for endpoint detection. Based on the starting and ending points, the shortest path method was used to obtain the centerline of the target branch on the image after vessel enhancement. The correct prediction was defined as the point located in the lumen, and the Percentage of Correct Keypoints and average distance between points were used to measure the performance of the model. The overlap proportion of the centerline in the blood vessel (OV) was used to measure the tracking ability of the extraction algorithm.

Result: The improved CNN achieved the highest point detection accuracy (0.982) and the minimum distance (1.90 pixel) compared with Hourglass and Res-U-Net model (Table 1 and Figure 2). The centerline extraction experiments (Figure 3) obtained more than 96% OV values on five test results by manual analysis.

Conclusion: Combined with the improved point detection model and traditional centerline extraction algorithm, we can extract the target branch centerline quickly and automatically with ultra-high detection accuracy and tracking ability.

Table 1 Statistical test results of key point detection

Methods	Our CNN	Hourglass	Res U-Net
Accuracy	0.982	0.955	0.866
Average distance (pixel)	1.90	2.31	2.37

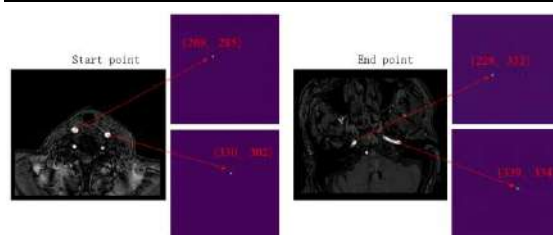


Figure 2 Point detection result

Figure 1 Our CNN architecture

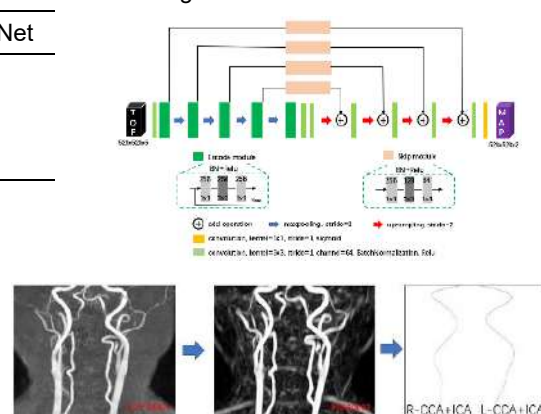


Figure 3 Centerline extraction result

Rapid 3D head-neck MRA using velocity-selective pulse train and spiral acquisition

Dan Zhu^{1,2}, Qin Qin^{1,2}

1. Kirby Research Center, Kennedy Krieger Institute; 2. Radiology, Johns Hopkins University, Baltimore, Maryland, U.S.A.

Purpose: MRA of the head and neck is of great clinical value for the diagnosis of carotid and intracranial artery diseases. Non-contrast-enhanced (NCE) head and neck MRA techniques such as TOF, ASL¹⁻², QLASH³, and QISS⁴, are time-consuming, usually > 3 minutes for an isotropic resolution of ~1mm. Recently, Fourier-transform-based velocity-selective (VS) MRA was successfully demonstrated for brain and abdominal NCE MRA⁵⁻⁷. In this work, we enabled a fast 3D VSMRA of head and neck with an isotropic resolution of 1 mm in about 1.5 min using efficient stack-of-spiral acquisition.

Methods: IRB approved experiments were conducted on a 3T Philips scanner with a 28-channel head-neck-spine coil. 8 healthy subjects (40.9±14.5 yo 5F) were evaluated with the spiral VSMRA sequence (Fig. 1a). An adiabatic spatially selective inversion (SSI) pulse with a 900ms inversion delay nulls the venous signal draining from brain tissue. Then an 80ms Fourier-transform-based velocity-selective saturation (VSS) pulse train (Fig. 1b, with phase-cycled composited refocusing) with a cutoff velocity of 1cm/s (profile shown in Fig. 1c) was applied to suppress the static brain signal, followed by an optimized composite pulses SPIR fat suppression⁸ and a 3D stack-of-spiral FLASH acquisition. Imaging parameters are: 3D coronal FOV=300(FH) x 300(RL) x 120(AP)mm, resolution = 1mm isotropic, FA = 15°, TR = 15ms (readout window = 10ms), TE = 1.3ms, echo train length = 38, SENSE factor = 2 (through plane), shot interval = 2s, and total scan time = 1'38". Two VSMRA sequences were compared with different SSI coverage: one higher SSI covering the brain only, and one lower SSI covering both the head and the neck.

Results: Fig. 2 demonstrates the coronal and sagittal maximum intensity projection (MIP) of the spiral VSMRA images from two representative subjects (31 yo M, 30 yo F) comparing a lower SSI (top) and a higher SSI (bottom) coverage. Major aortic arch, carotid, vertebral, intracranial and extracranial arteries are all well depicted. With lower SSI, venous contamination is reduced compared to the images with higher SSI, but the distal vertebral arteries, basilar arteries, intracranial arteries and extracranial arteries are better depicted with a higher SSI. Fig. 3 demonstrates the bilateral carotid bifurcations clearly depicted by the VSMRA with lower SSI.

Discussion: In this work, we demonstrate the feasibility of a 1mm isotropic resolution head-neck spiral VSMRA in 1.5min. Since only a low SENSE factor of 2 was used without any partial Fourier, this technique is capable of further acceleration such as compressed sensing⁹ and deep learning^{10,11}.

References: 1. Koktzoglou I, *JMRI*, 2011;34:384; 2. Koktzoglou I, *JMRI*, 2015;41:1150; 3. Koktzoglou I, *MRM*, 2016;75:2072; 4. Koktzoglou I, *JMRI*, 2019;50:1798; 5. Qin Q, *MRM*, 2016;75:1232; 6. Li W, *MRM*, 2018;79:2014; 7. Zhu D, *MRM*, 2020;84:1173; 8. Feng X, *MRI*, 2021;75:156; 9. Lustig M, *MRM*, 2007;58:1182; 10. Koktzoglou I, *MRM*, 2020;84:825; 11. Koktzoglou I, *MRM*, 2021;86:335

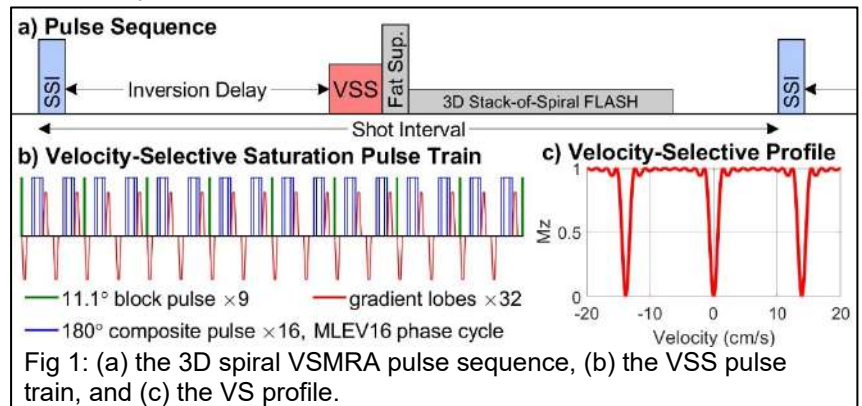


Fig 1: (a) the 3D spiral VSMRA pulse sequence, (b) the VSS pulse train, and (c) the VS profile.

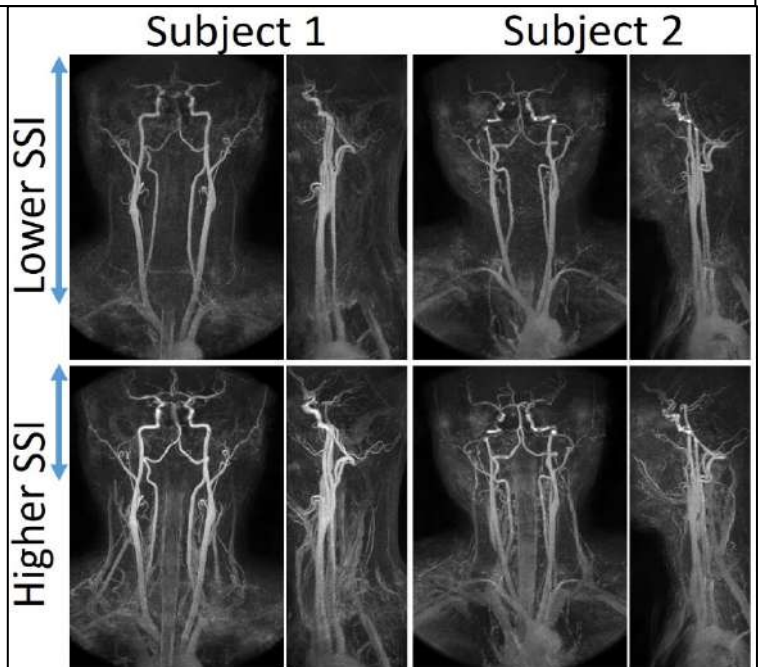


Fig 2. MIP of VSMRA with lower (top) and higher (bottom) SSI coverage (blue arrows). Vertebral, basilar, and intracranial and extracranial arteries are better visualized with higher SSI at a cost of more contamination from jugular veins and vertebra.

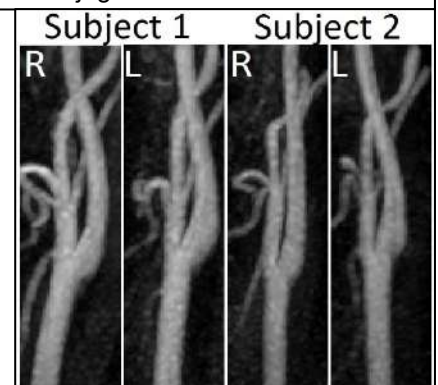


Fig. 3. Bilateral carotid bifurcations are clearly depicted by VSMRA with lower SSI coverage.

Optimization of 4D flow MRI spatial resolution using a patient-specific phantom model of a carotid web

Retta El Sayed^{1,2}, Alireza Sharifi², Charlie C. Park², Jason W. Allen^{1,2,3}, John N. Oshinski^{1,2}

¹Department of Biomedical Engineering, Georgia Institute of Technology & Emory University, Atlanta, GA, USA

²Department of Radiology & Imaging Sciences Emory University, Atlanta, GA, USA.

³Department of Neurology, Emory University, Atlanta, GA

Purpose: 4D flow MRI has been used extensively to measure blood velocity and to quantify different hemodynamic parameters in the great vessels.¹ A limited number of studies have demonstrated the use of 4D flow MRI in smaller vessels such as the carotids and cerebral vasculature, but the accuracy of the 4D flow MRI data in these vessels has not been well-studied, specifically in the setting of pathology.² Carotid artery webs (CaWs) are non-inflammatory intraluminal shelf-like projections in the ICA bulb that are associated with up to 21.2% of patients with cryptogenic stroke.³ We created a phantom model of CaW to study flow patterns and optimize 4D flow MRI for measuring the velocity field in the presence of complex flow induced by CaW. Different 4D flow MRI spatial parameters were compared to computational fluid dynamics (CFD) simulation of the flow field as a reference. *We hypothesized that an optimized spatial resolution of 4D flow MRI will allow a clinically feasible scan time (~5 mins), with adequate image quality for which velocity values will have a correlation coefficient with CFD values of ≥ 0.85 .*

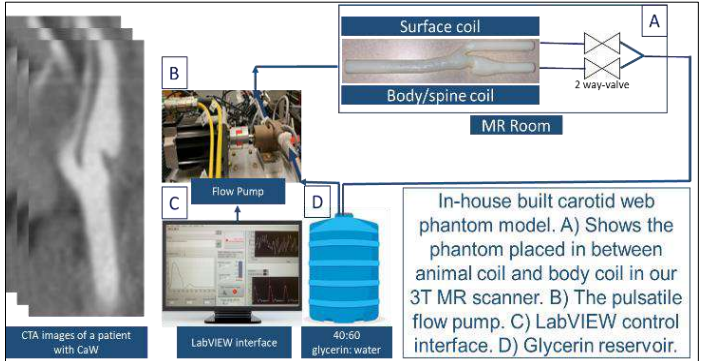


Figure 1. Overview of the flow system and phantom model. Patient with CaW CTA images of the segmented carotid geometry are shown.

Methods: A patient-specific 3D model of a carotid bifurcation with CaW that produced 44% stenosis was segmented from a CTA scan using Mimics (Materialise NV, 2019) (**Figure 1**). A model was 3D printed using an Object 30 printer (Stratasys Ltd, MN, 2020) and an MRI visible material (RGD525) in order to limit wall noise in the phase images.⁴ The phantom model was placed in an open loop flow system (**Figure 1**). A 60:40 by volume water:glycerol solution was used as a surrogate for blood. Pulsatile, carotid specific flow waveform was applied at the inlet with a simulated heart rate of 60 bpm using a flow pump controlled using LabVIEW interface. The phantom was placed in a surface coil and imaged using 3.0 Tesla MRI scanner (Siemens Prisma). 4D flow MRI was repeatedly acquired with varying spatial resolution (0.50-2.00 mm³, Isotropic). For the CFD study, multi-slab, transverse, 3D time of flight (TOF) images of the phantom were acquired through the bifurcation (pixel=0.5mm³, TR=23ms, TE=3.1ms) to provide geometric boundary conditions for the CFD. 2D, ECG-gated, cine phase contrast (PCMR) images were acquired 10mm below the bifurcation (pixel size=1x1x5mm, VENC=80cm/sec, TR=43.6, TE=7) to provide flow boundary conditions for CFD. Each 4D flow MRI scan was filtered for noise, eddy current, aliasing and imported into EnSight (Ansys, PA, 2019 R2).¹ Five planes perpendicular to the lumen of the CCA and ICA were placed and the velocity profiles were compared between 4D flow MRI and CFD. The 2D profiles from 4D flow MRI and CFD were re-gridded and voxel-to-voxel correlation coefficient was calculated.

Results. The 3D velocity profile at five different spatial resolutions and at five different planes were compared (**Figure 2**). **Figure 2** also shows the correlation coefficient of the voxel-to-voxel comparison between 4D flow MRI and CFD at ICA 10 mm plane above the bifurcation (profiles in red box). Resolution at 0.5mm³ showed noisy measurements and reduced correlation values. A resolution of 0.74 to 1.00 mm³ resulted in good agreement to CFD (best correlation coefficient), visually resolving complex flow patterns in CaWs with clinically reasonable scan time. A resolution of 1.5 and 2 mm³ blurred out the velocity skewing and resulted in the lowest correlation.

Conclusion. 4D flow MRI spatial resolution of 0.74 mm³ showed a correlation coefficient 0.89 with CFD in areas of highly complex flow and was performed in a clinically reasonable scan time.

References: [1]Bock J, et al. Optimized pre-processing of time-resolved 2D and 3D Phase Contrast MRI data. 2007. [2]Cibis M, et al. *PLoS ONE*. 2016; 11(9). [3]Sajed PI, et al. *AJNR Am J Neuroradiol*. 2017;38(7). [4] Mitsouras D, et al. *Magn Reson Med*. 2017;77(2):613- 622.

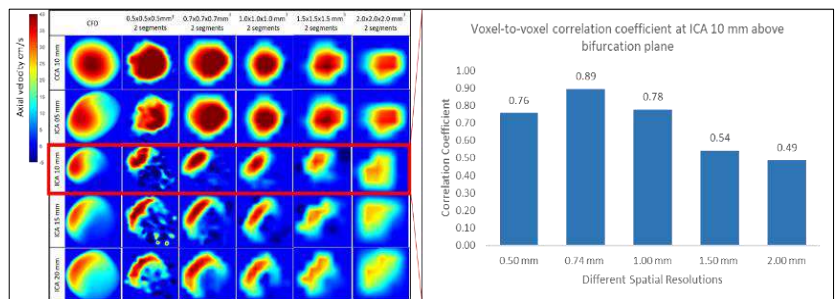


Figure 2. Velocity profiles from 4D flow MRI compared to CFD simulations at five 2D planes at 5 different spatial resolutions (left). Voxel-to-voxel correlation of 4D flow MRI and CFD at the location 10 mm distal to the bifurcation where complex flow is expected at the 5 spatial resolutions (right).

Image Processing Framework for Categorization of Intracerebral Hemorrhage Age Features

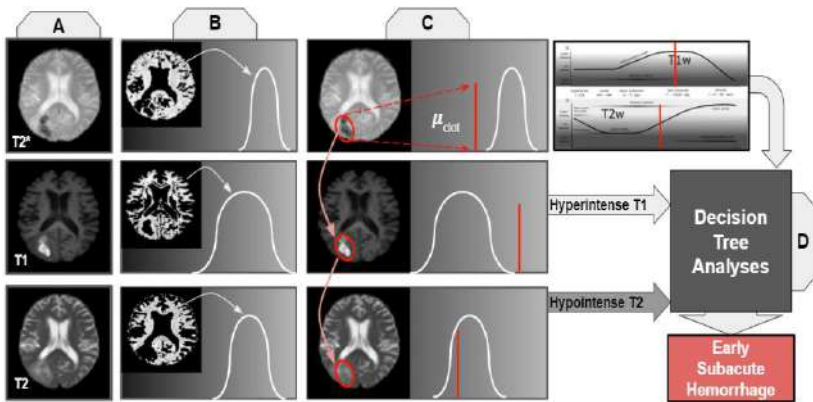
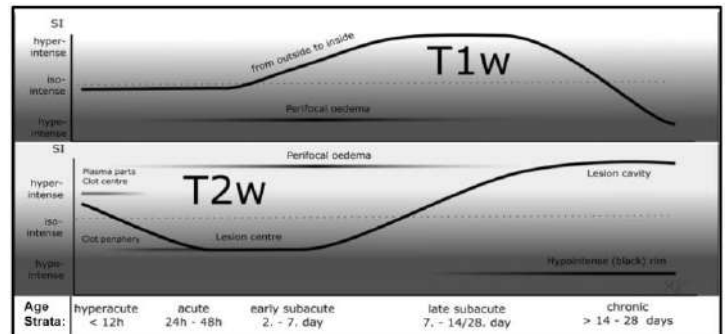
Thomas Lilieholm¹, Matt Larson², Azam Ahmed³, Walter F Block^{1, 2, 4}

¹ Medical Physics, University of Wisconsin- Madison, WI ² Radiology, University of Wisconsin- Madison, WI ³ Neurosurgery, University of Wisconsin- Madison, WI ⁴ Biomedical Engineering, University of Wisconsin- Madison, WI

Purpose: Automatic segmentation of intracerebral hemorrhage (ICH) would simplify visualization and characterization of ICH for neurosurgeons before and during minimally invasive surgery for clot evacuation. We have previously developed a successful CNN approach for clots less than 4 days old¹. But varying multiparametric contrast with clot age² forces the need for multiple tuned CNN networks based on approximate age of each ICH clot. Even non-ML-based automated solutions are restricted with regards to age-variation³. We present a Decision Tree Analytical approach for automatically determining the approximate clot age-category that would in turn be used to select a corresponding CNN for robust automatic segmentation independent of clot age.

Methods: MR scans of ICH patients were collected. Each case contained a T1w, T2w with fat saturation, and a T2* scan. All images were acquired on 3T GE machines at the UW hospital. Two brains in the dataset had multiple hematomas, making for 16 total clots for analysis. Ground truth determinations of clot age categorizations were done through independent manual inspection by two neuroradiologists. Their classifications were largely consistent, disagreeing on only 3 clots in the 16 clot dataset. Each scan in the dataset was skull-stripped, co-registered, and intensity normalized, as shown in Figure 2A. Intensity histograms were generated for each weighting to determine white matter intensity over the total brain volume, as shown in Figure 2B. The mode of each histogram was used as the intensity of white matter. Once per clot, a two-dimensional ellipsoid ROI was manually placed over hematoma regions using T2*-W scans for easier clot identification across cases. The mean intensity value from each clot ROI was compared to white matter intensity for each parametric image. Categorical decisions of hypo-, iso-, or hyper-intensities were quantified based on whether or not the clot regions' mean intensities fell within one standard deviation of the mode intensity of white matter. As shown in Figure 2D, a Decision Tree produces a clot age characterization based on the parametric comparisons computed in Figure 2C.

The internal specifications of the Decision Tree are based on the intensity trends outlined in Figure 1.



Results: The methodology proposed here was able to match expert age categorization for 11 of the cases in our initial 16 clot dataset. This was done swiftly and with minimal user input-requiring only the manual placement of an ROI over human-identified clot locations once per case. Of the 5 incorrect classifications, 3 were the cases that our expert raters disagreed on. In these cases, we defaulted to the more senior neuroradiologist's assessment.

Discussion: The developed methodology is able to categorize a clot as being hyperacute, acute, early subacute, late subacute, or chronic within

an acceptable margin of accuracy with no more user input than the placement of a single ROI per clot. This is done making use of multiparametric scan data, including T1-W, T2-W, and T2*-W scans of each ICH case. Future work will expand the dataset volume and further automate the process, employing autonomous methods to identify and select clot regions without user input. Results of this work may be used to inform later age- or contrast-dependent processing steps in autonomous workflows².

References: [1] Lilieholm T, Henningsen M, Ahmed A, McMillan, A Block WF, Neural Network for Autonomous Segmentation and Volumetric Assessment of Clot and Edema in Intracerebral Hemorrhages, Proc. of International Society of Magnetic Resonance in Medicine, 2021. [2] Gaillard, F., Jones, J. Hemorrhage on MRI. Reference article, Radiopaedia.org. (accessed on 08 Nov 2021) <https://doi.org/10.53347/rID-6671>. [3] 17. Pszczolkowski S, et al. Automated segmentation of haematoma and perihematoma oedema in MRI of acute spontaneous intracerebral haemorrhage. Comput Biol Med. 2019 Mar;106:126-139. doi: 10.1016/j.combiomed.2019.01.022. Epub 2019 Jan 29. PMID: 30711800; PMCID: PMC6382492.

Cerebral Microbleeds (CMBs) automatic detection system based on the “Deep Learning”

Pingping Fan, Wei Shan, Huajun Yang, Yu Zheng, Zhenzhou Wu, Shang Wei Chan, Qun

Wang, Peiyi Gao, Yaou Liu, Kunlun He, and Binbin Sui

Constitute: Beijing Tiantan Hospital, Capital Medical University, Beijing, China

Abstract:

Objective: To validate the reliability and efficiency of clinical diagnosis of cerebral microbleeds (CMBs) , we construct a deep learning system (DLS).

Method: We retrospectively included 1615 MRI-SWI datasets diagnosed with clear CMBs obtained between September 2018 and September 2019. The patients were divided into training, and validation cohorts of 1,285 and 330 patients respectively, and another 30 patients were used for internal testing. After labeling, a revised U-net was applied to construct a DLS and tested with another 72 patients. These results were evaluated by 5 radiologists and subjected to an output analysis divided into missed label, incorrect label and correct label. The inter-radiologists DLS agreement rate was assessed using kappa's test.

Results: In the detection of the CMBs, the DLS achieved a Dice coefficient of 0.72 and more than 90% of the lesions were detected by our DLS. The kappa value reached 0.79 on average.

Conclusion: Based on the results, the automatic detection system of CMBs is feasible.

Additional information: this paper was published this year.

Non-Contrast Carotid 3D TOF and Time-SLIP bSSFP with centric ky-kz k space trajectory

V Malis,¹ J Kungsumutr,² W Bae,^{1,3} X Zhang,¹ Y Falls,⁴ C Duxbury,⁴ Y Kassai,⁵ M. McDonald,¹ M Miyazaki¹

1. Dept. of Radiology, University of California-San Diego (UCSD), La Jolla, CA 2. Dept. of Bioengineering, University of California-San Diego (UCSD), La Jolla, CA 3. Dept. of Radiology, VA San Diego Healthcare System, San Diego, CA 4. Canon Medical Systems, USA, 5. Canon Medical Systems, Tochigi, Japan.

Purpose: Carotid artery stenosis (CAS) is a frequent disease seen in general practice. It is one of the most common causes of acute ischemic stroke, accounting for around 20% of occurrences. [1] Thus, it is critical to diagnose, prevent, and treat it early. Several MRA techniques are routinely utilized for CAS diagnostics, [2] yet among the challenges is a long scan time. In this study, we compared the depiction of carotid artery using: (i) 3D time-of-flight (TOF) and (ii) flow-in 3D balanced steady-state free precession (bSSFP) with time spatial labeling inversion pulse (Time-SLIP).[3,4] Both techniques were scanned using 3D MRA with and without centric k_y - k_z acquisition pattern (FAST3D) [5].

Table 1. Scan parameters

sequence parameter	3D TOF	3D TOF FAST3D	3D bSSFP with Time-SLIP	3D bSSFP with Time-SLIP FAST3D
TE/TR [ms]	3.4/10	3.4/10	2/4	2/4
FA [degree]	18°	18°	120	120
FOV [mm ²]	200 × 200	200 × 200	320 × 360	320 × 360
Voxel size [mm ³]	0.4 × 0.4 × 0.8	0.4 × 0.4 × 0.8	0.63 × 0.63 × 0.8	0.63 × 0.63 × 0.8
SPEEDER	3	3	2.8	2.8
Scan time	5:30	3:40	3:53	1:57

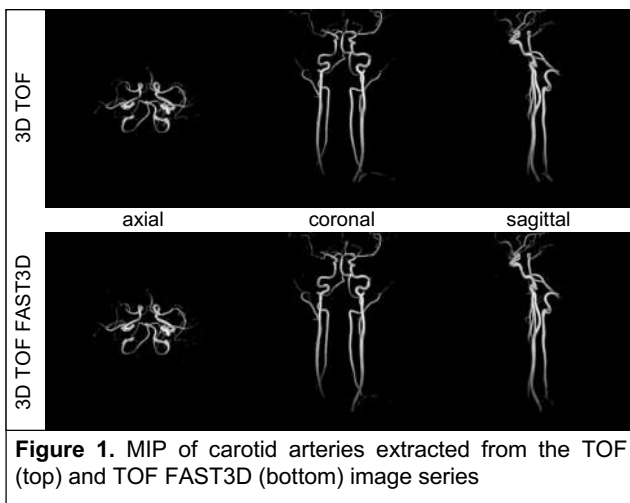


Figure 1. MIP of carotid arteries extracted from the TOF (top) and TOF FAST3D (bottom) image series

cord was manually cut out of the volume prior to filtering. Table 1 shows the detailed acquisition parameters.

Results: Figure 1 shows MIP in axial, coronal and sagittal orientation of regular and FAST3D TOF series. The arteries are well depicted with the FAST3D sequence without compromising the image quality. The vessel structures were extracted automatically using the Frangi filter. MIP in coronal orientation for 3DSSFP with Time-SLIP and zoomed in carotid artery region without a spinal cord are shown in Figure 2. Similar image quality between standard and sparse sequences can be visually appreciated. Note that tremendous scan time reduction in both 3D TOF and Time-SLIP 3D bSSFP with FAST3D, as shown in Table 1.

Discussion: Acquisition windows of FAST3D are extended due to filling of ky-kz k space trajectory, which cause blurring around aortic arch. We have increased the parallel imaging reduction factor (SPEEDER) to reduce the acquisition window. Both images of 3D TOF and Time-SLIP bSSFP with FAST3D show compatible image quality, as compared to those without FAST3D, yet with substantial scan time reductions.

Conclusions: Both TOF and Time-SLIP bSSFP with FAST3D provide remarkable scan time reduction with good image quality.

References: [1] Arasu R, et.al Aust J Gen Pract. 50(11) (2021). [2] Westwood ME, et.al BMJ. 324(7331):198 (2002). [3] Miyazaki M, et al JMRI 35:1-19 (2012). [4] Miyazaki M, et al EJMR 80:9-23 (2011). [5] Busse RF, et al MRM 60:640-649, (2008). [6] Frangi, et.al MICCAI. 1(1496) (1998).

Methods: Four healthy (51 ± 13 years) volunteers were scanned on a clinical 3T scanner (Vantage Galan 3T, Canon Medical Systems, Japan) after signing IRB-approved consent form. Images were acquired using Atlas Head and Neck SPEEDER coil. The scanning protocol consisted of the following series: (a) 3D TOF (b) 3D TOF FAST3D both with 11 slabs covering aortic arch to middle cerebral arteries without gating; (c) 3D bSSFP (d) 3D bSSFP FAST3D; both PPG-gated with Time-SLIP tag pulse (TI=1200 ms) applied to the carotid artery region in the coronal orientation. Maximum intensity projection (MIP) images were reconstructed for all the series and further improved using Hessian-based Frangi filter [6]. For T-SLIP images spinal

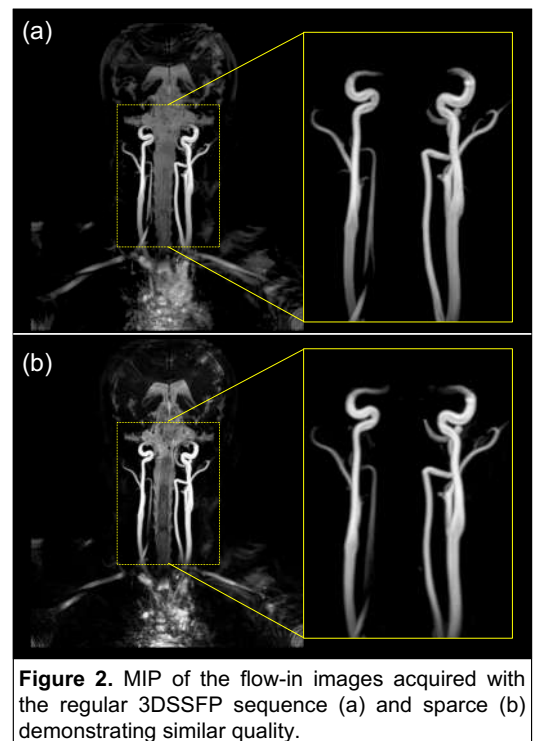


Figure 2. MIP of the flow-in images acquired with the regular 3DSSFP sequence (a) and sparse (b) demonstrating similar quality.

Usefulness of Arterial Spin Labeling MR Angiography for Follow-Up after endovascular treatment for unruptured intracranial aneurysm in comparison with Time-of-Flight MRA

Yiping Zhang

Department of Interventional Neuroradiology, Beijing Neurosurgical Institute, Beijing, China

Background and purpose: Time-of-Flight MRA is the most commonly used non-contrast-enhanced imaging method at present, but due to the influence of magnetic susceptibility and radiofrequency shielding, it is difficult to visual flow in the stent with TOF MRA. Arterial Spin Labeling (ASL) MR Angiography can minimize the influence of metal artifacts. The purpose of the study was to evaluate the clinical value of magnetic resonance angiography using arterial spin labeling (ASL) in patients with treated intracranial aneurysms.

METHODS: Four patients treated with Flow-Diverter Device and six patients with Stent-Assisted Coil Embolization for intracranial aneurysms underwent ASL MRA, 3D TOF-MRA at the same time. TOF-MRA and ASL MRA images were obtained during the same scan session imaging system. Two experienced neuroradiologists used a 4-point scale from 1 (not visible) to 4 (excellent) to grade the quality MRA visualization of the reconstructed artery. Occlusion status was assessed using the 3-grade Montreal scale. To explore the diagnostic performance of two MRA methods in evaluating aneurysm occlusion. The overall image quality and visualization of the treatment site were evaluated independently.

RESULTS: The mean scores of ASL MRA and TOF-MRA regarding the visualization of the reconstructed artery were 3.2 ± 0.7 and 2.3 ± 0.8 , respectively. Showing a higher score for the flow on silent MRA than on 3D TOF-MRA. ASL MRA is more clearly in showing the occlusive state of aneurysms.

CONCLUSION: ASL MRA was superior to TOF MRA for visualizing the parent artery and evaluating occlusion status. ASL MRA can be useful to evaluate treated intracranial aneurysms with superior visualization and higher diagnostic performance.

References: [1] Irie R, et al. AJNR Am J Neuroradiol.2015;36(5):967-970. [2] Oishi H, et al. AJNR Am J Neuroradiol.2019;40(5):808-814.

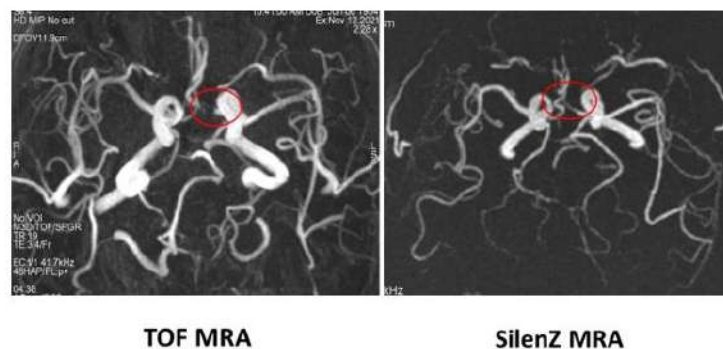


Figure 1 A 66-year-old female patient with a treated aneurysm in the anterior communicating artery by stent-assisted coil embolization.

Multi-delay multi-parametric arterial spin-labeled perfusion MRI in Moyamoya disease- Comparison with dynamic susceptibility contrast enhanced perfusion imaging

Hongtao Zhang¹, Mingming Lu¹, Shitong Liu¹, Jianming Cai¹

1. Department of Radiology, the Fifth Medical Centre of Chinese PLA General Hospital, Dongda Street 8, Beijing 100071, China

Purpose:

This study aims to evaluate multi-delay multi-parametric pseudo-continuous ASL (pCASL) accuracy comparison with dynamic susceptibility contrast (DSC) enhanced perfusion imaging.

Methods:

62 MMD patients underwent pCASL and DSC-MRI. We measured the brain, cerebellum, main cerebral artery blood supply areas and ASPECTS relevant areas. Six quantitative parameters were measured. The correlations of parameters between DSC and pCASL were determined. The consistency between the two techniques in assessing the cerebral ischemic state before and after revascularization were analyzed.

Results:

Significant correlation was exhibited between pCASL and DSC-MRI parameters ($p < 0.05$). For surgically treated patients, the blood perfusion parameters improvement on the operated side were statistically different ($p < 0.05$) and good consistency respectively.

Discussion:

Compared to DSC-MRI, pCASL can assess the cerebral hemodynamics in MMD before and after revascularization effectively.

Reference:

[1] Rui Wang, Songlin Yu, Jeffry R Alger, Zhentao Zuo, Juan Chen, Rong Wang, Jing An, Bo Wang, Jizong Zhao, Rong Xue, Danny J J Wang. Multi-delay arterial spin labeling perfusion MRI in moyamoya disease--comparison with CT perfusion imaging. *Eur Radiol* 2014; 24(5):1135-1144.

[2] Danny J J Wang, Jeffry R Alger, Joe X Qiao, Matthias Gunther, Whitney B Pope, Jeffrey L Saver, Noriko Salamon, David S Liebeskind, UCLA Stroke Investigators. Multi-delay multi-parametric arterial spin-labeled perfusion MRI in acute ischemic stroke - Comparison with dynamic susceptibility contrast enhanced perfusion imaging. *Neuroimage Clin* 2013; 3:1-7.

In Vivo T2* Mapping of Intracranial Atherosclerotic Plaque Distinguishes Symptom-Producing Plaques: a 7T MRI study

Ziming Xu¹, Xiaoyan Bai², Yajie Wang¹, Zhiye Li², Jiaqi Dou¹, Binbin Sui³, Huijun Chen¹

1. Center for Biomedical Imaging Research, Department of Biomedical Engineering, School of Medicine, Tsinghua University, Beijing, China. 2. Department of Radiology, Beijing Tiantan Hospital, Capital Medical University, Beijing Neurosurgical Institute, Beijing, China. 3. Tiantan Neuroimaging Center of Excellence, China National Clinical Research Center for Neurological Diseases, Beijing, China.

Purpose: Intracranial atherosclerotic plaque is one of the leading causes of ischemic stroke^{1,2} and is usually evaluated by qualitative vessel wall MRI^{3,4}. Previous in vivo studies on carotid plaque showed great potential of quantitative evaluation in plaque characterization^{5,6}. In particular, T2* mapping, which is related to intraplaque iron deposits, is essential in carotid plaque progression⁷. However, limited by the intracranial artery size and MR resolution, previous intracranial plaque quantitative studies were usually carried out ex vivo^{8,9}. In recent years, 7T MR has a huge breakthrough in imaging resolution, thus providing accessibility to observe intracranial plaque in vivo. Therefore, we aim to quantitatively measure T2* of intracranial atherosclerotic plaque in vivo using 7T MR and distinguish symptomatic and asymptomatic plaques.

Methods: Subjects: Patients with middle cerebral artery (MCA) atherosclerotic plaques diagnosed by 3T MRI were recruited. Age, gender and blood tests were also recorded. Imaging Protocol: Intracranial MR examinations of all patients were performed on a 7T MR scanner (MAGNETOM Terra, Siemens Healthcare, Erlangen, Germany) using a 32-channel head coil. A T1-weighted 3D Sampling Perfection with Application-optimized Contrast using different flip angle Evolutions (SPACE) was performed to localize the plane demonstrating the narrowest MCA lumen. Then multi-echo gradient-echo sequence was performed on this plane. T2* map was exponentially fitted by T2*-weighted images from 6 echo time (TE). Outer wall and lumen of intracranial plaque was manually drawn on T2*-weighted images from the first echo using CASCADE¹⁰, and the region between outer wall and lumen was regarded as plaque regions of interest (ROI). Mean T2* value within the plaque ROI was recorded. Clinical Data Assessment: Symptomatic patients were defined as patients who had ischemic stroke or transient ischemic attack in the distribution of the stenotic MCA within four weeks before MR examinations; while asymptomatic patients were considered if there was no history of cerebrovascular events or if the ischemic event occurred in a vascular territory outside the affected MCA^{11,12}. Statistical Analysis: Two-tailed independent Student's t test or Mann-Whitney U test was performed to compare each continuous variable between symptomatic and asymptomatic patients. Pearson correlation coefficients were calculated between T2* and the clinical characteristics. $p < 0.05$ was considered as statistically significant and all analyses were performed using R.

Results: 20 symptomatic patients and 15 asymptomatic patients were recruited in this study. No significant difference was found in age, gender and blood tests between the two groups. T2*-weighted images and map of one symptomatic patient are shown in Figure 1. Asymptomatic patients showed significantly higher intraplaque T2* value than symptomatic patients (29.87 ± 5.38 vs. 21.46 ± 6.01 ms, $p < 0.001$) (Figure 2).

Discussion and Conclusion: This quantitative and noninvasive T2* measurement of intracranial atherosclerotic plaque at 7T MR can significantly distinguish symptomatic patients from asymptomatic patients, providing a potential tool for identifying symptom-producing intracranial atherosclerotic plaques.

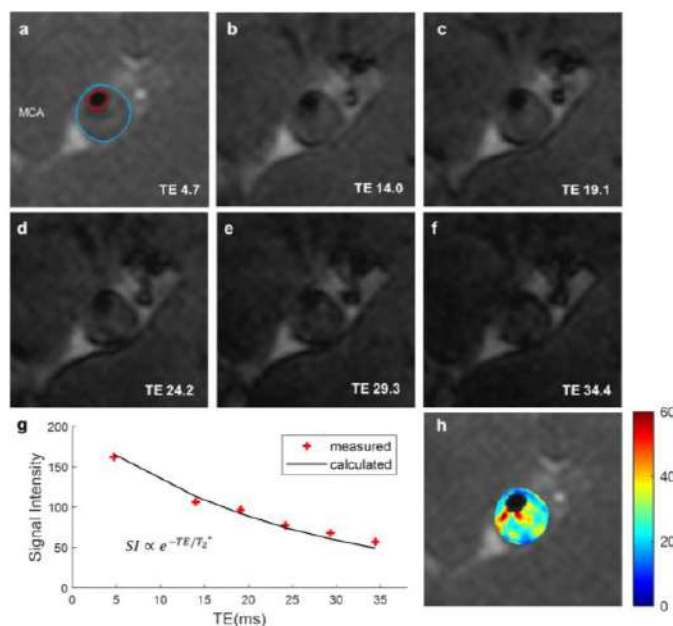


Figure 1. T2*-weighted images, plaque signals and T2* map.

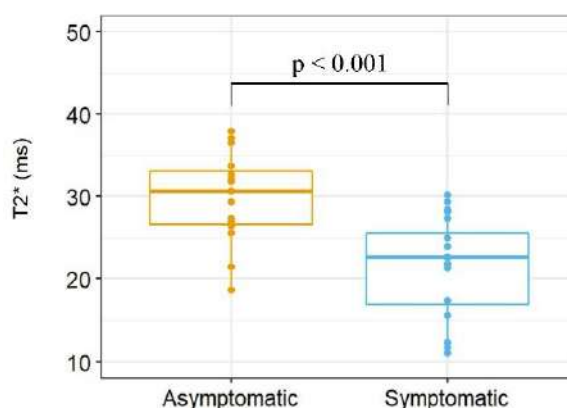


Figure 2. Intraplaque T2* values in two groups.

References: [1] Yu YN, et al. AJNR. 2019. [2] Wang Y, et al. Stroke. 2014. [3] Mandell DM, et al. AJNR. 2017. [4] Lee HN, et al. Front Neurol. 2018. [5] Qi H, et al. Radiology. 2018. [6] Chai JT, et al. JACC. 2017. [7] Raman SV, et al. JACC. 2008. [8] Jiang Y, et al. J. Atherosclerosis. 2016. [9] Azuma M, et al. AJNR. 2020. [10] Kerwin W, et al. TMRI. 2007. [11] Chung JW, et al. Stroke. 2016. [12] Gupta A, et al. Cerebrovasc Dis. 2015.

Comparison of Carotid Atherosclerosis Plaque Characteristics Between Elderly Men and Women Using Magnetic Resonance Vessel Wall

Lichen Zhang¹, Mingming Lu¹, Lina Zhu², Xihai Zhao³, Feiyu Li⁴, Jianming Cai¹, and Chun Yuan⁵

1. Department of Radiology, the Fifth Medical Center, Chinese PLA General Hospital; 2. Department of Radiology, The first Affiliated Hospital of Zhengzhou University, No.1; 3. Center For Biomedical Imaging Research, Department of Biomedical Engineering, School of Medicine, Tsinghua University; 4. Operation Department, RIMAG Medical Imaging Corporation; 5. Department of Radiology, University of Washington.

Purpose: Characteristics of carotid atherosclerosis are important to plaque stabilization and different between men and women. We aimed to investigate the differences of carotid atherosclerosis plaque characteristics between symptomatic elderly men and women using magnetic resonance vessel wall imaging.

Methods: A total of 327 elderly patients over 60 years old with ischemic stroke and (or) transient ischemic attack (TIA) within two weeks, and atherosclerotic plaques in both carotid arteries which were detected by ultrasound were recruited in more than ten medical centers from northeast, north, east, and south China, including 231 men and 96 women. We compared the carotid plaque morphology features such as lumen area(LA), wall area(WA), total vessel area(TVA), normalized wall index(NWI), mean wall thickness(MWT), and luminal stenosis, and composition features including the presence of calcification, lipid-rich necrotic core(LRNC), intraplaque hemorrhage(IPH), fibrous cap rupture(FCR), and high risk plaque (HRP)of the index carotid arteries and the features above in non-index carotid arteries between men and women. MR vessel wall imaging sequences were three-dimensional time-of-flight (3D TOF), T1-weighted (T1-W) quadruple inversion recovery (QIR), T2-weighted (T2-W) multislice double inversion recovery (MDIR), and Magnetization Prepared Acquisition Gradient Echo (MP-RAGE).

Results: In the subset of symptomatic atherosclerotic elderly patients, men had greater WA, TVA, NWI, higher MWT, luminal, and were more prevalent to have LRNC, IPH, FCR, and HRP in the comparison of the index carotid arteries between men and women (all $p < 0.05$). Then the clinical confounding factors ($p < 0.1$) were adjusted (Table 1). The significances of the differences in WA, TVA, MWT, and the prevalence of LRNC and IPH between sexes stayed still in multivariable Model 1 (all $p < 0.05$). After adjusting for the confounding factors in multivariable Model 1 and NWI (multivariable Model 2), there was no differences in carotid morphological characteristics between men and women (Table 2). In the comparison of the non-index carotid arteries, elderly men had greater LA, WA, TVA, NWI, higher MWT, luminal stenosis, and more prevalence to suffer from calcification, LRNC, IPH, FCR, and HRP (all $p < 0.05$). After adjusting for the clinical confounding factors, the significances of differences in WA, TVA, NWI, MWT, luminal stenosis, the prevalence of LRNC, IPH, FCR, and HRP existed in multivariable Model 1 (all $p < 0.05$). The prevalence of LRNC, IPH, and HRP between men and women were significantly different (all $p < 0.05$) after adjusting for the clinical confounding factors in multivariable Model 1 and NWI (multivariable Model 2) (Table 3). The figure shows an example of the symptomatic carotid artery in an elderly man[1].

Discussion:

We found elderly men had larger WA, TVA, and thicker MWT in both carotid arteries, also greater NWI, luminal stenosis, more prevalence of LRNC, IPH, and HRP in asymptomatic carotid arteries compared with women. We inferred that the similar terminal progression of symptomatic carotid atherosclerosis in elderly men and women leads to stroke and TIA. We found elderly men had more vulnerable carotid plaque in asymptomatic arteries compared with women. The asymptomatic carotid arteries atherosclerosis plaques are in a bad way because that suffered from the same severe clinical factors with symptomatic sides. Studies showed atherosclerosis can be conducted by hormones, genes, and other invariable factors, and the factors above make men more prone to have vulnerable plaques. Genes impact carotid intima-media thickness[2,3] also the uptake of lipoprotein from artery wall[4-6]. The stability of plaque and differences of HDL-cholesterol and apolipoprotein between men and women can be influenced by genes, too. Sex hormones play a role in atherosclerosis that sex hormone binding globulin, estrone, estradiol, and follicle-stimulating hormone all associate with plaque characteristics[7-10].

References:

- [1] Zhang L, et al. J Magn Reson Imaging, 2021, 54(2): 646-654.
- [2] Iovannisci DM, et al. Arterioscler Thromb Vasc Biol, 2007, 27(2): 394-399.
- [3] Dong C, et al. Atherosclerosis, 2015, 240(2): 462-467
- [4] Wang L, et al. Stroke, 2011, 42(3): 588-592.
- [5] Inoue K, et al. Circ Res, 2005, 97(2): 176-184.
- [6] Mehta JL, et al. Circ Res, 2007, 100(11): 1634-1642.
- [7] El Khoudary SR, et al. Atherosclerosis, 2012, 225(1): 180-186.
- [8] Karim R, et al. J Clin Endocrinol Metab, 2008, 93(1): 131-138.
- [9] Cortés YI, et al. J Clin Endocrinol Metab, 2020, 105(4): 1126-1136.
- [10] Glisic M, et al. Circ Res, 2018, 122(1): 97-105.

Table 1. Comparison of clinical characteristics between elderly men and women

	All (n=327)	Male (n=231)	Female (n=96)	P
Age (years)	68.2±6.2	67.7±6.1	69.2±6.5	0.050
Smoking	152(46.5)	148(64.1)	4(4.2)	<0.001
Body mass index, kg/m ²	24.6±3.1	24.6±2.8	24.6±3.7	0.830
Hypertension	259(79.2)	184(79.7)	75(78.1)	0.758
Diabetes	115(35.2)	89(38.5)	26(27.1)	0.048
Hyperlipidemia	190(58.1)	137(59.3)	53(55.2)	0.494
High-density lipoprotein, mmol/L	1.1±0.3	1.1±0.3	1.2±0.2	0.017
Low-density lipoprotein, mmol/L	2.9±1.0	2.9±0.9	3.1±1.0	0.032
Triglyceride, mmol/L	1.8±1.0	1.7±0.9	1.8±1.0	0.567
Total cholesterol, mmol/L	4.6±1.1	4.5±1.1	4.8±1.2	0.015
History of cardiovascular disease	68(20.8)	53(22.9)	15(15.6)	0.138

Table 2. Comparison of index carotid arteries atherosclerosis characteristics and Multivariable Regression Models

	Male(n=231)	Female(n=96)	P	β or OR	95%CI	p	OR	95%CI	p
Carotid plaque Morphology									
LA, mm ²	45.4±15.1	43.0±14.1	0.165	3.304	-1.057-8.666	0.137			
WA, mm ²	35.8±13.2	27.5±7.9	<0.001	4.680	1.243-8.118	0.008			
TVA, mm ²	81.2±20.2	70.5±19.8	<0.001	7.984	2.062-13.906	0.008			
NWI, %	44.5±10.8	40.2±7.1	0.001	0.019	-0.010-0.047	0.156			
MWT, mm	1.3±0.4	1.0±0.2	<0.001	0.133	0.018-0.248	0.024			
Luminal stenosis (%)	23.7±36.4	10.6±23.4	0.005	4.005	-5.129-14.460	0.346			
Carotid plaque Compositions									
Calcification	122(52.8)	41(42.7)	0.066	0.891	0.488-1.624	0.706	0.681	0.350-1.328	0.258
LRNC	175(75.8)	49(47.5)	<0.001	1.974	1.062-3.670	0.032	1.891	0.946-4.177	0.089
IPH	55(23.9)	5(5.2)	<0.001	3.862	1.230-10.900	0.020	2.699	0.745-9.772	0.131
FCR	28(12.1)	4(4.2)	0.027	1.310	0.345-4.974	0.691	0.850	0.202-3.673	0.824
HRP	76(33.3)	11(11.5)	<0.001	2.138	0.952-4.799	0.065	1.452	0.527-4.004	0.471

Table 3. Comparison of non-index carotid arteries atherosclerosis characteristics and Multivariable Regression Models

	Male(n=231)	Female(n=96)	P	β or OR	95%CI	p	OR	95%CI	p
Carotid plaque Morphology									
LA, mm ²	48.4±17.1	43.6±13.8	0.014	3.545	-1.203-8.295	0.143			
WA, mm ²	34.3±11.7	26.4±6.8	<0.001	6.199	3.146-9.253	<0.001			
TVA, mm ²	82.7±22.3	70.0±17.7	<0.001	9.745	3.576-15.914	0.002			
NWI, %	42.7±9.1	39.1±6.8	0.001	0.032	0.007-0.057	0.012			
MWT, mm	1.2±0.4	1.0±0.2	<0.001	0.185	0.089-0.282	<0.001			
Luminal stenosis (%)	17.7±30.5	6.5±17.2	<0.001	8.275	0.209-16.342	0.044			
Carotid plaque Compositions									
Calcification	112(48.5)	33(34.4)	0.019	1.433	0.777-2.646	0.250	0.977	0.495-1.929	0.947
LRNC	166(71.9)	37(38.5)	<0.001	3.623	2.042-7.159	<0.001	3.463	1.723-6.963	<0.001
IPH	44(19.0)	2(2.1)	<0.001	10.738	2.355-48.975	0.002	8.963	1.227-29.958	0.027
FCR	17(7.4)	1(1.0)	0.023	10.387	1.257-86.851	0.030	5.987	0.680-62.734	0.107
HRP	55(23.8)	5(5.2)	<0.001	6.004	2.122-16.984	0.001	4.062	1.250-13.208	0.020

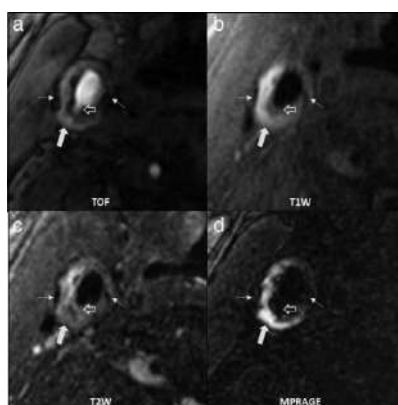


FIGURE: A symptomatic carotid artery of a 72-year-old man. The IPH is characterized by hyperintensities on (a) TOF, (b) T1W and (d) MP-RAGE, and isointensity to hyperintensity on (c) T2W (wide arrow); the calcification manifests hypointensities on all four sequences (narrow arrows); LRNC shows isointensities on TOF, T1W and T2W, and hypointensity on MP-RAGE (hollow arrow).

Simultaneous 3D aortic lumen and vessel wall imaging with iT2prep-BOOST

Camila Munoz¹, Anastasia Fotaki¹, Karl P Kunze^{1,2}, Radhouene Neji^{1,2}, René M Botnar¹, Claudia Prieto¹

¹School of Biomedical Engineering and Imaging Sciences, King's College London, UK

²MR Research Collaborations, Siemens Healthcare Limited, Frimley, United Kingdom

Purpose: Bright-blood and black-blood MR imaging are key contrasts for the comprehensive assessment of aortic disease¹. In clinical routine, these contrasts are acquired in separate scans: bright-blood images are usually acquired under free-breathing using 3D MR angiography (MRA) sequences that rely on diaphragmatic navigators to minimize respiratory motion, while black-blood images are generally acquired under breath-hold utilising 2D spin-echo sequences. This approach results in prolonged scan times and misregistration between images due to both patient motion and the different geometries and spatial resolution used for each scan. The purpose of this study was to further accelerate and extend a previously introduced motion-compensated iT2Prep-BOOST sequence², that provides high-quality co-registered 3D bright and black-blood images for the assessment of aortic lumen and vessel wall from a short scan of ~8 min.

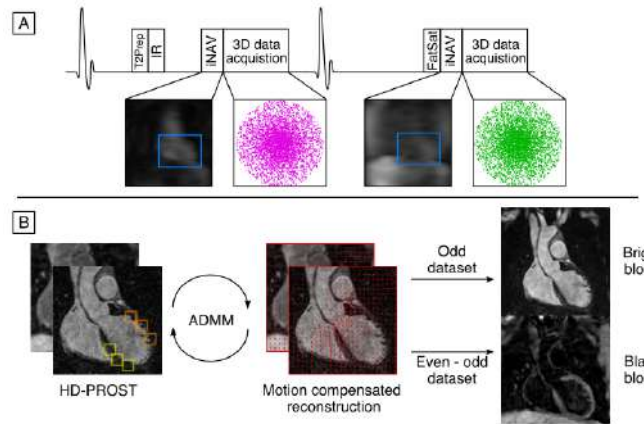


Fig 1 (A) Acquisition and (B) reconstruction method for bright and black-blood MRA

Methods: 3D aortic iT2prep-BOOST data are acquired with an ECG-triggered interleaved 3D bSSFP sequence with a 4-fold undersampled variable-density Cartesian trajectory, where a T2Prep-IR module is applied before data acquisition in odd heartbeats and no preparation is applied in even heartbeats² (Fig 1A). Beat-to-beat 2D translational and bin-to-bin 3D non-rigid respiratory motion are estimated from the iNAVs and the 3D data itself and integrated into a non-rigid motion-compensated reconstruction with low-rank patch-based regularization (HD-PROST)³ (Fig 1B). The first bright-blood dataset can be used for lumen visualization, while subtraction of the two bright-blood datasets is used to create the black-blood dataset for vessel wall visualization.

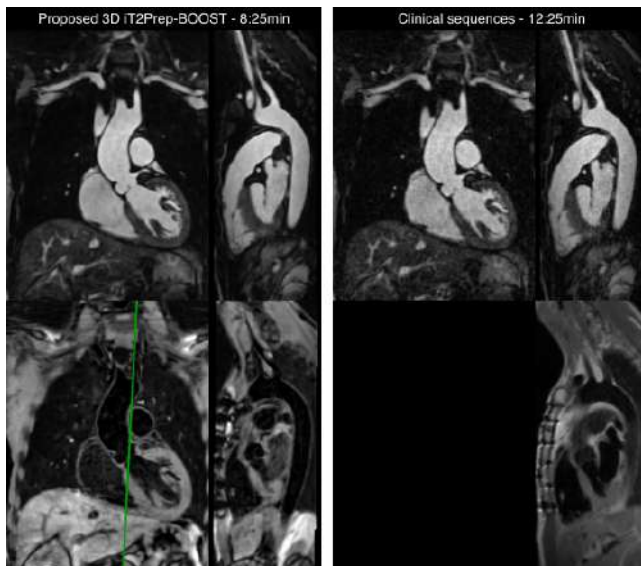


Fig 2 Proposed iT2prep-BOOST vs conventional imaging. iT2Prep-BOOST produces co-registered volumetric bright- and black-blood images with excellent depiction of the aortic lumen and wall.

Twenty patients with aortopathy (15 male, 30±11 years old) were scanned at a 1.5T system (MAGNETOM Aera, Siemens Healthcare, Germany) with the proposed sequence and the following parameters: coronal orientation, 1.3mm³ isotropic resolution, FOV = 300x400x104-156mm³, T2-prep=40ms, TI=110ms, TE/TR=1.41/3.24ms. Patients also underwent conventional bright-blood free-breathing diaphragmatic navigator gated 3D MRA (bSSFP sequence, sagittal orientation, 1.4-1.5mm³ isotropic resolution, FOV = 240x400x134-168mm³, T2-prep=40ms) and 2D breath-held black-blood single shot fast spin echo (HASTE) (axial orientation, 1.6mm in-plane resolution, 8mm slice thickness).

Results: Scans were successfully completed in all subjects. The average scan time for the conventional sequences (including both T2-prep bSSFP and HASTE) was 13.7±3.5 min while for the proposed 3D iT2Prep-BOOST method was 8.0±1.9min (P<0.001). Good image quality of the aortic luminal signal can be observed with the proposed bright-blood technique, comparable to the conventional T2-prep bSSFP; while the proposed sequence offers a complementary vessel-wall black-blood image with improved

coverage compared to the conventional 2D HASTE. A significantly increased contrast recovery coefficient (CRC) between blood and myocardium was observed for the proposed iT2Prep-BOOST sequence compared with the conventional bright blood approach across patients (Fig 3).

Discussion: We have here introduced an accelerated iT2Prep-BOOST sequence that provides excellent depiction of the aortic lumen and wall, with a predictable scan time of ~8min. This approach holds promise for the comprehensive assessment of aortic disease.

References: ¹Kramer CM, et al. JCMR 2020;22:17; ²Milotta G, et al. Magn Reson Med 2019;82:312–25; ³Bustin A, et al. Magn Reson Med 2019;81:3705–3719.

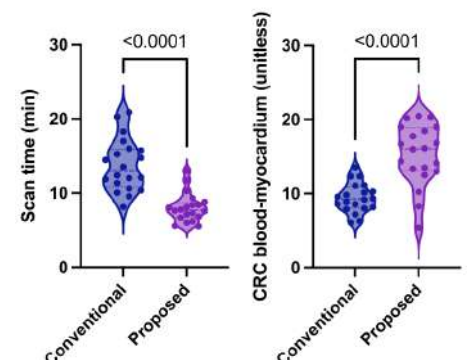


Fig 3 The proposed iT2prep-BOOST results in a shorter scan time and produces bright-blood images with higher blood-myocardium contrast.

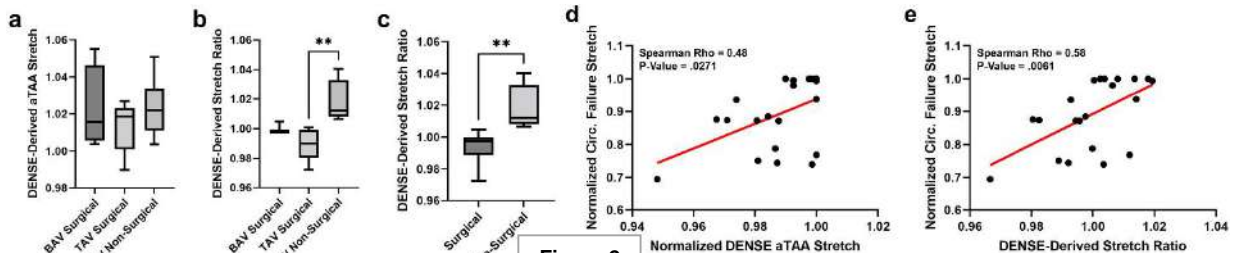
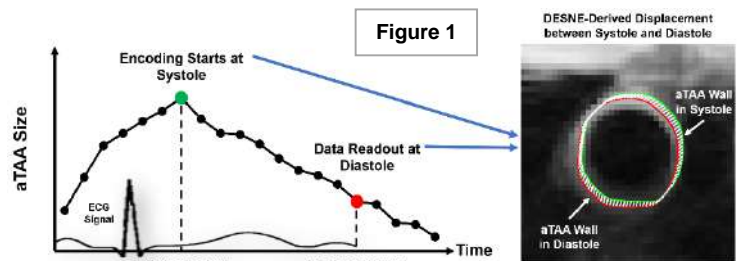
Imaging Ascending Thoracic Aortic Aneurysm Wall Stretch: A Comparison to Uniaxial Mechanical Testing

Huiming Dong¹, Henrik Haraldsson¹, Joseph Leach¹, Ang Zhou¹, Megan Ballweber¹, Chengcheng Zhu¹, Michael Hope¹, Yue Xuan², Zhongjie Wang², Liang Ge², Frederick H. Epstein³, David Saloner¹, Elaine Tseng², Dimitrios Mitsouras¹

¹Department of Radiology and Biomedical Imaging, ²Department of Surgery, University of California, San Francisco; ³Department of Biomedical Engineering, University of Virginia

Introduction: Rupture and dissection are life-threatening sequelae of ascending thoracic aortic aneurysms (aTAAs). Current management guidelines recommend surgical intervention based on aTAA size. Aneurysm development is associated with extracellular matrix (ECM) degradation which is reflected in its wall compliance, suggesting wall stretch as a relevant imaging marker for understanding the disease progression. Displacement encoding with stimulated echoes (DENSE) is a non-invasive phase-contrast MRI technique that measures tissue displacement produced by cardiac loading for quantifying local tissue stretch¹. DENSE was initially developed for assessing myocardium strain. No study to date has investigated DENSE-derived aneurysm wall stretch in different aTAA patient groups. Moreover, in vivo aortic DENSE has not been compared with mechanical testing. The aim of this study is to investigate DENSE-measured aTAA stretch in patients who met repair criteria versus those undergoing surveillance. We also sought to compare the in vivo DENSE-derived aneurysm stretch to mechanical testing on harvested surgical samples.

Methods: In vivo aortic DENSE imaging was performed on 15 male aTAA patients. Four bicuspid aortic valve (BAV) patients and five tricuspid valve (TAV) patients who met repair criteria underwent surgery while six TAV patients continued imaging surveillance. A single imaging plane was prescribed orthogonal to the vessel centerline at the level of maximum aTAA diameter in the tubular portion of the ascending aorta. A cardiac and respiratory navigator-gated DENSE acquisition² was performed on a 1.5T or 3T scanners (Avanto or Skyra, Siemens Healthcare, Erlangen, Germany). DENSE encoding was performed at the time of maximal aortic distension at systole, and the imaging readout was performed 400ms later in diastole to quantify the wall stretch that occurred between diastole and systole³ (**Figure 1**). Additionally, we calculated the ratio of stretch in the aTAA relative to that in the descending aorta from the same patient. Uniaxial mechanical testing was performed on aTAA specimens harvested from six surgical patients⁴. The specimen deformation at failure with respect to its original length was recorded as failure stretch. For each of the four patients, regional wall stretch was investigated by dividing the aTAA into anterior, posterior, medial and lateral quadrants. DENSE and the mechanical testing were compared for each quadrant.



Results: For BAV surgical patients, TAV surgical patients and TAV non-surgical patients, the mean DENSE-derived aTAA wall stretch between diastole and systole was $2.25 \pm 2.26\%$, $1.33 \pm 1.40\%$ and $2.33 \pm 1.59\%$, respectively (**Figure 2a**). The DENSE-derived ratio of aTAA stretch to descending aorta stretch was significantly lower among TAV surgical patients than the non-surgical groups ($P=0.0067$, **Figure 2b**). Pooling both BAV and TAV surgical patients, we also observed a significantly lower stretch ratio in the pooled surgical group compared to the non-surgical patients ($P=0.003$, **Figure 2c**), suggesting less compliant aneurysms in the patients who proceeded to surgical intervention. The mechanical testing-measured failure wall stretch of aTAA correlated to both a) DENSE-derived aTAA stretch (Spearman $\rho=0.48$, $P=0.0271$, $n=21$, **Figure 2d**) and b) stretch ratio (Spearman $\rho=0.58$, $P=0.0061$, $n=21$, **Figure 2e**).

Conclusion: DENSE-derived aortic stretch ratio was lower for surgical aTAA patients compared to non-surgical patients. In vivo DENSE measurements correlated to measures from ex vivo mechanical testing. Future work is warranted to evaluate whether DENSE has utility as a novel imaging marker of aTAA progression.

1. Kim D. et al., Radiology, 2004.
2. Zhong X. et al., MRM, 2010.
3. Haraldsson H. et al., JCMR, 2014.
4. Azadani AN. et al., Ann Thorac Surg, 2012.

Fusion of Ferumoxytol Enhanced MRA with Non-contrast CT: Filling in the Missing Pieces

Takegawa Yoshida, M.D.¹, Arash Bedayat, M.D.¹, Kim-Lien Nguyen, M.D.¹, J. Paul Finn, M.D.¹

¹Department of Radiology, Division of Cardiovascular Imaging, David Geffen School of Medicine at University of California Los Angeles, Los Angeles, CA, USA

Purpose: Ferumoxytol MRA has the potential to capture all vascular anatomy in the chest, abdomen and pelvis. However, MRA is insensitive to calcification and visualizes metal implants poorly, if at all. Accurate assessment of arterial calcification is important for planning of transcatheter aortic valve replacement (TAVR) and placement of endovascular stents (EVAR).^{1,2} Moreover, clear visualization of implanted cardiac devices, prosthetic heart valves and indwelling catheters may be important for accurate diagnosis. In many patients requiring evaluation for these conditions, iodinated contrast agents are contraindicated for CT. We aim to show that FE-MRA can be combined with unenhanced CT to form a hybrid 3D image with complementary features from both modalities and to determine the parameters within which image registration is reliable.

Materials and Methods:

Patients with renal impairment who were candidates for TAVR or EVAR were included in this IRB-approved and HIPPA-compliant study. FE-MRA was performed at 3.0T or 1.5T after infusion of ferumoxytol 4mg/kg. Following vascular segmentation on FE-MRA, the calcification and/or implantable medical devices from non-contrast CT were overlaid and fused to the vasculature using semi-auto registration tools, followed by manual adjustments as needed. OsiriX (Geneva, Switzerland) and Mimics Innovation Suite (Materialise, Leuven, Belgium) were used for exporting DICOM formatted images and 3D segmentation, respectively. The fused images were then evaluated by an experienced radiologists to assess the registration quality (5 = excellent; 1 = non-assessable) and the contribution to diagnosis (3 = excellent; 1 = no contribution).

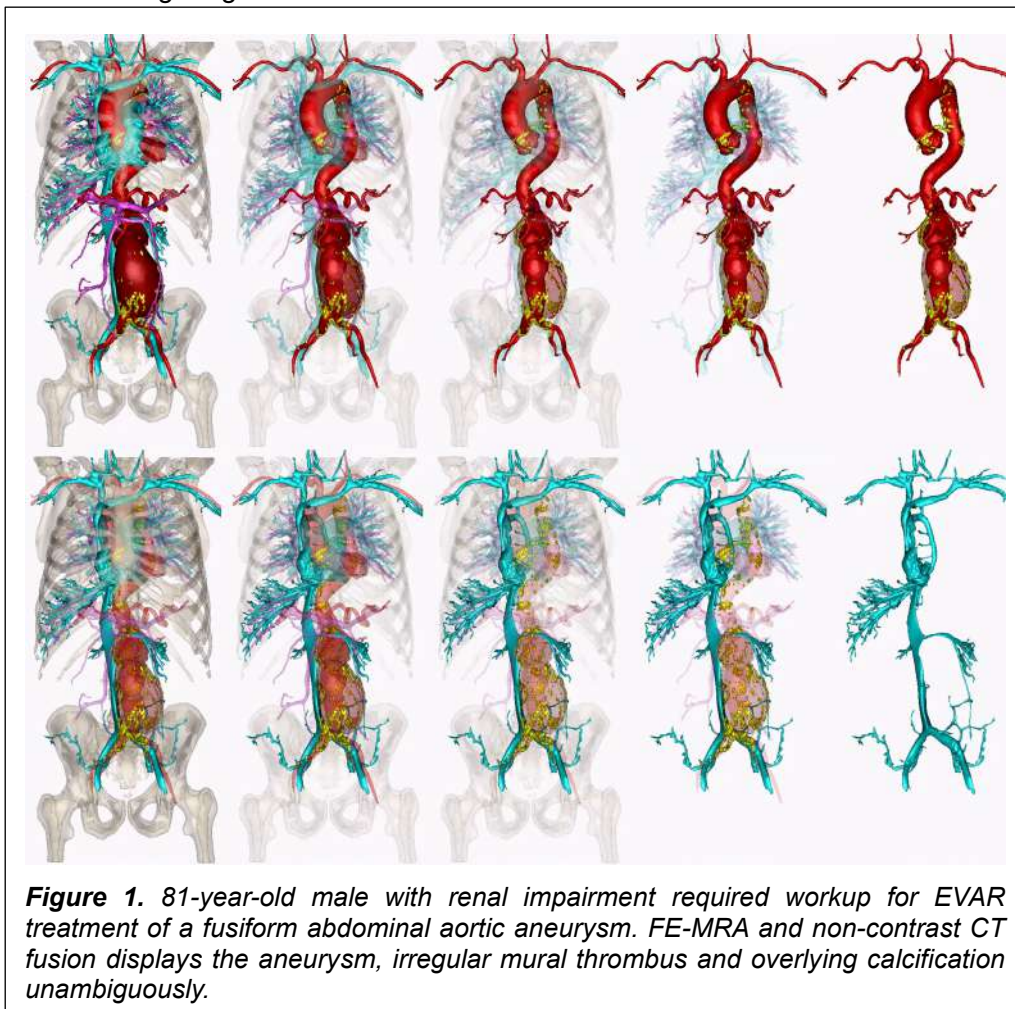


Figure 1. 81-year-old male with renal impairment required workup for EVAR treatment of a fusiform abdominal aortic aneurysm. FE-MRA and non-contrast CT fusion displays the aneurysm, irregular mural thrombus and overlying calcification unambiguously.

Results: A total of 59 patients (75.8 ± 19.1 years, 42 male) who were recruited for our study, including 37 TAVR candidates and 21 patients who were EVAR candidates. All patients had calcified plaque burden to varying degrees; 14 patients had aneurysms with thrombus and 4 patients had implantable cardiac devices. In all patients, the FE-MRA and the non-contrast CT datasets were successfully registered and fused. The radiologists confirmed that the calcified plaque, aneurysms and thrombus were clearly visualized and confidently registered with the corresponding vessel segment. They felt that the relationship with surrounding structures was definitive, excluding the distal subclavian arteries which could not be registered between CT and MRI due to arm abduction on CT. The score was assessed for 5 patients, the registration quality and the contribution to diagnosis were 4.8 ± 0.5 and 2 ± 0 , respectively.

Discussion: In patients with contraindication to Iodine-based contrast agents, FE-MRA and non-contrast CT combine to provide comprehensive information for surgical planning. Fusion of the datasets brings relevant information together for intuitive viewing in a single, composite 3D space, without the need to toggle between the individual sets of data.

References: [1] Francone M et al. Eur Radiol. 2020 May;30(5):2627-2650. [2] Yoshida T et al. J Vasc Surg. 2020 May;71(5):1674-1684.

Identification of intracranial atherosclerotic plaque features associated with recurrent stroke: a multi-modality imaging study using CTA and vessel wall MRI

Lingling Wang¹, Beibei Sun¹, Maysam Orouskhani², Chenyi Gu², Mahmud Mossa-Basha², Yan Zhou¹, Jianrong Xu¹, Chengcheng Zhu², Huilin Zhao¹

¹ Department of Radiology, Renji Hospital, Shanghai Jiao Tong University School of Medicine, China.

² Radiology, University of Washington, Seattle, United States

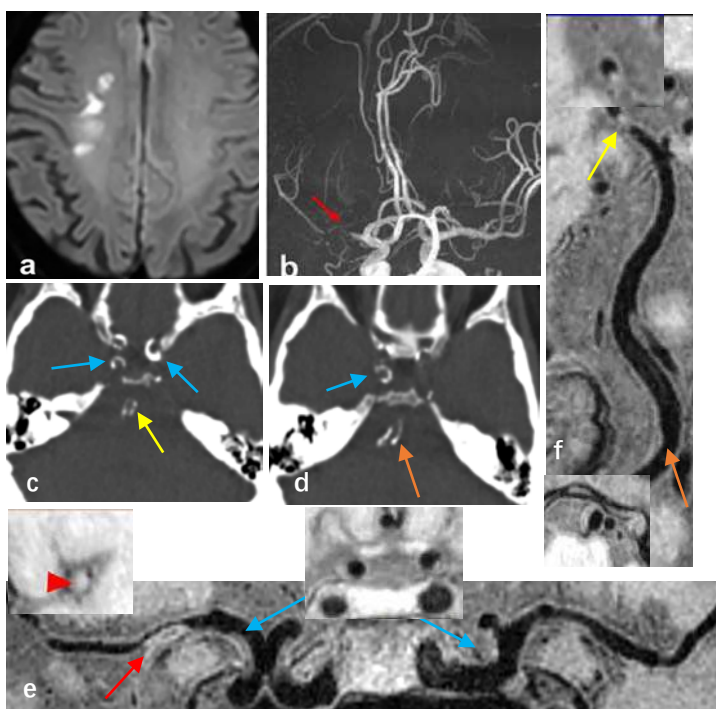
Abstract

Background and Purpose: Intracranial atherosclerotic plaque is a major cause of stroke. Both CT and vessel wall magnetic resonance imaging (VW-MRI) can identify high risk plaque features. However, the two imaging modalities have rarely been used together. We aim to investigate the intracranial atherosclerotic plaque features associated with recurrent stroke using a multi-modality imaging approach by combining CTA and whole brain VW-MRI.

Methods: Eighty-nine patients with acute ischemic stroke caused by intracranial plaque were included, and they had CTA and VW-MRI within 1 month of stroke. Participants were divided into two group: first-time acute stroke (n=50) and recurrent acute stroke (n=39). Calcium burden was quantified semiautomatically by calculating total spotty calcium number, whole-brain Agatston scores and calcium volumes on thin-section unenhanced CT images (resolution 0.5x0.4x0.4mm³). Meanwhile, whole-brain plaque number, degree of culprit plaque luminal stenosis, culprit plaque burden, intraplaque hemorrhage were assessed on VW-MRI sequences (0.6mm isotropic resolution). Those characteristics were compared between two groups. Multivariate regression analysis was performed to assess the correlation between plaque features and recurrent acute stroke.

Results: A total of 89 participants (age 61.3±8.7 years, 54[60.7%] male) were included in this study. More spotty calcium and whole-brain plaques were found in recurrent stroke patients than first-time stroke patients (p=0.041 and P=0.017). Recurrent stroke patients had larger calcium volume (p=0.031), higher calcium score (p=0.008) and greater culprit plaque burden (p=0.002). After adjustment of clinical demographic factors, in multivariate analysis, calcium volume (odds ratio, OR=7.787; p=0.044), calcium score (OR=1.421; p=0.035), whole-brain plaque number (OR=1.378; p=0.032) and culprit plaque burden (OR=3.087; P=0.002) were all independently associated with recurrent acute stroke compared to the first-time acute stroke. The AUC of MRI was 0.745 and CT was 0.723, and the combination of both CT and MRI achieved AUC of 0.803.

Conclusion: Higher calcium burden quantified by volume and Agatston score of intracranial arteries, as well as whole-brain plaque number and culprit plaque burden were independently associated with recurrent acute stroke. The use of both CT and MRI achieved better performance of differentiating high risk intracranial plaque than a single imaging modality.



A 62-year-old male patient presented with recurrent acute stroke. (a) Axial diffusion-weighted imaging detects high-signal-intensity lesions in the right corona radiata. (b) Time-of-flight magnetic resonance angiography image shows severe stenosis on the M1 segment of right middle cerebral artery (MCA) (red arrow). (c-d) Unenhanced CT images show diffuse calcification and spotty calcium in the bilateral C4-C7 segments of ICA, right vertebral artery (VA). (e-f) curved planar reconstruction images from pre-contrast T1 whole-brain vessel wall imaging show multiple plaques in the right MCA (red arrow) and bilateral C7 segment of ICA (blue arrow), P1 segment of right PCA (yellow arrow), and V4 segment of RVA (orange arrow).

Vasa vasorum of proximal cerebral arteries mimic intracranial vasculitis

Thorsten Bley¹, Giulia dalla Torre¹, Ute Ludwig², Patrick Vogel¹, Andreas Weng¹, Matthias Fröhlich³, Marc Schmalzing³, Esther Raithel⁴, Christoph Forman⁴, Stephan Meckel⁵, Konstanze Guggenberger^{1*}

¹Radiology & ³Rheumatology Wuerzburg, ²Medical Physics & ⁵Neuroradiology Freiburg, ⁴Siemens

Purpose: To characterize concentric vessel wall enhancement of the proximal internal carotid (ICA) and vertebral arteries (VA) due to intracranial vasa vasorum in a non-vasculitic elderly patient cohort to avoid misinterpretation of an imaging confounder for vasculitis.

Methods: Cranial compressed-sensing (CS) 3D SPACE contrast enhanced T1 black-blood VWI sequence in 43 patients (aged ≥ 50 years) without history / clinical findings of vasculitis who received MRI for exclusion of cerebral metastases. Imaging parameters: 64-channel head coil, TR/TE=800/10 ms, FOV=210×210×140 mm³, matrix=384×384×256 px³, pixel-bandwidth=450 Hz/px), whole-brain coverage, isotropic resolution 0.55 mm³, scan time 5:50 min. Bilateral proximal intradural ICA and VA segments were evaluated for presence and morphology of VWE including measurements of longitudinal extension.

Results: Concentric VWE of the proximal intradural ICA was found in 13 patients, and of the proximal intradural VA in 39 patients. The mean longitudinal extension of VWE after dural entry was 13 mm in the VA (right VA 12 mm, left VA 14 mm) and 2 mm in the ICA (right ICA 2 mm, left ICA 2 mm).

Figure 1: Circumferential mural hyperintensity without relevant VWE of the proximal intracranial VA (a). Substantial concentric VWE with parietal bumps (b), caused by vasa vasorum with additional atherosclerosis. VA in the same patient shows asymmetric VWE (c, red lines = enhancement's borders) with increasing wall irregularities. Eccentric vessel wall thickening and VWE indicating advanced atherosclerosis (d).

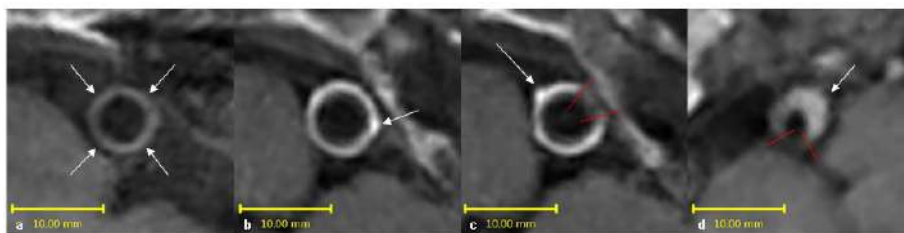
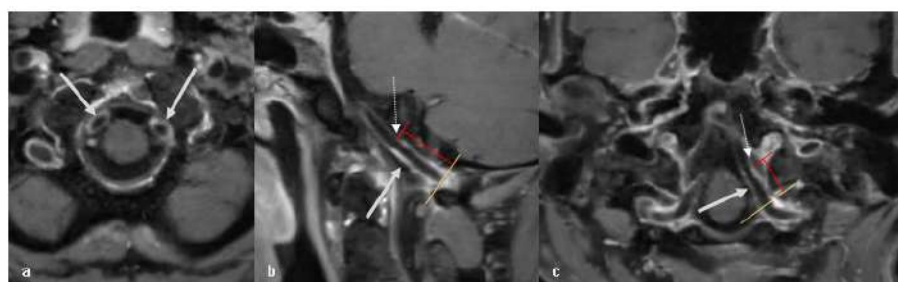


Figure 2: Post-contrast VWI shows significant concentric VWE within proximal intracranial V4 segments of bilateral VAs in asymptomatic patients likely related to vasa vasorum (a-c, white arrows). Red lines = length of the proximal intracranial VWE within the arteries, dashed arrows mark the crossover to the normal, non-enhancing vessel wall (b,c). Yellow line = vessel's dural crossing.



Discussion: Concentric VWE of vasa vasorum was found within the proximal 2 mm of the ICA and 13 mm of the VA after dural entry in elderly subjects without history or clinical signs of vasculitis. In these locations, concentric VWE should not be confused with large artery vasculitis. Distal to these segments, circumferential VWE is more likely related to pathologic conditions such as vasculitis while eccentric VWE may more likely be due to arteriosclerosis. However, further studies comparing VWE in asymptomatic patients with those suspected of large artery vasculitis are necessary.

References:

- 1) Portanova A et al. Radiology. 2013 Jun;267(3):667-79.
- 2) Guggenberger KV et al. Eur Radiol. 2022 Feb;32(2):1276-1284.

Grant support by the Deutsche Forschungsgemeinschaft (DFG) under grant numbers DFG HE 1875/26-2, and BL 1132/1-2 is gratefully acknowledged.

Predictors of Progression in Intraplaque Hemorrhage Volume in Patients with Carotid Atherosclerosis: A Serial Magnetic Resonance Imaging Study

Mingming Lu¹, Jianming Cai¹, Xihai Zhao³

1. Department of Radiology, Chinese PLA General Hospital, Beijing, China
2. Center for Biomedical Imaging Research, Department of Biomedical Engineering, Tsinghua University School of Medicine, Beijing, China

Purpose:

This study aimed to investigate the arterial disease risk factors for the progression of intraplaque hemorrhage (IPH) in patients with carotid atherosclerosis using serial high resolution magnetic resonance (MR) imaging.

Methods:

Consecutive symptomatic patients who had MRI evidence of intraplaque hemorrhage present in the ipsilateral carotid artery with respect to the side of the brain affected by stroke or TIA were recruited in the study. All the patients underwent follow-up MR imaging more than 6 months after baseline. Baseline information and carotid plaque features of patients were collected. The annual change of IPH and other carotid plaque morphology was calculated. Logistic regression and receiver-operating-characteristics (ROC) curve were conducted to evaluate the risk factors for the progression of IPH.

Results:

Thirty-four symptomatic patients (mean age: 67.1 years, standard deviation [SD]: 9.8 years, 27 males) were eligible for the final analysis and contralateral plaques containing IPH were seen in 29 of these patients (making 45 plaques with IPH in total). During mean 16.6 months (SD: 11.0 months) follow-up, the overall annual change of IPH volume in 45 plaques with IPH was mean -10.9 mm^3 (SD: 49.1 mm^3). The annual progression of IPH was significantly associated with taking an antiplatelet agent at baseline (OR: 9.76; 95%CI: 1.05 to 90.56; $p=0.045$), a baseline history of current or past smoking (OR: 9.28; 95%CI: 1.26 to 68.31; $p=0.029$), and larger baseline carotid vessel wall volume (OR: 1.36 per 10 mm^3 ; 95%CI: 1.02 to 1.81; $p=0.032$) after adjustments for confounding factors. ROC analysis indicated that the combination of these three risk factors in the final model produced good discriminatory value for IPH progression (area-under-the-curve: 0.887).

Discussion:

Taking an antiplatelet agent at baseline, a baseline history of current or past smoking, and larger baseline vessel wall volume were independently associated with the progression of IPH volume. Our findings indicate that awareness and management of such risk factors may reduce the risk of intraplaque hemorrhage progression and, therefore, may reduce the risk of arterial disease complications, including stroke.

Reference:

- [1] Hellings WE, Peeters W, Moll FL, et al. Composition of carotid atherosclerotic plaque is associated with cardiovascular outcome: a prognostic study. *Circulation* 2010;121:1941-1950.
- [2] Kurosaki Y, Yoshida K, Endo H, et al. Association between carotid atherosclerosis plaque with high signal intensity on T1-weighted imaging and subsequent ipsilateral ischemic events. *Neurosurgery* 2011;68:62-7.

Carotid Atherosclerotic Vulnerable Plaque Characteristics on Magnetic Resonance Imaging: Effective Predictors for Silent Stroke after Carotid Endarterectomy

Ran Huo¹, Wanzhong Yuan², Huimin Xu¹, Ying Liu¹, Dandan Yang³, Tao Wang², Huishu Yuan¹, Xihai Zhao³

1. Department of Radiology, Peking University Third Hospital, Beijing, China; 2. Department of Neurosurgery, Peking University Third Hospital, Beijing, China; 3. Department of Biomedical Engineering, Tsinghua University, Beijing, China

Background and Purpose: Carotid atherosclerotic stenosis is one of the major etiologies of ischemic stroke [1]. Carotid endarterectomy (CEA) was considered as an effective treatment of carotid atherosclerotic stenosis for prevention of future stroke [2]. However, a substantial number of patients (ranging from 9.2% to 34%) developed silent stroke (SS) after CEA. The SS has been demonstrated to be correlated with future cognitive impairment, stroke, or other adverse outcomes [3,4]. We hypothesized that carotid plaque vulnerability may play a critical role in occurrence of SS after CEA. This study sought to investigate the associations between carotid plaque characteristics and SS in patients with moderate and severe carotid stenosis after CEA using MR vessel wall imaging.

Methods: Study sample: Patients with unilateral moderate and severe carotid stenosis referred to CEA treatment were recruited in this study. **MR imaging:** All patients underwent carotid MR vessel wall imaging within 1 week before CEA, and brain imaging within 48 hours before and after CEA on a 3.0T MR scanner, respectively. **Image review:** Plaque burden, including area for lumen, wall, and vessel, maximum wall thickness, normalized wall index and vessel stenosis, and the presence of carotid lipid-rich necrotic core (LRNC), intraplaque hemorrhage (IPH), Type-I IPH, Type-II IPH, and calcification were evaluated (Figure 1). The volume and maximum area percentage of above plaque components were measured. The postoperative SS was identified as new high signal intensity on DWI images but with lower ADC values after CEA. **Statistics:** The associations between carotid plaque characteristics and SS were analyzed using univariate and multivariate logistic regression analyses. The study protocol was approved by institutional review board and written consent form was obtained from each participant.

Results: A total of 153 patients (mean age: 65.4 ± 7.9 years; 126 males) were included, of which 49 (32.0%) had moderate carotid stenosis and 104 (68.0%) had severe carotid stenosis. The SS was found in 16.3% of patients with moderate carotid stenosis and 20.2% of patients with severe carotid stenosis, respectively. In patients with severe carotid stenosis, presence of carotid IPH (OR 3.030, 95% CI 1.106-8.305; $P = 0.031$) and Type-I IPH (OR 3.187, 95% CI 1.162-8.745, $P = 0.024$) were found to be significantly associated with SS (Table 1). After adjusted for confounding factors, the associations of SS with presence of IPH (OR 3.394, 95% CI 1.122-9.669 $P = 0.030$) and Type I-IPH (OR 3.633; 95% CI 1.216-10.859, $P = 0.021$) remained statistically significant. After adjustment, the volume of Type II-IPH (OR 1.014, 95% CI, 1.001-1.028; $P = 0.036$), maximum area percentage of II-IPH (OR 1.070, 95% CI 1.002-1.142, $P = 0.043$) and maximum area percentage of LRNC (OR 1.030, 95% CI 1.000-1.061, $P = 0.049$) showed significant associations with SS though such associations were not significant before adjustment (Table 1).

Conclusions: Carotid vulnerable plaque features on MRI, particularly presence and the size of IPH, might be effective predictors for silent stroke after carotid endarterectomy.

Table 1 Associations between carotid plaque characteristics and silent stroke after CEA in patients with severe carotid stenosis

	Univariate regression			Multivariate regression		
	OR	95% CI	P	OR	95% CI	P
Morphology						
Mean lumen area, mm ²	0.983	0.938, 1.031	0.490	0.991	0.940, 1.044	0.733
Mean wall area, mm ²	1.018	0.977, 1.061	0.385	1.035	0.988, 1.083	0.147
Mean total vessel area, mm ²	1.002	0.975, 1.029	0.890	1.012	0.982, 1.042	0.440
Maximum wall thickness, mm	1.115	0.806, 1.543	0.511	1.125	0.779, 1.625	0.529
Mean normalized wall index, %	1.026	0.976, 1.079	0.316	1.039	0.977, 1.106	0.224
Stenosis, %	1.001	0.948, 1.057	0.963	-	-	-
Presence of plaque components						
LRNC	1.558	0.177, 13.696	0.689	1.428	0.147, 13.910	0.759
IPH	3.030	1.106, 8.305	0.031	3.294	1.122, 9.669	0.030
I-IPH	3.187	1.162, 8.745	0.024	3.633	1.216, 10.859	0.021
II-IPH	1.957	0.728, 5.260	0.183	2.144	0.731, 6.286	0.165
Calcification	4.776	0.596, 38.272	0.141	5.893	0.688, 50.465	0.105
Volume of plaque components *						
LRNC, mm ³	1.001	1.000, 1.002	0.193	1.001	1.000, 1.003	0.137
IPH, mm ³	1.001	0.999, 1.003	0.490	1.001	0.998, 1.003	0.569
I-IPH, mm ³	1.000	0.997, 1.003	0.896	1.000	0.996, 1.003	0.866
II-IPH, mm ³	1.010	0.998, 1.023	0.103	1.014	1.001, 1.028	0.036
Calcification, mm ³	0.997	0.990, 1.004	0.378	0.997	0.991, 1.004	0.443
Maximum-area-percentage of plaque components *						
LRNC, %	1.024	0.997, 1.052	0.085	1.030	1.000, 1.061	0.049
IPH, %	1.007	0.988, 1.028	0.468	1.006	0.985, 1.028	0.555
I-IPH, %	0.999	0.970, 1.029	0.947	0.999	0.967, 1.032	0.946
II-IPH, %	1.050	0.994, 1.110	0.079	1.070	1.002, 1.142	0.043
Calcification, %	1.003	0.960, 1.049	0.879	1.001	0.955, 1.050	0.959

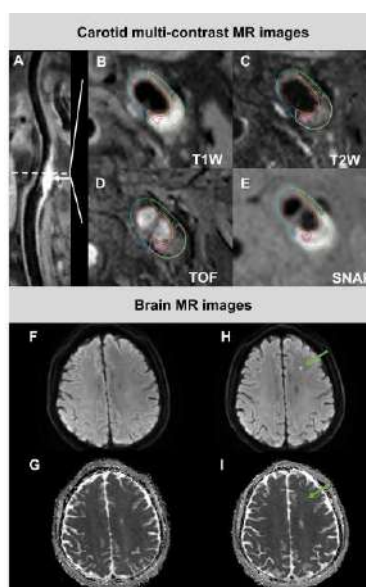


Figure 1 The images from a 56 years old male patients who had carotid plaque with Type-I IPH (pink), Type-II IPH (rose) and LRNC (yellow) in the left carotid artery (A-E), and silent stroke (green arrow) on DWI images following CEA (before CEA, F and G; after CEA, H and I).

References:

- [1] J Surg Res. 1995; 58(3): 330-6.
- [2] Eur J Vasc Endovasc Surg. 2007; 34(4): 470-9.
- [3] Ann Vasc Surg. 2018; 51: 225-33
- [4] Stroke. 2017; 48(2): e44-e71

The relationship of Chronic Carotid Artery Occlusion and Recurrent Stroke Risk: a carotid MR-VWI study

Jin Zhang¹, Jiaqi Tian¹, Beibei Sun¹, Xiao Li¹, Jianjian Zhang¹, Lingling Wang¹, Huilin Zhao¹

1. Department of Radiology, Ren Ji Hospital, Shanghai Jiao Tong University School of Medicine, 160 Pujian Road, Shanghai, China

Purpose: The aim of this study was to investigate the characteristics of chronic internal carotid artery occlusion and their relationships with recurrent stroke by using carotid magnetic resonance vessel wall imaging (MR-VWI).

Methods: Patients diagnosed with chronic internal carotid artery occlusion by ultrasound were retrospectively analyzed. All patients underwent carotid MR-VWI (3D-TOF, 3D T1-vista, CE-MRA, 3D T1-vista C+) and brain MR. The position, extent and signal features of carotid internal artery occlusion were identified. Whether cerebral acute infarcts or not in anterior circulation were evaluated.

Results: Sixty-five patients (mean age: 62.6 ± 7.9 years old, 55 males) were recruited in this study. Of the 65 patients, cerebral acute infarcts (lesions with hyperintense on DWI) in anterior circulation were found in 36 patients. Compared with patients of cerebral old infarcts or no infarcts in anterior circulation, patients of cerebral acute infarcts in anterior circulation had a higher prevalence of hemorrhage in the entry (36.1% vs 10.3%, $P=0.021$) and hyperintense signal in the route (50.0% vs 10.3%, $P=0.001$), and a lower prevalence of occlusion involving of C6 segment or above (41.7% vs 69.0%, $P=0.045$) and inhomogeneous enhancement in the lumen (55.6% vs 82.8%, $P=0.032$).

Conclusions: The characteristics of chronic internal carotid artery occlusion are associated with the risk of recurrent stroke. The carotid MR-VWI can help screen out patients with chronic carotid artery occlusion that need active intervention.

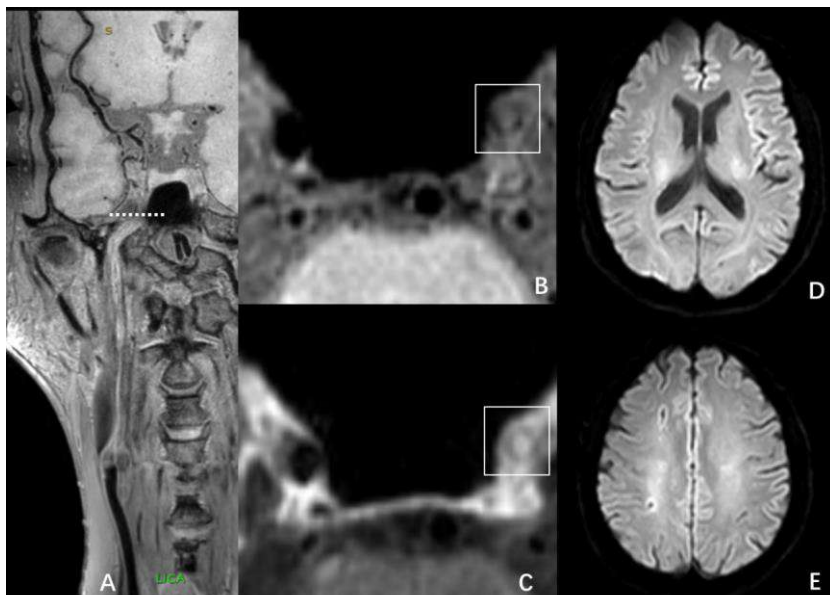


Fig. 1: The multiple planner reconstruction of occluded left carotid internal artery (A) and its axial images (B and C) before and after injecting contrast agent. No hemorrhage in the entry or HIS in the route were observed. The occlusion was found involving the C6 segment and Inhomogeneous enhancement in the lumen. No infarct was found on brain DWI images (D and E).

Added Value of Intracranial Vessel Wall Magnetic Resonance Imaging Across Stenosing Vasculopathies on a Per-Patient Basis

Nadin Zanaty, MD, Mehmet Aksakal, MD, Niranjana Balu PhD, Chun Yuan PhD, Gador Canton PhD, Thomas Hatsukami MD, D. Baylam MD, Mahmud Mossa-Basha, MD

University of Washington Department of Radiology

Purpose: Previous studies have shown added value of intracranial vessel wall MRI (IVW) in differentiating vasculopathies^{1, 2}, however, these studies only selected a few vasculopathies to differentiate, did not include normal cases, and did not evaluate on a per-patient basis. The purpose of this study is to evaluate the added value of intracranial vessel wall MRI (IVW) in differentiating and diagnosing intracranial vasculopathies on a per-patient basis.

Methods: Consecutive patients who underwent IVW with a clinically defined intracranial vasculopathy as identified by a panel of 3 stroke neurologists with evidence of arterial stenosis on luminal imaging between 1/15/2013 and 11/30/2020 were included in this study. Patients with more than one vascular disease diagnosis were excluded. Additionally, 40 IVW normal studies without clinical evidence of vasculopathy or luminal stenosis were included. Two board-certified neuroradiologist raters reviewed the de-identified luminal imaging in random order independently while blinded to patient clinical information and IVW data, and determined diagnosis, diagnostic confidence, and lesion characteristics that contributed to diagnosis on a per-patient basis. After a 4-week washout, the two raters re-reviewed the studies in a similar fashion but with inclusion of IVW in addition to the luminal imaging review, again determining diagnosis, confidence and lesion characteristics.

Results: A total of 106 atherosclerosis, 30 Moyamoya disease, 41 inflammatory vasculopathy and 20 reversible cerebral vasoconstriction syndrome cases were included in the analysis in addition to 40 normal controls. The inclusion of IVW in the diagnostic evaluation will show a significant improvement in diagnostic accuracy across all intracranial vasculopathies in total, as well as for individual vasculopathies. The confidence scores for intracranial vasculopathy assessment with IVW included will be significantly higher than luminal imaging alone.

Discussion & Conclusion: IVW included in the diagnostic imaging evaluation will show added value for intracranial vasculopathy differentiation, over luminal imaging alone, on a per-patient assessment basis.

References

1. Mossa-Basha M, de Havenon A, Becker KJ, et al. Added Value of Vessel Wall Magnetic Resonance Imaging in the Differentiation of Moyamoya Vasculopathies in a Non-Asian Cohort. *Stroke* 2016;47:1782-1788
2. Mossa-Basha M, Shibata DK, Hallam DK, et al. Added Value of Vessel Wall Magnetic Resonance Imaging for Differentiation of Nonocclusive Intracranial Vasculopathies. *Stroke* 2017;48:3026-3033

Accuracy of Characterizing Carotid Vulnerable Atherosclerotic Plaque by 3D MR Vessel Wall Imaging: A Histological Validation Study

Chenlin Du¹, Zihan Ning¹, Huiyu Qiao¹, Shuo Chen¹, Tao Wang², Ran Huo², Jingli Cao³, Dandan Yang¹, Xihai Zhao¹

1. Center for Biomedical Imaging Research, Department of Biomedical Engineering, School of Medicine, Tsinghua University, Beijing, China. 2. Peking University Third Hospital, Beijing, China. 3. Beijing Tiantan Hospital, Capital Medical University, Beijing China.

Purpose: Stroke is a major cause of disability and death worldwide¹. Disruption of carotid vulnerable atherosclerotic plaques is an important etiology for ischemic cerebrovascular events^{2,3}. Vulnerable plaque is characterized by presence of plaque compositional features including LRNC, IPH, surface or multiple CA and rupture of fibrous cap^{4,5}. Therefore, accurate evaluation of carotid plaque compositional features is critical for the prevention of cerebrovascular events. The 2D multi-contrast MR vessel wall imaging (VWI) has been demonstrated to be capable of identifying and quantifying the plaque compositions validated by histology. However, the accuracy of 3D MR VWI has not been validated by histology. This study sought to histologically validate the accuracy of 3D MR VWI in evaluating carotid vulnerable plaque compositional features.

Methods: Study sample: 21 patients with carotid atherosclerotic scheduled to CEA were recruited in this study. MR imaging: All patients underwent 3D multi-contrast MR VWI for carotid arteries on 3.0 T MR scanner with a dedicated 8-channel carotid coil within one week before the CEA. Histology and MR data analysis: Histological sections were analyzed by a histologist with >5 years' experience in pathology of atherosclerosis blinded to MR images. The LRNC, type 1 IPH, type 2 IPH, CA, and LM were evaluated using Thorough Wisdom software and published criteria⁶. The histological sections were matched with the 3D multi-contrast MR VWI. All matched MR VWI were analyzed by 2 radiologists with consensus utilizing VesselExplorer 2.0 blinded to histological results. The presence and areas of plaque compositions were evaluated on MR images using the published criteria⁷. Statistical analysis: Cohen's kappa (κ) analysis was used to determine the agreement between 3D multi-contrast MR VWI and histological sections in identifying carotid plaque compositions after exclusion of histological plaque compositions smaller than certain thresholds which was 0 mm², 0.79 mm² and 1.77 mm², respectively⁸. The agreement of the area for each plaque composition measured by MR VWI and histology was determined using Spearman's rho coefficients and Bland Altman plots.

Results: 76 histological sections were successfully matched with carotid MR images. After excluding histological sections where plaque components were under 1.77 mm², the highest κ value was reached and good agreement of each component between MR and histology was achieved (Figure 1, Table 1). Moderate agreements were reached in quantification of all components with r value ranged from 0.46 to 0.61 (Table 2). The Bland-Altman plots indicate that the bias in measuring plaque compositions ranged from 0.14 mm² to 5.40 mm² (Figure 2).

Discussion and Conclusion: 3D multi-contrast MR VWI enables accurately characterizing carotid vulnerable atherosclerotic plaques validated by histology.

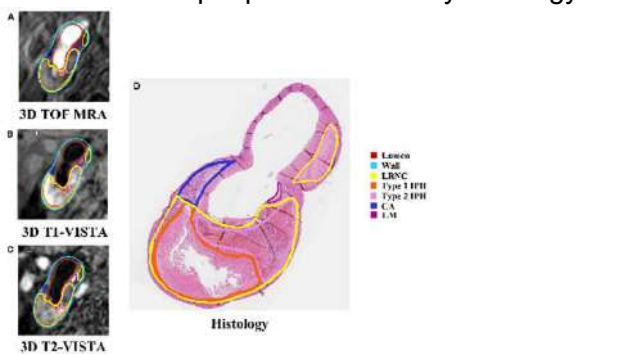


Figure 1. Represents examples showing LRNC, type 1 IPH, type 2 IPH CA and LM on 3D TOF MRA

Table 1. Agreements between 3D MR VWI imaging and histology in identifying carotid vulnerable plaque compositions

	Thresholds, mm ²	MRI	Histology	κ value	95% CI	Accuracy	Sensitivity	Specificity	PPV	NPV
LRNC	>0	(-) 6	(-) 3	0.62	0.28-0.87	92.1%	95.5%	66.7%	95.5%	66.7%
		(+) 3	(+) 04							
	>0.79	(-) 6	(-) 2	0.67	0.31-0.92	93.3%	97.0%	66.7%	95.5%	75.0%
		(+) 3	(+) 04							
	>1.77	(-) 6	(-) 2	0.67	0.36-0.92	93.2%	96.9%	66.7%	95.5%	75.0%
		(+) 3	(+) 03							
IPH	>0	(-) 11	(-) 7	0.61	0.35-0.82	86.8%	88.7%	78.6%	94.8%	61.1%
		(+) 3	(+) 55							
	>0.79	(-) 11	(-) 6	0.64	0.40-0.83	88.0%	90.2%	78.6%	94.8%	64.7%
		(+) 3	(+) 55							
	>1.77	(-) 11	(-) 5	0.66	0.42-0.86	88.9%	91.4%	78.6%	94.8%	68.8%
		(+) 3	(+) 53							
CA	>0	(-) 22	(-) 12	0.44	0.22-0.63	72.4%	73.3%	71.0%	78.6%	64.7%
		(+) 9	(+) 33							
	>0.79	(-) 22	(-) 3	0.61	0.41-0.80	80.6%	90.3%	71.0%	75.7%	88.0%
		(+) 9	(+) 28							
	>1.77	(-) 22	(-) 0	0.62	0.40-0.82	80.4%	100.0%	71.0%	62.5%	100.0%
		(+) 9	(+) 15							
LM	>0	(-) 39	(-) 12	0.59	0.40-0.76	80.3%	64.7%	92.9%	88.0%	76.5%
		(+) 3	(+) 22							
	>0.79	(-) 39	(-) 12	0.57	0.38-0.75	79.7%	62.5%	92.9%	87.0%	76.5%
		(+) 3	(+) 20							
	>1.77	(-) 39	(-) 9	0.62	0.42-0.80	82.6%	66.7%	92.9%	85.7%	81.3%
		(+) 3	(+) 18							

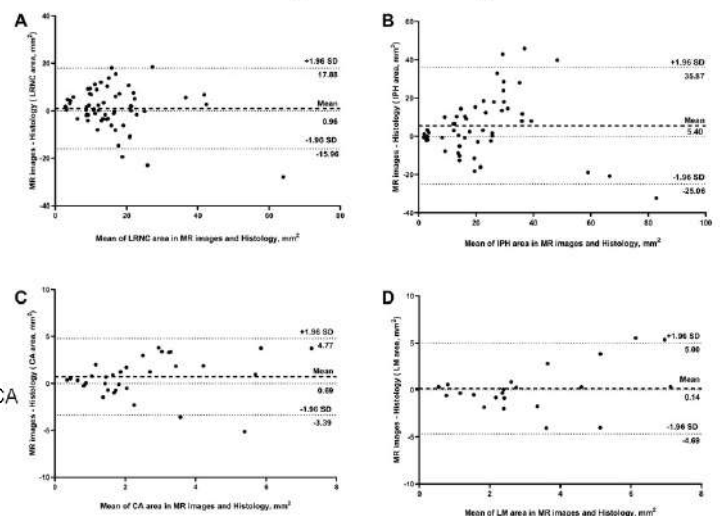


Figure 2. Bland-Altman plots for testing the bias of MR images in measuring LRNC (A), IPH (B), CA (C), LM (D) area with the reference of histology.

Table 2. Agreement of MR images in quantification of plaque components with histology

	Area on MRI, mm ²	Area on histology, mm ²	r value	P value
LRNC	19.30 \pm 13.43	21.45 \pm 17.08	0.52	<0.001
IPH	23.93 \pm 16.78	13.42 \pm 7.21	0.61	<0.001
CA	2.27 \pm 1.52	2.12 \pm 1.84	0.46	0.008
LM	3.23 \pm 2.65	3.08 \pm 1.76	0.61	0.003

References: [1] Hurd MD, et al. Regen Ther. 2021. [2] Zhao H, et al. Eur J Radiol. 2013. [3] Li D, et al. Eur Radiol. 2021.[4] Insull W Jr. Am J Med. 2009. [5] Lusby RJ, et al. Arch Surg 117:1479–14.[6] Stary HC. Arterioscler Thromb Vasc Biol. 2000. [7] Saam T, et al. Arterioscler Thromb Vasc Biol. 2005. [8] Ota H, et al. Radiology. 2010.

Associations of Morphology of Lenticulostriate Arteries and Plaque Characteristics with Single Subcortical Infarction: A High-resolution Vessel Wall Imaging Study

Jin Li¹, Yueyan Bian¹, Xiaoxu Yang¹, Fang Wu², Xihai Zhao³, Qi Yang¹

1. Department of Radiology, Beijing Chao-yang Hospital, Capital Medical University, Beijing, China; 2. Department of Radiology, Xuanwu Hospital, Capital Medical University, Beijing, China; 3. Department of Biomedical Engineering, Tsinghua University, Beijing, China.

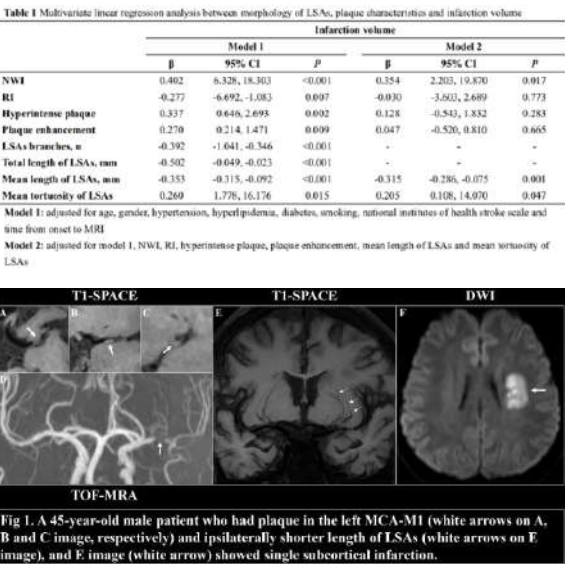
Purpose: Previous studies have shown that characteristics of lenticulostriate arteries (LSAs) and middle cerebral artery (MCA) plaque were associated with ischemic stroke [1,2]. However, the associations of morphology of LSA and plaque characteristics with infarction volume are unknown. This study aimed to determine the associations of morphology of LSAs and plaque characteristics with infarction volume utilizing high-resolution vessel wall imaging (HR-VWI).

Methods: Study sample: Patients with single subcortical infarction in the LSA territory were recruited. **MR imaging:** All patients underwent HR-VWI using a 3.0T MR scanner (Magnetom Prisma, Siemens, Erlangen, Germany) with a 32-channel head coil. A intracranial arteries protocol was performed with the following parameters: 1) 3D TOF-MRA: TR/TE=22/4 ms; voxel size=0.5×0.5×0.7 mm³; 2) precontrast and postcontrast 3D T1W inversion-recovery prepared SPACE (Sampling Perfection with Application-optimized Contrast using different flip angle Evolutions): TR/TE=900/14 ms; voxel size=0.53×0.53×0.53 mm³. All sequences used the same FOV of 17×17 cm². **Image review:** Precontrast T1W-SPACE images were generated using coronal minimum intensity projection for measuring the morphology of LSAs that including the number of branches, length, and tortuosity. The vessel area and lumen area were measured by manually tracing vessel and lumen boundaries. Plaque characteristics of MCA, including normalized wall index (NWI), remodeling index (RI), plaque enhancement and hyperintense plaques, were evaluated. Moreover, the volume of cerebral infarction was measured. **Statistics:** Multivariate linear regression was used to determine the associations of infarction volume with plaque features and morphology of LSAs.

Results: In total, 100 patients (mean age, 54.3±14.1 years; 79 males) were included. Univariate linear regression analysis showed that infarction volume was associated with NWI (β =0.360; 95% CI, 5.302 to 16.770; P <0.001), RI (β =-0.228; 95% CI, -5.939 to -0.457; P =0.023), hyperintense plaque (β =0.273; 95% CI, 0.397 to 2.307; P =0.006), plaque enhancement (β =0.291; 95% CI, 0.297 to 1.519; P =0.004), LSAs branches (β =-0.372; 95% CI, -0.986 to -0.328; P <0.001), total length of LSAs (β =-0.471; 95% CI, -0.046 to -0.021; P <0.001), mean length of LSAs (β =-0.320; 95% CI, -0.293 to -0.075; P =0.001) and mean tortuosity of LSAs (β =0.287; 95% CI, 3.294 to 16.554; P =0.004) with an increment of 0.1 mL of infarction volume. After adjusted for confounding factors (model 1), these associations remained statistically significant (Table 1). After further adjusted confounding factors (model 2), the associations of infarction volume with NWI (β =0.354; 95% CI, 2.203 to 19.870; P =0.017), mean length of LSAs (β =-0.315; 95% CI, -0.286 to -0.075; P =0.001) and mean tortuosity of LSAs (β =0.205; 95% CI, 0.108 to 14.070; P =0.047) still remained statistically significant (Fig 1) while the associations between infarction volume and other imaging characteristics were no longer significant (all P >0.05) (Table 1).

Conclusions: The morphology of LSAs and characteristics of MCA plaque are independently associated with infarction volume in the LSAs territory.

References: [1] Jiang S, et al. Stroke. 2020;51:2801-9. [2] Xie W, et al. Eur Radiol. 2021;31:5629-39.



Semi-automatic normalization and segmentation of contrast enhancement in intracranial atherosclerotic vessel wall imaging

Yin Guo¹, Gador Canton², Niranjan Balu², Thomas S Hatsukami³, Chun Yuan^{1,2}

¹Department of Bioengineering, ²Department of Radiology, ³Department of Surgery, University of Washington, Seattle, WA, United States

Introduction: Contrast enhancement (CE) of intracranial atherosclerotic diseases (ICAD) is often associated with increased neovascularization and endothelial permeability¹. CE is often found related with recent ischemic events and serves as an important marker of high-risk characteristics in plaques². Beyond presence/absence of CE, the degree of CE may demonstrate an additional feature. However, measuring the degree of CE using 3D intracranial vessel wall imaging (IVWI) requires normalization of CE for comparison across plaques. In this study, we aimed to 1) compare reference anatomical structures to normalize image intensity for better detection and quantification of CE, and 2) demonstrate a semi-automatic method for accurate and reproducible measurement of CE.

Methods: 11 subjects with diagnosed ICAD were scanned with two IVWIs using identical protocols within a 2-week interval on a Philips Ingenia 3T CX scanner. Cross-sectional images perpendicular to the artery centerline were generated using our recently developed pipeline MOCHA³. 43 plaques from 15 vessel segments were subsequently identified and delineated by expert reviewers³. In addition, a normal reference slice was identified for each detected plaque.

Comparing reference structures for intensity normalization: Enhancement ratio of identified plaques was calculated using signal intensities (SI) of precontrast and postcontrast T1-VISTA images with the formula $(SI_{post}/SI_{post_nor} - SI_{pre}/SI_{pre_nor})/(SI_{pre}/SI_{pre_nor})$. CE map was then generated for each slice. The following anatomical structures were considered for CE normalization (Fig 1): genu of the corpus callosum, pituitary stalk, and white matter (segmented with FSL fast). Inter-scan reproducibility of average enhancement ratio was evaluated.

Semi-automatic segmentation of CE: Areas with CE above a threshold value were segmented. Segmented enhancement areas were based on the following threshold criteria (Fig 2): 1) SIs > full width at half maximum (FWHM) of the postcontrast plaque SI histogram; 2) SIs > mean plus 3 times of the standard deviation (SD) of the postcontrast reference slice; 3) Enhancement ratio > 40% on the CE map. The segmented areas were subsequently filtered with a 2 × 2 morphological opening to exclude isolated pixels. The CE volume, as well as average enhancement ratio calculated only within segmented areas, were calculated, and compared for inter-scan reproducibility (Fig 3).

Results: Genu of the corpus callosum is the best candidate for SI normalization since it has the highest inter-scan ICCs among other anatomical structures, and the reproducibility is comparable to the non-normalized data (Table 1). Accurate and reproducible segmentation of CE was achieved using genu normalization. Future studies shall focus on studying the association between plaque progression and clinical outcomes, and the quantitative enhancement measurement.

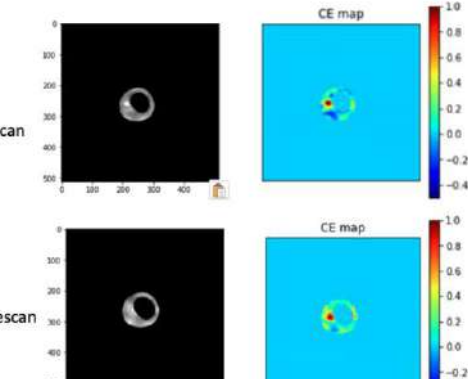


Fig 3 CE segmentation in scan and rescan

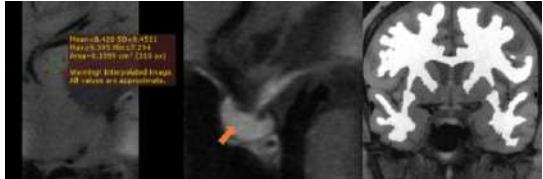


Fig 1 Candidates of structures for SI normalization (left: genu, middle: stalk, right: white matter)

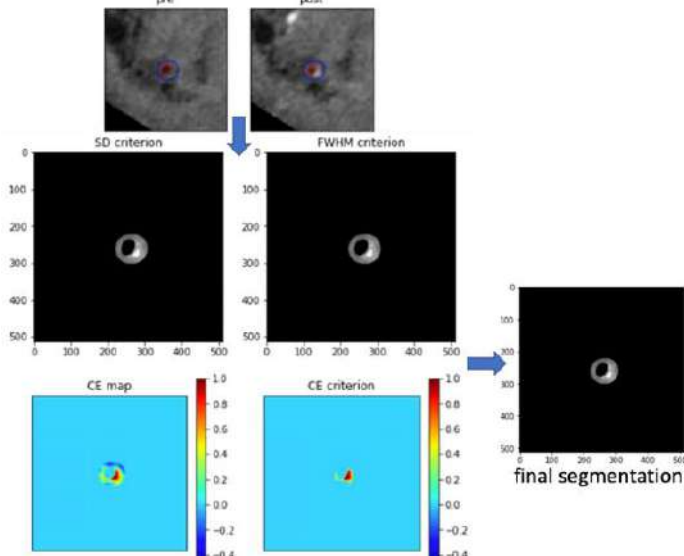


Fig 2 Diagram of semi-automatic segmentation of CE

Table 1 Inter-scan reproducibility of CE normalization and segmentation

	ICC	95% CI
For normalization (average enhancement ratio)		
Raw data (non-normalized)	0.942	(0.888,0.971)
Genu of corpus callosum	0.924	(0.835,0.959)
Pituitary stalk	0.873	(0.715,0.939)
White matter	0.904	(0.775,0.958)
For segmentation		
Enhancement volume	0.754	(0.692,0.805)
Average enhancement ratio	0.839	(0.716,0.890)

References: [1] Mandell AJNR (2017): 218-229. [2] Qiao Radiology (2014): 534-542. [3] Guo JMIR (2022) <http://doi.org/10.1002/jmri.28087>

Carotid artery perivascular adipose tissue quantified by MR imaging: A potential indicator for vulnerable atherosclerotic plaques

Shuwan Yu, Hualu Han, Rui Shen, Zihan Ning, Huiyu Qiao, Xihai Zhao

Center for Biomedical Imaging Research, Tsinghua University, Beijing, China

Background and Purpose: It has been shown that inflammation of perivascular adipose tissue (PVAT) is associated with atherosclerotic disease, particularly in coronary artery and carotid artery [1]. Increasing evidence demonstrated that carotid artery PVAT measured by computed tomography (CT) is associated with carotid plaque vulnerability [2, 3]. Apparently, CT can only provide CT attenuation for quantification of PVAT which may not be an ideal indicator for activity of PVAT. The signal intensity measured by magnetic resonance (MR) imaging can better quantitatively characterizing tissues. However, there lacks investigations of the association between PVAT quantified by MR imaging and carotid atherosclerosis. **The aim of this study was to investigate the association between PVAT measured by time-of-flight (TOF) magnetic resonance angiography (MRA) and carotid plaques.**

Methods: Study sample: A total of 20 symptomatic patients (16 males, 67.0 ± 9.3 years old) with carotid plaques were randomly selected from the Chinese Atherosclerosis Risk Evaluation (CARE II) study [4]. All patients underwent bilateral carotid multicontrast MR vessel wall imaging. The study protocol was approved by institutional review board and consent form was waived due to this retrospective analysis. **MR imaging:** The carotid MR imaging was performed on a 3.0T Philips MR scanner with 8-channel carotid coil. The imaging protocol included TOF MRA, T1W black-blood, T2W black-blood and MP-RAGE imaging sequences and the imaging parameters have been published in previous study [4]. All sequences were acquired with the identical in-plane spatial resolution of $0.55 \text{ mm} \times 0.55 \text{ mm}$ and slice thickness of 2 mm. **MR image analysis:** Two radiologists with >5 years' experience in neurovascular imaging reviewed bilateral carotid arteries to identify vulnerable compositional features of calcification (CA), lipid-rich necrotic core (LRNC), intraplaque hemorrhage (IPH) and loose matrix (LM). The lumen and outer wall boundaries were outlined and the outer wall boundaries were magnified 1.5 times which will be considered as the region of interest (ROI) (Figure 1). Carotid artery PVAT was manually segmented within ROI at each axial slice by removing lymph nodes and other vessels. The signal intensity ratio (SIR) between PVAT and muscle was respectively measured. **Statistical analysis:** The SIR of PVAT was compared between arteries with and without carotid vulnerable compositional feature using Mann-Whitney *U* test. Generalized estimating equation (GEE) was conducted to investigate the associations between carotid plaque compositional features and SIR of PVAT by minimizing the effect of two arteries from the same patient. *P* value <0.05 was statistically significant. All statistical analyses were performed on SPSS Statistics 26.

Results: The comparison results showed that carotid arteries with IPH ($P=0.011$) and LM ($P=0.020$) had significantly lower value of SIR of PVAT compared to those without (Figure 2). The GEE analysis demonstrated that SIR of PVAT was significantly associated with presence of vulnerable compositional features of IPH ($P=0.040$) (Table 1).

Discussion and Conclusion: Our study demonstrated that SIR of PVAT measured by TOF MRA is associated with carotid plaque vulnerable features, suggesting that the SIR of carotid PVAT on TOF MRA might be a potential indicator for vulnerable atherosclerotic plaques.

References: [1] Ross R., N Engl J Med. 1999; 340:115-26. [2] Antonopoulos AS., Sci Transl Med. 2017; 9:eaa12658. [3] Saba L., AJNR Am J Neuroradiol. 2020; 41:1460-1465. [4] Zhao X., Stroke Vasc Neurol. 2017; 2:15-20.

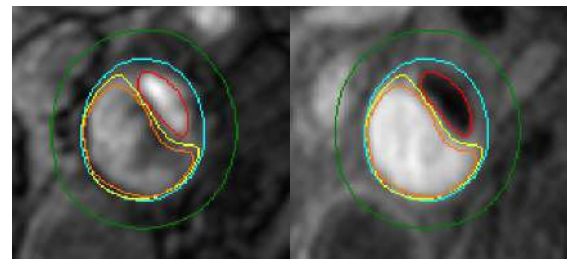


Figure 1. A typical segmentation results of TOF (left) and T1 (right) images (green: ROI; blue: outer wall; red: lumen; yellow: LRNC; orange: IPH).

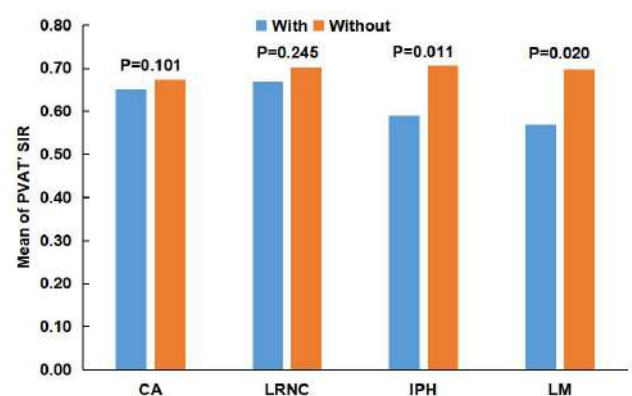


Figure 2. Mann-Whitney *U* test analysis results.

Table 1. GEE analysis results.

Dichotomous Variables	Predictor (SIR of PVAT)		
	Exp(B)	95%CI	P
CA	0.696	[0.237, 2.042]	0.510
LRNC	0.887	[0.373, 2.111]	0.786
IPH	0.407	[0.172, 0.960]	0.040
LM	0.268	[0.071, 1.008]	0.051

Evaluated the Relationships between Posterior cerebral artery Geometry and Atherosclerotic Disease Based on High-resolution Magnetic Resonance Vessel Wall Imaging

Lijuan Zheng¹ Xin Lin² Yunjing Xue^{1*}

¹ The school of Medical Technology and Engineering, Fujian Medical University , Fuzhou, China

²Department of Neonatology, Fujian Maternity and Child Health Hospital, Affiliated Hospital of Fujian Medical University, Fuzhou, China

*The author contributed equally to this work and is co-corresponding author.

Authors' contributions: L-J.Z wrote the main manuscript text, collected the clinical data and parameters. X.L analyzed the clinical data and parameters. Y-J.X amended the manuscript text.

Correspondence to: Yunjing Xue, MD Fujian Medical University Union Hospital, Department of Radiology, Fuzhou, 350001, China. Email: 1144150522@qq.com

Abstract

Background: Basal atherosclerotic disease is a major cause of posterior circulation ischemia, the study found that the brain morphology variation will cause vertebral basilar artery system hemodynamic changes, hemodynamics is an important factor in occurrence and development of atherosclerosis, but about the shape and structure of posterior cerebral artery and basilar artery atherosclerosis correlation study is less, To explore the correlation between posterior cerebral artery morphology and basilar plaque formation and plaque load under three types of vertebrobasilar artery anatomical morphology (Walking type, Lambda type and Tuning fork type), in order to study the mechanism of posterior circulation stroke caused by posterior cerebral artery variation.

Method: The patients hospitalized for posterior circulation ischemic in the Department of Neurology from October 2016 to June 2020 were enrolled for case-control analysis. According to the presence or absence of basilar plaque, patients were divided into basilar plaque group (n=102) and without basilar plaque group (n=219), and the basal artery plaque group was divided into 61 cases without posterior cerebral artery variation, 27 cases with complete embryonic posterior cerebral artery (CFTP), and 14 cases of partial embryonic cerebral artery (PFTP) according to the morphology of the posterior cerebral artery. The differences in basilar artery diameter, curvature and plaque load among the three groups were analyzed.

Results: In both Lambda and Walking vertebrobasilar types, the fetal posterior cerebral artery increased the risk of basilar plaque (OR=3.196, 95%CI: 1.77-5.78; OR = 12.091, 95% CI: 1.77 ~ 5.78; P < 0.05). In Walking type, the basilar artery diameter, mean lumen area were lower (P<0.05, r=-0.35, r=-0.29); Basilar artery curvature and mean standardized wall index were higher (P<0.05, R =0.43, r=0.25) in fetal posterior cerebral artery patients than those without posterior cerebral artery variation. There was statistical significance in posterior circulation infarction between fetal posterior cerebral artery patients (P<0.05). **Conclusions:** Fetal posterior cerebral artery is a risk factor for basilar artery plaque and play an important role in the development of basilar plaque, which can promote the occurrence of posterior circulation ischemic.

Combination of irregular pulsation and wall enhancement increased the accuracy in identifying symptomatic status in unruptured intracranial aneurysms

Purpose: Both irregular pulsation and aneurysm wall enhancement (AWE) have been suggested as potential candidates for intracranial aneurysms (IAs) instability. Our study aimed to investigate whether combination of irregular pulsation and AWE will increase the accuracy in identifying symptomatic status in unruptured IAs.

Methods: This retrospective study included consecutive patients with IAs who underwent four-dimensional computed tomography angiography (4D-CTA) and vessel wall MRI (VW-MRI) between January 2017 to July 2021. IAs were categorized as asymptomatic and symptomatic. The presence of irregular pulsation (defined as a temporary focal protuberance ≥ 1 mm on more than three successive frames) was identified on 4D-CTA movies. AWE was estimated on VW-MRI and classified as 4 grades (grade 0 for none or questionable focal trace enhancement, grade 1 for focal thick [<1 mm] enhancement, grade 2 for thin [maximum thickness, ≤ 1 mm] circumferential wall enhancement, or grade 3 for thick [maximum thickness, ≥ 1 mm] circumferential wall enhancement)¹. The association between irregular pulsation and AWE and symptoms was analyzed.

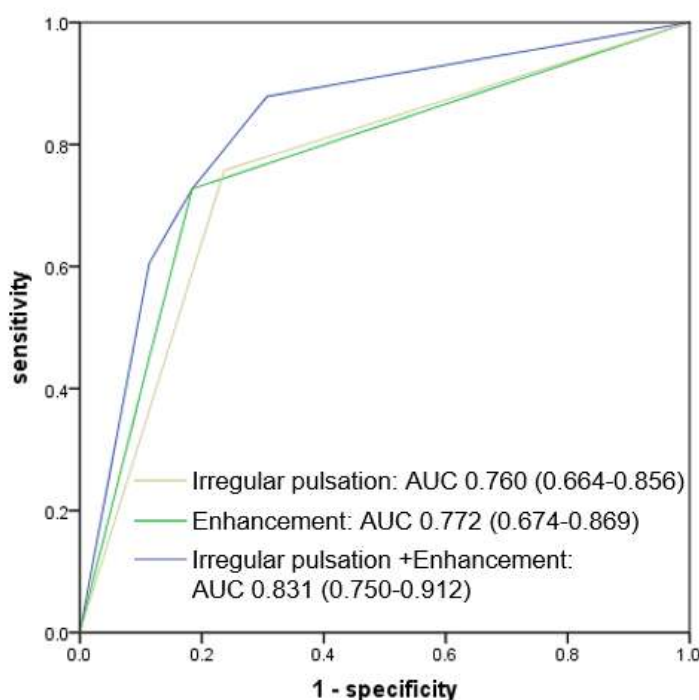
Results: One hundred and forty-seven saccular IAs were included in this study (114 asymptomatic, 33 symptomatic). Symptomatic IAs were significantly larger in size compared with asymptomatic IAs (9.31 ± 4.22 mm vs 5.86 ± 2.95 mm, $p < 0.001$) and had more irregular pulsations (45.5% vs 19.3%, $p = 0.002$) and AWE (72.6% vs 19.3%, $p < 0.001$). Both irregular pulsation (OR 4.621, 95% CI 1.716 to 12.444; $p = 0.002$) and AWE (OR 3.413, 95% CI 1.077 to 10.814; $p < 0.001$) were independently associated with aneurysm symptoms. The combination of irregular pulsation and AWE increased the accuracy over each alone in identifying symptomatic aneurysms (AUC 0.831 vs 0.760, 0.772; $p = 0.029$, $p = 0.013$; respectively).

Discussion: Recent studies have showed irregular pulsation, AWE was promising for identification of unstable aneurysms and it is gaining increasing attention^{2,3}. In a large cohort of patients with IAs detected by 4D-CTA and VW-MRI, the combination of irregular pulsation and AWE increased the accuracy over each alone in identifying symptoms aneurysms in unruptured IAs. Evaluation of irregular pulsation and AWE might provide additional value in stratifying the aneurysm rupture risk and such multi-modality imaging study helped determine the best predictors of aneurysm instability.

Figure 1. Receiver operating characteristic curve analysis for the prediction of unruptured intracranial aneurysm symptomatic status

References:

1. Edjlali M, Guedon A, Ben HW et al. Circumferential Thick Enhancement at Vessel Wall MRI Has High Specificity for Intracranial Aneurysm Instability. *Radiology* 2018;289(1):181-187.
2. Zhu C, Wang X, Eisenmenger L et al. Wall enhancement on black-blood MRI is independently associated with symptomatic status of unruptured intracranial saccular aneurysm. *Eur Radiol* 2020;30(12):6413-6420.
3. Zhang J, Li X, Zhao B et al. Irregular pulsation of intracranial unruptured



aneurysm detected by four-dimensional CT angiography is associated with increased estimated rupture risk and conventional risk factors. *J Neurointerv Surg* 2021;13:854-59.

An assessment on the incremental value of 3D high-resolution MRI to identify culprit plaques in the nonstenotic intracranial artery

Xia Tian, Bing Tian, Wenjia Peng, Xuefeng Zhang

Abstract Purpose To analyze the differences in imaging and histogram features between culprit and nonculprit intracranial plaque without substantial stenosis using 3D high-resolution magnetic resonance imaging (hr-MRI). **Methods** Morphological and histogram features were analyzed based on T1WI and contrast-enhanced T1WI. Multivariate regression analysis was performed to identify significant determinates differentiating culprit and nonculprit plaques. **Results** 111 culprit plaques and 39 nonculprit plaques were analyzed. Multivariate logistic regression analyses showed that plaque volume and maximum wall thickness were significantly associated with plaque type. **Discussion** Plaque volume and maximum wall thickness were independent risk factors for culprit plaque in patients with nonstenotic atherosclerosis.

Reference:

1. Shi Z, Li J, Zhao M, et al. Quantitative histogram analysis on intracranial atherosclerotic plaques: a high-resolution magnetic resonance imaging study. *Stroke*, 2020, 51(7):2161-2169.

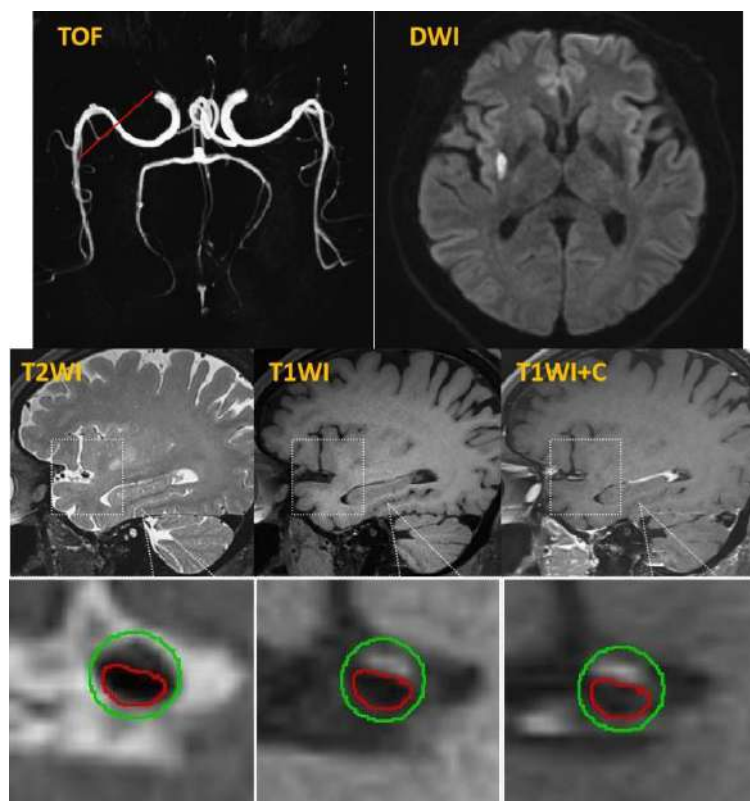


Fig 1 Image findings of patients with culprit intracranial plaque

An assessment on the incremental value of 3D high-resolution MRI in evaluating ESUS caused by non stenotic intracranial atherosclerosis

Xia Tian, Bing Tian, Chengcheng Zhu, Wenjia Peng, Xuefeng Zhang

Abstract Purpose To investigate the issue by evaluating the morphological and histogram features of nonstenotic intracranial plaque in patients with ESUS and small-vessel disease (SVD) using 3D high-resolution magnetic resonance imaging (hr-MRI). **Methods** Morphological and histogram features were analyzed. Multivariate regression analysis was performed to identify the association with cerebrovascular ischemic events. **Results** 47 ESUS patients and 64 SVD patients were analyzed. Multivariate logistic regression analyses showed that plaque volume, enhancement ratio of whole culprit plaque and coefficient of variation were independently associated with ESUS. **Discussion** The plaque volume, enhancement ratio of whole culprit plaque and coefficient of variation of responsible plaque are independent risk factors for ESUS.

Reference:

1. Tao L, Li XQ, Hou XW, et al. Intracranial atherosclerotic plaque as a potential cause of embolic stroke of undetermined source. J Am Coll Cardiol, 2021, 77(6):680-691.

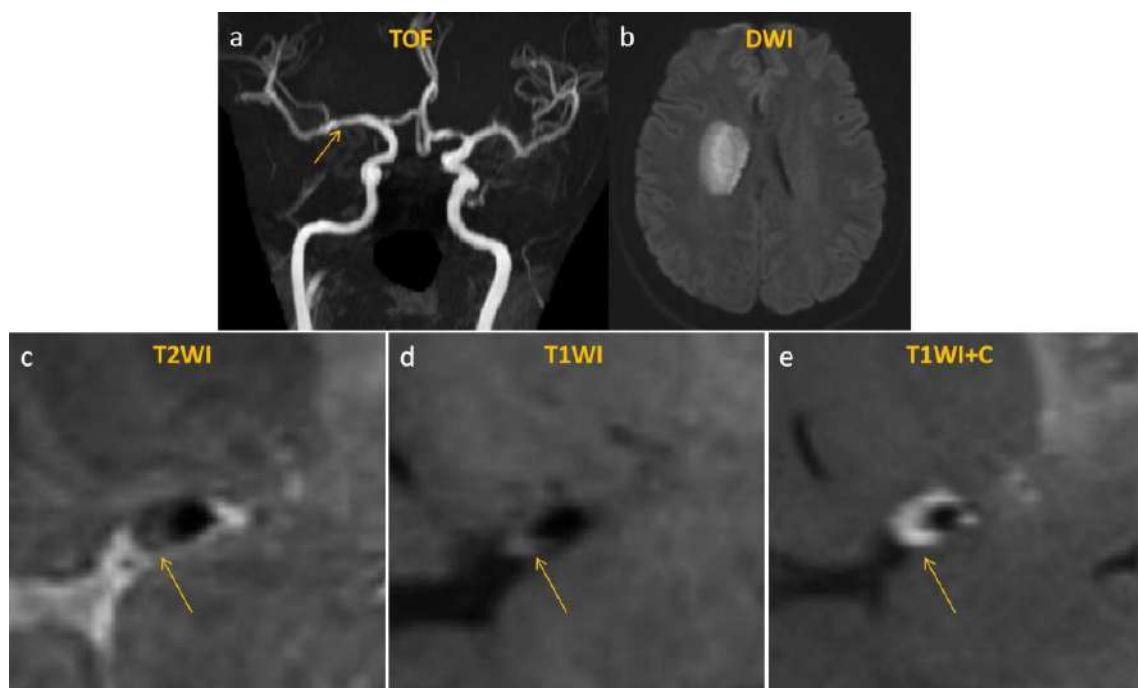


Fig 1 Image findings of patients with ESUS

An assessment on the incremental value of 3D high-resolution MRI in evaluating the risk of recurrence of ischemic stroke caused by non stenotic intracranial atherosclerosis

Xia Tian, Bing Tian, Wenjia Peng, Xuefeng Zhang

Abstract Purpose To analyze the image characteristics of recurrent and stable intracranial nonstenotic atherosclerotic plaques by 3D high-resolution magnetic resonance imaging (hr-MRI). **Methods** The relationship of quantitative characteristics (including imaging and histogram features) between recurrent and stable group were analyzed. **Results** 11 patients in recurrent group and 31 patients in stable group were recruited. Compared to stable group, recurrent group demonstrated higher degree of eccentricity index, enhancement ratio of stenosis and whole plaque, plaque volume, intraplaque hemorrhage, SD and maximum value. **Discussion** 3D hr-MRI can effectively evaluate the plaque imaging and histogram features of patients with recurrent stroke without stenotic atherosclerosis.

Reference:

1. Zhang X, Chen L, Li S, et al. Enhancement characteristics of middle cerebral arterial atherosclerotic plaques over time and their correlation with stroke recurrence. J Magn Reson Imaging, 2021, 53(3):953-962.

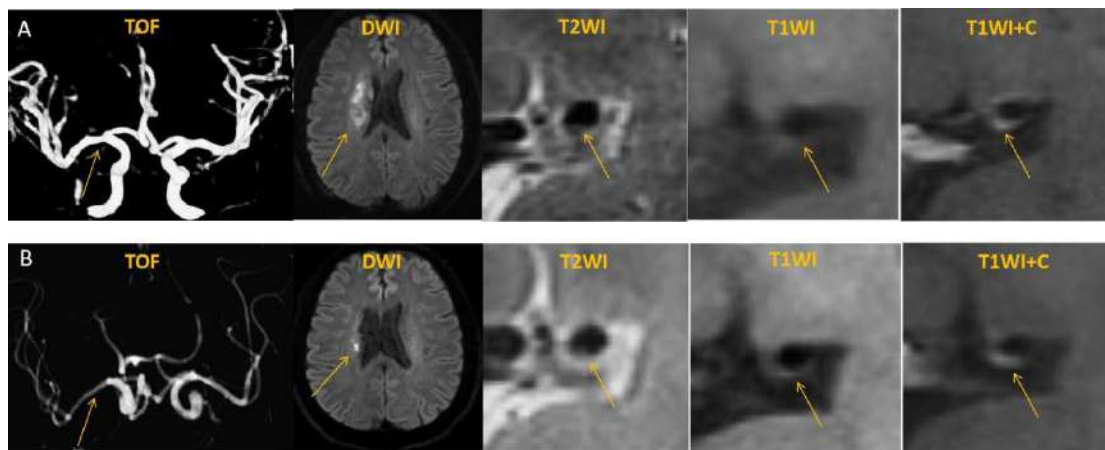


Fig 1 Image findings of patients with ischemic stroke in recurrence group

Diabetes and carotid plaque characteristics were independently associated with larger symptomatic WMHs volume.

Beibei Sun¹, Lingling Wang¹, Jie Sun², Chun Yuan², Huilin Zhao¹.

1 Department of Radiology, Renji Hospital, School of Medicine, Shanghai Jiaotong University, Shanghai 200127, P.R. China

2 Department of Radiology, University of Washington, Seattle, WA, United States.

Background: Diabetes has been associated with carotid atherosclerosis and white matter lesions (WML) which all increased the stroke risk. We aim to evaluate whether impact of diabetes on WML was independent of carotid atherosclerotic features of stroke patients.

Methods: Patients with recent cerebrovascular symptoms and carotid plaque were recruited from the cross-sectional, multicenter CARE-II study. MRI features of symptomatic carotid plaques (including luminal stenosis, plaque burden and composition) and white matter hyperintensities (WMHs) of bilateral cerebral hemispheres were quantitatively evaluated. Multivariate logistic regression and linear regression was performed to examine the associations between diabetes and carotid atherosclerosis and WMHs.

Results: 362 patients were enrolled (mean age: 61.7±9.8 years; 237 males), including 124 diabetic and 238 non-diabetic patients. Diabetic subjects had a greater plaque burden (mean wall thickness, $P=0.036$) and a higher prevalence of high-risk characteristics ($P=0.038$). Additionally, in the diabetic subjects showed higher prevalence of moderate-to-severe WMHs (a total Fazekas score of 3–6) ($P=0.002$) and larger whole brain WMHs volume ($P=0.048$) and symptomatic side WMHs volume ($P=0.002$) than those in the non-diabetic subjects. Diabetes was independently correlated with moderate-to-severe WMHs prevalence (Odds ratio=2.25, $P=0.008$). The association of diabetes with large symptomatic WMHs volume ($\beta=0.181$, $P=0.001$) was also independent of plaque characteristics after adjusting for patient characteristics. Carotid plaque characteristics were significantly and mildly correlated with symptomatic WMHs volume and did not vary between the diabetic and non-diabetic group though the difference of intraplaque hemorrhage was borderline significant ($P=0.065$).

Conclusions: Diabetes and carotid plaque characteristics were independently associated with larger symptomatic WMHs volume, and carotid plaque characteristics did not mediate the association between diabetes and symptomatic side WMHs volume.

Endovascularly treated aneurysm vessel wall MRI characteristics and association with symptomatic vasospasm and delayed cerebral infarction

Mehmet Aksakal¹, Dandan Chang¹, Nadin Zanaty¹, Chengcheng Zhu¹, Michael R. Levitt², Mahmud Mossa-Basha^{1,3}.

¹University of Washington Department of Radiology, ²University of Washington Department of Neurosurgery, ³University of North Carolina Department of Radiology

Purpose: Previous studies have shown the value of intracranial vessel wall MRI (IVW) in predicting angiographic vasospasm after aneurysm rupture in endovascularly treated patients. However, these studies only address angiographic vasospasm and not symptomatic vasospasm or delayed cerebral ischemia (DCI) primarily. The purpose of this study is to evaluate the association between IVW enhancement characteristics and the development of symptomatic vasospasm or delayed cerebral ischemia in endovascularly treated cerebral aneurysm patients after aneurysmal subarachnoid hemorrhage.

Methods: We retrospectively included endovascularly treated ruptured and unruptured aneurysm cases between September 2015 and November 2022 with IVW in the immediate post-procedure period. One rater, blinded to clinical data and follow-up imaging, independently evaluated the images for the presence, pattern (focal, eccentric, or concentric), extent (focal, heterogeneous, or diffuse), and intensity (none, less than, or greater than or equal to the pituitary infundibulum) of wall enhancement, presence of wall thickening, stenosis and presence of atherosclerosis. Paired internal carotid artery, M1 and M2 MCA, A1 and A2 ACA, P1 and P2 PCA, V4 vertebral arteries, and the basilar artery segments were individually evaluated. Clinical data were used to assess the development of symptomatic vasospasm. Delayed cerebral ischemia; cerebral infarct; procedural details; and presence and grade of subarachnoid, parenchymal, and intraventricular hemorrhage were charted independently by a separate reviewer. Statistical associations were determined on a per-vessel segment basis using the chi-squared test.

Results: A total of 98 treated ruptured and unruptured aneurysm cases were included in the analysis. In the preliminary results, patients who developed vasospasm had significantly more enhancing arterial segments than those that did not (60% vs. 33%, $p=.03$). Segment wall thickening was significantly more common in vasospasm patients (55% vs. 7%, $p<.001$), as was intense (42% vs. 6%) and intermediate (58% vs. 32%) wall enhancement ($p<.001$), respectively. There was no difference in pattern ($p=.32$) or extent ($p=.66$) of wall involvement between the two groups. In the vasospasm cohort, 1 enhancing segment was secondary to atherosclerosis, while in the non-vasospasm cohort, 2 enhancing segments were from vasa vasorum and 4 were due to atherosclerosis.

Conclusion: Based on the preliminary data; in patients who subsequently develop angiographic vasospasm, there is a significantly higher frequency of arterial segment wall enhancement, increased intensity of wall enhancement, and presence of wall thickening. These markers could potentially predict vasospasm and facilitate preventive treatment to avoid the severe consequences of vasospasm. We will further evaluate the association between the vessel wall enhancement and delayed cerebral ischemia and/or symptomatic vasospasm with two blinded raters.

References

1. Mossa-Basha M, Huynh TJ, Hippe DS, Fata P, Morton RP, Levitt MR. Vessel wall MRI characteristics of endovascularly treated aneurysms: association with angiographic vasospasm. *J Neurosurg*. 2018 Sep 21;131(3):859-867. doi: 10.3171/2018.4. JNS172829. PMID: 30239313; PMCID: PMC7719715.
2. Mossa-Basha M, Alexander M, Gaddikeri S, Yuan C, Gandhi D. Vessel wall imaging for intracranial vascular disease evaluation. *J Neurointerv Surg*. 2016 Nov;8(11):1154-1159. doi: 10.1136/neurintsurg-2015-012127. Epub 2016 Jan 14. PMID: 26769729; PMCID: PMC5484417.
3. Mossa-Basha M, Hwang WD, De Havenon A, Hippe D, Balu N, Becker KJ, Tirschwell DT, Hatsukami T, Anzai Y, Yuan C. Multicontrast high-resolution vessel wall magnetic resonance imaging and its value in differentiating intracranial vasculopathic processes. *Stroke*. 2015 Jun;46(6):1567-73. doi: 10.1161/STROKEAHA.115.009037. Epub 2015 May 7. PMID: 25953365.

Cardiovascular Risk Factors Associated with Blood Flow Characteristics Derived from 4D-flow MRI of the Left Atrium and Left Atrial Appendage: The Multi-Ethnic Study of Atherosclerosis

Maurice Pradella¹, Justin J. Baraboo¹, Stanley H. Chu¹, Anthony Maroun¹, Julia M. Hwang¹, Rod Passman^{2,3}, Susan R. Heckbert⁴, Philip Greenland³, Michael Markl¹

¹ Department of Radiology, Northwestern University Feinberg School of Medicine, Chicago, USA

² Department of Medicine, Northwestern University Feinberg School of Medicine, Chicago, USA

³ Department of Preventive Medicine, Northwestern University Feinberg School of Medicine, Chicago, USA

⁴ Department of Epidemiology, University of Washington, Seattle, USA

Purpose

Blood flow dynamics of the left atrium (LA) and left atrial appendage (LAA), such as increased LA and LAA flow stasis and reduced peak velocity, are known risk factors for atrial thrombus formation and stroke (1). These parameters can be assessed in-vivo using 4D-flow MRI, however there is a lack of healthy aging population studies investigating the effects of demographic and cardiovascular (CV) risk factors on changes in atrial blood flow.

Methods

Participants from the Multi-Ethnic Study of Atherosclerosis (MESA), a study of subclinical cardiovascular disease (CVD) in participants without prior clinical CVD at baseline, underwent a standard-of-care MRI including retrospectively ECG-gated 4D-flow series on a 1.5T system. Following phase offset corrections, 3D phase contrast angiograms (PC-MRA) were calculated and used for the 3D segmentation of the LA and LAA using commercial software (MIMICS, Materialise). LA and LAA segmentations were used to mask the 4D flow data and calculate volume, mean blood stasis (% cardiac time voxel velocity <0.1 m/s) and peak velocity (top 5% of velocities) for the LA and LAA (2), Fig 1. Demographics and CV risk factors (hypertension, diabetes, history of atrial fibrillation (AF), body mass index (BMI), current/former smokers, alcohol consumption and left ventricular (LV) ejection fraction (LVEF)) were investigated in multivariable models for each 4D-flow parameter.

Results

One-hundred-fifty-eight MESA participants were included (age: 72.8±7.3 years, 53% female). Factors associated with LA peak velocity were age (β : -0.0016, $p<0.01$), history of AF (β : -0.0281, $p<0.05$), diabetes (β : 0.0329, $p<0.01$) and LVEF (β : 0.0011, $p<0.05$). LA stasis was associated with age (β : 0.6391, $p<0.001$), history of AF (β : 5.5987, $p<0.05$) and diabetes (β : -6.1204, $p<0.05$). For the LAA, peak velocity was lower in Black participants (β : 0.0264, $p<0.01$) and when history of AF (β : -0.0433, $p<0.001$) was present. LAA stasis was associated with male sex (β : -5.3626, $p<0.01$), White participants (β : -3.6885, $p<0.05$), diabetes (β : -4.5453, $p<0.01$), LA volume (β : 0.1218, $p<0.01$) and BMI (β : -0.4208, $p<0.05$).

Parameters	LA peak velocity	LA stasis	LAA peak velocity	LAA stasis
Age	-0.0016**	0.6391***		
Male Sex				-5.3626**
Race				
Black			-0.0264**	
White				-3.6885*
History of AF	-0.0281*	5.5987*	-0.0433***	
Diabetes	0.0329**	-6.1204*		-4.5453*
LVEF	0.0011*			
LA Volume				0.1218**
BMI				-0.4208*

Values represent coefficients from multivariable models

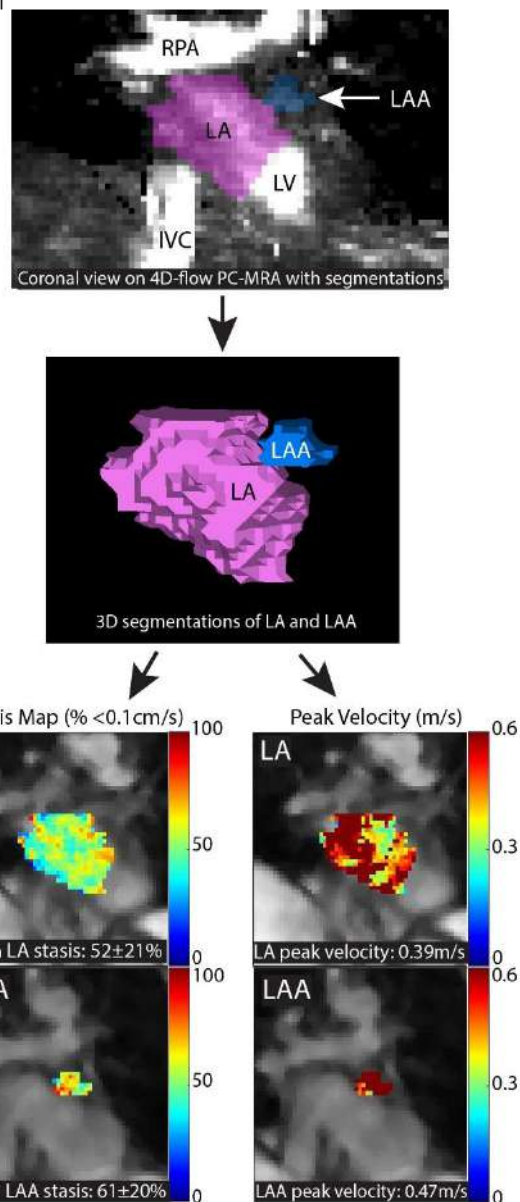
* $p<0.05$, ** $p<0.01$, *** $p<0.001$

Discussion

We describe CV risk factors associated with impaired flow hemodynamics in the LA and LAA which could indicate increased risk for thrombus formation and stroke. While history of AF, higher age, reduced LVEF, and higher LA volume were associated with worse flow characteristics, we found that diabetes, higher BMI and Black or White participants were associated with improved flow hemodynamics.

References: 1. Shen et. al. JACC Basic Transl 2019. 2. Markl et. al. Invest Radiol 2016.

Fig 1



Baseline 4D flow MRI-derived *in vivo* hemodynamic parameters stratify descending aortic dissection patients with enlarging aortas

Stanley Chu, BS¹, Ozden Kilinc, MD¹, Maurice Pradella, MD¹, Elizabeth Weiss, BS^{1,3}, Justin Baraboo, BS³, Anthony Maroun, MD¹, Kelly Jarvis, PhD^{1,3}, Chris Mehta, MD², S. Chris Malaisrie, MD², Andrew Hoel, MD², James C. Carr, MD¹, Bradley D. Allen, MD, MS¹, Michael Markl, PhD^{1,3}

¹Department of Radiology, Northwestern University, Chicago, IL, United States

²Department of Surgery (Cardiac Surgery), Northwestern University, Chicago, IL, United States

³Department of Biomedical Engineering, Northwestern University, Chicago, IL, United States

Purpose: Recent studies using 4D flow MRI have suggested that *in vivo* hemodynamic assessment of blood flow at entry tears and in the false lumen may help identify type B aortic dissection (TBAD) patients with growing aortas (1-4). The purpose of our study was to assess the value of true lumen and false lumen hemodynamics compared to aortic morphological measurements for predicting adverse-aorta related outcomes (AARO) and aortic growth in patients with TBAD.

Methods: Using an IRB approved protocol, we retrospectively identified patients with descending aorta (DAo) dissection at a large tertiary center. Inclusion criteria includes-known TBAD with ≥ 6 months of clinical follow-up after initial presentation for TBAD or after ascending aorta intervention for patients with repaired type A dissection with residual type B aortic dissection (rTAAD). Patients with prior descending aorta intervention were excluded. The FL and TL of each patient were manually segmented from 4D flow MRI data, and 3D parametric maps of aortic hemodynamics were generated (5) (Fig 1). Groups were divided based on 1) presence vs. absence of AARO and 2) growth rate \geq vs. < 3 mm/year. All hemodynamic parameters were indexed to aortic diameter by dividing each patient's parameters with their corresponding baseline aortic diameter. Indexed true and false lumen kinetic energy (KE), stasis, peak velocity (PV), reverse and forward flow (RF, FF), KE ratio (FL KE/TL KE), as well as index aortic diameter were compared between groups using the Mann-Whitney U or independent t-test.

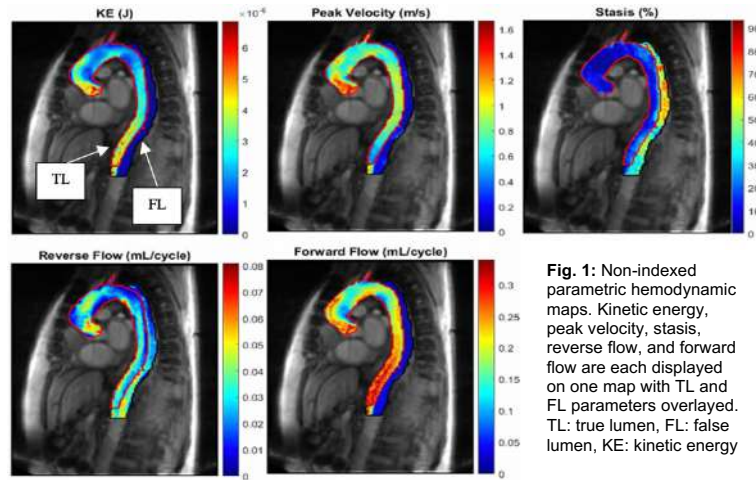


Fig. 1: Non-indexed parametric hemodynamic maps. Kinetic energy, peak velocity, stasis, reverse flow, and forward flow are each displayed on one map with TL and FL parameters overlaid. TL: true lumen, FL: false lumen, KE: kinetic energy

Results (Table 1): A total of 51 patients (age: 58.4 ± 15.0 years, M/F: 31/20) were included for analysis of AARO. This group contained 26 patients with TBAD and 25 patients with rTAAD. In the overall cohort, AARO patients had larger baseline diameter, and lower FL RF and stasis. They also had lower TL KE, FF, and PV. De novo TBAD patients with AARO had larger baseline diameter, lower FL stasis and lower TL_PV ($p < 0.05$). rTAAD patients with AARO had larger baseline diameter, lower FL RF, and lower TL FF ($p < 0.05$). In both the overall cohort and in the subgroup of de novo TBAD cases, patients with aortic growth > 3 mm/year had a higher KE ratio ($p < 0.05$). KE ratio was correlated with aortic growth rate in de novo TBAD patients ($r = 0.58$, $p = 0.01$).

Results (Table 1): A total of 51 patients (age: 58.4 ± 15.0 years, M/F: 31/20) were included for analysis of AARO. This group contained 26 patients with TBAD and 25 patients with rTAAD. In the overall cohort, AARO patients had larger baseline diameter, and lower FL RF and stasis. They also had lower TL KE, FF, and PV. De novo TBAD patients with AARO had larger baseline diameter, lower FL stasis and lower TL_PV ($p < 0.05$). rTAAD patients with AARO had larger baseline diameter, lower FL RF, and lower TL FF ($p < 0.05$). In both the overall cohort and in the subgroup of de novo TBAD cases, patients with aortic growth > 3 mm/year had a higher KE ratio ($p < 0.05$). KE ratio was correlated with aortic growth rate in de novo TBAD patients ($r = 0.58$, $p = 0.01$).

Discussion: Our study suggests that 4D flow MRI is a promising tool for TBAD evaluation that can provide information beyond traditional MRA or CTA. 4D flow has the potential to become an integral aspect of TBAD work-up, as hemodynamic assessment may allow earlier identification of at-risk patients who could benefit from earlier intervention.

References: [1]: Burriss et al., JVS 2016; [2]: Marlevi et al., JCMR 2021; [3]: Pathrose et al., MRM 2021; [4]: Stankovic et al. CDT 2014; [5]: Jarvis et al., JMRI 2020.

Overall Cohort						
Indexed Parameter (per mm)	No Adverse Outcome (n = 39)	Adverse Outcome (n = 12)	P-value	Rapid Aortic Growth (n = 10)	Slow Aortic Growth (n = 32)	P-Value
FL Mean Reverse Flow (mL/cycle)	$3.13E-4 \pm 1.46E-4$	$2.21E-4 \pm 9.44E-5$	0.02*	$2.37E-4 \pm 1.36E-4$	$2.98E-4 \pm 1.46E-4$	0.09
FL Mean Stasis (%)	1.55 ± 0.46	1.16 ± 0.36	0.01*	1.39 ± 0.36	1.46 ± 0.46	0.59
TL Mean KE (mJ)	$2.82E-5 \pm 1.38E-5$	$1.86E-5 \pm 1.03E-5$	0.02*	$2.29E-5 \pm 1.06E-5$	$2.75E-5 \pm 1.48E-5$	0.46
TL Forward Flow (mL/cycle)	$2.76E-3 \pm 9.57E-4$	$2.04E-3 \pm 7.09E-4$	0.01*	$2.29E-3 \pm 8.61E-4$	$2.63E-3 \pm 8.68E-4$	0.43
TL Peak Velocity (cm/s)	5.70 ± 2.05	3.84 ± 1.37	0.01*	4.75 ± 1.61	5.45 ± 2.22	0.61
Baseline Diameter (mm)	41.97 ± 7.33	50.50 ± 6.87	0.001*	45.90 ± 6.12	43.25 ± 8.00	0.28
KER	$3.11E-3 \pm 2.34E-3$	$3.93E-3 \pm 2.85E-3$	0.41	$4.23E-3 \pm 2.04E-3$	$3.02E-3 \pm 2.34E-3$	0.03*

Optimization of Complex-Difference Learning for Reconstructing Highly-Accelerated Real-Time Phase Contrast MRI with Radial k-space Sampling

Huili Yang¹, Amanda L. DiCarlo¹, Julia M. Hwang¹, Hassan Haji-Valizadeh¹, KyungPyo Hong¹, Daming Shen¹, Nikolay Iakovlev¹, Florian Schiffrers¹, Aggelos K. Katsaggelos¹, Daniel C. Lee¹, Philip Greenland¹, Rod Passman¹, Michael Markl¹, Daniel Kim¹

¹Northwestern University, Chicago, IL

Purpose: To optimize configurations of complex-difference learning (CDL)[1] for reconstructing prospective real-time phase contrast (rtPC) cardiac MRI obtained with radial k-space sampling.

Methods: We used existing 28.8-fold accelerated rtPC MRI (280 2D+time datasets; 60 frames per set; 210/70 training-testing split) collected from 140 patients (80 males, 60 females, age = 70.3 ± 9.7 yrs) at the mitral valve (MV) and mid left atrium (mid-LA). Using the CDL network proposed in [1], we conducted the following steps for optimization: Step 1 – an epoch-based training scheme (vs. iteration-based training [default]); step 2 – complex convolution (vs. concatenating real/imaginary data); step 3 – no dropout (vs 15% dropout [default]); step 4 – an additional MSE loss from velocity-encoded data to allow interaction between training velocity-compensated and complex-difference data. Images reconstructed using compressed sensing (CS) were used as the ground truth. We used the NRMSE of cropped view of the heart in phase difference as the metric to determine the optimal configuration.

Results: The following produced lower phase errors for each pair: epoch-based training vs. iteration-based training (NRMSE = 4.54% vs 5.40%); using epoch-based training, complex convolution vs. concatenation of real/imaging data (5.19% vs 4.54%); using epoch-based training and no complex convolution, no dropout vs. 15% dropout (4.22% vs 4.54%); using epoch-based training, no complex convolution and no dropout, an extra loss from velocity-encoded data vs. otherwise (4.13% vs 4.22%). As shown in Figure 1, optimal CDL produced better agreement with CS than conventional CDL. As summarized in Table 2 (n=70), there were significant differences in the NRMSE of phase difference at the mitral valve, and optimal CDL agreed better with CS than CDL (Figure 2).

Discussion: This study describes the optimization steps in CDL for reconstructing highly-accelerated rtPC MRI with radial k-space sampling. A series of optimization steps resulted in lower velocity errors.

References: [1] Haji-Valizadeh, Hassan, et al. Magn Reson Med 2021.

FOV	Matrix size	Spatial resolution	Temporal resolution	Slice thickness	TE/TR	Spokes per frame	Acceleration factor	Flip angle	Receiver bandwidth
300x300mm ²	144x144	2.1x2.1mm ²	42.5ms	8mm	3.78/8.5ms	5	28.8	15°	793Hz/pixel

Table 1. Relevant imaging parameters.

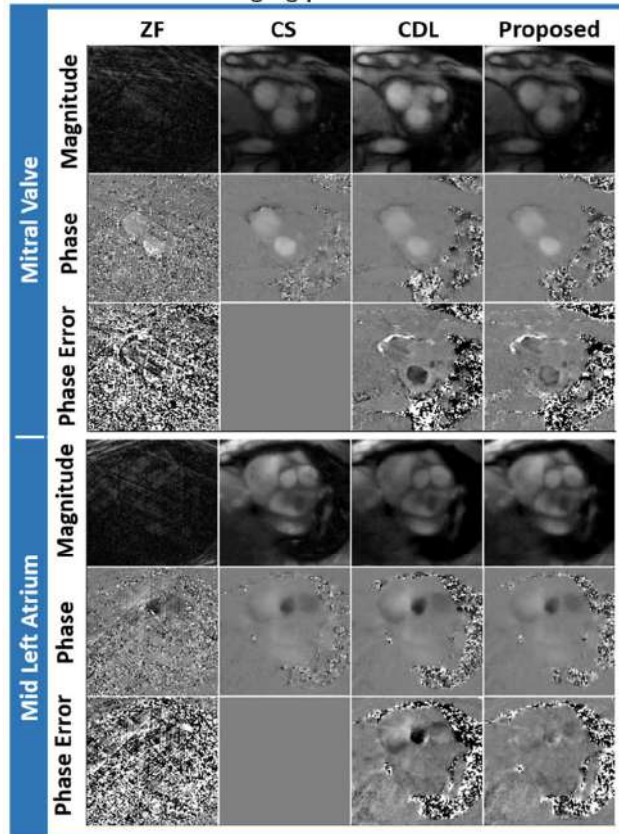


Figure 1. Magnitude, phase, and phase error (relative to CS) images. ZF: zero-filled, CS: compressed sensing, CDL: complex-difference learning.

Table 2. Results of measuring peak and mean velocity.

		CS	CDL	Proposed
Mitral Valve	Peak Vel (cm/s)	49.4 ± 8.3	50.1 ± 10.0	47.4 ± 7.9
	NRMSE of Phase (%)	-	5.4 ± 2.8*	3.3 ± 1.0*
Mid-Left Atrium	Peak Vel (cm/s)	23.8 ± 5.5	24.3 ± 6.6	21.7 ± 5.6
	NRMSE of Phase (%)	-	5.4 ± 2.1	4.9 ± 2.1

* significant differences (p<0.05).

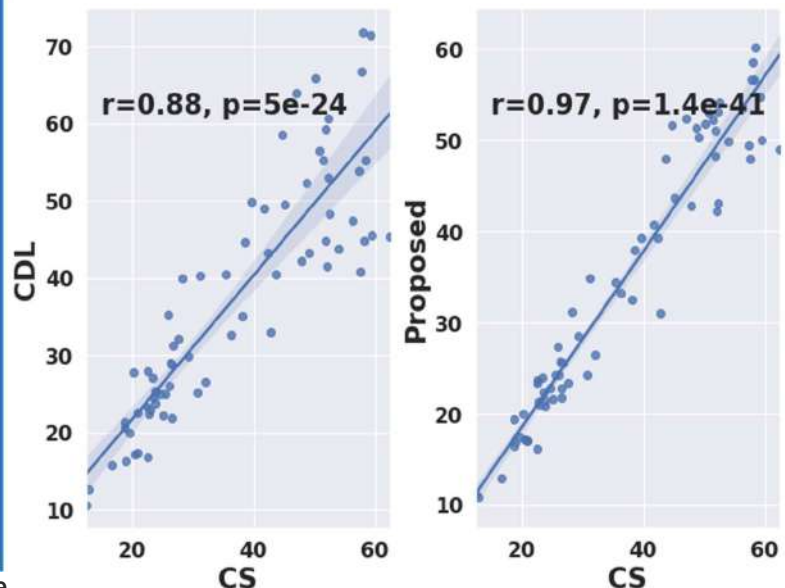


Figure 2. Linear regression of the peak velocity. CS: compressed sensing, CDL: complex-difference learning.

Flow Displacement and Wall Shear Stress in Individuals with Mild-to-Moderate Aortic Dilation and Tricuspid Aortic Valves

Chiara Trenti^{1,2}, Tino Ebbers^{1,2}, Eva Swahn^{1,3}, Lena Jonasson¹, Petter Dyverfeldt^{1,2}

¹Department of Health, Medicine and Caring Sciences; Linköping University, Linköping, Sweden

²Center for Medical Image Science and Visualization (CMIV), Linköping University, Linköping, Sweden

³Department of Cardiology in Linköping, and Department of Health, Medicine and Caring Sciences, Linköping University, Linköping, Sweden

Purpose: Ascending aortic (AA) aneurysm is an asymptomatic disease that it is often not detected until dissection or rupture occurs. Basic vessel dimensions are the primary measurements used clinically to risk-stratify patients. High circumferential wall shear stress (WSS) has been associated with aortic growth in patients with bicuspid aortic valve and aortic stenosis^(1,2), but less is known about patients with tricuspid aortic valve (TAV). A recent study suggested that AA growth is associated with low WSS and high flow displacement (FD) in patients with TAV⁽³⁾, although only a small number of patients were available. In this cross-sectional study, we sought to obtain a comprehensive view of WSS and FD in a cohort of TAV patients and age- and sex- matched controls.

Methods: 44 patients with AA diameter >40 mm and 44 age- and sex-matched controls with AA diameter <40 mm were recruited from the Swedish CARdioPulmonary bioImage Study (SCAPIS) in Linköping. Patients had a mild-to-moderate dilation classified from CT coronary angiography. 4D Flow MRI was acquired with a 3T Philips Ingenia scanner (Philips Healthcare, Best, the Netherlands) in all subjects. 4D flow datasets were corrected for background phase offset and phase wrapping. Time resolved segmentations were created automatically with an atlas-based method, combined with manual adjustments⁽⁴⁾. The AA was defined from the valve to the top of the arch, and peak systole was defined as the timeframe with maximum average velocity in the AA. Maximum and average diameter in the AA were obtained from the cross-sectional planes. 3D peak systolic WSS maps were computed with the method of Potters et al⁽⁵⁾, and average and maximum WSS in the AA were reported. FD at peak systole was assessed at 7 equidistant planes in the AA⁽⁶⁾. A workflow of the methods is represented in Figure 1. Results are reported as mean \pm (standard deviation). Student's t-tests were used to compare values between the two cohorts, with a p value <0.05 considered as significant.

Results: Results are reported in Table 1. Patients had larger maximum and average diameter in the AA compared to controls ($p < 0.001$). Heart rate (HR), stroke volume (SV) and cardiac output (CO) did not differ between groups. Patients had similar maximum velocities and maximum WSS at peak systole compared to controls, but lower average velocities ($p < 0.001$) and average WSS ($p < 0.001$). Also, patients had higher FD in planes 1-3 ($p < 0.001$) and similar flow displacement in the distal AA (planes 5-7) at peak systole.

Discussion: This study shows that patients with mild-to-moderate AA dilation and TAV have altered hemodynamics compared to age- and sex-matched controls. Patients had lower average WSS in the AA, which has been previously associated with aortic growth⁽³⁾. In patients with AA dilation, the maximum velocity was similar to controls, but flow was more eccentric. In absence of BAV morphology, aortic stenosis and severe dilation, this may be due to other factors such as abnormal cusp opening or the orientation of the left ventricular outflow tract⁽⁷⁾. Future studies will include more patients and controls, as well as longitudinal follow-up of these patients.

References

(1) Guala et al, JACC Cardiovasc Imaging, 2022 Jan 1;15(1):46–56; (2) Soulat et al, JACC Cardiovasc Imaging 2022 Jan 1;15(1):33–42; (3) Korpela et al, Eur J Cardiothorac Surg 2021; (4) Bustamante et al, J Cardiovasc Magn Reson 2015 Dec;17(1):87; (5) Potters et al, J Magn Reson Imaging 2015 Feb;41(2):505–16; (6) Sigovan et al, J Magn Reson Imaging 2011 Nov;34(5):1226–30; (7) Kauhanen et al J Magn Reson Imaging. 2019 Jul;50(1):136–45.

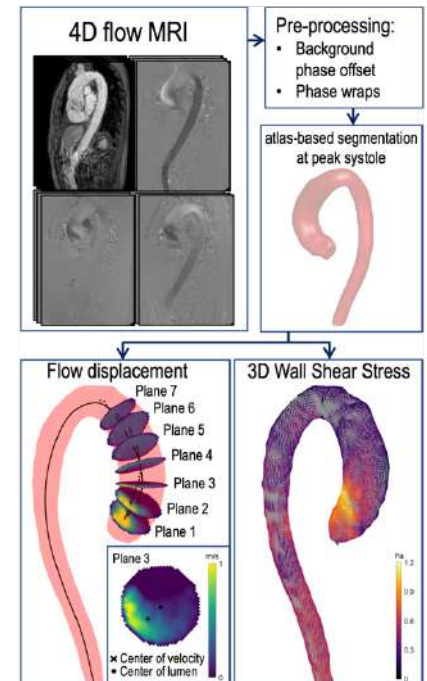


Figure 1 Workflow for analysis of 4D flow data

Table 1 Summary of results

	Patients	Controls	p value
SV [ml]	69.51 \pm (18.44)	65.54 \pm (15.58)	0.283
CO [l/min]	4.96 \pm (1.32)	4.47 \pm (0.97)	0.051
HR [bpm/min]	72.36 \pm (11.47)	69.11 \pm (10.08)	0.166
Mean Diameter [mm]	37.43 \pm (1.89)	31.23 \pm (2.17)	< 0.001
Max Diameter [mm]	43.69 \pm (1.89)	35.08 \pm (2.9)	< 0.001
Max Velocity [m/s]	2.07 \pm (0.9)	1.83 \pm (0.71)	0.167
Mean Velocity [m/s]	0.47 \pm (0.09)	0.59 \pm (0.11)	< 0.001
Max WSS [Pa]	1.14 \pm (0.33)	1.15 \pm (0.25)	0.967
Mean WSS [Pa]	0.37 \pm (0.08)	0.48 \pm (0.1)	< 0.001
FD plane 1 [%]	10.32 \pm (5.25)	6.54 \pm (3.82)	< 0.001
FD plane 2 [%]	12.42 \pm (5.89)	5.39 \pm (3.57)	< 0.001
FD plane 3 [%]	7.64 \pm (5.7)	3.51 \pm (1.8)	< 0.001
FD plane 4 [%]	3.6 \pm (3.49)	2.46 \pm (1.18)	0.045
FD plane 5 [%]	2.47 \pm (1.52)	2.59 \pm (1.69)	0.738
FD plane 6 [%]	3.65 \pm (1.69)	3.61 \pm (1.89)	0.923
FD plane 7 [%]	4.94 \pm (2.38)	5.14 \pm (6.58)	0.849

Deep-Learning Derived Systolic 3D Aortic Hemodynamics from Aortic Geometry

Haben Berhane¹, Anthony Maroun¹, Chris Malaisrie², Patrick McCarthy², Bradley D. Allen¹, Michael Mark¹

¹Radiology, ²Cardiac Surgery Northwestern University, Chicago, IL

Introduction: Quantification of aortic flow is important for diagnosis and patient management in aortic diseases. 4D Flow MRI provides a comprehensive assessment of aortic hemodynamics by acquiring time resolved 3-directional blood flow for the characterization of 3D hemodynamic changes in patients. However, 4D flow MRI requires long acquisition times (5-10 min) and access to advanced MRI sequences which may not be widely available. A technique that could derive 3D aortic hemodynamics from more widely available MR angiography alone would thus be highly desirable. Many studies have shown that Computational Fluid Dynamics (CFD) is capable of simulating 3D blood flow dynamics. However, CFD is hampered by requiring user-defined boundary conditions and model parameters, long simulation times, and patient-specific in-flow and pressure conditions [1]. Alternatively, deep learning

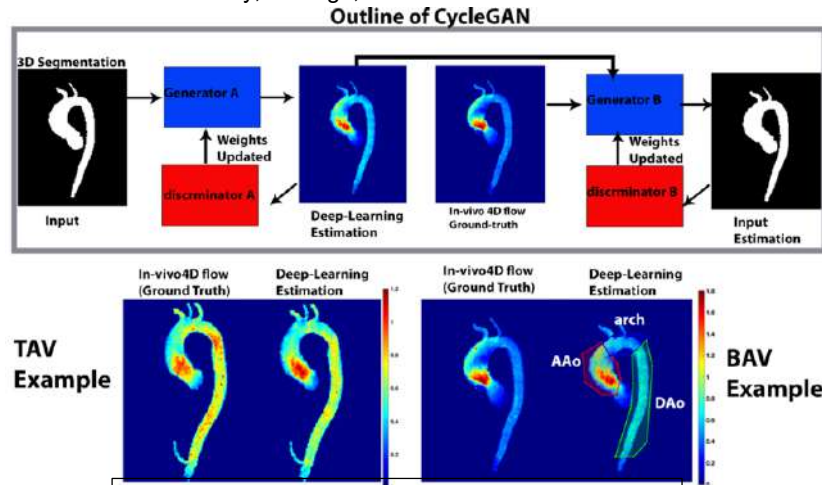


Figure 1: Outline of the cycleGAN training and examples of the AI output with the ground-truth (4D flow)

using CycleGANs

have recently demonstrated success in image-to-image translation [2]. As such, we sought to develop a CycleGAN framework to derive systolic 3D blood flow velocities in the aorta from 3D segmentation data of the aorta as the only input. To test the performance of this novel framework, CycleGAN derived aortic 3D velocities were compared to velocities measured by aortic 4D flow MRI.

Methods: This study used a total of N=720 patients (477 bicuspid aortic valve [BAV] patients, median age:42 years; 243 trileaflet aortic valve [TAV] patients, median age:45 years) with aortic 4D flow MRI acquired on either 1.5T or 3T MRI systems (Siemens, Erlangen, Germany). 4D flow MRI sequence parameters were: spatial res=1.2-5.0mm³, temp res=32.8-44.8ms, and venc=150-500cm/s. After pre-processing, the 4D flow data were used to calculate a 3D PC-MR angiogram (PC-MRA) which was used to generate a 3D aortic segmentation for all 720 subjects. Next, the 3D segmentation was used to mask the 4D flow data and extract the 3D distribution of systolic absolute velocities inside the aorta. For CycleGAN training, 3D aorta segmentations of 668 patient datasets served as network input to estimate 3D systolic velocity (ground truth data: 4D flow derived aortic 3D velocities). Subsequent CycleGAN testing was performed on 52 patient data that were not including in training. The CycleGAN was composed of two generators and two discriminators (Figure 1). The generator is trained in order to produce images that are able to trick the discriminator, which attempts

to distinguish which images are the ground-truth or from the generator. Further, the CycleGAN utilizes a cycle-consistency loss which attempts to enforce consistency between the translations of the two generators [2]. For the generators, we used a 3D hybrid Densenet/Unet [3]. For the discriminators, the architecture consisted of 5 convolution layers of a kernel size=[4x4]. The first 4 convolution layers are followed by a leaky relu and increasing filter sizes (64,128,256, and 512). The final layer was a convolution with a filter size=1. Two separate CycleGANs were trained: one for BAV datasets (N=443) and another for TAV (N=225). Maximum intensity plot (MIP) of systolic absolute aortic velocities were generated for both GAN-derived and 4D flow data (Figure 1). Region of interests were used to quantify peak velocities (top 5% of velocities) in the ascending (AAo), arch, and descending aorta (DAo).

Results: The total training time for the CycleGANs was 6 hours across 200 epochs on a RTX 3090. Figure 1 provides two examples of the GAN-derived velocity estimations for a TAV and BAV dataset, which show similar systolic velocity patterns. As shown in Figure 2, across all 52 testing datasets (34 BAV patients, 18 TAV patients), the CycleGAN successfully estimated systolic aortic 3D velocities with moderate to strong agreement compared to velocities measured by 4D flow MRI. Voxel-wise comparison of CycleGAN vs. 4D flow 3D systolic velocities (Figure 2A) showed strong correlation between methods (ICC = 0.92 [0.915-0.917], low bias (0.01m/s) and good limits of agreement (± 0.18 m/s). For regional peak velocity analysis (Figure 2B), correlation demonstrated excellent agreement across all three regions (AAo, arch, DAo, ICC = 0.98-0.99 [0.96-0.98 - 0.98-0.99]). Bland-Altman analysis showed small bias for all regions (AAo: <0.001m/s, arch: 0.02m/s, DAo: <0.001m/s) and good to moderate limits of agreement (AAo: 18% of the mean difference, arch: 19.2%, DAo: 22.1%).

Discussion: Deep-learning based peak systolic velocity estimation showed strong agreement to the 4D flow MRI. Future direction of this study is to develop velocity estimations from CT-derived 3D aortic geometry.

References: [1] Ferdian, E et al. Frontiers in Physics. 2020. [2] Zhu, J et al. Arxiv. 2017. [3] Berhane, H. et al. MRM. 2020

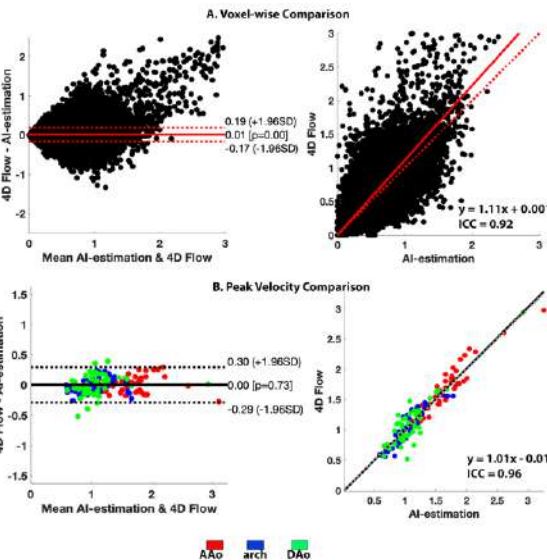


Figure 2: Bland-Altman plots for voxel-wise comparison and peak velocity; red=AAo, blue=arch, green=DAo

Impact of Flow Entrainment on Mitral Regurgitation Flow Quantification Using 4D flow MRI

Jeesoo Lee¹, Gloria Ayuba², Taimur Safder², Erik Wu², James D Thomas² and Michael Markl^{1,3}

Departments of ¹Radiology, ²Cardiology, and ³Biomedical Engineering
Northwestern University, Feinberg School of Medicine, Chicago, IL USA

Purpose: Quantification of mitral valvular regurgitation (MVR) flow provides crucial information to determine disease severity and risk-stratify MVR patients.¹ Echocardiography is the mainstay imaging modality but has limited precision and reproducibility due to inter-observer variability and 2D single-direction velocity imaging constraints. Cardiac MRI can be used to indirectly estimate MVR flow volume (RVol) by subtracting the left ventricle stroke volume (SV) measured using a stack short-axis cine images and aortic forward flow volume (AoFF) measured using 2D phase-contrast MRI at the aortic valve ($RVol = SV - AoFF$). However, integrating multiple measurements is subject to amplification of errors inherent in each measurement.² 4D flow MRI allows for the direct quantification of MVR flow by placing a plane directly across the MVR flow jet in the left atrium.^{2,3} However, we have previously shown that jet flow volume does not always coincide with RVol and, in fact, is prone to overestimate RVol due to the flow entrainment effect: jet flow volume linearly increases with the distance from the orifice (approx. 20% per cm) in our recent in-vitro investigation.⁴ This study sought to investigate the presence of this “flow entrainment effect” in in-vivo MVR flow jet and how much it impacts 4D flow MRI-based direct RVol quantification.

Methods: Ten patients (age 20–84, 7 male, 3 female) with MVR (3 mild, 4 moderate and 2 severe by echocardiography) underwent a prospectively-gated sagittal-oblique 4D flow MRI covering the left atrium (LA) with following parameters: TE = 2.2–2.4 ms, TR = 4.5–4.8 ms, temporal resolution = 36–38 ms, spatial resolution = 3.8–4.2 x 2.4–2.5 x 2.6–3 mm³, field-of-view = 309–375 x 380–400 x 84–108 mm³ and encoding velocity = 150–250 cm/s. Images were acquired using 1.5 T Siemens systems (Aera, Avanto). Background phase offset and velocity aliasing were corrected, and a manual 3D segmentation of the LA was created prior to flow quantification. RVol at 7 different locations along the regurgitant flow jet axis was quantified using an in-house post-processing tool written with MATLAB (Mathworks, USA). The middle plane was located at peak jet velocity which is assumed as vena contracta that forms close to the orifice. Quantification steps were as follows (**Fig. 1**), 1) Detect a start and end time frame of MVR, 2) Find the peak jet velocity location at each time frame during MVR, 3) Place a plane perpendicular to the peak velocity vector, 4) Move the plane up- and down-stream along the jet axis with 2.5 mm distance following the jet direction and 5) Contour jet region at each location to calculate flow rate which is then integrated over the duration of MVR to compute RVol for each jet flow analysis plane location.

Results: **Fig. 2** shows the percentage change in RVol along the jet compared to RVol at peak velocity location ($RVol_{peak}$). Distance, x indicates the location of plane relative to the peak velocity location ($x=0$). The $x>0$ and $x<0$ indicate the jet flow analysis plane is located downstream (into the LA) or upstream (closer to orifice), respectively. Moving the plane downstream/upstream was strongly associated with the increase/decrease in RVol ($r = 0.86$, $p < 0.0001$). The slope of a linear regression line indicated that RVol changed 4.5%/mm ($p < 0.0001$) with 95% confidence interval of ± 0.7 .

Discussion: This study demonstrated that directly quantified RVol using 4D flow MRI varies significantly depending on the measurement location. Assuming the peak velocity location corresponds to vena contracta (i.e., the narrowest section of a jet formed close to the orifice), the increase in RVol beyond the peak velocity location indicate the presence of flow entrainment in-vivo. On the other hand, RVol was decreased when the plane was moved toward upstream. This may be explained by the increase in spatial velocity acceleration as it approaches the orifice causing velocity to be underestimated due to partial volume effect. The findings of this study suggest that a clear landmark is needed to place a plane for accurate and reproducible RVol measurement using 4D flow MRI. In this study, peak jet velocity at each frame was suggested as the landmark, however, no ground-truth RVol is available to validate this approach. A future study is warranted to validate this approach in in-vitro MVR flow models with known ground-truth.

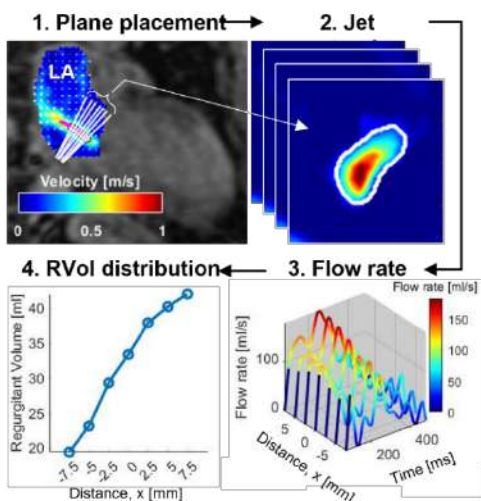


Fig. 1. MVR flow quantification process

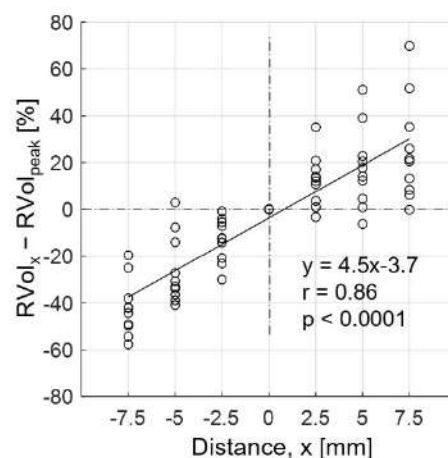


Fig. 2. Percentage RVol change along the jet

References:

1. *J Am Coll Cardiol.* 2020;75(17):2236-2270.
2. *Journal of Cardiovascular Magnetic Resonance.* 2021;23(1):1-13.
3. *Journal of Cardiovascular Magnetic Resonance.* 2015;17(1):1-9.
4. *Magnetic resonance in medicine.* 2022;87(4):1923-1937.

True Lumen 4D Flow MRI-derived Pulse Wave Velocity in Type B Aortic Dissection is Associated with Progressive Aortic Dilatation

Anthony Maroun¹, Kelly Jarvis¹, Elizabeth Weiss¹, Stanley Chu¹, Ozden Kilinc¹, Justin Baraboo¹, Ashitha Pathrose¹, Maurice Pradella¹, Chris Mehta², S Chris Malaisrie², Andrew Hoel³, Michael Markl¹, Bradley Allen¹

[1] Northwestern University – Radiology [2] Northwestern University - Cardiac Surgery [3] Northwestern University - Vascular Surgery

Purpose: Type B aortic dissection (TBAD) is a life-threatening disease often associated with progressive dilation of the descending aorta (DAo), leading to an increased risk of rupture. With no reliable predictors of aortic enlargement currently available, there is an increased need to find noninvasive parameters that could assess the risk of DAo growth and help in guiding treatment planning. Pulse wave velocity (PWV) is a well-known indicator of arterial stiffness used for cardiovascular risk assessment that could identify stiff aortas at low risk of progression [1]. Hence, the aim of this study was to investigate the potential of in vivo true lumen (TL) PWV from 4D flow MRI as a predictor of aortic growth rate.

Methods: We retrospectively identified 34 TBAD patients who underwent standard-of-care cardiothoracic MRI, including 3D magnetic resonance angiography (MRA) and 4D flow MRI of the aorta using 1.5T or 3.0T MR systems. All subjects had ≥ 9 months of imaging follow-up consisting of either 3D computed tomographic angiography (CTA) or 3D MRA. Patients who developed adverse outcomes (surgical intervention and/or death) were excluded. For each TBAD patient, maximum DAo diameters (defined as the largest diameter of the dissected DAo segment, orthogonal to the vessel centerline) were measured for baseline and follow-up scans by an experienced cardiovascular radiologist. Aortic growth rate was calculated by dividing the baseline vs follow-up diameter change by the time interval between the two scans.

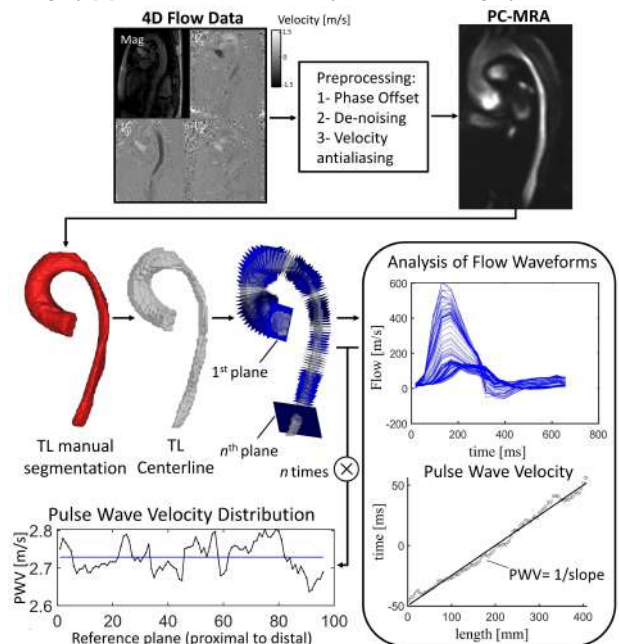


Fig. 1: 4D flow MRI analysis workflow.

PWV Estimation: Following 4D flow MRI pre-processing (noise masking, eddy current correction), a 3D phase-contrast angiogram (PC-MRA) was calculated and used to generate a 3D segmentation of the TL (Fig.1). PWV was then calculated using an in-house automated analysis algorithm previously described [2]. Briefly, a TL centerline with multiple analysis planes (inter-plane distance = 4 mm) were automatically positioned along the TL. Based on flow waveforms, PWV was automatically calculated according to the cross-correlation (xcor) technique, using the first plane as reference, and then repeated multiple times until all analysis planes were used as reference. This resulted in a PWV estimate distribution for each scan, from which, the mean or median of the distribution was extracted, depending on normality. A Shapiro-Wilk test was used to assess for normality, and Pearson's correlation was performed to evaluate the association between TL PWV and growth rate. A p -value < 0.05 was considered statistically significant.

Results: 34 patients were included (age: 70.0 ± 16.5 years; 21 male), and the average follow-up time was 3.1 ± 2.2 years. TL PWV was successfully quantified for all patients (4.3 ± 3.6 m/s), and a significant negative correlation was observed between TL PWV and aortic growth rate ($r = -0.54$, $p = 0.001$) (fig. 2).

Discussion: The main finding of this study is that increased PWV in the TL is correlated with reduced aortic growth rate, suggesting that TBAD patients with a higher TL PWV at baseline are at lower risk of progressive aortic dilatation. Hypothetically, higher TL PWV may reflect a more rigid dissection flap which is often associated with a chronic or more stable dissection course. Interestingly, prior studies assessed PWV in healthy adults over age 45 and found values that were on average between 7.2 and 9.4 m/s [3]. These measurements were considerably higher than most of the estimations we observed in the TL of TBAD patients. This finding suggests that, after dissection, PWV in the thoracic vasculature is no longer comparable to healthy controls but may be an interesting measure to study further for evaluating the mechanical effects of the dissection flap in TBAD.

References: [1] Kim HL, et al. *Front Cardiovasc Med*, 2019. [2] Jarvis K, et al. *J Magn Reson Imaging*, 2021. [3] Jarvis K, et al. *J Magn Reson Imaging*, 2022.

Funding Sources: Grant support by: AHA 20CDA35310687, NIH/NIA T32AG020506

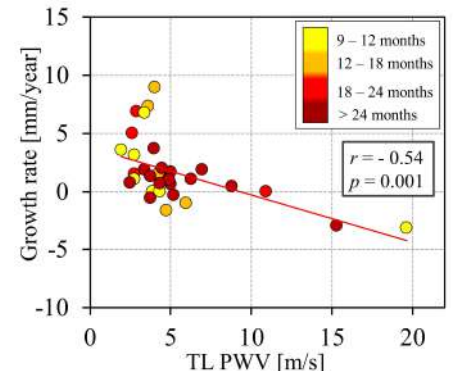


Fig. 2: Correlation analysis between TL PWV and growth rate. Datapoints are color coded according to the time interval between the baseline and follow-up scan.

Intra-cardiac kinetic energy and ventricular flow analysis in bicuspid aortic valve disease: impact on left ventricular function, dilation severity, and surgical outcome.

Julio Garcia¹, Alireza Sojoudi², Michael S. Bristow¹, Carmen Lydell¹, Bobby Heydari¹, Naeem Merchant¹, Andrew G. Howarth¹, Paul Fedak¹, James White¹

¹University of Calgary, Calgary, Canada; ²Circle Cardiovascular Imaging Inc, Calgary, Canada

Purpose: Intra-cardiac kinetic energy (KE) and ventricular flow analysis (VFA), as derived from 4D-flow MRI, can be used to understand the physiological burden impose to left ventricle (LV) due to bicuspid aortic valve (BAV) disease. VFA calculates the blood flow distribution using four components: direct flow (DF), retained inflow (RI), delayed ejection flow (DE), and residual volume (RV) [1]. Each VFA component expends a particular amount of KE. Our hypothesis is that the KE of each VFA component will impact the surgical referral outcome depending on LV function decrement, BAV phenotype, and aortic dilation severity. The aim of this study is to assess the KE individual contribution of each VFA component in BAV disease.

Method: A total of 60 subjects including 11 healthy volunteer controls (age: 32±14 years, 7 female) and 49 BAV patients (age: 45±17 years, 14 female) were recruited as part of a pre-defined sub-study of a prospective observational clinical registry. All subjects consent to participate and underwent a cardiac examination in a 3T MRI scanner (MAGNETOM Prisma/Skyra, Siemens, Erlangen, Germany). Imaging was performed in accordance with the current recommendations for valvular diseases and included a whole-heart 4D-flow MRI acquisition. Contrast-enhanced 3D magnetic resonance angiography of the thoracic aorta by administering 0.2 mmol/kg of gadolinium contrast (Gadovist, Bayer, Canada). Approximately 5-10 minutes following contrast administration, retrospective ECG-gated 4D-flow MRI (WIP 785A) was acquired during free-breathing using navigator gating of diaphragmatic motion. 4D-flow parameters were as follows: spatial resolution (2.0-2.5 mm × 2.0-2.5 mm × 2.5-3.5 mm), temporal resolution (36-40 ms), flip angle (15°), velocity encoding (150-550 cm/s), echo time (2.01-2.35 ms), repetition time (4.53-5.07 ms). All analyses were completed by a single observer using cvi⁴² v5.14 (Circle Cardiovascular Imaging Inc., Calgary, Canada). Standard corrections for phase-offset, static tissue, and velocity aliasing were performed when necessary. An automate detection of the aortic and mitral valve location and motion was performed using machine learning in a 3-chamber view and constrained to the 4D-flow volume [2]. Valvular flow contours were manually refined at each phase. The isovolumetric relaxation phase was identified for VFA. Statistical analysis included group comparison between controls and BAV, surgery vs. non-surgery referral, and valve type phenotype comparison (Type 0, Type 1 RN, and Type 1 RL). Associations between VFA, KE, LV function and surgery referral were performed.

Results: Control cohort was younger than BAV patients (32±14 yrs vs. 45±17 yrs, p=0.005), had less women included (7 vs. 14, p=0.029), and had inferior body surface area (1.77±0.24 m² vs. 1.98±0.23 m², p=0.01). LV mass was inferior in controls than in BAV (90±26 g vs. 126±48 g, p=0.025), as well as inferior ascending aorta diameter indexed (15.8±2.5 mm/m² vs. 19.3±3.5 mm/m², p=0.005). From VFA, RV was increased in the BAV cohort (21±7 % vs. 30±9 %, p=0.003). Overall, VFA KE was higher in the BAV group, significant increment was found for maximum KE in RV (324±215 µJ vs. 1083±1073 µJ, p=0.016) and mean KE in DE, RI, and RV components (p<0.05, Table 1). A total of 14 BAV subjects underwent surgery after scan. When comparing BAV non-surgery vs. surgery referred cohorts, aortic diameter was significantly higher (p<0.001), maximum KE in RV (p=0.013) and mean KE in RV (p=0.032) were similarly elevated. No differences were found in KE for BAV phenotype, but aortic dilation severity increased for mean KE in DF (p=0.05). DE showed correlated with LVED (r=0.352, p=0.016), LVESV (r=0.51, p<0.001), and LVEF (r=-0.323, p=0.029). Maximum and mean KE of DF, DE, RI and RV were positively correlated to LV volumes (r>0.35, p<0.01). Maximum and mean RV KE was also associated with surgical referral (r=0.438, p=0.002; and r=0.371, p=0.009; respectively).

Conclusions: KE from each VFA components significantly increased in BAV patients and in BAV patients undergoing surgery. KE was associated with LV function and referral for surgery. These findings may be useful to characterize BAV energetic changes due to LV remodelling and surgical therapy.

References: 1. Stoll et al. JCMR 2018; 20(1):15. 2. Garcia JRSM 2021; 10:1-8.

Table 1. Baseline characteristics.

Parameter	Control (n=11)	BAV (n=49)	p-value
Age (years)	32±14	45±17	0.005
Sex n female (%)	7 (64)	14 (29)	0.029
BSA (m ²)	1.77±0.24	1.98±0.23	0.010
LVEDV (mL)	161±42	191±59	0.111
LVESV (mL)	61±19	77±32	0.089
LVEF (%)	63±6	60±11	0.308
LV Mass (g)	90±26	126±48	0.025
AAo Diameter Indexed (mm/m ²)	15.8±2.5	19.3±3.5	0.005
DF (%)	32±8	27±10	0.135
DE (%)	27±4	25±5	0.134
RI (%)	20±4	18±5	0.106
RV (%)	21±7	30±9	0.003
KE DF Max (µJ)	2413±1154	3101±1736	0.339
KE DE Max (µJ)	1850±937	3156±2609	0.178
KE RI Max (µJ)	967±485	1532±1028	0.166
KE RV Max (µJ)	324±215	1083±1073	0.016
KE DF Mean (µJ)	689±317	889±552	0.225
KE DE Mean (µJ)	444±197	835±847	0.048
KE RI Mean (µJ)	245±115	411±300	0.080
KE RV Mean (µJ)	133±92	410±412	0.006

BSA: Body Surface Area; LVEDV: Left Ventricular End-Diastolic Volume; LVESV: Left Ventricular End-Systolic Volume; LVEF: Left Ventricular Ejection Fraction; AAo: Ascending Aorta; DF: Direct Flow; DE: Delayed Ejection flow; RI: Retained Inflow; RV: Residual Volume; KE: Kinetic Energy; Max: Maximum.

Hemodynamic evaluation of transverse venous sinus in patients with idiopathic intracranial hypertension: A preliminary 7-T 4D flow MRI study

Zhiye Li¹, Xiaoyan Bai^{1,2}, Dapeng Mo³, Qingle Kong⁴, Binbin Sui¹.

1. Tiantan Neuroimaging Center of Excellence, Beijing Tiantan Hospital, China 2. Department of Radiology, Beijing Tiantan Hospital, China 3. Department of Neurointervention, Beijing Tiantan Hospital, China 4. MR Collaboration, Siemens Healthineers Ltd., China

Purpose: The transverse sinus (TS) stenosis with venous drainage dysfunction has been suggested as one of the most important underlying pathophysiological causes of the idiopathic intracranial hypertension (IIH). 4D flow MRI allows for the visualization and quantification of the cerebral blood flow. The aim of this study was to perform the preliminary analysis on the intracerebral venous blood flow in IIH patients with TS stenosis using 7T 4D flow MRI.

Methods: Two patients with clinical diagnosis of IIH with TS stenosis were included in this study and underwent MR imaging 24-48 hours before cerebral venography. A 7T MAGNETOM System (Siemens Healthcare, Erlangen, Germany) with a 32-channel head coil was used for 4D flow data acquisition with the following parameters: TR/TE: 59.84/3.61 ms, FOV: 192×192 mm², matrix size: 240×240×120, slice thickness: 0.8 mm, flip angle: 15°, velocity encoding: 80 cm/s. The spatial resolution was 0.8×0.8×0.8 mm³, and the temporal resolution was 61 ms. Pulse prospective gating was used and the scan time was 14-18 mins dependent on the heartbeat rate of the subjects. 4D flow data were post-processed with GTflow software (Gyro Tools, version 2.2.14, Zurich, Switzerland) by a neuroradiologist with 2 years of hemodynamic postprocessing experience. Hemodynamic parameters including average (V_{avg} , cm/s) and maximum values of velocity (V_{max} , cm/s), as well as Netflow rates were measured at 1cm proximal and distal to the most stenosis site, recorded as the inflow and outflow site, respectively. Cerebral venography with manometry was performed to get the trans-stenosis pressure gradient (TSG) by a neurointerventionist with 20 years of experience.

Results: Patient 1 was a 24-year-old female presented with head pain accompanied by ocular discomfort for 3 months, with BMI as 30.11. DSA showed the stenosis of the left TS (dominant side), with the stenosis rate of 53% (figure 1a). TSG was 7mmHg. Patient 2 was a 33-year-old female with 6 months of binocular vision diminution, with BMI as 40.23. DSA showed stenosis of the right TS (dominant side), with the stenosis rate of 73% (figure 1c). TSG was 42mmHg.

4D flow parameters of the two cases were listed in the below table. With much higher TSG, the V_{max} at inflow site of patient 2 was about 3 times higher than that of the patient 1. V_{max} at the outflow site were similar between the two cases. In patient 1 with lower TSG, the outflow was significantly higher than inflow. Obvious difference was also observed in Netflow between inflow and outflow site for patient 2. Irregular flow with regurgitation is found in the case with high TSG.

	TSG (mmHg)	site	Net Flow (ml/s)	Vavg (cm/s)	Vmax (cm/s)	Forward Flow (ml/s)	Backward Flow (ml/s)
Patient 1	7	inflow	7.00	26.41	40.85	7.00	0.00
		outflow	7.21	33.95	100.57	7.35	0.14
Patient 2	42	inflow	10.06	44.86	124.01	10.99	0.93
		outflow	3.71	30.98	115.46	7.22	3.51

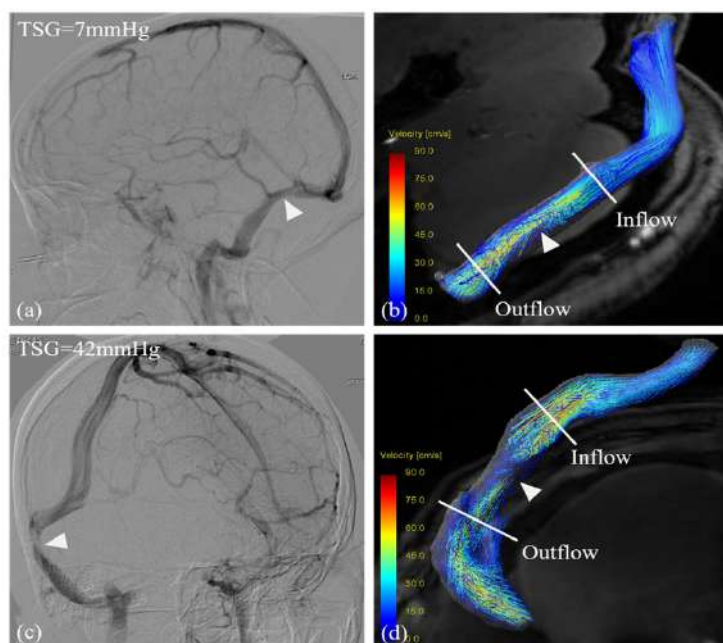


Figure 1. DSA and the corresponding 4D flow streamline images of patient 1 (a,b) and patient 2 (c,d). The stenosis is identified on DSA images (white triangle), with the TSG was 7mmHg for patient 1 (a) and 42mmHg for patient 2 (c). The 4D flow parameters were measured at inflow and outflow sites (short white line) 1cm proximal and distal to the most narrowing site. Irregular flow with regurgitation is found in the case with high TSG (d).

Discussion and conclusion: The results of this study provided the preliminary results in evaluating hemodynamics in IIH patients with TS using 7-T 4D flow MRI. Previous 3T MRI studies have shown that 4D flow parameters may have potential application value for patients with TS stenosis (1). Ultra-high magnetic field unit allows us to perform flow imaging with higher spatial resolution and better phase contrast. With more detailed information, 7-T MRI device would have a better scientific research prospect in evaluating hemodynamics for intracranial venous sinus in the future study.

Helicity of Ascending Arterial Flow in Patients With Hypertrophic Cardiomyopathy

Yuka Otaki¹, Naokazu Mizuno¹, Mitsuru Kanisawa¹, Yasuki Hen², Itaru Takamisawa², Yoshiaki Komori³, Ning Jin⁴, Nobuo Iguchi², Mitsuaki Isobe²

1. Department of Radiology, Sakakibara Heart Institute, Japan, 2. Department of Cardiology, Sakakibara Heart Institute, Japan, 3. Siemens Healthcare K.K, Japan, 4. Siemens Medical Solutions USA Inc., USA.

Purpose: We aimed to quantify helicity in proximal ascending aorta using compressed sensing (CS)-4D flow cardiac MRI in patients with hypertrophic cardiomyopathy (HCM).

Methods: Patients with HCM (n=34, 19 males, 60 ± 16 years) and controls (n=20, 11 males, 62 ± 14 years) underwent CS-4D flow study using a clinical 1.5T MRI scanner (MAGNETOM Sola, Siemens Healthcare, Erlangen, Germany). CS-4D flow images were acquired by prototype sequence with navigator echo based respiratory gating and retrospective electrocardiographic gating. The imaging parameters were as follows: 4.4/2.2 ms (repetition time/echo time), 11 deg flip angle, 304 × 380 mm field of view, 102 × 160 acquisition matrix, 3 mm slice thickness, 3 k-space lines per segment, 20 cardiac phases, 150 cm/sec velocity encoding and CS acceleration factor of 7.7. All CS-4D flow images were analyzed using 4D flow MRI postprocessing software iTFlow2 (Cardio Flow Design, Inc., Tokyo, Japan) to evaluate helicity values (Formula 1). Helicity in two directions (clockwise and anticlockwise) on 20 cine frames was obtained in the proximal ascending aorta (Figure 1). The summation and difference of helicity in two directions on each frame were calculated and the maximum of summation and difference among 20 cine frames was evaluated.

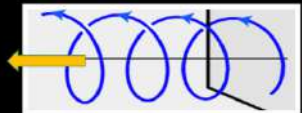
Results: Patients with HCM had a significantly increased summation of helicity compared to controls (p=0.003, Figure 2).

Among HCM patients, 12 patients had left ventricular outflow tract obstruction (LVOTO), 9 patients had percutaneous transluminal septal myocardial ablation

(PTSMA) and 13 patients had no LVOTO. The difference in helicity was lower in HCM without LVOTO compared to those with LVOTO or those undergoing PTSMA (p=0.03, Figure 3).

Conclusions: The helicity in patients with HCM assessed via CS-4D flow study is considerably different compared to controls.

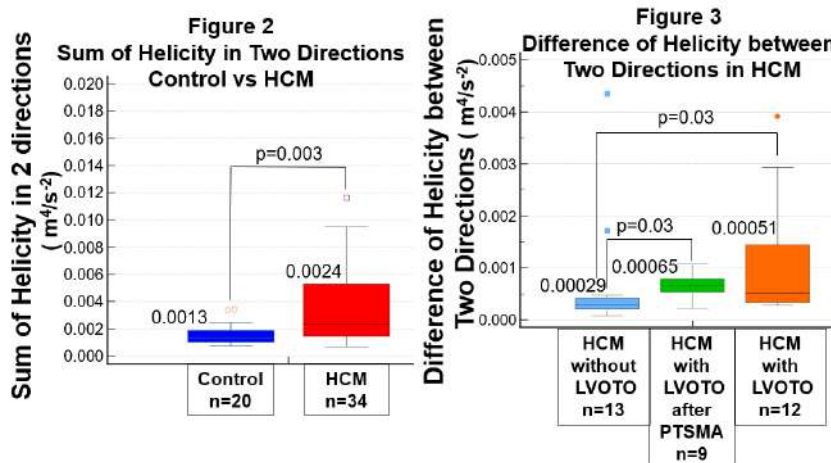
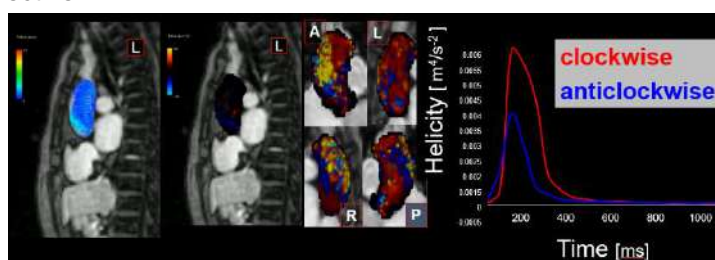
Formula 1. Helicity



$$H = \int_{\Omega} \mathbf{u} \cdot \boldsymbol{\omega} d\Omega$$

H: helicity
u: velocity
ω: vorticity
Ω: area

Figure 1. Helicity Time Curve



The Value of preoperative PC-MRI in predicting the clinical outcome of moyamoya disease after encephalo-duro-arterial synangiosis (EDAS) surgery

Shitong Liu, Jianming Cai

Department of Radiology, Chinese PLA General Hospital, Beijing, China

Abstract

Objective To explore the value of preoperative cine phase-contrast MRI (PC-MRI) parameters in predicting collateral formation and clinical outcomes after encephalo-duro-arterial synangiosis (EDAS) surgery in patients with moyamoya disease (MMD).

Materials and methods Participants with MMD were prospectively recruited and underwent preoperative PC-MRI. All of the participants were classified into good and poor groups according to the collateral formation evaluated by digital subtraction angiography (DSA) after EDAS surgery. Based on the change of modified Rankin Scale (mRS) system before and after surgery, participants were classified into improved mRS group and poor response group. Hemodynamic status included mean velocity (Vmean), peak velocity (Vpeak) and blood volume flow (BVF) of superficial temporal artery (STA) acquired by PC-MRI were compared between different groups. Logistic regression was performed to relate the PC-MRI parameters to collateral formation and clinical outcomes in MMD participants.

Results A total of 45 MMD patients with unilateral EDAS surgery were finally included in the study. Vmean, Vpeak and BVF of ipsilateral STA were significantly greater in participants with good collateral formation compared with those with poor collateral foundation after surgery ($p=0.011$, 0.004 and 0.013 , respectively). The Vmean, Vpeak and BVF were independently associated with postoperative collateral formation after adjusting for clinical and radiological factors. Furthermore, the Vpeak of ipsilateral STA was also significantly associated with the improvement of mRS after surgery before and after adjusting for confounding factors.

Conclusion The hemodynamic status of ipsilateral STA as donor artery evaluated by PC-MRI was significantly associated with collateral formation and change of mRS after EDAS surgery in MMD patients. Our results suggested that PC-MRI could provide valuable information on the prediction of clinical outcomes in MMD patients after EDAS surgery.

Keywords

Moyamoya disease; Phase contrast-magnetic resonance imaging; Digital subtraction angiography; Clinical outcome.

1. Pathology RCot, Willis ToSOotCo: **Guidelines for diagnosis and treatment of moyamoya disease (spontaneous occlusion of the circle of Willis)**. *Neurol Med Chir* 2012, **52**(5):245-266.
2. Acker G, Fekonja L, Vajkoczy P: **Surgical Management of Moyamoya Disease**. *Stroke* 2018, **49**(2):476-482.
3. Park SE, Kim JS, Park EK, Shim KW, Kim DS: **Direct versus indirect revascularization in the treatment of moyamoya disease**. *J Neurosurg* 2018, **129**(2):480-489.

Blood flow dynamics of the main pulmonary artery in repaired tetralogy of Fallot using 4D-flow MR angiography

Akio Inage, MD^{1,3}, Naokazu Mizuno², Kanako Kishiki³

1 Department of Pediatrics, Japanese Red Cross Medical Center, Tokyo, Japan, 2 Department of Radiology and 3 Division of Pediatric Cardiology, Sakakibara Heart Institute, Tokyo, Japan

Purpose: 4D flow MRI was used to evaluate blood flow dynamics at the main pulmonary artery (MPA) in repaired tetralogy of Fallot (TOF).

Methods: We measured the energy loss (EL) of MPA and helicity, which is a value indicating the spin rotation direction of particles in the bloodstream, in 15 patients who underwent cardiac MRI at Sakakibara Heart Institute. For EL, the maximum value (peak EL) and the total value during one heartbeat were calculated, and the total value was divided by the body surface area (EL/BSA) and the cardiac index (EL/BSA/CI) for standardization. Helicity defined the clockwise rotation as positive and the counterclockwise rotation as negative, and calculated the total value. 4D-flow analysis was performed with iTFlow 1.9 manufactured by Cardio Flow Design, Japan.

Results: The mean age was 26.1 ± 16.2 years, the right ventricular outflow tract reconstruction procedure was pulmonary valve preservation (n-TAP) in 10 cases, transannular patch (TAP) in 5 cases, and the postoperative period was 20.9 ± 10.0 years. The total value of EL was significantly higher during systole, but peak EL was observed during diastole in 6 cases (40%). The total mean value of helicity became positive, and in 9 cases (60%), the clock rotation was dominant. In the comparison between the surgical procedures, the EL of the TAP group was higher than that of the n-TAP group, but there was no significant difference. Helicity with predominant clock rotation was observed in 6 patients in the N-TAP group and 3 patients in the TAP group (60% in each case), but there was no significant difference in helicity between the two groups. A correlation was found between the average through-plane velocity ($r = 0.48, 0.52$) and area ($r = -0.49, -0.63$) of the whole cardiac cycle and systolic EL/BSA at MPA. A strong correlation was found between peak EL and clockwise rotation helicity ($r = 0.76$) and counterclockwise rotation helicity ($r = -0.79$). We also found a correlation between diastolic EL/BSA and diastolic clock rotation helicity ($r = 0.52$) and diastolic counterclockwise helicity ($r = -0.56$), and diastolic EL/BSA/CI and MPA regurgitant fraction ($r = 0.45$).

Conclusion: In this study, there was no significant difference in EL and helicity between surgical procedures. Helicity in MPA was predominantly clockwise repaired TOF. It was suggested that EL is involved in helicity throughout the whole cardiac cycle, and that peak EL has a particularly large effect.

Automatic 4D Flow MRI Segmentation of Thoracic Vessels using the Standardized Difference of Means Velocity

S. M. Rothenberger¹, N. M. Patel¹, J. Zhang², B. Craig³, S. A. Ansari⁴, M. Markl⁴, P. P. Vlachos^{1,2} and V. L. Rayz^{1,2}

¹Biomedical Engineering, Purdue University; ²Mechanical Engineering, Purdue University; ³Statistics, Purdue University;

⁴Radiology, Northwestern University School of Medicine

Purpose: 4D flow MRI is capable of capturing velocity fields in various vascular territories; however, improving the accuracy and repeatability of 4D flow data segmentation is critical for reliable assessment of hemodynamic (e.g., wall shear stress) and morphological metrics associated with cardiovascular disease [1]. Despite serving as the gold standard, manual 4D flow segmentation is time-consuming, and the results can vary across users. Recently, we have developed an automatic segmentation algorithm for the cerebral vasculature based on the standardized difference of means (SDM) velocity [2]. The SDM algorithm's performance was found to be repeatable across a range of scan settings and imaging conditions *in vitro* and *in vivo*. In this study, we demonstrate the application of the SDM segmentation method to the thoracic vasculature.

Methods: 4D flow MRI data were acquired in the thoracic aortas of six subjects at the Northwestern University School of Medicine according to an IRB-approved protocol. A 1.5 T scanner (MAGNETOM Avanto, Aera, Siemens, Erlangen, Germany) was used to collect the images with voxel sizes of $2.50 \times 3.75 \times 2.40 \text{ mm}^3$ in three patients and $2.38 \times 3.56 \times 2.40 \text{ mm}^3$ in the three other patients. The number of cardiac phases ranged from 15 to 21. The v_{enc} and flip angle for all patients was 150 cm/s and 7 degrees, respectively. TR and TE values ranged from 4.80-4.90ms and 2.43-2.46ms, respectively. The 4D flow data were segmented manually using the pseudo-complex difference intensity in Mimics (Materialise NV, Belgium). The manual segmentations serve as the benchmark masks to evaluate the SDM method's performance. Automatic 4D flow data segmentations with the SDM method were performed in all patients using the MRI-measured velocity, $U_{i,M}$ [2]. The measured velocity was used to calculate the SDM velocity, \tilde{U}_i , for each voxel and velocity component, $i = x, y, z$. \tilde{U}_i quantifies the ratio between net flow effects and flow pulsatility in each voxel. The SDM velocity is calculated as the difference between the time-averaged velocity at each voxel and the mean tissue velocity ($\hat{\mu}_i$) relative to the standard error, $\tilde{U}_i = \frac{\text{mean}(U_{i,M}) - \hat{\mu}_i}{\text{stddev}(U_{i,M}) / \sqrt{N_t}}$, where N_t is the total number of acquired cardiac phases. Vessel segmentation is performed using an F-test to identify voxels with significantly higher SDM velocity values than tissue voxels. Voxels with a significant difference are presumed to contain flow and are included in the vessel segmentation. P-values for each voxel are reported to estimate the segmentation accuracy. Erroneous voxels resulting from noise are removed by considering the first moment invariance, and partial volume voxels are included by dilating the final SDM segmentation.

Results: The SDM algorithm was computed for all patients' data within 7.0 to 11.4 seconds using 16-core Intel® Xeon® CPU E5-1660 v4 @ 3.20GHz processors. Figure 1 presents a sagittal cross-section through the volume of p-values reported using the SDM algorithm. An outline of the manual segmentation is shown in red, indicating the aorta (Ao) and proximal brachiocephalic trunk (BCT). The low p-values associated with net blood flow correspond to the manually segmented ascending aorta (AscAo), descending aorta (DscAo), and BCT. We note other structures indicated by low p-values, which were not manually segmented. These structures include the superior vena cava (SVC), pulmonary artery (PA), left atrium (LA), and right ventricle (RV). The sensitivity metric computed as the ratio of the number of true positives to the total number of manually segmented voxels was used to quantitatively assess the performance of the SDM method in the aorta and BCT for each patient. The sensitivity values ranged from 74.6% to 93.4%, with a root mean square of 87.6%.

Discussion: This work demonstrates the application of the SDM segmentation algorithm to thoracic vessels. The automatic SDM segmentations facilitate comparisons of 4D flow MRI findings across different studies by mitigating variability introduced across different users. Furthermore, SDM segmentations are generated within seconds, saving time for those processing 4D flow MRI results. In addition to segmenting vessels, the SDM method also reports p-values expressing the significance of fluid flow in all voxels. These p-values express the segmentation accuracy and can be extended to derive accuracy metrics for hemodynamic and morphological parameters associated with cardiovascular disease.

References: [1] Schnell *et al.*, Three-dimensional hemodynamics in intracranial aneurysms: influence of size and morphology. *J Magn Reson Imaging*, 2014. [2] Rothenberger *et al.*, Automatic 4D flow MRI Segmentation Using the Standardized Difference of Means Velocity. *IEEE-TMI*, 2022 (Under Review).

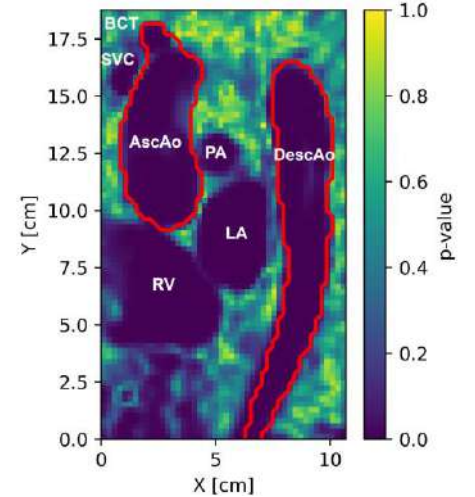


Figure 1: P-values obtained using the SDM segmentation algorithm with the manual segmentation mask shown in red. The SDM algorithm detected the ascending aorta (AscAo), descending aorta (DscAo), brachiocephalic trunk (BCT), superior vena cava (SVC), pulmonary artery (PA), left atrium (LA) and right ventricle (RV).

Quantitative Time-of-Flight (qTOF) Brain MRA Velocimetry using Deep Machine Learning: Initial Experience

Ioannis Koktzoglou, PhD^{1,2}, Rong Huang, PhD¹,

Fulvio R. Gil, MD^{2,3}, Archie L. Ong, MD^{2,3}, Brian P. Walcott, MD^{2,4}, Robert R. Edelman, MD^{1,5}

¹Department of Radiology, NorthShore University HealthSystem, Evanston, IL, USA, ²University of Chicago Pritzker School of Medicine, Chicago, IL, USA, ³Department of Neurology, NorthShore University HealthSystem, Evanston, IL, USA, ⁴Department of Neurosurgery, NorthShore University HealthSystem, Evanston, IL, USA, ⁵Department of Radiology, Northwestern University Feinberg School of Medicine, Chicago, IL, USA

Purpose

Time-of-flight (TOF) magnetic resonance angiography (MRA) of the brain is routinely used to diagnose and monitor a number of neurovascular disorders [1], but as currently implemented, does not provide any quantitative hemodynamic information. Addressing this gap, multi-echo quantitative TOF (qTOF) MRA has recently been proposed for simultaneous high-resolution morphologic and hemodynamic evaluation of the intracranial arteries [2]. Arterial velocity information from the qTOF acquisition has so far been obtained using a hand-crafted computer-vision procedure. Using phase contrast (PC)-measured velocities as target data, we hypothesized that deep machine learning could be applied to qTOF MRA to rapidly quantify intracranial arterial flow velocity.

Methods

This was an IRB-approved study and all participants provided written informed consent. The intracranial arteries of 15 human subjects (8 male, 7 female, age 45 ± 15 years, range=22-71 years) were imaged with 3D qTOF and 3D PC MRA. Imaging parameters for qTOF MRA were: TR/flip angle=21.0ms/15°, 0.58×0.58×1.0mm³ spatial resolution interpolated to 0.29×0.29×0.5mm³, scan time 4min 3s, TEs of 2.9ms (TE₁), 5.1ms (TE₂), and 7.2ms (TE₃), from which the flow-compensated TE₁ and TE₃ images were analyzed to quantify intracranial arterial flow velocity. Imaging parameters for 3D PC were: TR/TE/flip angle=39.9ms/5.9ms/ 10°, 0.85×0.85×1.30mm³ spatial resolution interpolated to 0.43×0.43×0.65mm³, 60cm/s velocity encoding sensitivity, scan time 4min 4s. qTOF and PC volumes were spatially registered. Velocimetric data from qTOF were obtained using a hand-crafted computer-vision procedure described previously [2], and using deep machine learning leveraging U-Net convolution neural networks. A leave-one-out deep machine learning training strategy was used, using qTOF image data and PC velocity data as the training input and output data, respectively. Intraclass correlation coefficient (ICC) for absolute agreement, Bland-Altman, and linear regression (*r*) analyses were used to compare flow velocity values obtained with qTOF and PC.

Results

Compared with hand-crafted image analysis, deep machine learning-based image analysis of qTOF image data substantially improved the agreement (ICC=0.835 versus 0.662) and linear correlation (*r*=0.875 versus 0.685) of spatially-averaged total flow velocity measures between qTOF and PC, narrowed the 95% Bland-Altman limits of agreement ([-6.8, +3.6] cm/s versus [-8.0, +10.5] cm/s), and reduced analysis times by approximately two orders of magnitude.

Discussion

This initial study suggests that deep machine learning can be applied to qTOF MRA data to rapidly quantify intracranial arterial flow velocity measures that show good to excellent agreement with PC-derived measures. Future work will seek to refine and validate this and related deep machine learning image analysis strategies in more subjects and in patients with neurovascular disorders.

References

1. Parker DL, Yuan C, Blatter DD. Magn Reson Med. 1991;17:434–451. doi: 10.1002/mrm.1910170215
2. Koktzoglou I, Huang R, Edelman RR. Magn Reson Med. 2022;87:150–162. doi: 10.1002/mrm.28969

Acknowledgement: This work was supported in part by NIH NIBIB R01EB027475.

2.5D flow MRI of tricuspid valvular flow:

An accurate automated valve-following phase-contrast approach.

Jerome Lamy¹, Felicia Seemann², Ricardo Gonzales Vera³, Jie Xiang¹, Einar Heiberg⁴, and Dana Peters¹
¹Yale University, New Haven CT, ² NIH, Bethesda, MD, ³Oxford University, Oxford, England, ⁴Lund University, Lund Sweden.

Purpose: An unmet need in cardiac MRI is evaluation of diastolic dysfunction, which by echo requires measurement of LA volumes, E/e'

and tricuspid regurgitant flow velocity (1). Of these parameters, tricuspid regurgitant flow (indicating right heart pressure) is not yet feasible. 4D flow (2-3) has been investigated, but scan times are long, and trade-offs are needed. 2D flow cannot map TV regurgitant velocities due to the valvular motion. Recently, we adapted 2D valve-following PC (4) that follows the displacement of the mitral valve throughout the heartbeat, to use modern feature tracking. (5-6) Here we present a pilot study in tricuspid 2D flow using a valve-following slice, which we call **2.5D flow**, due to its partial third dimension. The valve-following is now automated using deep-learning networks for tracking the valves (7-8).

Methods: Ten healthy subjects were imaged on a 3T MRI (Siemens), acquiring 4ch cine and RV 2ch cine and using TVnet to track the TV valve automatically. The displacements and rotations were provided to the scanner for prospectively tracking the valve with a dynamic slice prescription (Figure 1). PC data sets of the tricuspid valve were acquired during a single breath-hold with retrospective-gating using the following scan parameters: VENC=150cm/s, TR/TE/θ=5.3ms/3.2ms/15, matrix size 256x156, FOV 380mm, voxel size 1.48x1.48x6mm, 4 bipolar pairs per repetition and 42ms temporal resolution. This acquisition was repeated for a static TV plane coinciding with the systolic valve plane. Standard PC of the main pulmonary artery (PA), aorta and cine were performed to compare resultant stroke volumes (SV) values. PC analysis was done using Segment software. Velocity correction was performed for eddy currents and for valve plane motion.

Results: A plot of the resulting flow patterns is shown in Figure 2A. A comparison of diastolic forward flow of the tricuspid valve vs. PA stroke volume is shown in Figure 2B. The 2.5D method outperformed static PC of the tricuspid valve in their agreement with PA flow; agreement was strong.

Discussion: Tricuspid valve forward flow was accurately measured using 2.5D PC, but less so with conventional 2D PC. Future studies in patients with regurgitant jets will demonstrate its accuracy in regurgitant velocity measurement.

References: 1) Nagueh SF, Eur Heart J-Card Img Dec 2016;17:1321-1360. 2) V. P. Kamphuis et al., Radiology, 290:1, pp. 70–78: 2018. 3) Feneis JF et al. J Magn Reson Imaging Oct 2018;48:1147-1158. 4) Kozerke S, JMRI, 2001;14:106-112. 5) Seemann F et al. . BMC Med Imaging 2017;17. 1. 6) Seemann F et al. JMRI 2019. 7) Gonzales R, EACVI ISMRM meeting 2022. 8) Gonzales R et al. MICCAI 2021.

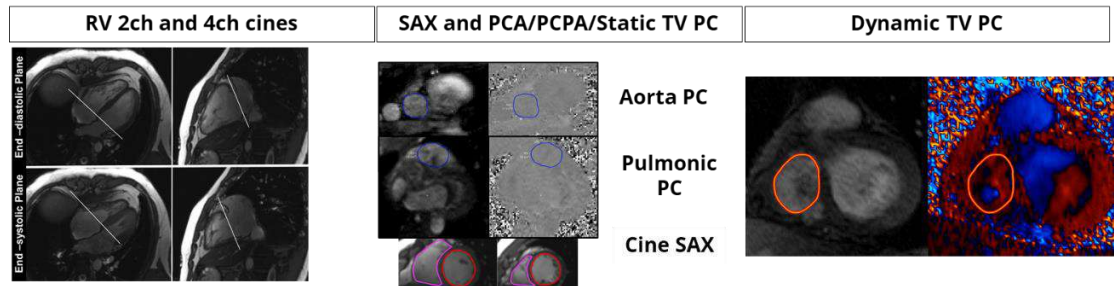


Figure 2: RV 2ch and 4Ch were automatically tracked through the cardiac cycle, and 2.5D PC with dynamic slice-prescription was obtained of the tricuspid valve (TV), for comparison with stroke volume by pulmonic (PA) flow.

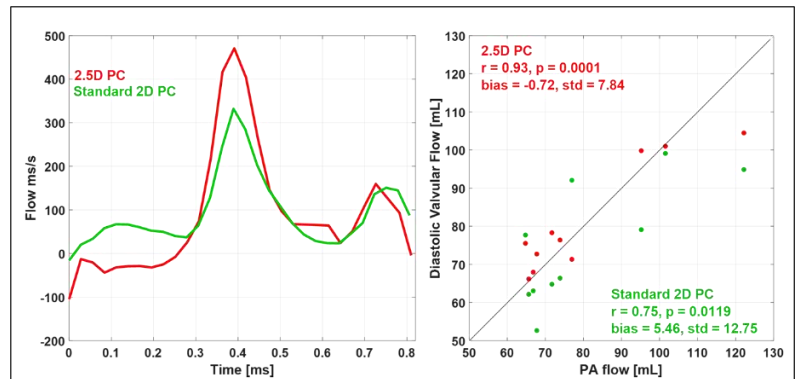


Figure 1: A) Flow wave-forms across the tricuspid valve, show physiologically reasonable flow pattern for 2.5D flow (i.e., no flow in systole, E and A waves in diastole). B) Comparison of tricuspid forward flow with PA flow showed stronger agreement using 2.5D flow, vs. standard 2D PC.

Comprehensive Imaging of Fontan and Glenn Shunts in Adult Congenital Heart Disease Patients using Ferumoxytol-Enhanced MR Angiography

Gentian Lluri¹, Ashley E. Prosper², Arash Bedayat², Takegawa Yoshida², Jeannette Lin¹, Leigh C. Reardon^{1,3}, Kim-Lien Nguyen^{2,4}, Jamil A. Aboulhosn¹, J. Paul Finn²

¹Ahmanson/UCLA Adult Congenital Heart Disease Center, Division of Cardiology; ²Department of Radiological Sciences; ³Children's Heart Center, Division of Pediatric Cardiology; ⁴Division of Cardiology, David Geffen School of Medicine, University of California, Los Angeles, Los Angeles, CA, USA

Introduction: As more children with complex congenital heart disease survive into adulthood, the prevalence of patients with total cavo-pulmonary connection (TCPC) shunts is increasing. With TCPC, the superior vena cava (SVC) and inferior vena cava (IVC) are connected directly to the pulmonary arteries via Glenn (SVC) and Fontan (IVC) shunts. These shunts may fail due to stenosis, thrombosis or occlusion. Meanwhile, conventional non-invasive methods to diagnose these complications have serious limitations due to absent acoustic windows with ultrasound and complex bolus timing requirements for CT and conventional MRI (1,2). Ferumoxytol is an intravenous iron therapy agent that has been used successfully off-label for cardiovascular MRI. Once injected, ferumoxytol becomes uniformly distributed throughout the entire intravascular space and remains there for several hours, reflecting ideal behavior for imaging TCPCs without complex injection schemes. The purpose of our study was to evaluate the performance of ferumoxytol-enhanced MRA (FE-MRA) for evaluation of adult patients with Fontan and Glenn shunts.

Materials and Methods: This was an IRB approved, retrospective analysis of data obtained from our database of adult congenital heart disease patients with TCPC who underwent FE-MRA from 2018 to 2022. Included in the analysis were patients with pacemakers, defibrillators, prosthetic heart valves, occlusion devices, stents and embolization coils. Breath-held, high-resolution 3D MRA was performed on a clinical 1.5T magnet (Avanto Fit, Siemens) during the steady state distribution of ferumoxytol dose of 4 mg /kg. The imaging volume included the neck, chest, abdomen and pelvis. FE-MRA studies were analyzed by 2 experienced board certified ACHD radiologists, who scored the images on a 5-point scale (5 = excellent; 1 = non-diagnostic) for overall quality, visualization of Glenn and Fontan shunts and for severity of artifact due to devices and hardware (1 = none; 5 severe and extensive). They also rated their confidence in diagnosis of shunt status (1 = very confident, 2 = moderately confident, 3 = not confident). The readers had access to all source images as well as to MIP and 3D VR reconstructions. Diagnostic imaging findings on FE-MRA reports were correlated with clinical follow-up and echocardiographic, angiographic, CT and/or surgical findings as available.

Results: A total of 58 ACHD patients (mean age 28 yrs, range 19-47 yrs) underwent successful FE-MRA and ferumoxytol infusion was well tolerated. Average scores for overall image quality and visualization of Glenn and Fontan shunts were respectively 4.2, 4.1, and 4.3 (max 5). Stents and embolization coils were common in the study cohort and artifact from hardware was scored at 1.96 (moderate, precluding visualization of some vessels) (Figure 1). Four patients had severe metal artifact that precluded confident diagnosis. The average score for confidence in diagnosing shunt status was 1.3. In all patients where the findings on FE-MRA were felt to be definitive, the diagnosis was supported by correlative clinical, imaging, and surgical data.

Conclusion: FE-MRA routinely produces unrestricted and reliable visualization of the entire cavo-pulmonary circulation without the need for bolus timing, eliminating vulnerability to mixing artifact and the requirement for dual injection schemes.

References:

1. Bonnicksen C, Ammash N. Choosing Between MRI and CT Imaging in the Adult with Congenital Heart Disease. *Curr Cardiol Rep.* 2016;18(5):45.
2. K.L. Sandler, et al. Optimizing CT angiography in patients with Fontan physiology: single-center experience of dual-site power injection. *Clinical Radiology* 69 (2014) e562ee567.

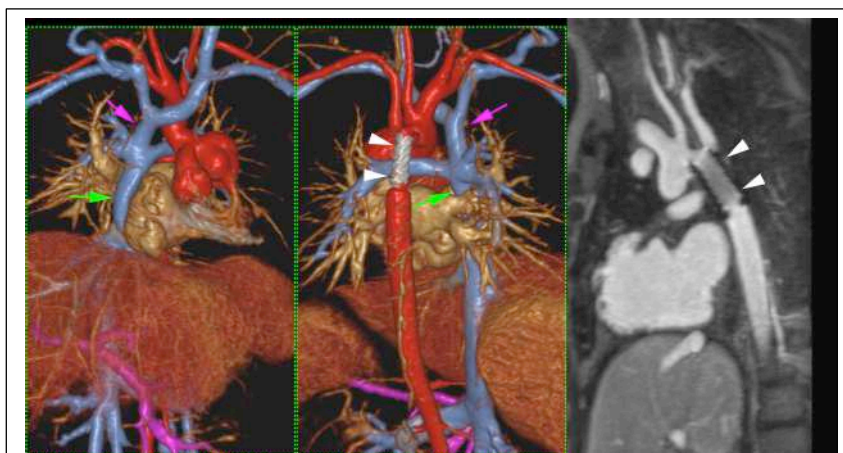


Figure 1. 24-year-old female with single ventricle physiology post Norwood procedure and TCPC. The Glenn (magenta arrows) and Fontan (green arrows) shunts are widely patent. A stent (arrowheads) is present in the distal aortic arch and proximal descending aorta. Despite some local signal loss, the stent is clearly patent.

Translatability of Fully Automated Deep Learning 3D Segmentation of CE-MRA Left Atrial Structures of AF Patients Across Two Sites

Justin Baraboo^{1,2}, Maurice Pradella², Anthony Maroun², Rod Passman³, Mina Chung⁴, Ben Shoemaker⁵, Majd El-Harasis⁵, Daniel Lee³, Dan Kim^{1,2}, Michael Markl^{1,2}

¹Northwestern Biomedical Engineering, ²Northwestern Radiology, ³Northwestern Medicine- Cardiology, ⁴Cleveland Clinic - Cardiology, ⁵Vanderbilt University Medical Center- Cardiovascular Medicine

Introduction Deep learning allows for efficient, automated processing of MRI images, including left atrial anatomical segmentation. Recently, we have created a convolutional neural network (CNN) to automatically segment the left atrium (LA), appendage (LAA), and pulmonary veins (PV) of atrial fibrillation patients from 3D contrast enhanced (CE) MRA data.¹ In this multi-site study, we tested the translatability of our CE-MRA left atrial segmentation network, trained Northwestern University (NU), to perform on data from another site (Vanderbilt University Medical Center, VUMC).

Methods 84 AF patients [age 63 ± 9 , 64 Male] underwent dynamic TWIST 3D CE-MRA pulmonary vein mapping [spatial resolution = $1.3\text{-}1.8\text{ mm}^3$] for clinical standard of care prior to catheter ablation at Northwestern. The 3D CE-MRA time frame with peak LA contrast was used to manually generate 3D segmentations of the LA, LAA, and PV (to the first branching point) using commercial software (MIMICS, Materialise, Belgium) by a single CV radiologist. These data served as the ground truth for training and testing the deep learning network, which was based on a 3D U-Net² with dense layers architecture with 4 label outputs to learn how to individually segment the LA, LAA, and PV from a CE-MRA volume input (Figure 1, left). Fivefold cross validation was utilized (67-68 training sets and 16-17 test sets per fold). Hole-filling and island removal were utilized in post-processing of network output. To quantify agreement between automated and manual 3D segmentations, DSC scores were calculated for each left atrial structure. The fully trained network was deployed, without any additional retraining, on an external 496 3D bolus triggered CE-MRA 3D image volumes from VUMC to automatically derive 3D segmentation of the LA, LAA, and PV (Figure 1, right). Ten of these cases were manually segmented for quantitative assessment of human vs machine performance by DSC scores. 32 cases were qualitatively reviewed (through coronal and axial views) by a board certified radiologist, scoring if LA segmentation was excellent (accurate atrial 3D segmentations), good (minor inconsistencies such as incorrect boundaries or missing small parts of atrium wall), or poor (missing parts of LA or inclusion of other regions) (Figure 2).

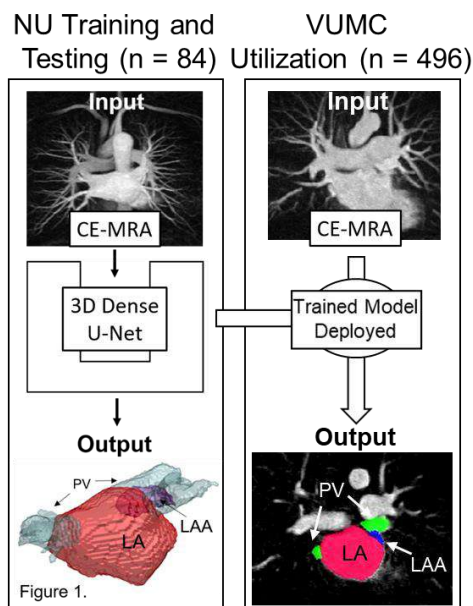


Table 1. Segmentation Results

Anatomy	NU Test Sets (n=84)
LA DSC	0.93 [0.91, 0.95]
LAA DSC	0.77 [0.68, 0.85]
PV DSC	0.71 [0.50, 0.82]
VUMC Test Sets (n = 10)	
LA DSC	0.90 [0.89, 0.91]
LAA DSC	0.66 [0.60, 0.70]
PV DSC	0.67 [0.62, 0.78]

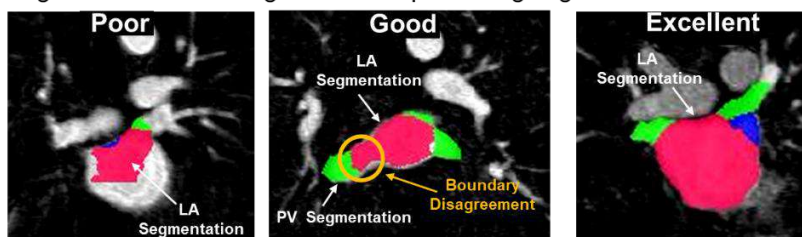
Results For NU data, deep learning processing demonstrated excellent performance for the 3D LA segmentation (median DSC: 0.93 [0.91, 0.95]), and moderate to good performance for the LAA (median DSC: 0.77 [0.68, 0.85]) and PV (median DSC: 0.71 [0.50, 0.82]) (table 1). Application of the deep learning network to VUMC data resulted in similar 3D LA segmentation accuracy (median DSC: 0.90 [0.89, 0.92]). However, machine vs. human performance was lower for LAA and PV segmentations (median DSC: 0.66 [0.60, 0.70] and 0.67 [0.62, 0.78], respectively). Semi-quantitative grading of 3D LA segmentation quality found excellent quality in 47% of VUMC cases, while 43% were rated as good, and 9% as poor.

Discussion This study demonstrated that a deep learning tool from NU for the 3D left atrial segmentation could be successfully applied to extremal data at VUMC.

Notably, this project used a smaller training and validation sets at NU to be utilized on a much larger data set at VUMC. Within NU validation, the models reduced performance for LAA and PV is likely related to the more complex and variant morphology of these structures. Additional training data in larger cohorts may be needed to overcome these difficulties. Differences in CE-MRA sequences between NU and VUMC may explain some performance discrepancies; while the LA has great contrast in both CE-MRAs, the contrast of other structures (e.g. aorta, right atrium, or ventricles) may differ. Importantly, 91% of VUMC segmentations were reviewed as good or excellent, indicating its potential diagnostic utilization for the reliable LA 3D segmentation.

References 1)Baraboo et al. SMRA 2021. 2) Cicek et al. MICCAI 2016.

Fig 2. Qualitative categories of deep learning segmented VUMC data



4-Dimensional CMR and Echocardiography in Pediatric Congenital Heart Disease - Segmental Sequential Analysis and Pre-Surgical Planning

Takegawa Yoshida, M.D.¹, Greg Perens, M.D.², Shi-Joon Yoo, M.D.³, Ankavipar Saprungruang, M.D.³, Kim-Lien Nguyen, M.D.^{1,4}, J Paul Finn, M.D.¹

¹Department of Radiology, Division of Cardiovascular Imaging, UCLA Medical Center, David Geffen School of Medicine

²Pediatric Cardiology, UCLA Medical Center, David Geffen School of Medicine

³Department of Diagnostic Imaging, The Hospital for Sick Children, University of Toronto

⁴Division of Cardiology, David Geffen School of Medicine at UCLA and VA Greater Los Angeles Healthcare System

Purpose: Visualization of detailed anatomy is crucial in clinical diagnosis, especially in patients with complex congenital abnormalities. Cardiovascular magnetic resonance (CMR) imaging and echocardiography have contributed to patient care for decades as non-invasive imaging modalities; however, each has specific strengths and limitations. Recent developments in 4D CMR have pushed the boundaries for dynamic 3D relationships among cardiovascular structures with an unrestricted field of view and shortened image acquisition time.¹ When 4D-CMR is combined with ferumoxytol, the intravascular blood pool signal is greatly enhanced, supporting accelerated high resolution imaging.² Meanwhile, echocardiography remains the default initial modality for valvular and intracardiac structure visualization due to its high temporal resolution, portability, and wide accessibility. We aim to evaluate 4D-CMR and dynamic 2D echocardiography to demonstrate overlap and differences in their diagnostic scope for pediatric congenital heart disease.

Materials and Methods: We retrospectively enrolled 200 consecutive pediatric patient of whom 122 patients met the selection criteria who had the congenital cardiac disease (CHD) or underwent palliative surgery in our IRB-approved, HIPPA-compliant study. CMR was performed with 4D multiphase steady-state imaging with contrast (4D-MUSIC) enhancement and 2D-echocardiography was performed by specialized pediatric cardiologists as per institutional standard. Two reviewers evaluated the 4D-MUSIC images, and one reviewer evaluated the paired echocardiograms. OsiriX workstation and Syngo Visualization platform were used for CMR and echocardiography evaluation, respectively. The 2 reviewers assigned to evaluate CMR were blinded to clinical diagnosis, while the 1 reviewer who evaluated echo was not. All reviewers had access to the complete image datasets for all patients and used the segmental sequential analysis method² to independently evaluate the images which included determination of situs, atrioventricular and ventriculoarterial connections, the associated lesions involving the systemic and pulmonary veins, atria, ventricles, arterial trunks, coronary arteries, and systemic and pulmonary arterial branches. The reviewers were allowed to arbitrarily reslice the 4D-MUSIC datasets to any 2D cine images in any plane, as well as MIP and 4D volume-rendered reconstruction.

Results: The patient's age range was 1 day – 3.5 years (1.5 ± 2.7 years). There were 62 females and 60 males. The diagnoses including heterotaxia (n=12 cases), tetralogy of Fallot (n=14), transpositions (n=9), various forms of left-sided obstructive lesions (n=26), isolated septal defects (n=17), vascular rings (n=9), and other (n=35). The time interval between 4D-MUSIC and echo was 3.04 ± 5.33 days. 4D-MUSIC acquisition required controlled ventilation whereas 2D echocardiographic imaging was typically performed without sedation. A full sequential segmental approach was feasible in all cases; however, several elements were seen differently between CMR and echocardiography. Whereas echo has limited visualization of aortic arch anomalies (n=5), coronary artery anomalies (n=2), pulmonary vein and artery anomalies (n=6), systemic vein anomalies (n=5), heterotaxia (n=6), double inlet right atrium (n=1), ventricular noncompaction (n=2), and major aortopulmonary collateral arteries (n=1), 4D-MUSIC depicts these features definitively. 4D-MUSIC occasionally did not visualize small ventricular septal defects (n=3), subtle valvular anomalies (n=4), and coronary sinus anomalies (n=1). In 102 CMR cases, the proximal coronary arteries were definitively seen.

Discussion: 4D-MUSIC provided definitive visualization of complex vascular anatomy and cardiac morphology in all 122 patients. Its unrestricted field of view and ability to view dynamic cine in any plane enabled reviewers to analyze complex anatomic anomalies within the entire chest cavity, including structures that are frequently obscured on echocardiography. Meanwhile, 2D-echocardiography demonstrated some valvular anomalies and small septal defects better than CMR. Atrioventricular and ventriculoarterial relationships were evaluable at a comparable rate. Our findings suggest that in patients with complex CHD where questions remain unanswered on echocardiography, 4D-CMR can provide the required information in all cases. When evaluation of complex ventricular geometry is require for surgical planning, 4D-MUSIC can provide the substrate for 3D printing of all chambers with uniform contrast.

References: [1] Nguyen KL et al. Radiology. 2021 Jul;300(1):162-173. [2] Finn JP et al. Clin Radiol. 2016 Aug;71(8):796-806. [3] Bierhals AJ et al. Int J Cardiovasc Imaging. 2014 Aug;30(6):1161-72.

Pediatric BAV Flow Abnormalities Detected by 4D Flow MRI and Seismocardiography

Ethan Johnson¹, Aparna Sodhi², Alex Barker³, Joshua Robinson^{1,2}, Cynthia Rigsby^{1,2}, Michael Markl¹

¹ Northwestern University, ² Ann & Robert H. Lurie Children's Hospital, ³ University of Colorado Anschutz

[Purpose] Bicuspid aortic valve (BAV) is associated with high lifetime risk of developing valve dysfunction/aortopathy [1]. Regular monitoring by echocardiography or CMR is essential for identifying and managing disease associated with BAV. Recent work with quick, non-invasive seismocardiography (SCG) chest-vibration measurements in adult patients with valve disease has shown elevated SCG energy in patients, corresponding to presence of valve-mediated flow abnormalities, such as elevated aortic peak velocities [2]. Other potential clinical applications for SCG have been investigated [3,4], but mainly in adults. Given its ease and sensitivity, SCG could be valuable in the context of pediatric valve disease when used as a first-line screening tool to refer for advanced echo or CMR, thereby mitigating some costs from serial imaging, and easing the challenges of pediatric imaging-related anesthesia and contrast administration. Here, we present novel data from SCG and 4D flow MRI that include pediatric BAV patients, and we evaluate potential utility of SCG to screen for disease.

[Methods] Adult and pediatric patients with aortic valve disease (AVD) and healthy controls receiving CMR were recruited for an additional two-minute SCG measurement on the day of imaging. Patients had tricuspid or bicuspid aortic valve (TAV, BAV) and were presenting for routine CMR to assess valve/flow function. Healthy control subjects had no known cardiovascular disease. All subjects gave informed consent and were enrolled with IRB supervision. CMR exams included 4D flow MRI (1-3mm³/30-40ms res., 1.5T or 3T). Standard aortic valve function assessment was performed from clinical CMR for patients, and patients' and healthy subjects' mid-ascending aortic (AAo) velocities (V_{max}) were measured from 4D flow. SCG energy was calculated by ECG R wave-aligned spectral decomposition [2]. Patient and control measurements were compared with two-sample *t*-test. Predictive performance for SCG energy classifying patients vs. controls was evaluated with receiver-operator curve (ROC) analysis.

[Results] In total 76 subjects were enrolled, with 52 healthy control subjects (48±17.4y, 23 F), 10 adult subjects (4 BAV, 6 TAV, 52±11.1y, 2 F), and 14 pediatric BAV subjects (18±5.7y, 3 F; tbl.1). A subcohort of the 8 youngest healthy subjects (25±2.1y, 2 F) was selected for comparison to pediatric BAV subjects. A significant relationship between elevated MRI-measured mid-AAo V_{max} and increased SCG late-systole mid-frequency energy ($R=0.40$, $p<0.01$) demonstrated the sensitivity of SCG to detect altered chest acceleration energy associated with aortic valve disease in adults (fig.2). In addition, ROC analysis demonstrated excellent performance of SCG to separate patients with AVD from controls (ROC area = 0.92/0.96 for pediatric/adult subjects; fig.3). SCG energy level distributions in the pediatric cohort differ from those of the adult cohort, including the particular metric most discriminative between patients/controls (fig.3).

[Discussion] This preliminary evaluation of SCG in the context of pediatric BAV shows the potential use of SCG energy to screen for BAV-mediated aortic flow changes. The correlation observed between SCG energy and peak velocities, a key metric for management of valve disease and aortopathy, indicates the relevance of SCG measurements in this context. Potential screening performance in adult and pediatric subjects is similar, but different signal features were found most effective for identifying abnormalities in pediatric BAV patients versus adult patients. Further investigation into these characteristics is needed. Expanded cohort size may help confirm these findings, in addition to allowing for potential study of SCG for assessing disease severity in pediatric BAV.

[1] Otto CM, et al. JACC. 2021 Feb;77(4):e25–197. [2] Johnson EMI, et al. ABME. 2020 Jun;48(6):1779–92. [3] Zanetti JM, Tavakolian K. IEEE:EMBC; 2013. p. 7004–7. [4] Taebi A, et al. Vibration. 2019 Jan 14;2(1):64–86.

	<i>n</i>	age [y]	sex	valve	AS [none, mild, moderate, severe]	AR [none, mild, moderate, severe]	<i>Table 1.</i> Characteristics of the cohort studied. The healthy young-adult subcohort is drawn from the full cohort of healthy subjects recruited into the study (AS: aortic valve stenosis; AR: aortic regurgitation).
healthy cohort (all)	52	48 ± 17.4	23 female	52 TAV	52, 0, 0, 0	52, 0, 0, 0	
adult aortic valve disease	10	52 ± 11.1	2 female	4 BAV, 6 TAV	1, 5, 3, 1	3, 5, 2, 0	
healthy subcohort (young adult)	8	25 ± 2.1	2 female	8 TAV	8, 0, 0, 0	8, 0, 0, 0	
pediatric bicuspid aortic valve	14	18 ± 5.7	3 female	14 BAV	8, 2, 2, 1	7, 3, 4, 0	

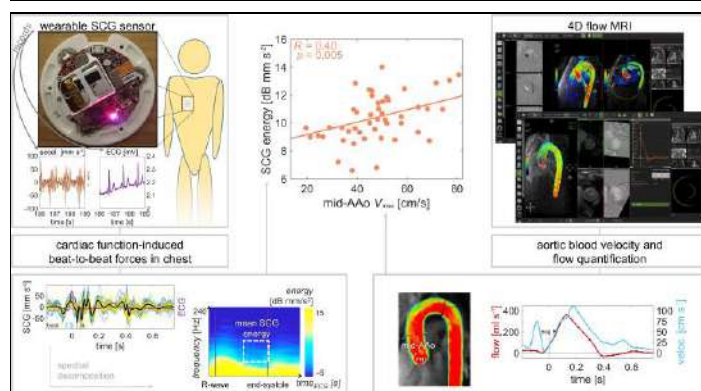


Figure 2. Same-day SCG (left) and 4D flow MRI (right) collected from the adult healthy subjects and valve patients show correlation (center) in some features, such as late-systole mid-frequency SCG energy and mid-ascending aorta (mid-AAo) maximal through-plane velocity (V_{max}).

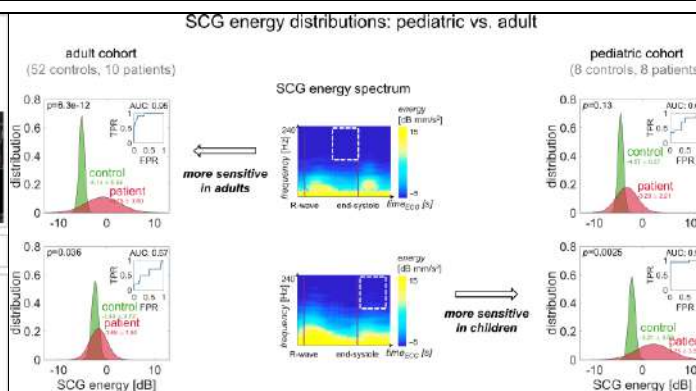


Figure 3. Comparison of SCG energy distributions in adult valve-disease patients vs. healthy adult controls (left) with distributions in pediatric BAV patients vs. controls (right). Late-systole high-frequency SCG distinguishes patients/controls better in adults, while early-diastole high-frequency SCG distinguishes better in children.

Five-Dimensional Respiratory-Motion Resolved Volumetric Lung Imaging for Fractional Ventilation and T1 Mapping Using MR Multitasking

Chaowei Wu^{1,2}, Nan Wang³, Fei Han⁴, Hsu-Lei Lee¹, Vibhas Deshpande⁵, Andreas Voskrebenez⁶, Jens Vogel-Claussen⁶, Anthony G. Christodoulou^{1,2}, Yibin Xie¹, and Debiao Li^{1,2}

¹Biomedical Imaging Research Institute, Cedars-Sinai Medical Center, Los Angeles, CA, United States

²Bioengineering, University of California, Los Angeles, Los Angeles, CA, United States

³Radiology Department, Stanford University, Stanford, California

⁴Siemens Healthcare, Los Angeles, CA, United States ⁵Siemens Healthcare, Austin, TX, United States

⁶Institute for Diagnostic and Interventional Radiology, Hannover Medical School, Germany

Purpose

The evaluation of lung tissue and pulmonary function has taken on particular importance during the global COVID-19 pandemic. Studies have shown that fractional ventilation (FV) estimated from a series of time-resolved MR images is capable of revealing potential pulmonary disorder^{2,3}. T1 mapping can be used in the detection of fibrosis⁵ and embolism⁴. However, pulmonary MRI faces challenges in spatial coverage, SNR, and motion artifacts. Ventilation mapping methods usually use 2D acquisition⁶ to avoid severe motion artifacts or 3D acquisition⁷ with limited in-plane resolution. Existing lung T1 mapping techniques are 2D acquisition and typically require breath-holding or respiratory averaging, which results in compromises in coverage and image quality. Simultaneous acquisition of T1 maps and FV map is not yet available. To address those limitations, we propose a novel 5D MR Multitasking technique¹ to enable respiratory motion resolved imaging of the entire lung and investigate the feasibility of simultaneous respiratory motion-resolved T1 mapping and FV mapping using a 6-minute scan.

Methods

Sequence Design: T1 contrast was generated using periodic non-selective inversion recovery pulses followed by 3D FLASH readouts with variable flip angles (IR-VFA)⁸. A stack-of-spiral sampling pattern with randomized reordering following Gaussian distribution in-plane and in partition encoding was designed for data sampling. Ultra-short TE was enabled to maximize signal-noise-ratio. One spiral interleave in the partition $k_z=0$ was repeated every 8 readouts¹.

Imaging Model: In the reconstruction, images were represented as a 3-way tensor $\mathcal{A} = I(r, t_{T1}, t_r)$ with one way representing 3D spatial location $r = (x, y, z)$, one IR-VFA T1 recovery dimension t_{T1} , and one respiratory motion state dimension t_r . The tensor can be decomposed in collapsed form as

$$\mathcal{A}_{(1)} = \mathbf{U}\mathbf{G}_{(1)}(\mathbf{W}\otimes\mathbf{V})^T, \quad (1)$$

Where \mathbf{U} contains spatial basis functions and \mathbf{V}, \mathbf{W} contain temporal basis functions for IR-VFA T1 recovery dimension and respiratory motion state dimension, respectively, and \mathbf{G} is the core tensor. \mathbf{G}, \mathbf{V} and \mathbf{W} are determined by the training data \mathbf{d} . The spatial factor \mathbf{U} is reconstructed by:

$$\hat{\mathbf{U}} = \arg \min_{\mathbf{U}} \|\mathbf{d} - \Omega[\mathbf{F}\mathbf{S}\mathbf{U}\Phi]\|_2^2 + \lambda R(\mathbf{U}), \quad (2)$$

With $\Phi = \mathbf{G}_{(1)}(\mathbf{W}\otimes\mathbf{V})^T$, undersampling operator Ω , spatial Fourier transform operator \mathbf{F} , coil sensitivity \mathbf{S} , regularization function $R(\cdot)$ and regularization parameter λ .

T1 Mapping and Fractional Ventilation Analysis

T1 maps were fit based on the Bloch equations for IR-VFA contrast. The fractional ventilation map was estimated using a third-party prototype software (MR Lung; Siemens Healthcare, Erlangen, Germany)⁹.

Imaging Experiments: 11 healthy volunteers were scanned on a 3T scanner (MAGNETOM Vida, Siemens Healthcare, Germany). The imaging parameters were: FOV = 500x500x240mm³ in coronal view, resolution = 1.6x1.6x10mm³, TE/TR=0.17/3ms, variable flip angle = 2°/8°. Subjects were free-breathing during scan. Eight respiratory bins were used for reconstruction.

Results

Figure1 shows the sequence diagram and k-space trajectory. Figure 2 shows representative T1 maps and ventilation maps from three volunteers. The statistics of lung parenchyma T1 values are 1061.2±88.5ms, which are consistent with the literature⁴.

Discussions and Conclusion

The presented pilot study demonstrated the feasibility of simultaneous acquisition of respiratory motion resolved T1 map and fractional ventilation map using the proposed 5D pulmonary MR Multitasking technique within a single 6-min scan. Further testing in patients with various lung disorders is warranted.

Reference 1. Christodoulou, A.G. et al. *Nature BME* 2018; **2**.

Voskrebenez, A. et al. *MRM* 2018; **3**. Nyilas, S. et al. *Journal of*

cystic fibrosis 2019. **4.** Mirsadraee, S. et al. Quantitative imaging in medicine and surgery 2016 **5.** Gai, N.D. et al.

JMRI 2017. **6.** Bauman, G. et al. *MRM* 2017 **7.** Klimesh, F. et al. *MRM* 2021 **8.** Serry, F.M. et al. *MRM* 2021. **9.**

Voskrebenez, A. et al. *MRM* 2018

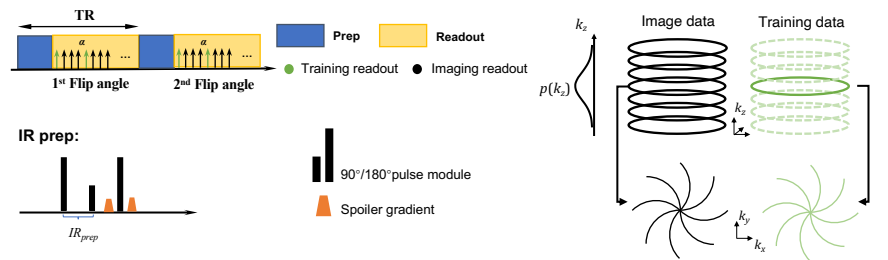


Figure 1 Sequence diagram and k-space trajectory

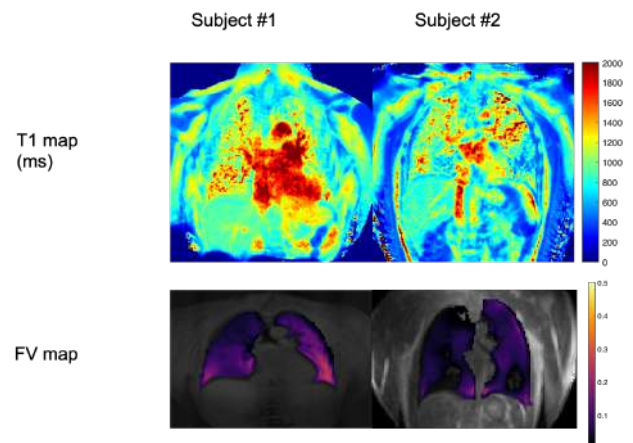


Figure 2 Representative Results

Accelerated whole-heart free-breathing CMRA in 3 min in patients with congenital heart disease

A Fotaki¹, C Munoz¹, C. Velasco¹, K Kunze^{1,2}, R Neji^{1,2}, K Pushparajah^{1,3}, RM Botnar¹ and C Prieto¹

¹ School of Biomedical Engineering and Imaging Sciences, King's College London, London, United Kingdom, ²MR Research Collaborations, Siemens Healthcare Limited, Frimley, United Kingdom

Purpose: Cardiovascular MRA (CMRA) is established for serial anatomical evaluation in patients with congenital heart disease (CHD)¹. Conventional 3D T2-prepared balanced steady state free precession (bSSFP) whole-heart imaging techniques employ diaphragmatic respiratory gating (dT2prep-bSSFP) to minimize the effects of respiratory motion, leading to unpredictable and long acquisition times and residual artefacts from respiratory and non-rigid cardiac motion. To address these challenges, we recently proposed an accelerated contrast-free CMRA framework that incorporates image-based navigation^{2,3} for translational and non-rigid motion-correction along with 3D patch-based denoising (iT2prep-bSSFP PROST)⁴ for efficient, free-breathing 3D whole-heart imaging. Here we prospectively evaluated the proposed approach in adult patients with CHD and compared it against the current clinical sequence.

Methods: An ECG-triggered free-breathing 3D iT2prep-bSSFP sequence acquired with a 4-fold undersampled variable-density Cartesian trajectory⁵ is employed. 2D image navigators (iNAV)s² are acquired at each cardiac cycle by spatially encoding the start-up echoes preceding the 3D CMRA acquisition to enable 100% respiratory scan efficiency and predictable scan time. Motion estimation and non-rigid motion correction is performed inline in the scanner software. Additional 3D-PROST denoising is performed off-line. Imaging parameters include: FOV: 400x300x72-108 mm³, resolution 1.5 mm³, flip angle = 90°, T2-prep duration = 40ms, TE/TR = 1.75/238 ms, coronal

orientation. The research sequence was evaluated against the clinical 3D dT2prep bSSFP (FOV 400x300x88-120, resolution 1.5 mm³, T2-prep duration = 40 ms, TE/TR = 1.52/294 ms GRAPPA parallel imaging 2x undersampled, flip angle = 90°, sagittal orientation) for the visualization of the cardiac anatomy and cardiac connections to the thoracic vasculature. Twenty-five patients with CHD and different underlying pathologies (tetralogy of Fallot, coarctation of the aorta, hypoplastic left heart syndrome, atrioventricular septal defect, transposition of the great arteries, anomalous pulmonary venous drainage) were scanned in a 1.5T MRI scanner (MAGNETOM Aera, Siemens Healthcare, Erlangen, Germany). Two experts blinded to the technique used, recorded their diagnostic confidence to perform full anatomical analysis (1: poor diagnostic confidence to 3: full diagnostic confidence). Diagnostic quality of the pulmonary and systemic venous return, intracardiac chambers, coronary and great arteries was assessed and compared between the two methods using a 1-5 Likert scale (1: non-diagnostic, 5: excellent image quality, ≥3: diagnostic). Co-axial aortic dimensions at the aortic root were measured by one reader with both techniques to assess inter-method agreement.

Results: Good quality depiction of all cardiac segments in short scan time was achieved with the iT2prep-bSSFP PROST approach [3.2±0.8min (research) versus 16±3min (clinical), P<0.0001]. The inline reconstruction time was 2±0.5min and the offline denoising time was 1.5±0.5min. Remaining respiratory motion artefacts are less noticeable and luminal signal is significantly improved due to the reduction of flow and off resonance artefacts (Fig. 1). Diagnostic confidence was higher for the proposed approach compared to the clinical sequence for both reviewers (Reviewer 1: 3 (2.5, 3) vs 2.5 (2, 2.5), P=0.007; Reviewer 2: 3 (3, 3) vs 2.75 (2, 3), P=0.05). Bland Altman analysis showed very good agreement in the co-axial aortic measurements of the aortic root with a small mean difference of 0.01cm and narrow limits of agreement (<0.2cm) (Fig.2). Image quality scores were statistically significantly higher for the proposed approach for the systemic and pulmonary veins, left atrium, left main coronary artery and comparable between the two approaches for the remaining structures (Fig. 3)

Discussion: The proposed respiratory-motion compensation and reconstruction strategy offers a novel framework for sequential, segmental 3D whole-heart imaging in a ~3min acquisition time. iNAV-based 3D-whole heart MRA provided high quality visualisation of the heart and thoracic vessels in a cohort of patients with congenital heart disease, in shorter and more consistent scan times than the current clinical standard. High diagnostic confidence and reproducible vascular measurements are promising for imminent clinical integration.

References: 1. Fratz et al. JCMR.2013. 2.Henningsson M et al. Magn Reson Med. 2012; 3. Cruz G et al. Magn Reson Med. 201; 4. Bustin A et al. Magn Reson Med. 2019; 5. Prieto C. et al. J Magn Reson Imaging.

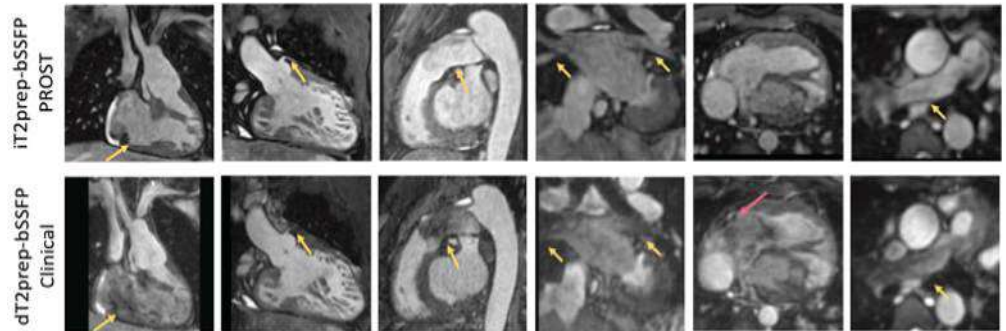


Fig. 1: Attenuation of flow, respiratory and off resonance artefacts with the proposed iT2prep-iNAV bSSFP (first row) versus the clinical sequence (second row) in CHD patients.

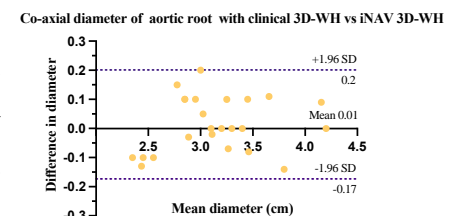


Figure 2: Bland-Altman plot of the co-axial dimensions of the aortic root.

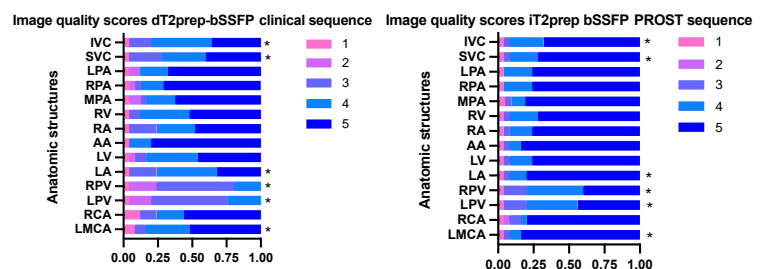


Figure 3: Distribution of image quality scores across all intrapericardiac structures for the proposed and the clinical sequences. * indicate P<0.05 in image quality score comparison.

Impact of Pulmonary Artery Flow Distribution on Fontan Hemodynamics and Flow Energetics

Elizabeth K. Weiss,^{1,2} Cynthia K. Rigsby,^{2,3} Joshua D. Robinson,³ Michael Markl^{1,2}

¹Northwestern Biomedical Engineering, ²Northwestern Radiology, ³Ann & Robert H. Lurie Children's Hospital of Chicago

Purpose: Single ventricle physiology is a severe congenital heart defect often requiring multi-step palliative surgical corrections, completed with a total cavo-pulmonary connection (TCPC, Fontan Connection). While these patients have a 20-year survival rate of 76% [1], 70% percent of patients will experience Fontan failure by age 50 [2]. However, individual risk factors for Fontan failure are poorly understood. Previous studies have shown that TCPC hemodynamic measures may be implicated in Fontan failure, but there is a dearth of data to investigate these measures over time. We aimed to investigate longitudinal changes in Fontan hemodynamics and flow energetics in patients with TCPC.

Methods: 10 patients with TCPC who underwent at least two standard-cardiac MRI exams (including 4D flow) were included in this retrospective study. Manual 3D segmentation of the TCPC, including the inferior and superior vena cava (IVC and SVC) and the left and right pulmonary arteries (LPA and RPA) was completed for baseline and follow-up 4D flow MRI for each patient. An automated centerline was calculated for the RPA, LPA and the caval veins (fig 1a) and used to define the following 3D Fontan segments: IVC, SVC, LPA, RPA and the connection (fig1b). Parametric flow maps (fig 1c) were calculated to quantify voxel-wise viscous energy loss (EL) [3] and peak velocity. The IVC segment was largely composed of the Fontan conduit. Mean values for EL and peak velocity were quantified for each Fontan segment and changes between baseline (BL) and follow up (FU) were calculated for each patient and normalized for follow-up time. The flow distribution (FD) [4] from the IVC to the LPA and RPA was measured using Ensight (Ansys, Inc., Canonsburg, PA) to release pathlines from the IVC volume and an in-house MATLAB tool to measure percent of pathlines reaching each pulmonary artery. Patients were stratified as having equal FD (FD <75% or >25% to the LPA) or unequal FD (FD >75% or <25% to the LPA).

	Equal FD			Unequal FD		
	BL	FU	Δ/year	BL	FU	Δ/year
Peak Velocity: IVC (m/s)	0.36 \pm 0.09	0.38 \pm 0.1	0.019 \pm 0.04 (p=0.44)	0.28 \pm 0.06	0.48 \pm 0.13	0.042 \pm 0.035 (p=0.062)
EL: SVC+connection+IVC (μJ)	6.5 \pm 1.6e4	8.2 \pm 3.9e4	5.1 \pm 1.0e3 (p=0.44)	6.6 \pm 4.9e4	13 \pm 7.5e4	1.4 \pm 1.8e4 (p=0.18)

Table 1. EL and peak velocity stratified by FD. P-value for Wilcoxon sign-rank test.

Results: The cohort (17.7 \pm 8.8 years at BL, 40% female) had an average follow-up time of 4.4 \pm 2.6 years. Two patients had general anesthesia during both scans and two patients had general anesthesia at BL only. Five patients had an extracardiac Fontan conduit while the remaining five had a lateral tunnel Fontan. There were no significant differences in EL or peak velocity in any region when stratified by Fontan type (p>0.3). At baseline 5 patients had an unequal FD to the LPA and 5 had an equal FD. As seen in table 1 and figure 2, those with unequal FD at BL had a 71% increase in peak velocity while those with equal FD at BL had only a 5.5% increase. We also found that those with unequal FD had a 97% increase in mean EL in the combined IVC + Connection + SVC region while the equal FD group had a 26% increase (Table 1, Fig 3). Bolstering these trends in the FD stratified groups, we found a significant correlation between per year changes in peak velocity and mean EL in both the IVC (r=0.82, p=0.004) and SVC (r=0.76, p=0.01) when including all 10 patients. When combining measurements from the SVC and IVC, a linear regression ($\Delta\text{EL} \sim \Delta\text{peak velocity}$) revealed that change in peak velocity was a significant predictor of change in EL (coefficient = 4.6e6, p=8e-6, $R^2 = 0.68$).

Discussion: The findings of our study indicate that unequal FD in TCPC patients may be associated with the development of unfavorable Fontan hemodynamic and flow energetics. A recent study has shown that viscous energy loss is associated with worse exercise capacity [5]. Thus, our results suggest that patients with unequal IVC flow distribution may be more likely to progress towards worsening flow efficiencies and potentially worse exercise capacity. While viscous energy loss requires more complex computation, our results also suggest that changes in peak velocity may serve as an easier to measure proxy for worsening flow efficiency. While these are important results, a substantial limitation in our study is a small cohort (n=10). However, follow-up 4D flow data in Fontan patients is rare and this small cohort analysis supports the continued investigation of flow parameters and flow as markers for Fontan outcomes.

References: [1] Dabal, R. J. et al. *JTCS*. 2014. [2] Dennis, M. et al *JACC*. 2018. [3] Barker, A. et al. *MRM*. 2014 [4] Jarvis, K. et al. *MRM*. 2019 [5] Rijnberg, F. et al. *JCMR*. 2022

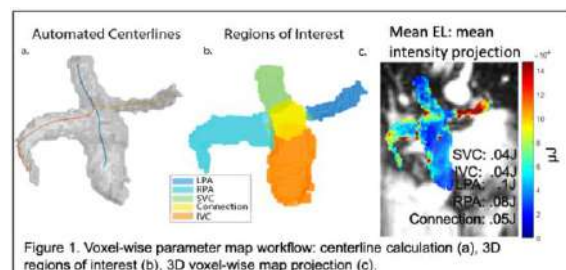


Figure 1. Voxel-wise parameter map workflow: centerline calculation (a), 3D regions of interest (b), 3D voxel-wise map projection (c).

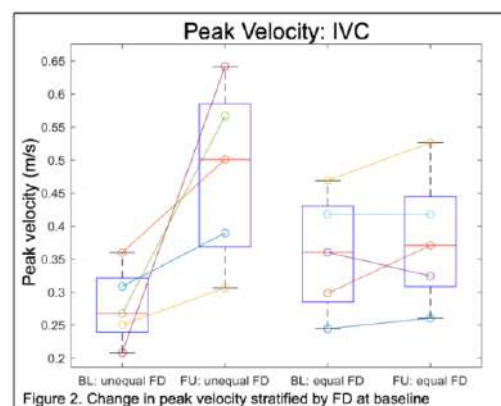


Figure 2. Change in peak velocity stratified by FD at baseline

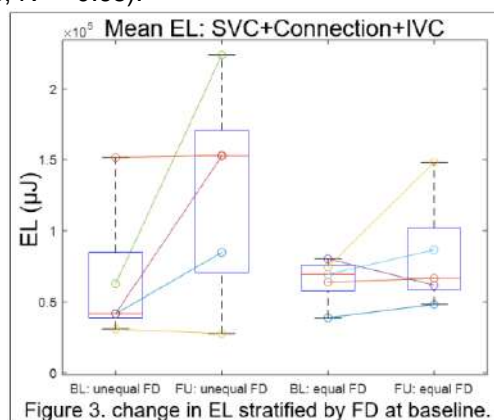


Figure 3. change in EL stratified by FD at baseline.

On the effects of contrast agents in free-running whole-heart 5D flow Imaging

Mariana B.L. Falcão¹, Tobias Rutz², Milan Prša³, Estelle Tenisch², Liliana Ma^{4,5}, Michael Markl^{4,5}, Matthias Stuber^{1,6}, Christopher W. Roy¹

¹ Department of Diagnostic and Interventional Radiology, Lausanne University Hospital (CHUV) and University of Lausanne (UNIL), Lausanne, Switzerland. ² Service of Cardiology, Centre de resonance magnétique cardiaque (CRMC), CHUV and UNIL, Lausanne, Switzerland. ³ Woman-Mother-Child Department, CHUV and UNIL, Lausanne, Switzerland. ⁴ Department of Radiology, Feinberg School of Medicine, Northwestern University, Chicago, IL, United States. ⁵ Department of Biomedical Engineering, Northwestern University, Chicago, IL, United States. ⁶ Center for Biomedical Imaging (CIBM), Lausanne, Switzerland.

Purpose: In free-running whole-heart radial phase-contrast (PC) MRI^[1], fully self-gated respiratory and cardiac motion-resolved 3D images are reconstructed with velocity sensitivity across three orthogonal directions (5D flow MRI)^[1, 2]. Compared to the current clinical gold standard 2D PC MRI^[3], this framework improves scanning efficiency as well as ease-of-use^[1]. However, to date, the effect of using contrast in 5D flow MRI has not been investigated. In this study, we compared flow measurements from 5D flow datasets collected without contrast agent, with Ferumoxytol, and with Gadolinium. 2D PC MRI was acquired as reference. We tested the hypothesis that post-contrast 5D flow MRI improves the accuracy of flow measurements relative to no contrast.

Methods: 15 congenital heart disease (CHD) patients (age 22.5 ± 11.4 , 4 F) were scanned on a 1.5T MAGNETOM Sola system (Siemens Healthcare, Erlangen, Germany) using the 5D flow MRI sequence^[1]. Additionally, 2D PC MRI was acquired in the proximal ascending aorta (AAo), descending aorta (DAo) and main pulmonary artery (MPA). Prior to the scanning, five subjects received Gadolinium, and five subjects received Ferumoxytol. The five remaining subjects were scanned without a contrast agent. 2D PC MRI contours were drawn on magnitude images. Using a compressed-sensing-based image reconstruction framework^[1,2], end-expiratory 5D flow images were selected. 3D vessel segmentation was based on retrospectively computed phase-contrast angiography images for each 5D flow dataset. Orientations and anatomical levels from the 2D PC MRI planes (AAo, DAo, MPA) were used for reformatting and comparison with the 2D images, using Circle's cvi42 (Calgary, Canada) post-processing software. 5D flow segmentation and flow streamlines were visually inspected during the analysis. Net volumes and peak flow rates were measured, and Bland-Altman analysis was used to compare 5D flow MRI and 2D PC MRI. A Wilcoxon signed-rank test was used for statistical analysis.

Results: Segmentation and streamline visualization were qualitatively similar between each contrast group (Figure 1). Good agreement between 5D flow MRI and 2D PC MRI net volume measurements (Figure 2) can be reported for both Ferumoxytol ($p=0.72$) and Gadolinium groups ($p=0.17$), while significant differences were found when acquiring without contrast ($p=0.03$). Significant peak flow rate biases were identified in the Gadolinium group ($p=0.001$) and in the no contrast group ($p=0.00006$), but not for Ferumoxytol ($p=0.17$). Overall, flow measurements showed better agreement with 2D PC MRI in the Ferumoxytol group followed by its Gadolinium and no contrast counterpart.

Discussion: In this preliminary study, we tested the effects of different types of contrast agents on 5D flow MRI measurements. We report that Ferumoxytol leads to an improvement in 5D flow assessment with respect to the reference 2D PC MRI, while 5D flow MRI without contrast agent showed the least favorable results. This confirms our hypothesis that contrast injection improves the quantification of flow measurements in 5D flow MRI, with regard to 2D PC MRI. The significant differences reported in the no contrast group suggests a larger sensitivity to noise, which is reduced when using Gadolinium, and even more so with Ferumoxytol. This study did not include a quantitative evaluation of signal-to-noise ratio, but future work will focus on adding related metrics and on scanning more subjects.

References: [1] Ma LE, et al. 5D Flow MRI: A Fully Self-gated, Free-running Framework for Cardiac and Respiratory Motion – resolved 3D Hemodynamics. *Radiol. Cardiothorac. Imaging* 2020;2(6). [2] Di Sopra, et al. An automated approach to fully self-gated free-running cardiac and respiratory motion-resolved 5D whole-heart MRI. *Magn. Reson. Med.* 2019;1–15. [3] Kramer CM, et al. Standardized cardiovascular magnetic resonance imaging (CMR) protocols: 2020 update. *J. Cardiovasc. Magn. Reson.* 2020;22:1–18.

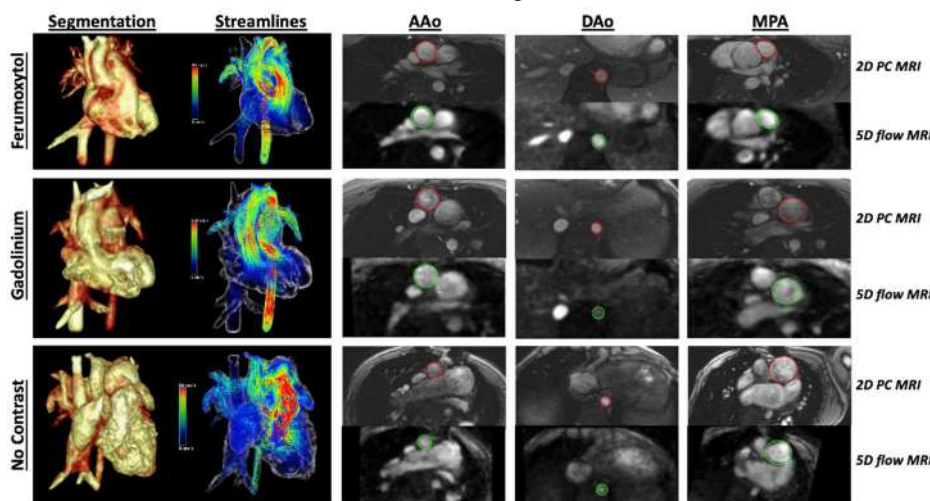


Figure 1. Comparison between three CHD patients acquired with 5D flow MRI. Top to bottom: Ferumoxytol (19y, M, Marfan syndrome), Gadolinium (21y, M, transposition of the great arteries, post-atrial switch), and no contrast (34y, M, tricuspid atresia). Left to right: 3D Segmentation, 3D Streamlines, and 2D contours of AAo, DAo, and MPA.

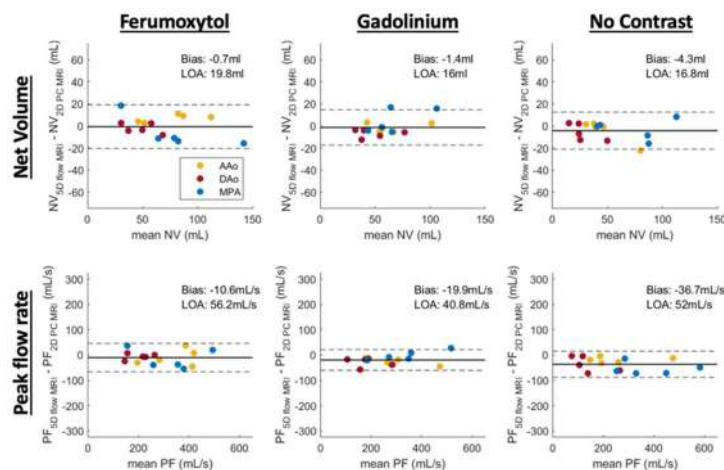


Figure 2. Bland-Altman plots between 5D flow MRI and 2D PC MRI measurements, for each contrast group. Top to bottom: net volume (NV) and peak flow rate (PF). Left to right: Ferumoxytol, Gadolinium and no contrast. Black continuous lines: bias. Black dashed lines: limits of agreement (LOA). AAo, DAo and MPA are visualized in different colors.

Hemodynamic Evaluation of Type B Aortic Dissection with Compressed Sensing Accelerated Single and Dual-Venc 4D Flow MRI

Ozden Kilinc¹, Justin Baraboo^{1,2}, Stanley Chu¹, Elizabeth K. Weiss^{1,2}, Anthony Maroun¹, John Wence Cerne¹, Daniel Giese³, Ning Jin³, Kelvin Chow^{1,3}, Xiaoming Bi³, Rachel Davids³, Chris Mehta⁴, S. Chris Malaisrie⁴, Andrew Hoel⁵, Michael Markl^{1,2}, Bradley D. Allen¹

1. Radiology, Northwestern University 2. Biomedical Engineering, Northwestern University 3. Siemens Healthcare 4. Cardiac Surgery, Northwestern University 5. Vascular Surgery, Northwestern University

Purpose: Type B Aortic dissection (TBAD) can be associated with serious adverse outcomes with significant morbidity/mortality rates, and appropriate treatment selection in a timely manner is crucial for optimal outcomes. 4D Flow MRI hemodynamic evaluation may help risk-stratify TBAD patients, but its use in daily practice is limited due to long scan times (~10-12 minutes). Further, the large dynamic velocity range exhibited by the true (TL) and false lumen (FL) may be incompletely characterized with a single-venc (SV) acquisition technique. We hypothesize that dual-venc (DV) acquisition which simultaneously acquires high-venc (HV) and low-venc (LV) data and uses HV data to unwrap LV can improve flow characterization in TBAD by improving velocity-to-noise ratio (VNR) while capturing the full range of TL and FL velocities. Here we investigate how compressed sensing (CS) accelerated 4D Flow MRI combined with DV technique impacts aorta hemodynamic quantification in TBAD.

Methods: Twelve TBAD patients (57.75 ± 7.04 years old; 5 F) and 2 healthy volunteers (28-year old M, 21-year old F) were prospectively recruited and scanned with prototype non-contrast and free-breathing CS-accelerated SV (R=7.7, venc = 160 cm/s, coronal orientation) and CS-accelerated DV (R=7.7, venc = 160 and 80 cm/s, sagittal oblique orientation) 4D Flow MRI scans on a 1.5T MRI system (MAGNETOM Sola, Siemens Healthcare, Germany) using ~ 2.6 x 2.6 x 2.8 mm³ spatial, 40 ms acquired temporal resolution and retrospective ECG-gating. HV data is used to unwrap LV data using Bayesian unwrapping. HV data from DV acquisition was also analyzed separately. TL and FL were manually segmented (fig. 1, Mimics, Materialise NV, Leuven, Belgium). Total kinetic energy (KE), mean voxel-wise forward flow (FF), and 5th percentile peak velocity (PV) were calculated over the entire volume through the cardiac cycle in TL and FL of the patients and in the entire aorta of the volunteers. Mean reverse flow (RF) and mean stasis were also compared in FL in the patient group. A follow-up scan was performed for all cases 5-10 days after the first scan and results of both scans were used for comparisons between acquisition types using repeated measures ANOVA method. VNR was calculated as the mean velocity in TL divided by the standard deviation of velocity noise derived from segmentation of the static spine in the patient group. Average scan times were also calculated.

Results: PV and FF in the TL did not show statistically significant difference in any pairwise comparison (p>0.05). Total TL KE did not show difference between SV and DV and between SV and HV acquisitions (p>0.05, fig. 2). Total KE was slightly higher in the HV compared to DV (p=0.041). In the FL, no parameter showed significant difference between SV and HV except stasis, which was higher in the SV (p=0.030). The KE, FF and RF were higher and stasis was lower in the SV compared to DV (p<0.05 for all) whereas PV did not show difference between these two acquisition types. All FL parameters except stasis were lower (p<0.05 for all), and stasis was higher (p=0.000) in the DV compared to HV (fig. 2). VNR in DV (mean: 3.8 ± 1.3) was significantly higher (p=0.000) than HV (mean: 2.8 ± 1.2). VNR in SV (mean: 2.7 ± 0.8) did not show difference from other acquisition types. Average scan time for SV and DV acquisitions were 5.13 ± 1.80 min and 5.96 ± 1.33 min respectively. Average scan time for regular 4D Flow MRI acquisition in the same cohort was 11.12 ± 2.64 min.

Discussion: In this study we demonstrate consistent results between CS accelerated SV and DV 4D flow MRI results in the TL. The low noise level of the LV data and corrected unaliased velocity levels of the HV data to obtain DV data significantly improved VNR which likely benefits low velocity flow features, specifically quantification of stasis and slow flow in the FL. In summary, these results support the feasibility and reliability of CS accelerated SV and DV 4D Flow MRI in TBAD, which, in both cases, reduce acquisition time relative to standard 4D flow.

References: 1. Jarvis. K., et al., J Mag Reson Imaging, 2020. 2. Ma, L.E., et al., Magn Reson Med, 2019. 3. Binter. C., et al., Magn Reason Med. 2013

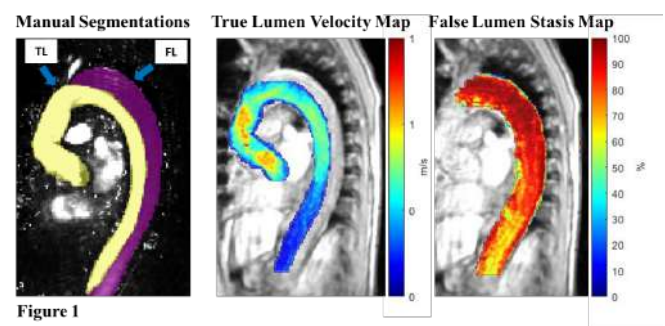
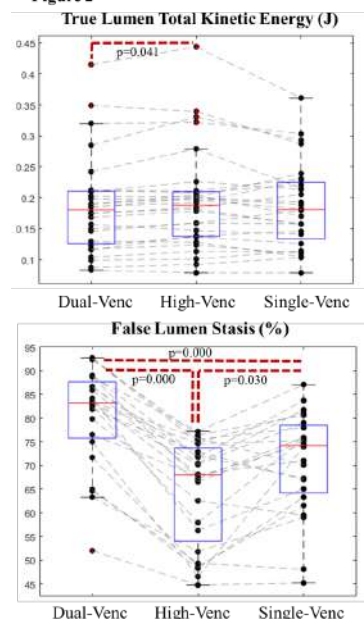


Figure 2



Exploration of age-related hemodynamic changes using an atlas based analysis of 4D Flow MRI. A preliminary study.

E. Piot¹, N. Duchateau^{1,2}, P. Douek^{1,3}, S. Boccacini³, M. Sigovan¹

¹ Univ Lyon, UCBL, INSA-Lyon, CNRS, Inserm, CREATIS UMR 5220, U1294, Lyon, France

² Institut Universitaire de France (IUF)

³ Department of Interventional Radiology and Cardio-vascular and Thoracic Diagnostic Imaging, HCL, Lyon, France

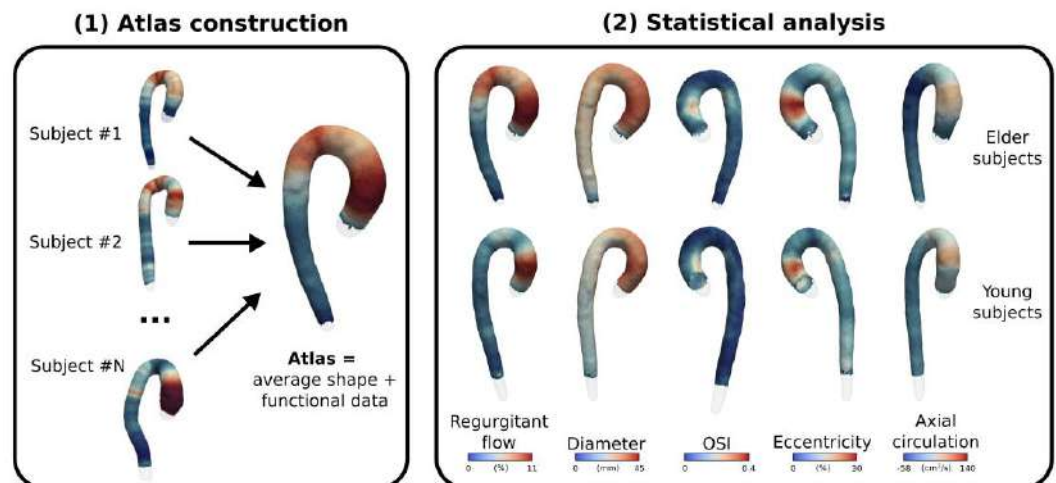
Purpose: 4D Flow MRI offers valuable hemodynamic information in individual subjects. Yet, understanding the hemodynamic involvement in a vascular pathology requires inter-subject comparisons that are not straightforward due to variability in terms of aorta morphology. Hemodynamic atlases can facilitate these comparisons and facilitate detection of intra-group characteristics. We propose here a workflow to create a hemodynamic atlas using 4D Flow MRI. We then explore age related differences in aorta hemodynamics using the proposed workflow.

Methods: 11 male subjects without any known cardiovascular pathology were included as follows: 6 in the young group (mean age = 28 ± 3 years) and 5 in the elder group (mean age = 55 ± 6 years).

Imaging was performed on a 1.5T system (Siemens Avanto) and included a retrospectively cardiac gated 4D Flow MRI Cartesian acquisition covering the thoracic aorta with TE=2.7 ms, TR=43 ms, FA=8°, VENC=120-180 cm/s, 2.3x2.3x2.8 mm voxel. An acceleration factor of 7.6 was used in combination with compressed-sensing reconstruction for an approximate acquisition time of 6 minutes.

4D Flow data was analyzed using a Matlab-based toolbox; briefly, time averaged PCMRA was semi-automatically segmented and then meshed. Several hemodynamic parameters were then computed using a finite element method [1].

Atlas creation: State-of-the-art atlas estimation software (Deformetrica, v.4.3.0) was used to estimate a reference shape for each subgroup and to define anatomical correspondences between each subject and this reference. Then, hemodynamic parameters for each subject were transported to this reference using the aforementioned anatomical correspondences. Finally, representative patterns were estimated for each subgroup by averaging the hemodynamic data of each subject aligned to the reference.



Results Examples of the computed morphological and hemodynamic atlases are displayed in the figure. Morphologically, the aorta presented overall larger diameters and higher curvature of the aortic arch in the elder group, while curvature of the ascending aorta was slightly lower. In the same region of increased curvature, flow disturbance appeared to be stronger, as demonstrated by increased regurgitant flow, OSI, and eccentricity. Flow eccentricity and area of increased OSI were also higher in the elder group in the ascending aorta.

Discussion: We presented here initial results of an atlas based method to investigate age-related changes in aorta shape and hemodynamics. Our results are in agreement with the recent study of Callaghan et al. [2]. While it was performed in a large population, the actual assessment of the parameters was done only at specific locations along the aorta. The atlas-based analysis allows much finer assessment of both shape and hemodynamic differences, up to each element of the reference aortic mesh. This type of analysis is expected to improve pathophysiological understanding of pathologies [3].

Funding: ANR-18-CE19-0025-01, Institut Universitaire de France.

References:

1. Sotelo J, Urbina J, Valverde I, et al (2016) IEEE Trans Med Imaging 35:1475–1487.
2. Callaghan FM, Bannon P, Barin E, et al (2019) J Magn Reson Imaging 49:90–100.
3. van Ooij P, Potters WV, Nederveen AJ, et al (2014) Magn Reson Med

Contrast-Enhanced CT Radiomics Improves the Prediction of Abdominal Aortic Aneurysm Progression

Yan Wang, Fei Xiong, Joseph Leach, Evan Kao, David Saloner, Dimitrios Mitsouras
Department of Radiology and Biomedical Imaging, University of California, San Francisco

Purpose: Clinical assessment of abdominal aortic aneurysm (AAA), primarily based on aneurysm diameter, has limited utility to predict rapidly progressing AAA. MRA methods can be used to measure AAA progression in patients who have had a baseline CECT study. Using that information, together with CECT follow-up studies radiomics models can be developed to identify features of the baseline imaging that are predictive of rapid growth.

Method: This longitudinal cohort study analyzed 195 consecutive patients (mean age, 72.4 years \pm 9.1, all male) with a baseline CECT and a subsequent CT or MR at least 6 months later. Radiomics features were measured for each of 3 regions of the AAA, viz. the vessel lumen only; the intraluminal thrombus (ILT) and aortic wall only; and the entire AAA (lumen, ILT and wall). Multiple machine learning (ML) models to predict rapid growth, defined as the upper tertile of observed growth (>0.25 cm/year), were developed using data from 60% of the patients. Prediction accuracy for the best model and maximum AAA diameter was compared using the area under the receiver operating characteristic curve (AUC) in the remaining 40% of patients. Figure 1 shows steps in radiomics analysis.

Results: The median AAA diameter was 3.9 cm (interquartile range [IQR], 3.3-4.4 cm) at baseline, and 4.4 cm (IQR, 3.7-5.4 cm) at the mean follow-up time of 3.2 ± 2.4 years (range, 0.5-9 years). A model using 7 radiomic features of the ILT and wall and a logistic regression classifier had the highest AUC (0.83, 95% confidence interval [CI]: 0.73 – 0.88) in the development cohort. In an independent test cohort, this radiomics-based model had statistically significantly higher AUC than clinical factors including maximum diameter^{1,2} (AUC = 0.67, 95% CI: 0.55 – 0.77, $P = .03$). Figure 2 shows the comparison of performance for the test set between the radiomics-based ML model and clinical characteristics-based models.

Conclusion: A radiomics-based method focused on the ILT and wall, improved prediction of rapid AAA growth from CECT imaging.

References: 1. Soden et al., J Vasc Surg. 2016. 2. Chaikof et al., J Vasc Surg. 2018.

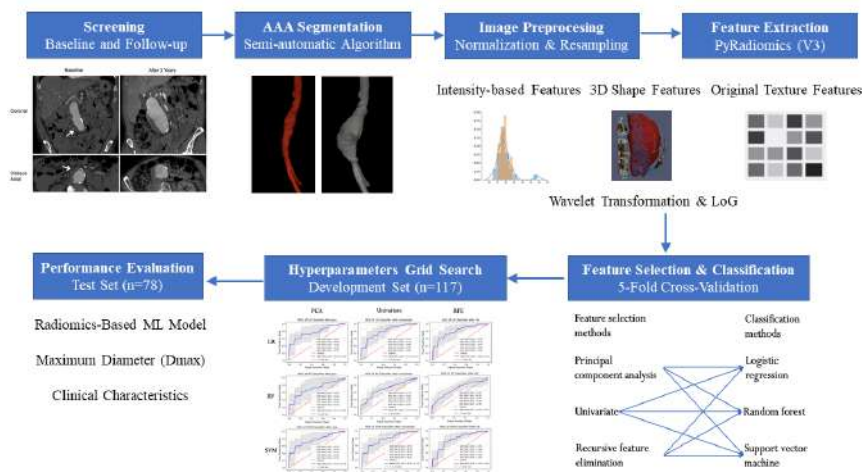


Figure 1: Steps in radiomics analysis starting from subject screening, semi-automatic AAA segmentation to define region-of-interest (ROI), image preprocessing and feature extraction, development of ML models with feature selection and classification algorithms on development set using 5-fold cross-validation, hyperparameters tuning based on Grid Search, and ROC performance comparison for the test set using the selected radiomics-based ML model, maximum diameter (Dmax) and clinical characteristics.

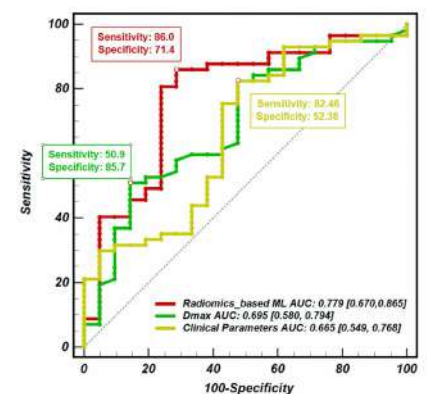


Figure 2: Comparison of ROC performance for the test set between the radiomics-based ML model with 7 features extracted from RBLOW, the maximum diameter (Dmax) and clinical characteristics-based models.

Evaluation of Aortic Stent Endoleaks Using Ferumoxytol Enhanced MR Angiography

Sipan Mathevosian MD^{1,2}; Yoshida Takegawa MD¹; Cameron Hassani MD¹; Mohammad Hassan Jalili MD¹; J. Paul Finn MD¹; Arash Bedayat MD¹

1. Department of Radiology, Division of Cardiovascular Imaging, UCLA Medical Center, David Geffen School of Medicine
2. Department of Radiology, Division of Interventional Radiology, UCLA Medical Center, David Geffen School of Medicine

Purpose:

To evaluate ferumoxytol enhanced magnetic resonance angiography (FE-MRA) for the detection of aortic stent endoleaks after endovascular aneurysm repair (EVAR).

Materials and Methods:

FE-MRA is accurate for pre-procedural aortic mapping for transcatheter aortic valve replacement and has been suggested as a sensitive method to detect endoleaks following EVAR. In this IRB-approved study, 20 patients with a history of chronic renal failure and abdominal aortic aneurysm status post EVAR, who required assessment for endoleaks were evaluated. Because of the patients' renal functional status, vascular enhancement was achieved via administration of intravenous ferumoxytol (avoiding the use of Gadolinium or Iodine-based contrast agents). 23 studies were performed in 20 patients using intravenous ferumoxytol (Feraheme, Covis Pharma, Luxembourg) pharmaceuticals – Waltham, MA), at a dose of 4 mg/kg. Any combination of chest, abdomen, and/or pelvis imaging in a single setting was regarded as a single imaging study. Examinations were performed on Siemens Prisma Fit 3.0 Tesla (n=10), TIM Trio 3.0 Tesla (n=4), Avanto 1.5 Tesla (n=6), Skyra 3.0 Tesla (n=2), or Vida 3.0 Tesla (n=1) MR scanners. Multiplanar pre- and post-contrast HASTE, T1 vibe, and high-resolution breath-held 3D MRA were acquired. Post processing included reconstruction of multiplanar images, MIP images and 3-D volume rendered images in OsiriX software (Pixmeo – Bernex, Switzerland) and Vitrea software (Vital Images – Minnetonka, MN).

Results:

All 23 FE-MRA examinations were technically successful and were diagnostic for vascular imaging evaluation. Endoleaks were successfully identified in 10 studies performed in 7 patients. The site of the endoleak was identified on early steady state imaging and no patients required delayed imaging for diagnosis. Type IA (n=3), type IB (n=2), and type II (n=5) endoleaks were identified. Type II endoleaks included retrograde filling from the inferior mesenteric artery and lumbar arteries. Furthermore, a single patient with three exams over nine months consistently demonstrated a stable large Type IA endoleak from the superior aspect of the endograft. No immediate or delayed adverse reactions were observed.

Discussion:

In patients with history of EVAR and chronic renal failure or allergy to intravenous Gadolinium-based or Iodine-based contrast agents, ferumoxytol enhanced MRA is a promising method of safe and effective evaluation of endoleaks.

Clinical importance statement:

Ferumoxytol enhanced MRA is sensitive and reliable technique for evaluation of endoleaks after endovascular aneurysm repair and can be used safely in patients with renal impairment of any severity.

References:

1. Hope MD, Hope TA, Zhu C, et al. Vascular Imaging With Ferumoxytol as a Contrast Agent. *AJR Am J Roentgenol.* 2015;205(3):W366–W373. doi:10.2214/AJR.15.14534.
2. Kim-Lien Nguyen, John M. Moriarty, Adam N. Plotnik, et al. Feasibility of Ferumoxytol MRA for Pre-TAVR Vascular Access Mapping in Patients with Renal Impairment: A Step Towards Patient-Specific Care. *Radiology* 2019 Dec;293(3):554-564.
3. Ichihashi S, et al. Preliminary experience with superparamagnetic iron oxide-enhanced dynamic magnetic resonance imaging and comparison with contrast enhanced CT in endoleak detection after endovascular aneurysm repair. *J Vasc Surg* 2013;58:66-72.
4. Nguyen KL, Yoshida T, Kathuria-Prakash N, et al. Multicenter Safety and Practice for Off-Label Diagnostic Use of Ferumoxytol in MRI. *Radiology.* 2019 Dec;293(3):554-564. doi:10.1148/radiol.2019190477. Epub 2019 Oct 22. PubMed PMID: 31638489; PubMed Central PMCID: PMC6884068.

Pulmonary Vasculature of Healthy and post-COVID subjects using Free-Breathing Time-SLIP 3D UTE

V Malis,¹ J Kungsamutr,² W Bae,^{1,3} Y Kassai,⁴ A. Yen,¹ Y Ohno,⁵ M Miyazaki¹

1. Dept. of Radiology, University of California-San Diego (UCSD), La Jolla, CA 2. Dept. of Bioengineering, University of California-San Diego (UCSD), La Jolla, CA 3. Dept. of Radiology, VA San Diego Healthcare System, San Diego, CA 4. Canon Medical Systems, Tochigi, Japan. 5. Fujita Health University, Aichi, Japan

Purpose: As of April 2022, over 489M people have suffered severe acute respiratory syndrome coronavirus 2 (SARS-CoV-2) disease, resulting in over 6M deaths [1]. Most healthy individuals recover within a few weeks, however up to 30% of people continue to have post-COVID-19 symptoms such as tiredness, cough, shortness of breath, headache, and joint discomfort, which are referred to as long COVID-19 symptoms [2]. MRI can make a valuable contribution in studying the impact of COVID-19 on lungs. Use of Ultra-short TE (UTE) imaging with TE of less than 0.1 ms allows visualization of lungs despite low proton density. The purpose of this study was to examine pulmonary vasculature of healthy and COVID-affected individuals.

Methods: Three healthy (38 ± 8 years) and two post-COVID (50 ± 8 years) subjects were examined on a clinical 3T scanner (Vantage Galan 3T, Canon Medical Systems, Japan) after obtaining IRB-approved written informed consent. Images were acquired using body SPEEDER and spine SPEEDER coils. The scanning protocol consisted of the following series: **(a)** 3D UTE without fat suppression (TE/TR = $96 \mu\text{s}/3.7$ ms, NEX = 1, FA = 5°); **(b)** 3D UTE with fat suppression: five SPectral Adiabatic Inversion Recovery (SPAIR) pulses per 64 segments were applied, resulting in approximately one SPAIR per 36 UTE lines (TI = 500, 1000, and 1500 ms, TR = 3.7 ms, TE = 0.096 ms, NEX = 1, FA = 5°) with a 5-cm wide Time-Spatial Labeling Inversion Pulse (Time-SLIP) applied on the heart. Sequence diagram and tag pulse position are shown in Figure 1A-C. Both study series were acquired during the expiratory phase and shared the same geometric parameters: coronal orientation, FOV = 40×40 cm, matrix size 256×256 . Image series (a) was utilized for the automated lungs segmentation using a set of morphological operations. The lung region from Time-SLIP 3D UTE images (b) was visualized after applying lungs mask from (a) by plotting Maximum Intensity Projections (MIP) for each of the TI.

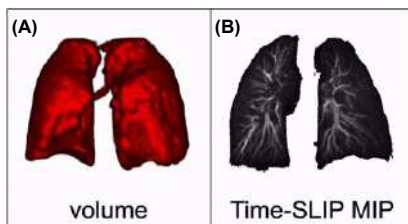


Figure 2. segmented lungs volume (A) and a Maximum intensity projection (B)

Results: Figure 3 demonstrates MIP images with changes in TI. Simplistic pulse sequence diagram is shown at the bottom. Note that the TI period is measured from the middle of the tag pulse to the start of read-out time. UTE acquisition window is about 950 ms and considering the contrast $T_{lc} = TI + 475$ ms. Resultant TI of 500 ms before the 3D UTE readout acquisition allows tagged blood to travel from the heart and reach pulmonary arteries and branches. At TI of 1500 ms, periphery regions of lung vessels are depicted. The TI periods of 500, 1000, 1500 ms are T_{lc} of 975, 1475, and 1975 ms, respectively.

Discussion: Both post-COVID-19 subjects have no symptoms but have frequent cough and shortness of breath. Chest angiography shows no irregularity. Non-contrast MR perfusion shows normal appearance of lung perfusion in healthy subjects and hypoperfusion area in post-COVID-19 subjects. Assessment with the non-contrast MR perfusion technique showed uniform high perfusion around $T_{lc} = 1475$ and 1975 ms amongst healthy subjects.

Conclusions: Free-breathing 3D UTE MR imaging techniques successfully provide visualization of pulmonary vasculature in post-COVID-19 adults. Future studies may focus on quantitative assessment of pulmonary vasculature to monitor lung functions during the post-COVID-19 recovery.

References:

- [1] <https://www.who.int/publications/m/item/weekly-epidemiological-update-on-covid-19---5-april-2022>
- [2] L. Huang *et al.*, *Lancet*. 398, 747–758 (2021).

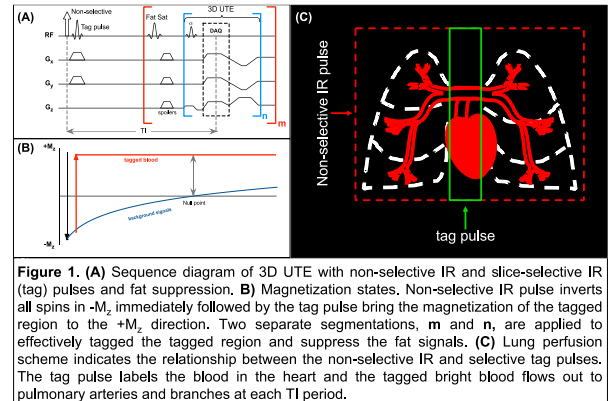


Figure 1. (A) Sequence diagram of 3D UTE with non-selective IR and slice-selective IR (tag) pulses and fat suppression. (B) Magnetization states. Non-selective IR pulse inverts all spins in $-M_z$ immediately followed by the tag pulse bring the magnetization of the tagged region to the $+M_z$ direction. Two separate segmentations, m and n , are applied to effectively tagged the tagged region and suppress the fat signals. (C) Lung perfusion scheme indicates the relationship between the non-selective IR and selective tag pulses. The tag pulse labels the blood in the heart and the tagged bright blood flows out to pulmonary arteries and branches at each TI period.

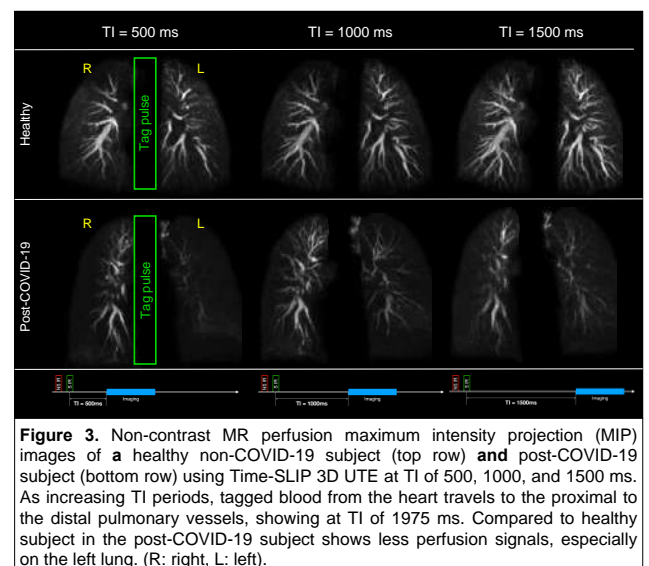


Figure 3. Non-contrast MR perfusion maximum intensity projection (MIP) images of a healthy non-COVID-19 subject (top row) and post-COVID-19 subject (bottom row) using Time-SLIP 3D UTE at TI of 500, 1000, and 1500 ms. As increasing TI periods, tagged blood from the heart travels to the proximal to the distal pulmonary vessels, showing at TI of 1975 ms. Compared to healthy subject in the post-COVID-19 subject shows less perfusion signals, especially on the left lung. (R: right, L: left).

Dual MR Cardiolymphangiography in Congenital Heart Disease – Initial Experience

Ashley E. Prosper¹, Takegawa Yoshida, MD¹; MD; Sanjay Sinha, MD^{2,3}; Aarti Luhar MD¹; Edward Lee, MD; Arash Bedayat, MD¹; Paul Finn, MD¹

¹ UCLA Dept. of Radiological Sciences, ² UCLA Dept. of Pediatric Cardiology, ³ Childrens Hospital of Orange County

Chylous pleural & pericardial effusions are a growing & potentially debilitating complication of treatment for pediatric congenital heart disease. Recently, dynamic MR lymphangiography (DMRL) with gadolinium based contrast agents (GBCA) has been used successfully for diagnosis & pre-procedural lymphatic pathway mapping. The relatively high dose of GBCA used for DMRL limits use of GBCA for simultaneous evaluation of vascular & cardiac anatomy, which would ideally be performed under a single anaesthesia session. We evaluated the feasibility of combining DMRL with high resolution 4-D cardiac & blood flow imaging using gadobutrol & ferumoxytol.

METHOD AND MATERIALS

In IRB-approved and HIPAA-compliant study, retrospective review of 9 DCMRL studies performed in 8 patients (age 3 mo-17 y at time of exam; mean 6 years 6 months; 4/9 studies performed in 3 M), following infusion of gadavist & ferumoxytol. Breath-held, high resolution, 3D SGE imaging was performed through the chest, abdomen & pelvis during intra-nodal infusion of dilute gadobutrol. Subsequently, ferumoxytol (Feraheme, AMAG Pharmaceuticals) was administered by slow IV infusion, total dose 4 mg/kg. 4-D MUSIC was acquired during uninterrupted positive pressure ventilation. Supplemental 4-D flow imaging was performed in 6/9 exams. Following 6/9 exams, patients were transported to the cath lab immediately after MRI. 3D processing of DMRL images was performed using MPR, MIP & VR reconstructions. Image processing of 4D MUSIC images was performed on MacOsiriX & Vitrea (Canon Medical) workstations. 4D flow was analyzed on the Arterys Cloud (Arterys.com). 3D DMRL & 4D MUSIC data was fused in 3 patients using Mimics (Materialize, Belgium).

RESULTS

All patients underwent technically successful DC-MRCL without adverse events. 100% of vascular segments were of diagnostic quality. Lymphatic imaging was satisfactory for lymphatic intervention planning in all exams. No additional imaging was required prior to a clinical management decision in any of the patients.

CONCLUSION

DC-MRCL is feasible in children with CHD under a single anesthesia session & informs management of both lymphatic & cardiovascular disorders.

CLINICAL RELEVANCE/APPLICATION

The use of dynamic 3D acquisitions for MR lymphangiography & 4D acquisitions for cardiovascular imaging restricts the total duration of the MR study to a predictable time window & facilitates planning for subsequent procedures in the catheter laboratory.

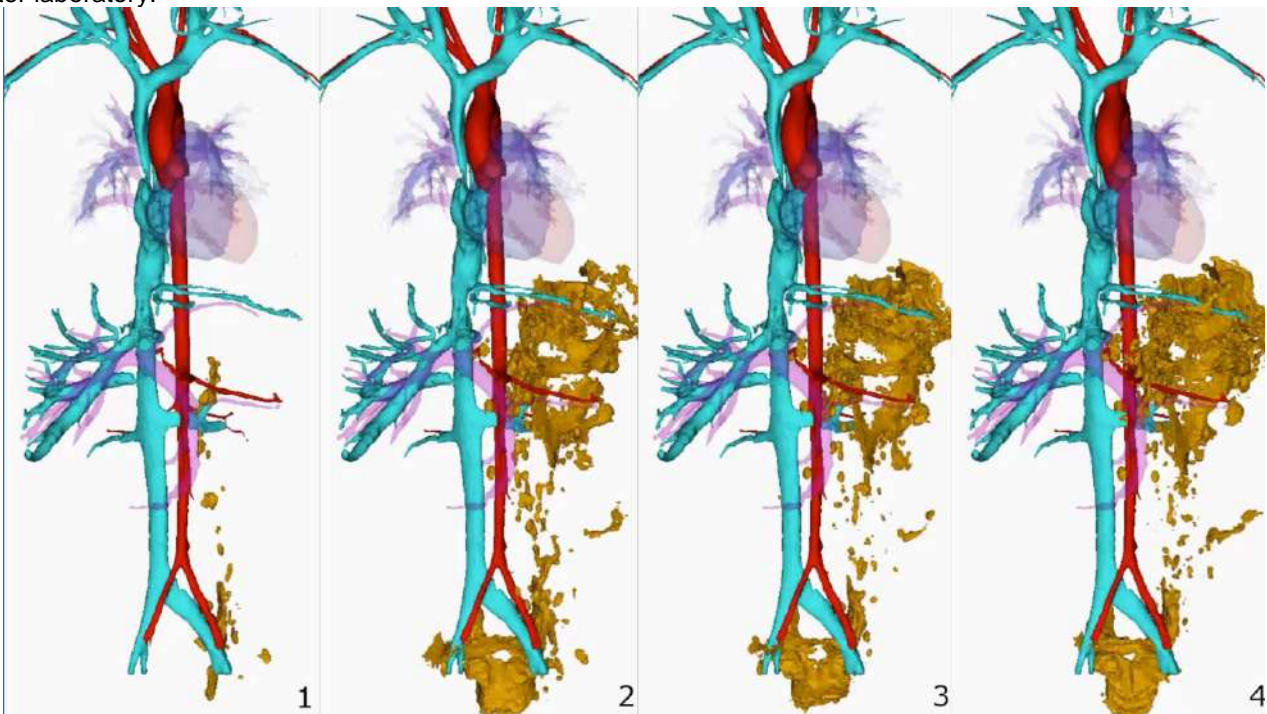


Figure 1: Time-resolved fused cardiolymphangiographic imaging in a patient with intestinal lymphangiectasia.

Motion-resolved motion-corrected reconstruction for ferumoxytol-enhanced free-running whole-heart MRI

Ludovica Romanin^{1,2}, Bastien Milani¹, Christopher W. Roy¹, Aurélien Bustin^{1,6,7}, Milan Prsa³, Tobias Rutz⁴, Estelle Tenisch¹, Matthias Stuber^{1,5}, Davide Piccini^{1,2}

¹Department of Diagnostic and Interventional Radiology, Lausanne University Hospital and University of Lausanne, Lausanne, Switzerland; ²Advanced Clinical Imaging Technology, Siemens Healthcare AG, Lausanne, Switzerland; ³Division of Pediatric Cardiology, Woman-Mother-Child Department, Lausanne University Hospital and University of Lausanne, Lausanne, Switzerland; ⁴Service of Cardiology, Heart and Vessel Department, Lausanne University Hospital and University of Lausanne, Lausanne, Switzerland; ⁵Center for Biomedical Imaging (CIBM), Lausanne, Switzerland; ⁶Université de Bordeaux, Centre de recherche Cardio-Thoracique de Bordeaux, INSERM U1045, France; ⁷IHU LIRYC, Electrophysiology and Heart Modeling Institute, Fondation Bordeaux Université, Pessac-Bordeaux, France.

Purpose: Ferumoxytol-enhanced whole-heart MRI is a potential game changer in the evaluation of congenital heart disease (CHD)¹. Owing to its high and uniform blood-pool signal, it allows for the use of free-running acquisitions², which enable ECG- and navigator-free scans, self-gated physiological signal extraction, and dynamic XD-GRASP reconstructions³. A computationally efficient, static reconstruction of free-running data can be obtained using a similarity-driven multi-dimensional binning algorithm (SIMBA)⁴ without making assumptions on the underlying physiology. In the original SIMBA technique, multiple bins are obtained but only one bin of motion-consistent data is automatically selected for image reconstruction, while the rest of the data is discarded. In this work, we propose to leverage data from additional bins by incorporating a non-rigid inter-bin motion-field registration into an existing XD-GRASP motion-resolved reconstruction framework, aiming to improve the final image quality.

Methods: Datasets from ten CHD patients (age range 1-60yo, 48±32kg, 7 males) were acquired on a 1.5T clinical MRI scanner (MAGNETOM Sola, Siemens Healthcare), after injection of ferumoxytol (2mg/kg) using a prototype free-running GRE sequence with a 3D radial phyllotaxis trajectory⁵. The original SIMBA reconstruction was applied as previously described⁴ to obtain a set of motion-consistent bins. Figure 1 illustrates the complete reconstruction pipeline. First, a 3D gridded reconstruction of the selected SIMBA bins is computed (A, B, C). Consequently (D), motion fields between adjacent bins (for the first bin the reference is the last bin) are estimated using a 3D non-rigid motion registration algorithm⁶. Finally (E), a motion-resolved (XD) motion-corrected (MC) reconstruction is performed by solving the following optimization problem:

$$\argmin_x \sum_{i=1}^K \|F^{(i)} C x^{(i)} - y^{(i)}\|_{Y^{(i)},2}^2 + \lambda \sum_{i=1}^K \|T_u^{(i)} x^{(i)} - x^{(i-1)}\|_{x,1}, \text{ where } F \text{ is the}$$

NUFFT, C the coil sensitivities, $x^{(i)}$ the image reconstructed from the bin i where cyclical motion was considered by setting $x^{(0)} = x^{(K)}$, $y^{(i)}$ the k-space data in the bin i , K the number of SIMBA bins taken ($K=4$), and $T_u^{(i)}$ the image deformation operator that applies the 3D non-rigid motion fields u from the image $x^{(i)}$ to the reference image $x^{(i-1)}$. The regularization parameter λ was experimentally optimized and was set to 0.3. The image obtained from the gridded reconstruction of the largest bin (SIMBA) was compared to the image from the same bin obtained after performing the motion-resolved motion-corrected reconstruction (XD-MC-SIMBA). Image analyses included computing the lung-liver and blood-myocardium interface sharpness, and the total visible length and sharpness of the first 2 cm of the right coronary artery (RCA) and the combined left main (LM) and left anterior descending coronary artery (LAD)⁷.

Results: Only the lung-liver sharpness was significantly higher for XD-MC-SIMBA compared to SIMBA (2.16 ± 0.81 vs 1.83 ± 0.56) ($P < 0.05$). The blood-myocardium sharpness (SIMBA: 2.00 ± 0.58 ; XD-MC-SIMBA: 2.11 ± 0.55) didn't show any statistically significant difference ($P = 0.51$). Both RCA and LM+LAD visible lengths were higher for XD-MC-SIMBA (RCA: 5.81 ± 3.64 cm; LM+LAD: 6.93 ± 2.82 cm) compared to SIMBA (RCA: 5.69 ± 3.59 cm; LM+LAD: 5.72 ± 2.09 cm), although not statistically significant ($P = 0.51$; $P = 0.09$). On average, the LM+LAD coronary sharpness was higher for SIMBA ($49.77 \pm 6.70\%$) compared to XD-MC-SIMBA (47.59 ± 5.14), while the RCA sharpness was slightly higher for XD-MC-SIMBA (36.83 ± 6.19) than SIMBA (36.61 ± 8.56). Both comparisons are not statistically significant (Figure 2).

Discussion: In this work we extended the original SIMBA framework into a 3D motion-resolved motion-corrected reconstruction where not only the data from one but from multiple motion-consistent data clusters are exploited by incorporating motion fields and XD-GRASP reconstruction. We plan to increase our patient cohort and further optimize the reconstruction parameters.

References: 1. Finn J.P. et al., Clin. Radiol 2016. 2. Di Sopra L. et al., MRM 2019. 4. Heerfordt J. et al., MRM 2021. 5. Piccini D. et al., MRM 2011. 6. Modat M. et al., Comput. Methods. Programs Biomed. 2010. 7. Etienne A. et al., MRM 2002.

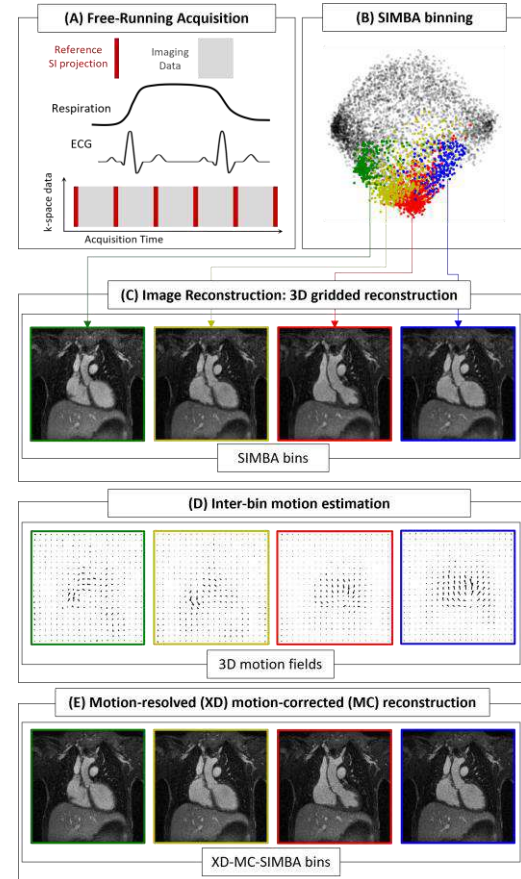


Figure 1. Reconstruction pipeline.

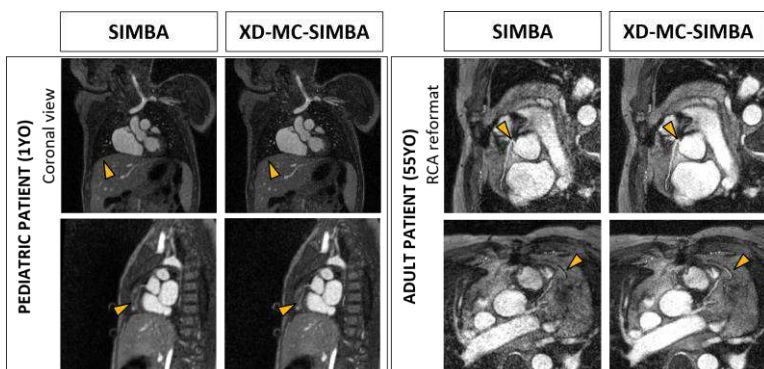


Figure 2. Coronal view and RCA reformat of a pediatric patient and multiplanar coronary reformats of an adult patient. The arrows indicate regions in which XD-MC-SIMBA resulted in increased sharpness or visibility.

Chronic thromboembolic pulmonary hypertension (CTEPH) patients show reduced right ventricular myocardial perfusion reserve (MPR)

Lexiaozi Fan¹, Daniel C. Lee¹, Brandon C. Benefield¹, Chris Malaisrie¹, Michael Cuttica¹, Li-Yueh Hsu², Bradley D. Allen¹, Daniel Schimmel¹, Ryan Avery¹, Benjamin H. Freed¹, Daniel Kim¹
¹Northwestern University Feinberg School of Medicine, Chicago, IL
²National Institutes of Health, Bethesda, MD

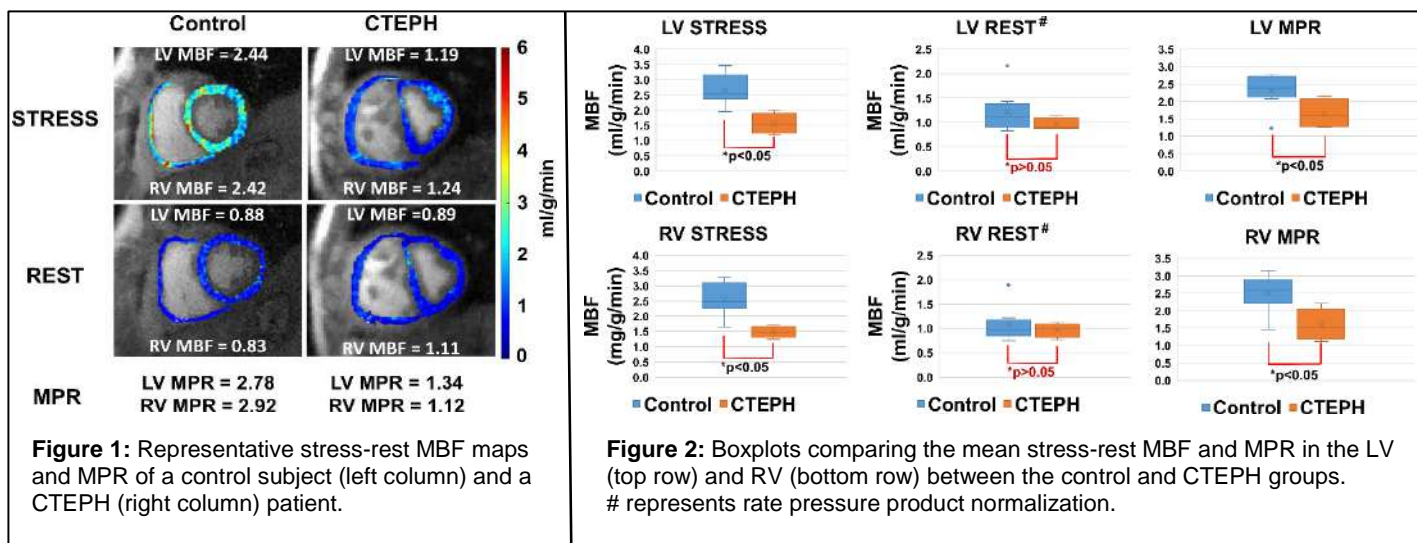
Purpose: Right ventricular (RV) perfusion reserve is understudied due to inadequate spatial resolution of conventional perfusion imaging modalities such as SPECT and PET. This study seeks to determine whether RV myocardial perfusion reserve (MPR) is reduced in patients with chronic thromboembolic pulmonary hypertension (CTEPH) compared to a control group using quantitative myocardial perfusion MRI.

Methods: We prospectively enrolled 4 CTEPH subjects (mean age = 55±14 years, 4/0 males/females) and performed stress-rest (10 min apart) protocol with 0.0075 mmol/kg of gadobutrol (Gd) using our 5-fold accelerated radial perfusion sequence [1]. As a control group, we retrospectively identified 8 subjects (mean age = 49±12 years, 5/3 males/females) with no evidence of vascular late gadolinium enhancement or perfusion defects who underwent an identical stress-rest protocol but using our 5-fold accelerated wideband Cartesian perfusion sequence [2]. Relevant imaging parameters included: 2 x 2 mm² spatial resolution, 8 mm slice thickness, 15° flip angle, 744 Hz/pixel receiver bandwidth, 100ms saturation recovery time, free-breathing, at least three short-axis planes per heartbeat. Both undersampled images were reconstructed using a compressed sensing [3] framework with temporal total variation and temporal principal component as two orthogonal sparsifying transforms with regularization weights optimized separately. The image processing steps included, motion correction [4], signal normalization by the proton density weighted image, signal to T1 conversion based on the Bloch equation with corresponding parameters used, T1 to gadolinium concentration conversion assuming fast water exchange, T2* correction to the arterial input function [5], gadolinium concentration to myocardial blood flow (MBF) conversion based on a Fermi model, rate pressure product (RPP) normalization for resting MBF, and MPR calculation as a ratio of mean stress and rest MBF. We did the abovementioned image processing steps in both the left ventricular (LV) and RV free walls. Two sample t-test was used to compare between the CTEPH and control groups, and paired t-test was used to compare between LV and RV per group.

Results: Figure 1 shows representative stress and rest MBF maps and the corresponding MPR values comparing a CTEPH patient and a control subject. Summarizing the results of all patients (Figure 2), compared to the control group, the CTEPH group had significantly (p<0.05) lower stress MBF (LV: 2.66±0.50 vs. 1.56±0.34 ml/g/min, RV: 2.56±0.53 vs. 1.48±0.19 ml/g/min) and MPR (LV: 2.32±0.50 vs. 1.65±0.43, RV: 2.50±0.53 vs. 1.59±0.46), but no significant differences (p>0.05) in rest MBF (LV: 1.21±0.43 vs. 0.96±0.12 ml/g/min, RV: 1.07±0.36 vs. 0.96±0.14 ml/g/min). Additionally, there were no significant differences (p>0.05) between LV and RV perfusion parameters within each group.

Discussion: This study demonstrates that it is feasible to quantify RV MPR using our pulse sequence and post-processing pipeline. To our knowledge, this work represents the first study quantifying pixel-by-pixel RV MBF maps and MPR using first-pass cardiac perfusion MRI. Furthermore, our results suggest that both LV and RV MPR are reduced in CTEPH patients compared with controls. Future studies include additional enrollment of CTEPH patients, determining the diagnostic and prognostic role of RV MPR, and evaluating the effects of surgical intervention on biventricular MPR.

References: [1] Naresh NK, et. al. Magn Reson Med 2019 [2] Hong K, et. al. Radiology: Cardiothoracic Imaging 2020 [3] Lustig M, et. al. Magn Reson Med 2007 [4] Benovoy M, , et. al. J Magn Reson Imaging 2017 [5] Fan L, et. al. Magn Reson Med 2021



SYNGO.VIA versus SYNGO.PLAZA regarding aortic diameters after therapy of aortic dissections

Manuela A. Aschauer, A. Kneidinger, I. Keeling, R. Neuwirth, M. Eibisberger, A. Yates, Medical University Graz

PURPOSE: Find possible differences between the two radiological systems "syngo via" and "syngo plaza" concerning the measurement of the aortic diameter from MRA pictures.

MATERIAL/METHODS: For the imaging follow ups 89 CE MRA (contrast enhanced magnetic resonance angiography) examinations were evaluated. The comparison of the two systems was conducted with bland - Altman diagrams. Data concerning any complications and necessary reinterventions or reoperations were collected.

RESULTS: The evaluation of 639 measuring points showed a highly significant difference between the two radiological systems regarding the measured aortic diameters ($p < 0,001$), especially at high aortic diameters. Because both systems need subjective correction and /or subjective line drawing it is necessary to store the final pictures with the measure points and lines for comparison. Furthermore, intervals of MRA follow ups in patients with uncomplicated type B dissection varied between patients according to their courses of disease. MRA is recommended and with no radiation and iodinated CM a better option as CTA especially in young patients as woman with dissection after delivery or men after accidents.

DISCUSSION: This study comparing two radiological systems, did not reveal a difference in accuracy or closeness to the real aortic diameter but recommended to measure MRA acquired diameters to make therapeutic decisions as watchful waiting, surgery or transfemoral intervention with stent planning. A traceable opportunity for saving is a "conditio sine qua non" but was withdrawn by the hospital. Double measurement of aortic diameters is not necessary, with MRA pictures it is reliable. Volumetry seems to be a better option for evaluating the whole aorta.

Literature: in case of interest send request to manuela.aschauer@medunigraz.at

Micro-Vascularity of the Feet and Toes Using Non-Contrast MRI

Won C. Bae,^{1,7} PhD; Vadim Malis,¹ PhD; Asako Yamamoto,² MD; Yoshimori Kassai,³ MS; Jun Isogai,⁴ MD; Katsumi Nakamura,⁵ MD; John Lane,⁶ MD; Mitsue Miyazaki,¹ PhD

1. Dept. of Radiology, University of California-San Diego (UCSD), La Jolla, CA. 2. Dept. of Radiology, Teikyo University, Tokyo Japan. 3. Canon Medical Systems, Tochigi, Japan. 4. Asahi General Hospital, Asahi, Chiba, Japan. 5. Kyoritsu Tobata Hospital, Kitakyusyu, Fukuoka, Japan. 6. Dept. of Surgery, UCSD, La Jolla, CA. 7. Dept. of Radiology, VA San Diego Healthcare System, San Diego, CA

Purpose: Non-contrast magnetic resonance (MR) evaluation of macro- and micro-vascularity in the foot of peripheral artery disease (PAD)¹ in diabetes with insufficient renal function is clinically essential. Existing contrast-enhanced MR has not been successful in distal foot due to inseparable arteries and veins due to fast turnover, and use of gadolinium contrast agents is contra-indicated in those with renal impairment. MR perfusion imaging based on arterial spin labeling has been used widely in the brain³ and other organs,⁴ but rarely in the foot. We sought to introduce novel applications of non-contrast MR technique for assessing macro- and micro-vascularity of the foot in human subjects.

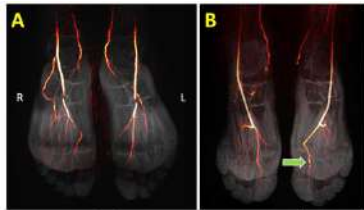


Figure 1. Macro-vascularity visualized with FBI technique in (A) healthy normal and (B) abnormal subjects. Images of blood vessels (colored) were fused with anatomic PD FS images for visualization. In a foot injury subject (B), a tortuous vessel can be seen (arrow).

Methods: All experiments were performed on a clinical 3T scanner using non-contrast MR angiography and perfusion. Eight subjects (19 to 64 years old, 5 males and 3 females) were enrolled in this study, including two abnormal subjects with diabetes and foot injury. Bilateral feet of the subjects were imaged in oblique coronal plane with centric ky-kz fresh blood imaging (cFBI) for visualizing macro-vascularity (**Fig.1**) and with tag-on and tag-off

alternating inversion recovery spin labeling (**Fig.2**) for determining perfusion in micro-vascularity. This was a flow-in technique using 3D single shot fast spin echo read-out that reduces issues with B_0 inhomogeneity and motion artifacts. Fig.2 shows flow-in sequences of tag-on and tag-off 3D acquisitions, which were subtracted and divided by tag-off image to determine signal increase ratio (SIR) at varying inversion times (TI) from 0.5 to 2 sec (**Fig.3**). SIR versus TI data were first fit to a gamma variate function⁵ and then

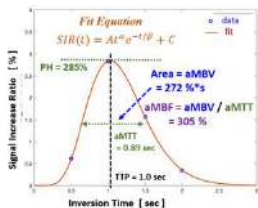


Figure 4. Time-resolved perfusion of SIR vs. TI.

empirically analyzed (**Fig.4**) to determine perfusion metrics of peak height (PH), time to peak (TTP), apparent mean transit time (aMTT), apparent muscle blood volume (aMBV) and apparent muscle blood flow (aMBF) in the 12 regions of interest including the left and right 5 toes and metatarsals. Additionally, voxel-wise colormaps were created to visualize the metrics (**Fig.5**).

Results: Using cFBI, we visualized morphology of large blood vessels in the foot (**Fig.1**). While no clinical assessment was performed, we noted a tortuous vessel in an injured foot of an abnormal subject (**Fig.1B**, arrow). Otherwise, all subjects had similar depiction of major foot arteries such as anterior and posterior tibial, and medial tarsal arteries. Using MR perfusion technique, SIR versus TI data (**Fig.4**) showed well-defined leading and trailing edges, with sharply increasing SIR to TI of ~1.25 sec subsiding quickly to near zero by TI of 2 sec. In six normal subjects, the mean \pm standard error values of PH, TTP, aMTT, aMBV, and aMBF were $492 \pm 12.3\%$, 1.10 ± 0.03 sec, 0.80 ± 0.01 sec, 479 ± 9.5 %*sec, and 425 ± 16.1 %, respectively. In abnormal subjects, we found a diminished PH ($402 \pm 21.2\%$, $p < 0.001$) and aMBV (380 ± 16.4 %*sec, $p < 0.001$). This difference was apparent in colormaps as well (**Fig.5**).

Conclusion: Feasibility of an MR perfusion imaging of the distal foot was demonstrated, showing consistency among normal subjects and potentially diminished perfusion in abnormal subjects. Compared to other non-contrast techniques such as QUIPSS⁶ and FAIR,⁷ our technique showed better-defined leading and trailing edges of the time-resolved signal, useful for facile quantification of perfusion metrics. Limitations of the study includes additional validation against reference measurement, long scan time (2 min for each TI), and small number of subjects. Future work will address these issues and also evaluate patients with PAD.

References: 1. WHO Media Center. 2. Huysman E et al. Acta Chir Belg 2009; 109:587-94. 3. Detre JA et al. Magn Reson Med 1992; 23:37-45. 4. Miyazaki M et al. Microvasc Res 2015; 98:94-101. 5. Chan AA et al. IEEE Biomed Imag 2004; 2:1067-70. 6. Wong EC et al. Magn Reson Med 1998; 39:702-8. 7. Kim SG et al. Magn Reson Med 1997; 37:425-35.

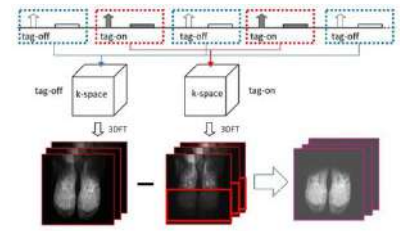


Figure 2. (A) Flow-in tag-on and tag-off acquisitions and (B) the subtraction method. The tag pulse is placed at the distal feet including toes. During the TI period, arterial blood flows into the tagged region.

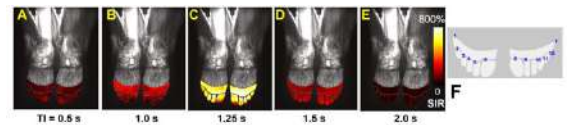


Figure 3. Color maps of Signal Increase Ratio (SIR) of a foot of a healthy male subject at inversion times (TI) of (A) 0.5, (B) 1.0, (C) 1.25, (D) 1.5, and (E) 2.0 sec. (F) shows a drawing of 12 regions of interest segmenting the right and left toes and the level of metatarsals.



Figure 5. Color maps of (A-C) peak height (PH, %) and (D-F) muscle blood flow (aMBF, %) in a healthy normal (A, D), an injured / disused (B, E), a diabetic (C, F) subject showing visual differences.

Using multi-contrast MRI histology to Characterize Plaque Composition in PAD for Endovascular Treatment Planning

K. Wilhoit¹, K. Sinha², C. Karmonik^{1,3}, T. Roy^{2,3}

¹Translational Imaging Center, Houston Methodist Research Institute, ²Department of Vascular Surgery, Houston Methodist Hospital, Houston, TX, USA, ³Weill Cornell Medical College, Houston, TX, USA

PURPOSE: A dedicated ultra-high field magnetic resonance imaging (MRI) histology protocol was developed on a clinical FDA-approved 7 Tesla human MRI scanner to characterize peripheral arterial lesion (PAD) composition with the goal to identify hard and soft components in-vivo. The latter is of importance for surgical treatment planning as soft lesions are more amenable to endovascular crossing and therefore treatment success [1].

METHODS: Acquisition: Amputated legs containing PAD lesions from six patients were collected immediately after amputation surgery. Legs were placed into a human 7 Tesla MRI scanner (MAGNETOM Terra, Siemens Healthineers, Erlangen, Germany). An 28 receive channel single-transmit knee coil was used to acquire images. This setup mimics the in-vivo setup used in a separate patient study and is therefore optimal for in-vivo MRI protocol development. **Scan Parameters:** The duration of the MRI examination was less than one hour which is considered tolerable in a clinical setting.

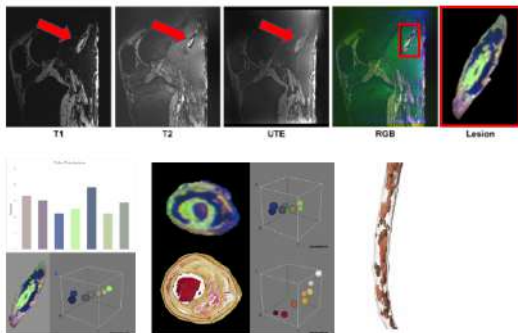


Figure 1: Top row: Sagittal view of different MRI contrasts (T1, T2 and UTE) combined into color (RGB) and lesion outlined. Bottom row: On left illustration of color reduction. Center: Comparison of MRI histology (top) with histological slice at same location (bottom). On right: 3D visualization of calcified tissue in the imaged artery segment.

The MRI protocol used UTE, T1-weighted and T2-weighted contrast with the following parameters: UTE (PETRA, FOV: 150 mm, phase FOV 100 %, in-plane resolution 0.2x0.2 mm, slice thickness: 0.22 mm, TR 10 ms, TE 0.07 ms, FA 4. T2-weighted (DESS, FOV 160 mm, phase FOV 87.5 %, slice thickness 0.2 mm, TR 12.57 ms, TE 6 ms, FA 25, water excitation, 512 slices). T1-weighted (T1-weighted: 3D FLASH, FOV 160 mm, phase FOV 87.6 %, in-plane resolution 0.2x0.2 mm, slice thickness 0.2 mm, TR 9.5 ms, TE 4.09 ms, FA 7, GRAPPA 2, phase encode direction A>>P, 512 slices, water excitation). **Analysis:** Image volumes were co-registered with the 3D Slicer software [2] using the General Registration module (with the options 'useMomentsAlign' and 'Rigid+Scale, 7 degrees of freedom'). The aligned volumes were exported in NIFTI format and after loaded into ImageJ [3], combined into an RGB stack. The plugin 'Color Inspector' was

then used to group pixels with similar color utilizing the built-in color quantizer. Each RGB stack was reduced to six color classes corresponding to background (excluded in the further analysis), calcified tissue (Ca), collagen (Col), other tissue (Oth), healthy wall (HW) and free lumen (Lu). The relative percentage for each tissue type was quantified. Dark color corresponding to image voids in the UTE sequence most likely attributed to calcified regions were visualized in 3D with the Paraview software. Preliminary comparison with histology slides obtained from the amputated legs were conducted.

RESULTS: Automated image registration was successful in all cases. The final color composites exhibited similar appearances (RGB) despite presence of image gradient which is common in ultra-high field MRI. Identifying the artery and lesion using manual outlining could readily be accomplished due to the high image contrast between the lesion and adjacent tissue. Comparing MRI histology slices and histology from excised lesion yielded good qualitative agreement (figure 1). Relative percentage of tissue types was similar for all samples. Average percentages were as follows: Ca 20±3 %, Col 21±6 %, HW 19±10 %, Oth 19±7% and Lu 21±5 %. Representative 3D visualization of calcified tissue demonstrated semi-circular to circular appearance (figure 1).

DISCUSSION: Multi-contrast imaging at ultra-high field seven Tesla MRI yields insight into PAD tissue composition comparable to histological slides. Lesion components were identified in combined color composites. Strong contrast between calcified tissue and other lesions components allowed 3D visualization of the distribution of hard plaque components. The here presented methodology may be useful for presurgical planning of endovascular procedures where knowledge of soft and hard plaque tissue may be essential to evaluate treatment options.

REFERENCES:

1. Roy T, Liu G, Shaikh N, Dueck AD, Wright GA. Puncturing Plaques. J Endovasc Ther. 2017 Feb;24(1):35-46.
2. Fedorov A, Beichel R, Kalpathy-Cramer J, Finet J, Fillion-Robin JC, Pujol S, Bauer C, Jennings D, Fennessy F, Sonka M, Buatti J, Aylward S, Miller JV, Pieper S, Kikinis R. 3D Slicer as an image computing platform for the Quantitative Imaging Network. Magn Reson Imaging. 2012 Nov;30(9):1323-41.
3. Schroeder AB, Dobson ETA, Rueden CT, Tomancak P, Jug F, Eliceiri KW. The ImageJ ecosystem: Open-source software for image visualization, processing, and analysis. Protein Sci. 2021 Jan;30(1):234-249.

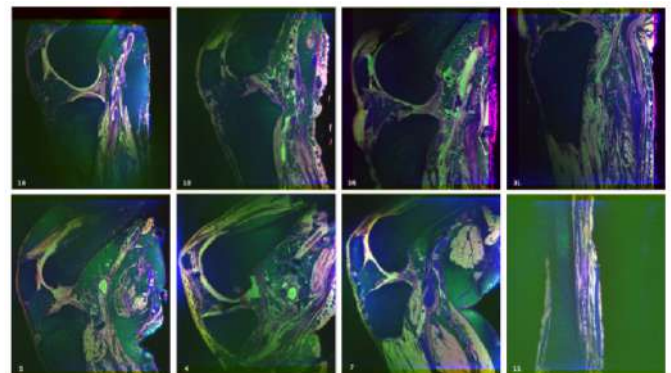


Figure 2: Sagittal representative color composite (RGB) slides for all cases.

Visualization of the Entire Portal and Hepatic Venous systems in a Single Acquisition with Ferumoxytol-Enhanced MRA

Amir Imanzadeh¹, Krishan R. Arora¹, Mohammad H. Jalili¹, Cameron Hassani¹, Arash Bedayat¹, J. Paul Finn¹

¹Department of Radiology, Division of Cardiovascular Imaging, David Geffen School of Medicine at University of California Los Angeles, Los Angeles, CA, USA

Purpose: With dynamic contrast enhancement as is typical with MR and CT, appropriate time windows to capture portal and hepatic venous filling are very different. Multiphase imaging with both CT and MR is therefore necessary and is frequently suboptimal for at least one territory. High-quality imaging, especially of the smaller terminal vessels, improves the diagnosis of portal hypertension, portal and hepatic venous thromboses, porto-systemic shunts, and vascular malformations (AVMs). We aimed to assess the visualization, diagnostic confidence, and presence of artifact in the portal and hepatic venous systems in patients who underwent ferumoxytol-enhanced steady-state MRA (FE-MRA).

Methods: We conducted an IRB-approved and HIPAA-compliant study of 20 consecutive patients (mean age = 62.5 years) who underwent breath-held 3D MRA of the abdomen during the steady state distribution of ferumoxytol, 4 mg /kg. One radiologist blinded to all clinical data scored the images. Overall image quality, visualization of the hepatic venous system and visualization of the portal system were each scored with a 5-point modified Likert image quality scale. Secondary and tertiary vessels were emphasized in scoring. A 5 represented high, uniform contrast and sharp vessel boundaries, and a 1 was non-diagnostic. Confidence in diagnosing vessel patency, stenosis, or occlusions was scored with a 3-point modified Likert image quality scale (3 = high confidence including smaller vessels, 1 = low confidence). Artifact due to motion, stents, devices, or embolization coils was scored with a 5-point modified Likert image quality scale (1 = none, 5 = severe).

Results: Image quality scores were excellent (4.5 ± 0.7) and visualization scores for the hepatic and portal systems were 4.6 ± 0.5 and 4.6 ± 1.3 respectively. Confidence in diagnosis of vessel patency, stenoses or occlusions was high (2.9 ± 0.3) and included smaller vessels (fig 1). Scores for artifact due to motion or hardware devices was low (1.5 ± 0.6).

Discussion: The entire portal and hepatic venous systems can be evaluated in a single breath-held 3D acquisition during the steady state distribution of ferumoxytol. Smaller, terminal vessels were routinely seen on FE-MRA. Future work will require comparison with gadolinium-based contrast agents. Because of its kinetics and relaxivity, ferumoxytol holds promise to become the new standard for imaging visceral venous anatomy.

References: Shahrouki P, Moriarty JM, Khan SN, et al.. J Cardiovasc Magn Reson. 2019 Mar 11;21(1):17.

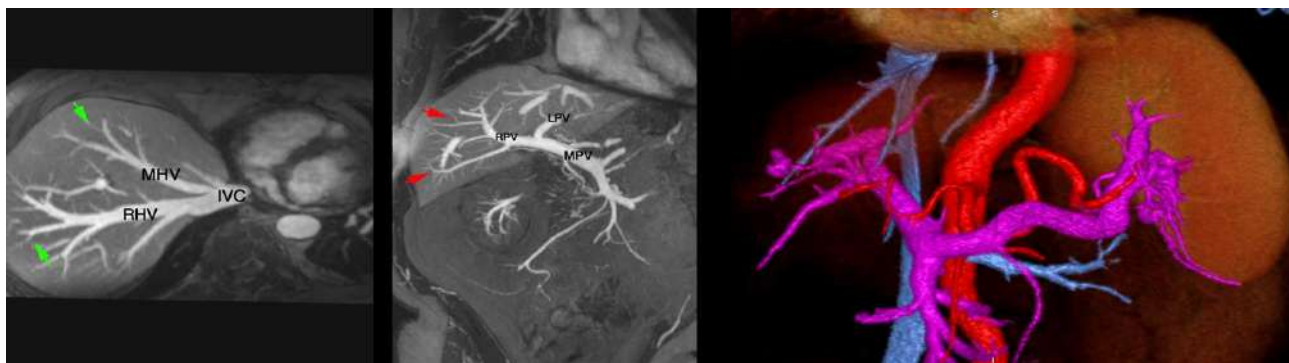


Figure 1. Thin MIP reconstructions of the hepatic (left) and portal venous systems. Note the high order HV tributaries and PV branches (arrows). Volume rendered reconstruction of the portal vein in a different patient in the right panel.

Retrospective Quantification of Clinical Multi-phasic DCE-MRI using a Pharmacokinetics-Informed Neural Network

Chaowei Wu^{1,2}, Nan Wang⁴, Srinivas Gaddam³, Hui Han¹, Stephen Pandol³, Anthony G. Christodoulou^{1,2}, Yibin Xie¹, Debiao Li^{1,2}

¹Biomedical Imaging Research Institute, Cedars-Sinai Medical Center, Los Angeles, CA, United States

²Department of Bioengineering, University of California, Los Angeles, California

³Division of Digestive and Liver Diseases, Cedars-Sinai Medical Center, Los Angeles, California

⁴Radiology Department, Stanford University, Stanford, California

Purpose

Pharmacokinetic modeling using quantitative dynamic contrast-enhanced (DCE) MRI may provide objective and absolute measurements for tissue perfusion and flow characterization. However, standard-of-care DCE-MRI is multi-phasic and has too limited temporal resolution for quantification. A recent method, Multitasking DCE-MRI^{1,2} provides quantitative measurements of high-temporal-resolution T1 values and pharmacokinetic parameters, but is not clinically available because it requires a custom sequence. In this study, we aimed to synthesize multi-phasic abdominal DCE-MRI from Multitasking DCE-MRI and retrospectively quantify it by improving temporal resolution via a pharmacokinetics-informed neural network.

Methods

Data Preparation: Thirty subjects, including sixteen healthy volunteers and fourteen patients with pathologically confirmed pancreatic ductal adenocarcinoma (PDAC) underwent Multitasking DCE-MRI scans to obtain dynamic T1 mapping at 2-sec temporal resolution. Scans were converted to GRE T1w signal (1) and downsampled based on clinical abdominal DCE-MRI protocol timings. The synthesized 2-sec temporal-resolution T1w signals and downsampled T1w signals served as label and input in training, respectively.

Network Design: A pharmacokinetics-informed neural network was constructed as shown in Fig.1. Multi-phasic input was converted into high-temporal resolution output by the upsampling block. To enforce data consistency, an extra penalty on known phases was applied. Later, the deconvolution block converted signal curves to three pharmacokinetic parameters K^{trans} , k_{ep} and v_e (Tofts model³). The output curve was enforced to be consistent with the model-reconstruction by imposing self-supervised loss. During inference, pharmacokinetic parameters were estimated from the network output by variable projection⁴.

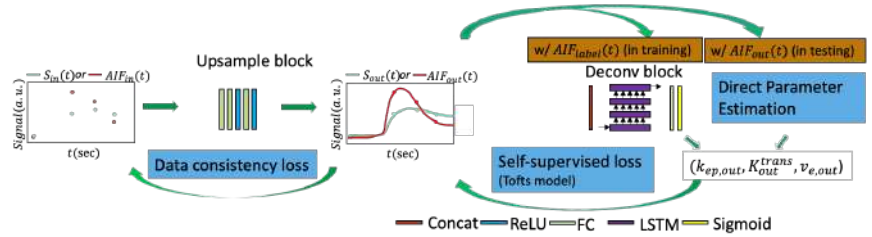


Figure 1 Pharmacokinetics-Informed Network Architecture

Results

Box plots in Fig. 2 showed that retrospective quantification found the same significant differences between tumor regions that were also present in the ground truth. The subgroup statistics against ground truth showed no significant differences in non-tumor and control. Significant differences were found for tumor, but the tumor contrast against the non-tumor area was not compromised. All three kinetic parameters K^{trans} , k_{ep} and v_e achieved 0.87~0.89 in ICC and R value. They also achieved 13.8%, 17.3% and 5.6% in coefficient of variation (CoV), respectively. Fig. 3 displays a representative example of retrospectively-quantified and ground-truth pharmacokinetic maps from a PDAC patient with marked ROI (yellow - benign cyst, red - tumor mass). It showed the delineation of proposed agreed with ground truth well. These findings showed that the retrospective parameters were comparable with the ground truth.

Discussions and Conclusion

This work demonstrated that quantification of clinical multiphasic DCE-MRI is possible by pharmacokinetics-informed deep learning. Future work will prospectively acquire MT-DCE and clinical multiphasic DCE images on the same subjects and validate the approach. If validated, this approach may serve as the estimation of tissue microvascular properties (e.x. permeability and blood flow), and can be applied in disease early detection, therapeutic effect evaluation, etc.

References

1. Christodoulou, AG, et al. *Nature biomedical engineering* 2.4 (2018): 215-226.
2. Wang, Nan, et al. *Magnetic resonance in medicine* 84.2 (2020): 928-948.
3. Tofts, Paul S., et al. *Magnetic resonance in medicine* 33.4 (1995): 564-568.
4. Golub, Gene H., et al. *SIAM Journal on numerical analysis* 10.2 (1973): 413-432.

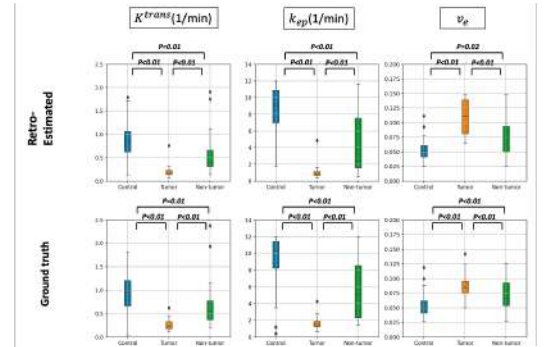


Figure 2 Box Plots of Control, Tumor and Non-tumor

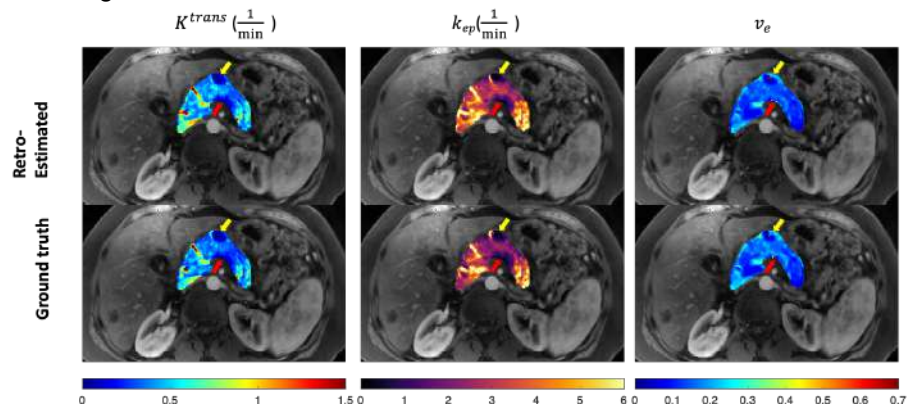


Figure 3 Representative Example from a PDAC Patient

Multi-slice Saturated Multi-delay Arterial Spin Labeling (MS-SAMURAI) Technique for Multiparametric Kidney MRI

Zihan Ning¹, Shuo Chen¹, Zhensen Chen², Hualu Han¹, Huiyu Qiao¹, and Xihai Zhao¹

¹ Center for Biomedical Imaging Research, Tsinghua University, Beijing, China ² Institute of Science and Technology for Brain-Inspired Intelligence, Fudan University, Shanghai, China

Purpose: Recent years, several studies attempted to evaluate kidney comprehensively by combining multiple MR parameters for early detection of kidney diseases, including renal blood flow (RBF) and T1-map reflecting function and structure characteristics respectively [1-3]. Our study group has developed a technique named SAMURAI (Saturated Multi-delay Arterial Spin Labeling) [4], which can simultaneously acquire RBF and T1-map of kidneys. However, the previous SAMURAI technique was only a 2D technique, while it can be time-consuming for large-coverage imaging. **In this study, we proposed a multi-slice SAMURAI (MS-SAMURAI) technique to achieve simultaneous acquisition of RBF and T1 map of whole kidneys with a 4-minute single scan.**

Methods: **Sequence** The MS-SAMURAI sequence consists of a pre-saturation pulse at imaging slice followed by Signal Targeting with Alternating Radio (STAR) pulses for ASL acquisition and multi-slice Look-Locker single-shot EPI readout with SPGR strategy (Fig 1). Six TIs of the multi-slice Look-Locker single-shot EPI sampling series were set as 0.3, 0.7, 1.1, 1.5, 1.9, 2.3 s (for the 1st slice). Other imaging parameters include: TE/TR 16/32ms, EPI factor 30, flip angle 31°, xbase duration 42ms, slice thickness 6mm, number of slice 6, in-plane resolution 3×3 mm², FOV 288×288 mm², 40 averages and scan time 4min 6s. A proton density image (to measure M0) was obtained with no inversion proceeding it. **Kinetic Model** The TIs of every slices were calculated based on the xbase duration. The kinetic model in the recommendation [5] was used to calculate RBF [Eq.1].

T1 mapping A dictionary searching-based method for T1 estimation was conducted. The dictionary was generated using simulation based on Bloch Equation. For dictionary generation, the T1 value was set to range from 100 to 3000ms with 5ms interval. The signal intensity of

the images of each TI was normalized by dividing the M0 image. The best match of T1 was found based on the minimum Euclidean distance between the simulated and experimental time courses. **In-vivo Experiments** Three healthy subjects (2 males, 24±2 years old) were recruited for MRI experiments with informed consent. The experiments were conducted on the same MR scanner with a 16-channel torso coil and a 12-channel posterior coil. The MS-SAMURAI sequence was acquired after a MRA scan for location. **Image Analysis** All analyses were performed on MATLAB (MathWorks, Natick). Before quantification, source images for every slice were registered first by a non-rigid principle component analysis-based (PCA-based) groupwise registration using Elastix [6] for respiratory motion correction. T1-map of MS-SAMURAI was obtained by above mentioned dictionary searching-based method. RBF was calculated based on Eq.1, with $\lambda=0.90$, $TI_1=3s$, $T_{1,blood}=1.65s$ and $\alpha=0.98$.

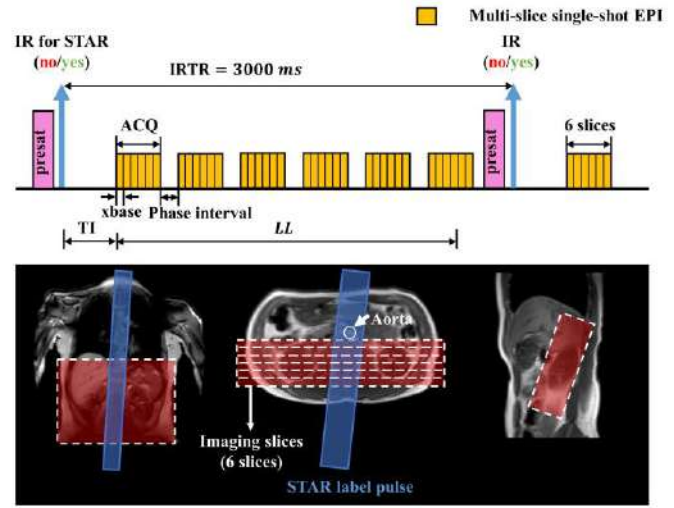


Fig 1. Sequence (a) and positioning (b) diagram of MS-SAMURAI.

$$RBF = \frac{6000 \cdot \lambda \cdot (SI_{control} - SI_{label}) \cdot \exp(TI/T_{1,blood})}{2 \cdot \alpha \cdot TI_1 \cdot SI_{M0}} \quad [Eq. 1]$$

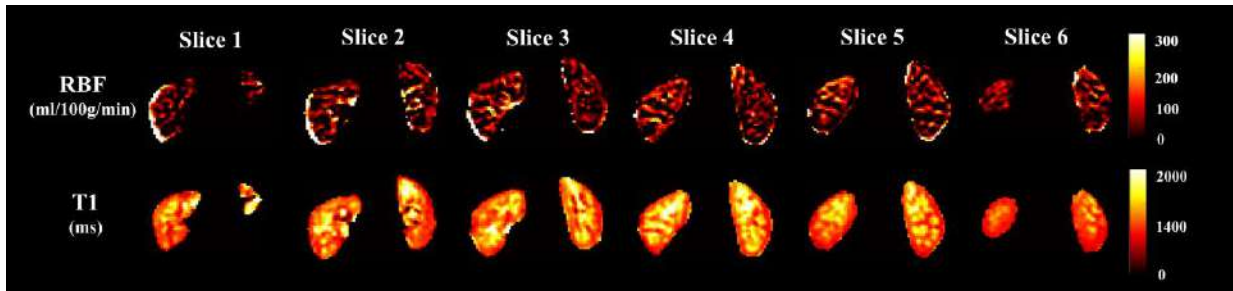


Fig 2. RBF map (first row) and T1 map (second row) obtained by MS-SAMURAI technique of one healthy subject (male, 24 years old).

Results: The proposed MS-SAMURAI technique provided T1 map and RBF map of the whole kidneys simultaneously with a 4-minute single scan (Fig.2). Compared with SAMURAI technique (4min 6s for one slice), the time efficiency of MS-SAMURAI (4min 6s for six slices) was highly improved.

Discussion and Conclusion: This study proposed the MS-SAMURAI technique for simultaneous acquisition of RBF and T1 map of the whole kidneys in 4-minute single scan.

References: [1] Cox EF, et al. Front Physiol 2017;8:696. [2] Shirvani S, et al. Eur Radiol 2019;29:232-40. [3] de Boer A, et al. J Magn Reson Imaging 2020;53:859-874. [4] Ning Z, et al. SMRA 2021. [5] Alsop DC, et al. Magn Reson Med 2015;73:102-16. [6] Klein S, et al. IEEE Trans Med Imaging 2010;29:196-205.

Dynamic assessment of regional peripheral perfusion and phosphocreatine with ¹H MRI in diabetes and peripheral arterial disease

Jie Zheng¹, Ryan Wahidi¹, Yi Zhang², Jiadi Xu³, Ran Li¹, Mary K Hastings¹, Mohamed A Zayed¹

¹ Washington University School of Medicine, Missouri, Saint Louis, USA

² Zhejiang University, Hangzhou, Zhejiang, China, ³ John Hopkins University, Baltimore, MD, USA

Purpose Both type 2 diabetes (T2D) and/or peripheral arterial disease (PAD) are associated with reduced peripheral perfusion and/or impaired cellular energetics [1-3]. The purpose of this study is to develop temporally and spatially resolved ¹H magnetic resonance imaging (MRI) techniques for dynamic assessment of skeletal muscle blood flow (SMBF) and phosphocreatine content (SMPCr), without any contrast injection and additional hardware.

Methods **SMPCr:** An MRI chemical exchange saturation transfer (CEST) imaging sequence was implemented at a 3T Prisma system (Siemens Healthcare, Erlangen, Germany) to measure SMPCr quantitatively. The sequence consisted of a continuous wave saturation module and a single-shot turbo-spin-echo readout. The imaging parameters were: TR/TE = 1870 ms / 7.1 ms, resolution = 2.9 x 2.9 x 8.0 mm³, saturation power/duration = 0.6 μ T/800 ms, 31 frequency offsets = 1.3 to 3.5 ppm, and acquisition time = 1 min. Quantification of SMPCr was performed by solving the Bloch-McConnell equation with a three-pool system: water, SMPCr, and magnetization transfer contrast (MTC).

SMBF: This perfusion quantity was dynamically measured using an established contrast free arterial spin labeling method. The SMBF sequence is a slice-selective and non-slice-selective inversion recovery pulse with single-shot gradient-echo acquisition. Other imaging parameters were: TR/TE = 4.0 msec/1.3 msec; fat saturation; resolution = 1.7 x 1.7 x 8 mm³; average number = 4, and acquisition time = 1 min.

Participants: Three groups of participants were recruited: healthy control or HC (age: 49-74y, n=7), T2D (age: 51-79y, n= 7), PAD (age: 53-70y, n=3). In the imaging session, participants were first scanned in their right calf area by utilizing a noncontrast 3D angiographic sequence to screen significant arterial stenosis. They were then instructed to perform a standardized plantar flexion isometric exercise for 4 minutes, followed by a 6-min recovery time. Region-of-interest (ROI) was drawn on medial gastrocnemius (MG) and soleus muscles on SMBF and SMPCr maps to obtain respective mean values.

Results None of participants in HC and T2D groups had significant peripheral arterial stenosis. **Figure 1** shows the examples of MR angiography, SMPCr maps, as well as time course of dynamic SMPCr and SMBF curves. **Table 1** shows quantitative parameters derived from SMPCr curves including SMPCr recovery time (τ_{SMPCr}) after exercise, and metabolic capacity (Q_{max}). Although none of them reach statistical significance, τ_{SMPCr} and Q_{max} demonstrate progressively increased and decreased values, respectively, from HC to T2D and then to PAD. Interestingly, T2D had the longest SMBF decay time, compared to HC and PAD, indicating vasoconstriction effect due to long-term hyperglycemia.

Conclusion

Feasibility of ¹H MRI for dynamical assessment of regional SMBF and SMPCr (mapping) is shown in healthy participants and participants with T2D and PAD. The quantitative outcomes in SMPCr agreed with other studies. To accelerate temporal resolution, deep learning methods are under development for both SMBF and SMPCr mapping techniques, aiming at 4- to 8- folder improvement.

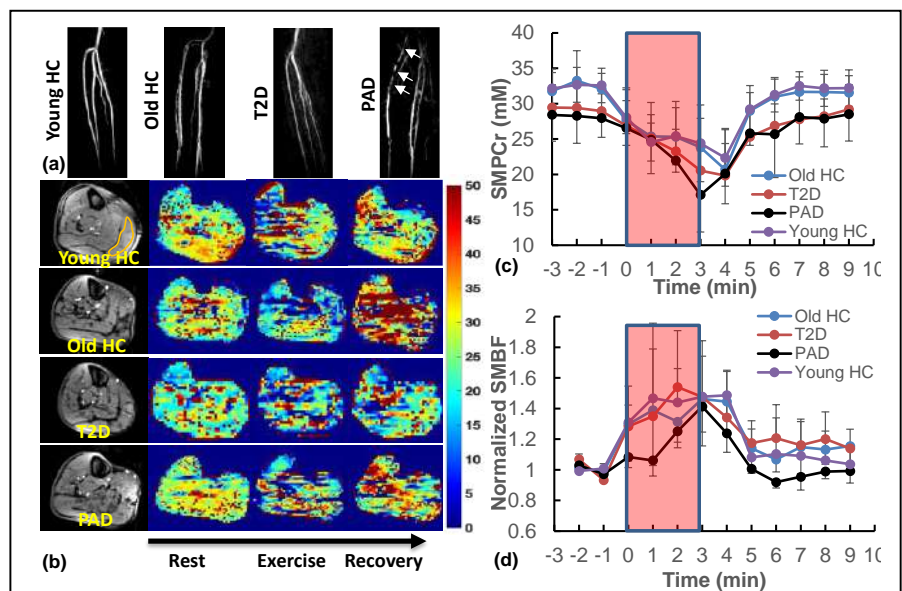


Figure 1. Representative MRA from 4 groups (arrows indicate stenosis in PAD)(a) and corresponding SMPCr maps along time course (orange ROI indicate MG region) (b). The dynamic averaged SMPCr curves (c) and normalized SMBF curves (d), all measured in MG muscle.

Table 1. Quantitative results in SMPCr mapping (* $P < 0.05$ vs Young HC)

Participants	SMPCr _{rest} (mM)	τ_{SMPCr} (min)	Q_{max} (mM/s)
Young HC (10)	32.4 \pm 2.5	0.81 \pm 0.53	0.93 \pm 0.52
Old HC (7)	32.3 \pm 2.6	1.22 \pm 0.38	0.48 \pm 0.15
T2D (7)	29.7 \pm 2.7	1.41 \pm 0.51	0.43 \pm 0.26*
PAD (3)	28.2 \pm 3.3	1.83 \pm 0.72*	0.29 \pm 0.12*

Screening for Polyvascular Diseases in ApoE-deficient Dogs and Diabetes Patients Using Ferumoxytol-Enhanced MR Angiography

Yuehong Liu¹, Bin Cao², Jiali Zhong³, Bin Sun⁴, Jidong Mi⁵, Zhenyu Li⁶, Ruchen Peng³, Dong Zhao², Ning Gu⁷, Qi Yang¹

¹Department of Radiology, Beijing Chaoyang Hospital, Capital Medical University, Beijing, China, ²Department of Endocrinology, Beijing Luhe Hospital, Capital Medical University, Beijing, China, ³Department of Radiology, Beijing Luhe Hospital, Capital Medical University, Beijing, China, ⁴Department of Radiology, Fujian Medical University Union Hospital, Fuzhou, China, ⁵Beijing Sinogene Biotechnology Co. Ltd, Beijing, China, ⁶Department of Radiology, Central Hospital Affiliated to Xinxiang Medical University, Xinxiang, China, ⁷Jiangsu Key Laboratory for Biomaterials and Devices, School of Biological Science and Medical Engineering, Southeast University, Jiangsu, China

Purpose: Atherosclerosis in two or more artery beds is known as polyvascular disease (PVD), and it has long been associated with a strong risk of cardiovascular events^[1]. However, the pathophysiology and optimal management of PVD remain unknown. Our understanding of PVD may be limited by the lack of a safe imaging strategy with high-resolution and a wide time-window to cover the scanning view of whole-body vessels. Ferumoxytol is a potent blood pool contrast agent, having an intravascular half-life of 10–15 h^[2]. Its steady distribution will be reached within 2-3 minutes of injection, allowing for the imaging of multiple vessel beds using a single-dose administration. We aim to investigate the feasibility of ferumoxytol-enhanced MR angiography (Fe-MRA) for screening PVD in the canine model developed for atherosclerosis, healthy volunteers, and patients with diabetes.

Methods: Institutional review board approval and informed consent were obtained for this study. We studied 10 beagle dogs (3 wild-type, 5 heterozygous ApoE mutants, and 2 homozygous mutants), 4 healthy volunteers, and 9 diabetes patients with chronic kidney disease (CKD). 3D FLASH examinations were performed with a 1.00-mm isotropic space resolution for dogs and human subjects on 3.0T MR scanners (MAGNETOM Skyra/Prisma Siemens Healthcare, uMR 780, United Imaging Healthcare) with 16/20/24-channel head-neck coils, 6/12/18-channel body coils, and 36-channel lower-limb coils. Ferumoxytol (Chia Tai Tianqing Pharmaceutical Group Co., Ltd., Jiangsu, China) was administered at a total dose of 4 mg/kg of iron for dogs and 3 mg/kg (determined by our prior dose-ranging work) for human subjects, and at a flow rate of approximately 0.07 mL/s. Five arterial beds, including intracranial arteries, cervical arteries, aorta, common iliac arteries (CIAs), and run-off arteries, were assessed. The signal-to-noise ratio (SNR), image quality score, the frequency of filling defects, and the frequency of $\geq 50\%$ stenosis on whole-body Fe-MRA images were evaluated.

Results: Ten dogs and 13 human subjects underwent Fe-MRA without adverse events. Fe-MRA scanning took 3 minutes on average. On the Fe-MRA images of healthy volunteers, the SNR were 184.6 ± 47.5 for intracranial and cervical arteries (20C coil), 159.7 ± 30.3 for aorta and CIA (18C coil), and 144.0 ± 25.6 for run-off arteries. The image quality score was 4 for 96% (48/50) of the arterial beds in dogs and for all arterial beds in human subjects. In the artery beds of wild-type dogs and healthy volunteers, there were no filling defects. Filling defects with $<50\%$ stenosis were found in one arterial bed of an ApoE (+/-) dog. The lesions with $\geq 50\%$ stenosis of CIAs and run-off arteries of ApoE (-/-) dogs were detected using Fe-MRA. In 9 diabetic patients, lesions with filling defects were detected in 91% (41/45) of arterial beds, with 34% (14/41) having a stenosis of over 50%.

Discussion and Conclusions: Ferumoxytol is a powerful agent with a stable vascular distribution that allows for whole-body MR vasculature imaging by a single-dose, excellently delineating arteries and veins. Our findings support the feasibility of whole-body Fe-MRA for quickly screening PVD in atherosclerosis canine models, which has been further investigated in diabetes and CKD patients with high risk of polyvascular atherosclerosis, suggesting that Fe-MRA could be useful for risk stratification in PVD. However, Fe-MRA is not more widely used due to off-label diagnostic use and a price point. Recently, the Chinese Food and Drug Administration approved ferumoxytol for clinical trials in MR diagnosis. This work is the first feasibility study of whole-body Fe-MRA in China. Additional work is required to systematically define its safety and efficacy for MR diagnosis.

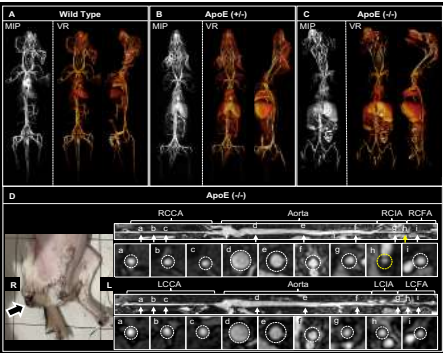


Fig 1. Whole-body FE-MRA (dose: 4mg/kg Fe) images of a wild type dog (A) and ApoE-deficient dogs (B and C). A significant stenosis in the right common iliac artery is depicted in curved-MPR FE-MRA images of a homozygous mutant dog with right lower extremities gangrene (D, yellow arrow).

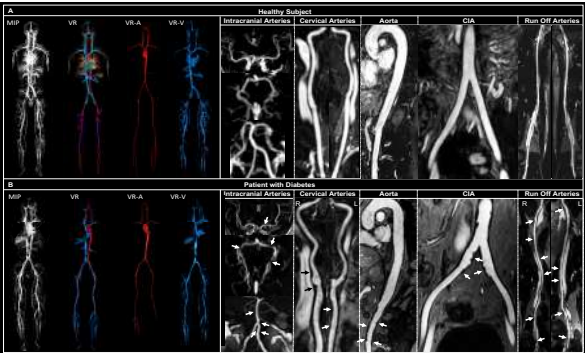


Fig 2. Whole-body FE-MRA (dose: 3mg/kg Fe) images of a healthy volunteer (A) and a patient with diabetes (B). In the FE-MRA images of the diabetes patient, there are multiple filling defects in more than 3 arterial beds (B, white arrows).

Table 1. Characteristics of canine models

	Wild Type (n=3)	ApoE (+/-) (n=5)	ApoE (-/-) (n=2)	P value
Age [†] , months	29.3 ± 6.1	23.7 ± 6.7	19.0 ± 5.0	0.300
Weight [†] , kg	14.7 ± 0.6	17.3 ± 2.2	10.5 ± 0.7	0.009*
Male, n (%)	3 (100)	3 (60)	2 (100)	0.667

[†] Mean values ± standard deviation.
* The mean weight of ApoE (+/-) dogs was significantly higher than that of ApoE (-/-) dogs (post-hoc test: P = 0.006).

Table 2. Clinical characteristics of healthy volunteers and diabetes patients

	Healthy Volunteers (n=4)	Diabetes Patients (n=9)	P value
Age [†] , y	30.8 ± 6.7	68.7 ± 5.8	< 0.001
Weight [†] , kg	71.7 ± 8.1	76.4 ± 13.0	0.520
Male, n (%)	4 (100)	7 (78)	0.538
eGFR [†] , mL/min/1.73m ²	NA	69.9 ± 18.7	NA
HbA1c [†] , (%)	NA	9.5 ± 1.6	NA
Hypertension, n (%)	0	6 (67)	NA

[†] Mean values ± standard deviation.

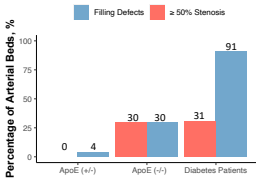


Fig 3. The percentage of arterial beds with filling defects and $\geq 50\%$ stenosis on Fe-MRA images in ApoE-deficient dogs and diabetes patients.

Using Quantitative MRI to Characterize Acute and Chronic DVT Clot Tissue at 9.4T

C. D. Jordan^{1,2}, K. Sinha², C. Karmonik^{2,3}, T. Roy^{2,3}

¹EnMed, Texas A&M University, Houston, TX, USA, ²Houston Methodist Hospital, Houston, TX, USA, ³Weill Cornell Medical College, Houston, TX, USA

PURPOSE: Deep venous thrombosis (DVT) is common¹ and growing in incidence with the COVID-19 pandemic². The mainstay of treatment for DVT is medical therapy with anticoagulation. More recently, mechanical thrombectomy, performed under X-ray fluoroscopy guidance, is used in some centers, and resulted in reduced acute symptoms, hospital stay, recurrent VTE and post-thrombolytic syndrome at 6 months, as compared to medical therapy alone³. Not all DVTs are amenable to mechanical thrombectomy and current devices are not effective for chronic DVT clots that have aged and organized with higher collagen content. There is currently no way of knowing the composition of clot in advance to determine if patients are good candidates for thrombectomy. MRI relaxation times, such as T_1 , T_2 , and T_2^* , could provide quantitative metrics, but there has been limited work done in distal extremity DVT, particularly at higher field strength. T_1 relaxation times have shown correlation to iron accumulating in venous thrombus as paramagnetic Fe^{3+} , and may predict the thrombus susceptibility to lysis⁴. T_2 relaxation times have shown correlation to spatial collagen structure in other tissues, such as articular cartilage⁵, which may be useful for DVT. R_2^* ($1/T_2^*$) has shown correlation with aging hematocrit of *in vitro* thrombus⁶. In this work, we assess the feasibility of T_1 mapping using rapid acquisition with relaxation enhancement (RARE), T_2 mapping using multi-slice multi-echo (MSME), and T_2^* mapping using multi-gradient echo (MGE) sequences on *ex vivo* DVT clots at 9.4T.

METHODS: Acquisition: Five patients with DVT (3F/2M, mean age 52.2 ± 18.3 years, mean BMI 30.1 ± 6.8) underwent a thrombectomy and the removed clot was scanned within 24 hours. IRB approval and informed consent were obtained. Images were acquired using a Bruker 9.4T Advance 400 scanner (Bruker Corp., Billerica, MA). One clot was split into two because it was too large. **Scan Parameters:** T_1 maps were acquired using a rapid acquisition with relaxation enhancement (RARE) sequence, and a parametric fit was performed on the scanner using a T_1 saturation recovery technique. T_2 maps were calculated from the multi-slice multi-echo (MSME), and T_2^* maps were obtained using a multi-gradient echo (MGE) sequence, both using a mono-exponential fit (Table 1). **Analysis:** Data analysis was performed in Matlab (R2022a, Mathworks, Natick, MA). A mask was created by thresholding magnitude images of the first echo of the MGE magnitude images. The mask for the T_1 maps was interpolated to fit its lower in-plane resolution, compared to the magnitude. For each map, mean and standard deviation over the entire volume were calculated.

RESULTS: The magnitude, T_1 , T_2 , and T_2^* maps are shown for an acute clot (Fig. 1A) and a chronic clot (Fig. 1B). Amongst the datasets, the mean T_1 was 1,396.3 ms for acute, and 1,340.8 ms for chronic clots. The mean T_2 was 69.9 ms for acute, and 84.0 ms for chronic clots. The mean T_2^* was 7.9 ms for acute, and 9.3 ms for chronic clots (Fig. 2, Table 2).

DISCUSSION: A prior study at 1.5T found an average of $T_1 = 843$ ms *in vivo* for patients with an acute DVT, and $T_1 = 1,317$ ms after 6 months⁷, which may be consistent with our *ex vivo* results at 9.4T, since T_1 is expected to increase with higher field strengths, and the different environment⁸. A prior study found R_2^* was $5\text{--}20\text{ s}^{-1}$ for acute, and $5\text{--}100\text{ s}^{-1}$ for chronic clot *in vitro* at 3T, corresponding to T_2^* of $5\text{--}200$ ms⁶, which may also be consistent with our results, since T_2^* is expected to shorten at higher field strengths. This dataset is very preliminary, since there are only five patients; however, this is an ongoing study. These initial results suggest that quantitative MRI of *ex vivo* DVT clots at high field strength is feasible, and may provide a reference for future DVT research.

REFERENCES: [1] SM Bates et al. *Chest* **141**, e351S-e418S (2012). [2] G Avruscio et al. *Transl. Sci.* **13**, 1108–1114 (2020). [3] M Sharifi et al. *Cardiovasc. Interv.* **76**, 316–325 (2010). [4] P Saha et al. *Circulation* **128**, 729–736 (2013). [5] MT Nieminen et al. *Magn. Reson. Med.* **46**, 487–493 (2001). [6] SD Christiansen et al. *J. Neurointerv. Surg.* **11**, 1155–1161 (2019). [7] U Blume et al. *Magn. Reson. Mater. Physics, Biol. Med.* **22**, 375–383 (2009). [8] PA Bottomley et al. *Med. Phys.* **11**, 425–48 (1984).

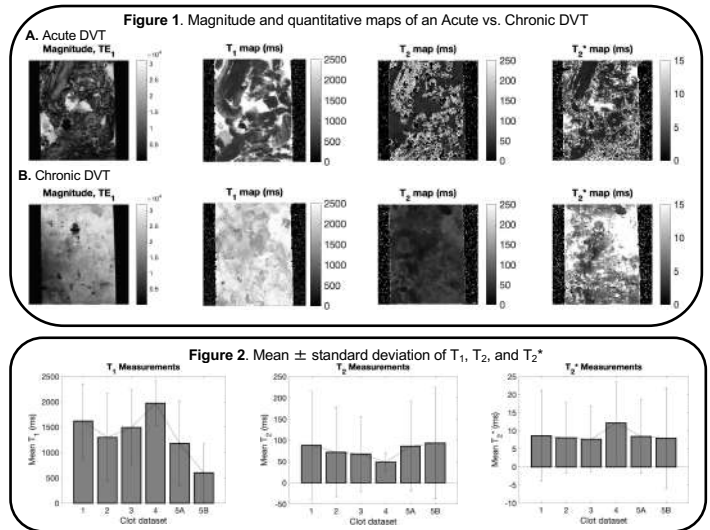


Table 1: Scan Parameters					
Sequence	Parameter	TE (ms)	TR (ms)	FA (°)	Resolution (mm ³)
RARE	T1	6.5	5500	90	0.078 × 0.104 × 1.0
MSME	T2	[7, 14, ..., 210]	3308.1	90	0.078 × 0.078 × 1.0
MGE	T2*	[3, 7, ..., 39]	800	50	0.078 × 0.078 × 1.0

Table 2: Quantitative MRI Results					
Clot	Prep	Clot age	Clot retrieved?	T ₁ (ms)	T ₂ (ms)
1	fresh	chronic	Limited	1,618.2 ± 738.2	88.3 ± 127.3
2	fresh	subacute	Yes	1,298.6 ± 869.6	72.0 ± 104.9
3	fixed	acute	Yes	1,494.0 ± 745.4	67.8 ± 88.3
4	fixed	chronic	Yes	1,972.2 ± 441.2	48.6 ± 22.0
5A	fresh	chronic	Yes	1,175.5 ± 846.4	105.9 ± 85.9
5B				597.2 ± 574.1	93.2 ± 131.5

Calibration of Plaque to Myocardium Ratio in T1-weighted Coronary Plaque Imaging

Meng Lu¹, Hui Han, PhD¹, Debiao Li, PhD^{1,2}, Yibin Xie, PhD¹

1. Biomedical Imaging Research Institute, Cedars-Sinai Medical Center, Los Angeles, CA, United States

2. Department of Bioengineering, University of California Los Angeles, Los Angeles, CA, United States

Purpose

Early identification of vulnerable coronary plaque is important for risk-stratify coronary heart disease. Plaque to Myocardium Ratio (PMR) has proven its effectiveness as a biomarker for the evaluation of high-risk coronary plaque in the previous studies^{1,2,3}. However, PMR is based on relative signal intensities and can be sensitive to variations in physiological and acquisition conditions. In this study, we aim to explore the impact of heart rate, flip angle, and the number of readout segments on PMR measurements. Further, we propose a computational modeling method to calibrate PMR under different scanning conditions.

Methods

Bloch equation simulations: The Simulation, based on the Bloch equation, was performed on MATLAB 2016b (MathWorks, Natick, MA). Inversion recovery prepared spoiled gradient-echo readout (IR-FLASH) sequence was used to prepare T1 weighted signal. PMR's variation is tested by implementing change on three parameters: 1) heart rate (HR) between 40 to 78 beats/min; 2) the number of readout segments (SEG) between 15 to 50, and 3) readout flip angle (FA) between 10° to 20°. Three targeted tissue types were included in the simulations with corresponding literature T1 values at 3T (blood of 1650 ms; myocardium of 1229 ms, and plaque with various T1 ranging from 500 ms to 1700ms)^{4,5}.

Computational modeling and application for PMR calibration: An application was developed in Python based on the simulation result and computational model. It converts PMR measurement from different sequence parameters and physiological conditions to a preset standardized condition.

Phantom and in vivo studies: A series T1 phantom with the range from 367.46 ms to 1767.5 ms was constructed with various concentrations of nickel chloride to mimic coronary plaque. The phantom was placed between the legs of a healthy volunteer to allow the use of calf muscle to mimic a myocardium reference (**Figure 1**). A total of 34 scans were acquired under various conditions similar to the Bloch simulation. Inversion time was set to 600 ms^{6,7}. PMR was measured by dividing the mean intensity of ROI in each tube by the mean intensity of adjacent calf muscle reference. The measured PMR was then calibrated with the proposed numerical model. Pearson's correlation and Bland-Altman analyses were used for comparing uncalibrated and calibrated PMR with the standard PMR.

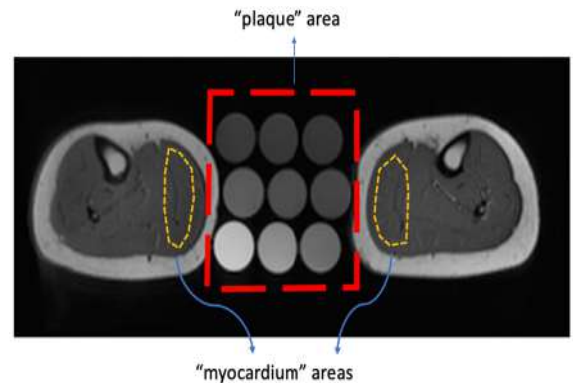


Figure 1 Phantom setup schematic

Results

Simulation: The simulation result shows relationships between PMR and scanning parameters were nonlinear but monotonal (**Figure 2**). All three scan condition variables (FA, HR, and SEG) inversely affected PMR when plaque T1 was shorter than myocardium T1. Vice versa when plaque T1 is longer than myocardium T1, with HR variations having a more substantial impact than other parameters.

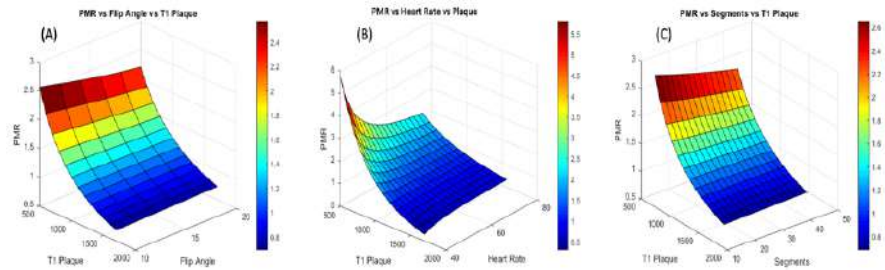


Figure 2 the variations of PMR depending on different plaque T1, FA (2.A), HR (2.B) and SEG (2.C) combinations.

Phantom study: **Table 1** summarizes the statistical results of Heart rate by comparing calibrated and uncalibrated PMR measurements against the reference. Heart rate variations have the largest impact among all parameters investigated.

Discussion

Overall, calibrated PMR measurements have better agreement compared with the uncalibrated ones against the standard reference. Among the three evaluated scan variables, heart rate has the most impact on PMR. Coil sensitivity variation was an important confounding factor that necessitated normalization (unpublished data). In conclusion, the proposed calibration method significantly reduced measurement variations of PMR in T1 imaging due to differences in heart rate and scan parameters.

References

- [1] Ehara et al., Eu heart., 2012.
- [2] Noguchi et al., JACC., 2014.
- [3] Noguchi et al., JACC 2015.
- [4] Stanisiz et al.,JMRM 2005.
- [5] Roy et al., JCMR 2017.
- [6] Hosoda et al., JCMR 2020.
- [7] Asaumi et al., JACC 2015.

Table 1 Calibration performance for heart rate

COMPARISON METRIC	Uncalibrated PMR vs True PMR	Calibrated PMR vs True PMR	p-Value
MEAN PERCENTAGE ERROR	8% (0%-50%)	3% (0%-13%)	<0.0001
PEARSON'S COEFFICIENT	0.9643	0.9951	N/A
LIMITS OF AGREEMENT	-0.45/0.48	-0.17/0.11	N/A

Contrast Enhanced MRV in the Evaluation of Cryptogenic Stroke using Gadobenate Dimeglumine

Purpose: Magnetic resonance venography (MRV) of the pelvic venous system is utilized to evaluate for a source of emboli in patients with cryptogenic stroke and the presence of a patent foramen of ovale (PFO). Because of the tortuosity of the pelvic veins and the presence of valves, flow artifacts due to turbulence are common and can simulate a clot on standard 2D time-of-flight (2DTOF) sequences and overestimate DVT of pelvis. These artifacts are greatly diminished with contrast enhanced MRV (CEMRV) with the intravascular agent, gadofosveset trisodium, reducing the rate of studies with positive DVT from 20% to 6%. Although ideally suited for pelvic DVT work-up because of its long intravascular half-life, gadofosveset trisodium was taken off the market in 2017 due to poor sales. Of the remaining commercially available gadolinium-based contrast agents, gadobenate dimeglumine (Multihance) having excellent T1 relaxivity and a prolonged intravascular phase was selected to replace gadofosveset trisodium in the evaluation of pelvic DVT in our practice. The goal of this study was to determine if the CEMRV with Multihance is an efficacious replacement of gadofosveset in evaluation of the pelvic DVT.

Methods: Retrospective review of consecutive pelvic MRV studies was performed from 2018 to 2021. Only patients with acute CVA, right to left shunt by echocardiogram and negative Doppler ultrasound evidence of lower extremity DVT were included in the study. Studies were performed using a 1.5 Tesla magnet using body surface coils. MRV was performed within 72 hours of onset of symptoms. CEMRV was performed 5 minutes following an intravenous dose of 0.02 mmol/kg of Multihance using an axial fast 3D TOF sequence (TR = 4.8msec, TE = 2.4 msec, FA = 10 degrees; 4 mm thick sections interpolated to 2mm) in the axial plane. Intravascular signal of the pelvic veins was characterized as adequate or inadequate. On the CEMRV any non-enhancing filling defect was considered positive for a thrombus.

Results: A total 146 patients met inclusion criteria (age range = 22 – 81 years; mean age = 43 years) and underwent a CEMRV study. The intravascular signal of the pelvic venous system was rated as adequate in all 146 studies. On the CEMRV, a total of 9/146 (6.2%) patients had positive filling defects in the following distribution: left external iliac vein (n=2), left internal iliac vein (n=1), left common iliac vein (n=1), right common iliac vein (n=2), right common femoral vein (n=1), left common femoral vein (n=1) and left deep femoral vein (n=1).

Discussion: CEMRV is utilized to noninvasively to evaluate the pelvic venous system in patients with cryptogenic stroke. A DVT diagnosis implicates future embolic events requiring long-term anticoagulation therapy and therefore is a critical component of patient care. CEMRV with intravenous Multihance showed excellent steady-state signal characteristics in the pelvic venous system and was positive in 5% of studies. This incidence rate is similar to that previous found with the dedicated intravascular agent gadofosveset trisodium at our institution. Our results suggest that Multihance is a suitable replacement for gadofosveset in the workup of pelvic DVT.

References:

Cramer SC, Maki JH, Waitches GM, D'Souza N, Grotta JC, Burgin WS, Kramer LA. Paradoxical emboli from calf and pelvic veins in cryptogenic stroke. *J Neuroimaging* 2003;13(3):218-223.

Kramer LA, Cohen AM, Hasan KM, Heimbigner JH, Barreto AD, Brod SA, Narayana PA, Wolinsky JS. Contrast enhanced MR venography with gadofosveset trisodium: evaluation of the intracranial and extracranial venous system. *J Magn Reson Imaging* 2014;40(3):630-640. doi: 10.1002/jmri.2440

Scott Thompson, MD, Ph.D.¹; Ahmed Negm²; Erica Knavel, MD³; Emily Bendel, MD¹; Jeremy D. Collins, MD²
Department of Radiology, Divisions of Interventional Radiology¹ and Cardiovascular Imaging², Mayo Clinic, Rochester, Minnesota, USA; Department of Radiology, Section of Interventional Radiology, University of Wisconsin, Madison³

Synopsis: MR Lymphangiography (MRL) is a useful diagnostic imaging adjunct to conventional lymphangiography (CL). Abdominopelvic and Thoracic MRL can be performed via ultrasound-guided nodal access or via transdermal injection via the feet. When suitable inguinal lymph nodes are not present or in patients with prior CLs via nodal access peripheral MRL is a favored diagnostic approach. Peripheral MRL also enables assessment of thigh and calf lymphatics in suspected lower extremity lymphedema. This educational exhibit will detail the experience to date integrating peripheral MRL into the hybrid procedural suite with a 1.5T magnet at the Mayo Clinic in Rochester, MN

Objectives:

1. MR Hybrid procedural suite configuration, ultrasound integration, and use of anesthesiology for MRL.
2. Review the anatomy of the lower extremity lymphatic channels, known variations.
3. Review the method for injection of dilute gadolinium contrast into different regions of the feet to achieve opacification of unique calf lymphatic channels¹:
 - a. Webspaces: Anteromedial
 - b. Medial foot to medial malleolus: Posteromedial
 - c. Lateral forefoot: Anterolateral
 - d. Posterior (heel) and posterior lateral foot: Posterolateral
4. Review imaging techniques to optimize visualization of lymphatic channels in the lower extremities
 - a. High-resolution Dixon imaging: Sagittal plane, Limited to affected Limb
 - b. Time-Resolved MR Angiography: Sagittal plane, temporal update 1 minute
 - c. T2-weighted non-contrast peripheral MRL
 - d. Dual-agent relaxation contrast MRL using Ferumoxytol (intravenous) for venous suppression²
5. Case-based review of peripheral MRL Utility
 - a. Unilateral limb lymphedema in a patient with a lymphangioma
 - b. Unilateral limb lymphedema in a patient with a lymphatic malformation of the thigh and pelvic soft tissues
 - c. Diagnosing source of post-operative lymphatic leak in patients with prior CL limiting feasibility of intranodal access
 - i. Post EVAR explant with graft placement for infection, continued peritoneal leak Post CL without visualization of thoracic duct
 - ii. Post soft tissue mass resection with ongoing lymphatic leak in wound
6. Challenges in peripheral MRL
 - a. Distinguishing normal lymph channels from enhancing veins with “intravasation” of intradermal contrast
 - b. Diffuse venous shunting with long-standing lymphedema



Figure 1: Peripheral MRL demonstrating early (left) and late (right) progressive filling of a lymphatic malformation along the anteromedial thigh.

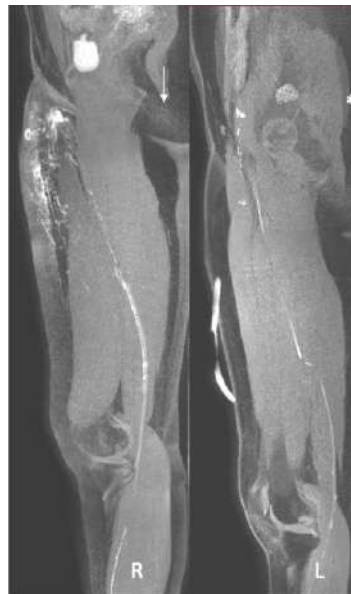


Figure 2: Peripheral MRL demonstrating late filling of a biopsy-proven lymphangioma (arrow) on the right without central lymphatic filling. Peripheral MRL of the left side demonstrates normal lymphatic channels with filling of inguinal lymphatics and lymph nodes, with central drainage (asterisk).

References: 1.
Shinaoka A et al.
Radiology
2020;294:223-29.
2.
Ripley B et al.
Radiology
2018;286:705-14.

Imaging Of Venous Thrombosis with Ferumoxytol Enhanced Magnetic Resonance Angiography

Sipan Mathevosian MD^{1,2}, Cameron Hassani MD¹, Mohammad Jalili Bahabadi MD¹, Takegawa Yoshida MD¹, Tyler Callese MD^{1,2}, Lucas Cusumano MD^{1,2}, J. Paul Finn MD¹, Arash Bedayat MD¹

1. Department of Radiology, Division of Cardiovascular Imaging, UCLA Medical Center, David Geffen School of Medicine
2. Department of Radiology, Division of Interventional Radiology, UCLA Medical Center, David Geffen School of Medicine

Purpose: Ferumoxytol is increasingly being used for vascular imaging as an alternative to gadolinium-based agents, especially in critically ill or complex patients and those with renal failure. Ferumoxytol enhanced magnetic resonance angiography (FE-MRA) can address a wide variety of arterial and venous applications. However, existing data on the utility of FE-MRA in the detection of deep venous thrombus (DVT) are limited, especially in critically ill patients. The purpose of this study was to evaluate the utility of FE-MRA for imaging of DVT in a large cohort of patients across a range of vascular territories.

Methods and Materials: After IRB approval, a single-center retrospective review was performed on all patients undergoing FE-MRA. A total of 798 patients with MR Angiograms and MR Venograms of the neck, chest, abdomen, pelvis, and extremities from July 2013 to June 2020 were included in this study. Reports from these studies were reviewed for presence of DVT. In all cases, patients had a history of chronic renal failure with contraindication to Gadolinium-based contrast agents. Vascular enhancement was achieved via administration of ferumoxytol (Feraheme, Covis Pharma, Luxembourg) at a dose of 4 mg/kg.

Examinations were performed on Siemens 1.5T and 3.0T MR scanners. All studies included multiplanar post-contrast high-resolution breath-held 3D MRA. Post processing included reconstruction of multiplanar images, MIP images and 3-D volume rendered images in OsiriX software (Pixmeo - Bernex, Switzerland) and Vitrea software (Vital Images - Minnetonka, MN).

Results: Venous thrombosis was identified in 83 of 798 studies (10.4%). 40 of 83 (48.2%) of DVT positive studies had a specific indication to evaluate for venous stenosis or thrombosis. Venous thrombosis was identified in a number of vascular beds with many patients having overlapping sites, and included: central thoracic veins (n=56), IVC or iliac veins (n=25), portomesenteric veins (n=9), peripheral extremity veins (n=4), renal veins (n=2), pulmonary veins (n=1), and intracardiac thrombus that included right atrial and Fontan conduit thrombus (n=2). Average patient age was 41.2 ± 22.6 years (0.4 - 78.3). 48 patients were male and 35 were female. Average patient weight was 64.1 ± 28.4 kg (6.5 - 131.5) and average weight-based contrast dose was 8.7 ± 4.0 mL (0.9 - 17). There were no adverse reactions.

Conclusions: Ferumoxytol enhanced MRA is a powerful efficient modality for detection of venous thrombosis in a variety of vascular beds and may set a new standard for venographic imaging.

Clinical Relevance/Application: FE-MRA is a powerful modality for detection of venous thrombosis across the full spectrum of vascular beds and may set a new standard for venographic imaging.

References:

1. Hope MD, Hope TA, Zhu C, et al. Vascular Imaging With Ferumoxytol as a Contrast Agent. *AJR Am J Roentgenol.* 2015;205(3):W366–W373. doi:10.2214/AJR.15.14534.
2. Kim-Lien Nguyen, John M. Moriarty, Adam N. Plotnik, et al. Feasibility of Ferumoxytol MRA for Pre-TAVR Vascular Access Mapping in Patients with Renal Impairment: A Step Towards Patient-Specific Care. *Radiology* 2019 Dec;293(3):554-564.
3. Ichihashi S, et al. Preliminary experience with superparamagnetic iron oxide-enhanced dynamic magnetic resonance imaging and comparison with contrast enhanced CT in endoleak detection after endovascular aneurysm repair. *J Vasc Surg* 2013;58:66-72.
4. Nguyen KL, Yoshida T, Kathuria-Prakash N, et al. Multicenter Safety and Practice for Off-Label Diagnostic Use of Ferumoxytol in MRI. *Radiology.* 2019 Dec;293(3):554-564. doi:10.1148/radiol.2019190477. Epub 2019 Oct 22. PubMed PMID: 31638489; PubMed Central PMCID: PMC6884068.

Free-breathing, non-ECG, simultaneous myocardial T1, T2, T2*, and fat-fraction mapping with motion-resolved cardiovascular magnetic resonance Multitasking

Tianle Cao^{1,2}, Nan Wang³, Alan C. Kwan^{1,4}, Hsu-Lei Lee¹, Xianglun Mao⁵, Yibin Xie¹, Kim-Lien Nguyen^{1,2,6}, Caroline M. Colbert^{6,7}, Fei Han⁸, Pei Han^{1,2}, Hui Han^{1,2}, Anthony G. Christodoulou^{1,2}, Debiao Li^{1,2}

¹Biomedical Imaging Research Institute, Cedars-Sinai Medical Center, Los Angeles, CA, USA ²Department of Bioengineering, University of California, Los Angeles, Los Angeles, CA, USA ³Radiology Department, Stanford University, Stanford, CA, USA ⁴Department of Imaging and Cardiology, Cedars-Sinai Medical Center, Los Angeles, CA, USA ⁵GE Healthcare, Menlo Park, CA, USA ⁶David Geffen School of Medicine and VA Greater Los Angeles Healthcare System, Los Angeles, CA, USA ⁷Physics and Biology in Medicine, University of California, Los Angeles, Los Angeles, CA, USA ⁸Siemens Medical Solutions USA, Inc., Los Angeles, CA, USA

Introduction: Quantitative CMR has major advantages over qualitative imaging¹⁻³ but conventional approaches require serial sequences, breath-holding, and ECG-triggering, which may result in misaligned parameter maps and artifacts related to patient fatigue from multiple breath-holds. In this work, we validate a technique for simultaneous myocardial T1, T2, T2*, and fat-fraction (FF) mapping based on the Multitasking framework⁴, which eliminates the need for breath-holding and ECG gating, resulting in a simplified and accelerated workflow.

Methods: Sequence design: The Variable T_R (VTR) Multitasking acquisition cycles through hybrid T2prep/IR preparation modules with different preparation times, which are followed by interleaved radial acquisition of imaging data and training data readout modules. The imaging data is incremented by golden angle and collects multi-echo FLASH readouts, while navigator data is acquired with 0° radial spoke every other readout module and only consists of a single FLASH readout.

Imaging framework: The underlying image series is modelled as a 7D tensor with 2 spatial dimensions and 5 temporal dimensions encoding cardiac time index, respiratory time index, T2 prep time, inversion time and echo time (for both T2* and fat-fraction mapping), which can be effectively reconstructed with spatial-temporal correlations⁴.

Data Collection: N=12 healthy consented volunteers were imaged on a 3T scanner (MAGNETOM Vida, Siemens Healthcare, Erlangen, Germany). To further validate the proposed technique on abnormal T2* values, Multitasking was also added to a clinical protocol with ferumoxytol enhancement, to simulate iron overload in N=3 consented patients with known ischemic heart disease. Patients were scanned at 3T (MAGNETOM Skyra, Siemens Healthineers, Erlangen, Germany) at baseline and following a 12-min infusion of ferumoxytol (4.0 mg/kg). Multitasking parameters include FA=5°, FOV=270x270x8 mm³, spatial resolution=1.7x1.7 mm², TR/TE₁/ΔTE=16.6 ms/1.6 ms/1.3 ms for imaging data (11 echoes), TR/TE=3.6 ms/1.6 ms for training data, 3 short-axis slices, and scan time=2.5 min/slice. In healthy volunteers, reference 2D T1 maps with MOLLI, T2 maps with T2-prep FLASH, T2* maps with multi-echo GRE were acquired at diastole with ECG triggering and end-expiration breath-hold for comparison. In patients, only reference sequences that were part of the clinical protocol were available (T1 and T2*).

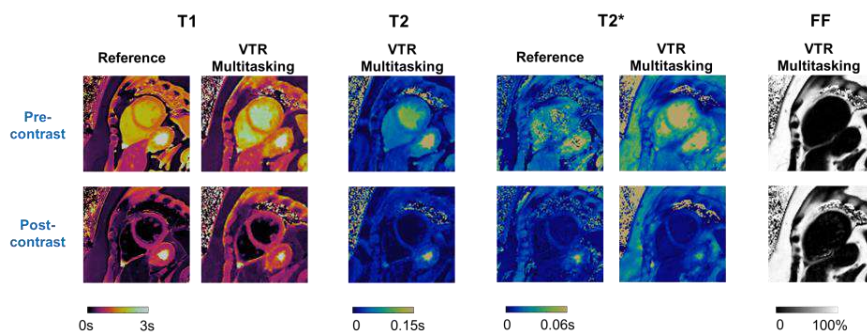


Figure 1. Short-axis 2D reference and the proposed Multitasking maps and images of a middle slice for a patient.

Results: The Multitasking maps and available reference maps for a patient are in Figure 1; both methods showed reduced T2* values after ferumoxytol administration. Fig. 2 shows Bland-Altman plots comparing VTR Multitasking measurements and references.

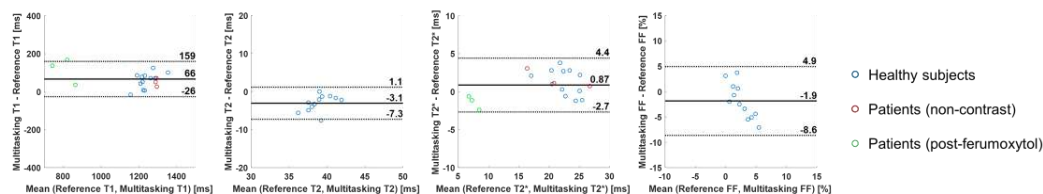


Figure 2. Bland-Altman plots comparing T1, T2, T2*, and FF measurements from references and Multitasking techniques in global myocardium

Conclusion: The proposed technique provides simultaneous myocardial T1, T2, T2*, and FF quantification without breath-hold and ECG signal in a single 2.5-min scan and produced measurements that agreed with the references.

References: [1] Bull S, et al. Heart 2013; [2] Ugander M, et al. Jacc-Cardiovasc Imag 2012; [3] Triadyaksa P et al. MRI. 2020; [4] Christodoulou AG et al. Nat Biomed Eng 2018

Accelerated Wideband Cardiac Stress Perfusion MRI Produces Clinically Acceptable Image Quality in Patients with a Cardiac Implantable Electronic Device

Daniel Kim¹, Sarah M Schwartz¹, Lexiaozi Fan¹, Bradley D Allen¹, Kyungpyo Hong¹, James C Carr¹, Brandon Benefield², Amit Patel³, Jeremy D Collins⁴, Daniel C. Lee³

¹Department of Radiology, Northwestern University Feinberg School of Medicine, Chicago, IL

²Division of Cardiology, Internal Medicine, Northwestern University Feinberg School of Medicine, Chicago, IL

³Division of Cardiology, Internal Medicine, University of Virginia, Charlottesville, VA

⁴Department of Radiology, Mayo Clinic, Rochester, MN

Purpose: Symptomatic patients with a cardiac implantable electronic device (CIED) often undergo two cardiac imaging tests (stress SPECT, resting echo), which may be replaced by a single comprehensive cardiac MRI including stress perfusion, cine, and late gadolinium enhancement. The purpose of this study was to determine whether a 5-fold accelerated wideband cardiac stress perfusion MRI pulse sequence in patients with a CIED produces image quality comparable to a standard perfusion MRI sequence in matched non-device patients.

Methods: We retrospectively identified 25 consecutive patients with a CIED (age= 66.8 ± 11.7 yrs, 56%males, EF=45% ±14.5%, BMI=28.6 ± 5.1 kg/m²) and 25 matched non-device patients (age= 65.5 ±10.4 yrs, 56%males, EF=49% ± 14.9, BMI=29.1 ± 4.3 kg/m²) who underwent identical adenosine stress-rest (10 min apart) protocol with 0.075 mmol/kg of gadobutrol per scan using our 5-fold accelerated wideband GRE perfusion sequence [1] and 2-fold accelerated standard GRE sequence, respectively, on a 1.5 T whole-body scanner (Siemens, Avanto). Relevant imaging parameters for both sequences are summarized in Table 1. Accelerated wideband perfusion images – both arterial input function and myocardial wall enhancement - were reconstructed using compressed sensing, as previously described [1]. Two clinical raters (cardiologist, radiologist) independently evaluated the image quality in three categories on a 5-point Likert scale (1: worst, 3: acceptable, 5: best): conspicuity of the myocardium enhancement, image artifacts within the heart, and noise throughout the image. The overall image quality was defined as the summed visual scores (SVS), where SVS > 9 is defined clinically acceptable. The two raters were given training datasets to calibrate their scores together prior to independent reads. Each rater provided a composite score for all slices. Inter-rater agreement was calculated using Cohen's kappa coefficient. The average rater scores (CIED vs. non-device patients) were compared using the Mann-Whitney's test.

Results: As shown in Figure 1, both wideband and standard pulse sequences produced diagnostically acceptable image quality during stress and at rest. As summarized in Table 2, the median SVS was not significantly different between wideband perfusion sequence in CIED patients and standard perfusion sequence in non-device patients, and greater than 9.0 (clinically acceptable). The inter-rater agreement was moderate for both wideband (k=0.6, 95% CI, 0.5 to 0.7) and standard pulse sequences (k=0.6, 95% CI, 0.5 to 0.7).

Discussion: This study demonstrates that our 5-fold accelerated wideband cardiac perfusion sequence produces diagnostically acceptable image quality (SVS > 9) in CIED patients in the context of stress testing. Future possible studies include quantification of myocardial blood flow, regional analysis of image quality, and additional strategies to eliminate residual image artifacts.

References: [1] Hong K, et. al. Radiology: Cardiothoracic Imaging 2020; **Funding Support:** NIH (R01HL116895, R01HL138578, R21EB024315, R21AG055954, R01HL151079, R21EB030806) and AHA (19IPLOI34760317, 949899).

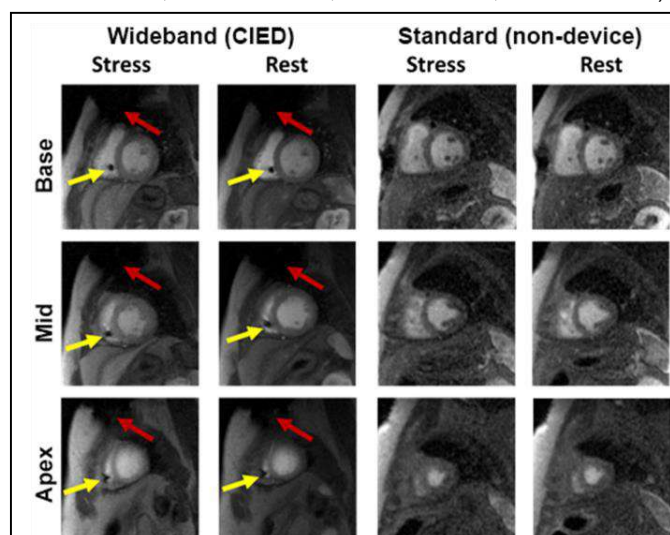


Figure 1: Representative images of base, mid, and apical slices produced by wideband (columns 1-2) and standard (columns 3-4) pulse sequences during stress and at rest. Red arrows point to signal void secondary to the CIED generator, whereas yellow arrows point to signal void secondary to intracardiac lead.

Table 1. Relevant imaging parameters.

Sequence	TE/TR	Resolution	bandwidth	Flip angle	TS
Standard	1.4/2.5 ms	3 x 3 mm ²	700 Hz/pixel	15°	130 ms
Wideband	1.4/2.8 ms	2.1x 2.1 mm ²	744 Hz/pixel	15°	118 ms

Table 2. Median [IQR] visual scores. *p <0.05.

Overall				
	Conspicuity	Artifact	Noise	SVS
Wideband	4.5 [4.0, 5.0]	4.0 [3.5, 4.5]*	4.5 [4.0, 5.0]*	13.0 [12.0, 14.0]
Standard	4.0 [3.5, 4.5]	4.5 [4.5, 5.0]*	4.0 [3.5, 4.0]*	12.5 [12.0, 13.5]
Stress				
	Conspicuity	Artifact	Noise	SVS
Wideband	4.5 [4.0, 5.0]	4.0 [3.5, 4.5]*	4.5 [4.0, 5.0]*	13.0 [12.0, 13.5]
Standard	4.0 [3.5, 4.5]	4.5 [4.5, 5.0]*	4.0 [3.5, 4.0]*	12.5 [12.0, 13.5]
Rest				
	Conspicuity	Artifact	Noise	SVS
Wideband	4.5 [4.0, 5.0]	4.0 [3.5, 4.5]*	4.5 [4.0, 5.0]*	13.0 [12.0, 14.0]
Standard	4.0 [3.5, 4.5]	4.5 [4.5, 5.0]*	4.0 [3.5, 4.0]*	13.0 [12.0, 13.5]

Adiabatic spin-lock preparations for robust in-vivo myocardial $T_{1\rho}$ -mapping at 3T

Chiara Coletti¹, Joao Tourais¹, Mehmet Akcakaya², Christal van de Steeg-Henzen³, Sebastian Weingärtner¹

¹Department of Imaging Physics, TU Delft, Delft, Netherlands, ²Department of Electrical and Computer Engineering, University of Minnesota, Minneapolis, MN, United States, ³HollandPTC, Delft, Netherlands

Purpose: While LGE remains the clinical standard for the assessment of myocardial viability, $T_{1\rho}$ -mapping has emerged as a promising endogenous contrast alternative to discriminate between healthy and infarcted myocardium¹⁻³. However, its application at high field strengths is hindered by the susceptibility of spin-lock preparations to B_0 and B_1^+ field inhomogeneities. Adiabatic preparations bear the potential to enable $T_{1\rho}$ contrast while overcoming these limitations⁴⁻⁵. In this work, we sought to enable robust in-vivo $T_{1\rho}$ -mapping at 3T in a single breath-hold using adiabatic spin-locks (aSL).

Methods: aSL preparations, consisting of blocks of 2 hyperbolic secant pulses⁶ (amplitude, frequency modulation:

$$B_1(t) = B_{1,max} \sec\left(\beta \left(\frac{2t}{\tau_{HS}} - 1\right)\right),$$

$$\Delta\omega_1(t) = f_{max} \tanh\left(\beta \left(\frac{2t}{\tau_{HS}} - 1\right)\right)$$

were optimized through simulations

($\tau_{HS}=30\text{ms}$, $B_{1,max}=13.5\mu\text{T}$ or max allowed by SAR). Preparation efficiency (M_z/M_0)

was computed for 3 design regions (Fig.1) to identify the combination of $\{\beta; f_{max}\}$

yielding 3 optimized preparations: B_0 -aSL, Bal-aSL, B_1 -aSL. These were

simulated and tested in phantoms for $\Delta B_0=\pm 200\text{Hz}$, $\Delta B_1^+=0.1:1$. $T_{1\rho}$ -mapping

was performed on a 3T scanner (Ingenia, Philips) with a breath-hold ECG-triggered

single-shot bSSFP sequence, comparing aSL with a conventional SL (RefSL)⁷. The

sequence was tested in-vivo in 4 healthy subjects. $T_{1\rho}$ maps were generated using a 3

parameter model from 4 SL-prepared images and 1 saturation-prepared image, used to approximate infinite SL duration and capture the image readout effects.

Results: Simulation results for aSL preparations averaged over the design window show the best preparation efficiency for low sweep amplitudes and inversely-proportional β (Fig. 1). Phantom experiments show excellent agreement with the simulations, while also reflecting relaxation during the preparation, ignored in the simulations. In-vivo cardiac short-axis $T_{1\rho}$ -maps are shown in Fig.2. Average $T_{1\rho}$ values are higher for aSL and increase linearly with β . Compared to Ref-SL, aSLs yield on average 14.6 ± 2.7 times better precision, 8.2 ± 2.1 times better reproducibility and 7.4 lower inter-subject variability. **Discussion:** Our results suggest that adiabatic $T_{1\rho}$ -mapping allows for robust in-vivo quantification of myocardial spin-lock relaxation times at high field strengths. Improved map quality is observed for adiabatic preparations both in phantom and in-vivo, compared to the RefSL implementation. Adiabatically-prepared sequences demonstrate good blood/myocardium contrast and retain image quality across different repetitions and subjects. Compared to mono-frequency conventional spin-lock, each adiabatic $T_{1\rho}$ -preparation probes a wider spectrum of frequencies through the adiabatic sweep. This may lead to a different sensitivity profile in pathological remodelling and its clinical value remains to be evaluated.

References: ¹Witschey et al. *JCMR* 2012, ²van Oorschot et al. *JCMR* 2014, ³Berisha et al. *Plos One* 2016, ⁴Michaeli et al. *JMR* 2006, ⁵Mangia et al. *MRI* 2009, ⁶Garwood et al. *JMR* 2001, ⁷Gram et al. *MRM* 2020.

References: ¹Witschey et al. *JCMR* 2012, ²van Oorschot et al. *JCMR* 2014, ³Berisha et al. *Plos One* 2016, ⁴Michaeli et al. *JMR* 2006, ⁵Mangia et al. *MRI* 2009, ⁶Garwood et al. *JMR* 2001, ⁷Gram et al. *MRM* 2020.

References: ¹Witschey et al. *JCMR* 2012, ²van Oorschot et al. *JCMR* 2014, ³Berisha et al. *Plos One* 2016, ⁴Michaeli et al. *JMR* 2006, ⁵Mangia et al. *MRI* 2009, ⁶Garwood et al. *JMR* 2001, ⁷Gram et al. *MRM* 2020.

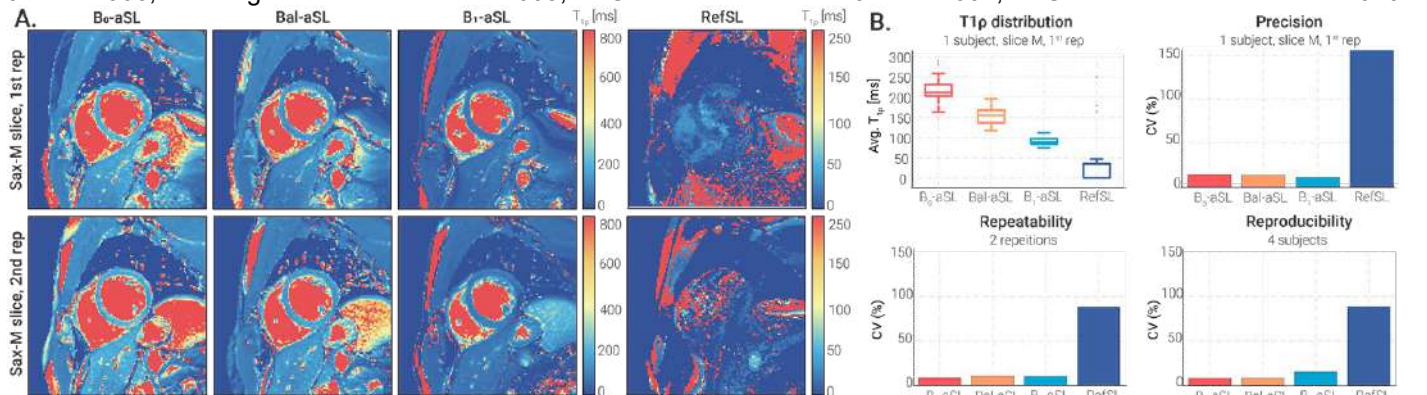


Fig. 2 A: In-vivo short-axis $T_{1\rho}$ -maps for representative subject, 2 repetitions. **B:** $T_{1\rho}$ distributions and precision for 1 subject, repeatability over 2 repetitions and reproducibility over 4 subjects. Coefficient of variability (CV) computed as std/mean.

All-in-one CMR Multitasking with Joint Reconstruction of Pre- and Post-Contrast Images

Xianglun Mao¹, Zihao Chen^{2,3}, Hsu-Lei Lee², Alan C Kwan^{2,4}, Tianle Cao^{2,3}, Fei Han⁵, Ivan Cokic², Yibin Xie², Debiao Li^{2,3}, Anthony G. Christodoulou^{2,3}
¹ GE Healthcare, Menlo Park, CA ² Biomedical Imaging Research Institute, Cedars-Sinai Medical Center, Los Angeles, CA ³ Department of Bioengineering, UCLA, Los Angeles, CA ⁴ Smidt Heart Institute, Cedars-Sinai Medical Center, Los Angeles, CA ⁵ Siemens Medical Solutions, Inc., Los Angeles, CA

Purpose: CMR tissue characterization (e.g., T1/T2/extracellular volume fraction [ECV]/late gadolinium enhancement [LGE]) is useful for cardiac disease diagnosis, but requires a series of distinct, specific sequences within a CMR protocol. This framework of sequential acquisition results in prolonged scan time, lack of strict co-registration, and requires significant expertise to ensure quality across the complete protocol. This work assessed the feasibility of implementing a Joint Reconstruction of uninterrupted CMR Multitasking acquisition (i.e., Multitasking-JR)^{1,2} comprising both pre- (native) and post-contrast scanning to simplify the workflow into a single 20 minute free-breathing non-ECG-gated acquisition. This single scan provides co-registered cardiac cine, T1, T2, ECV, and phase sensitive inversion recovery (PSIR)-LGE.

Methods: Sequence Design: A prototype 3D stack-of-stars FLASH pulse sequence was modified to collect image data incremented by a tiny golden angle (23.67°) interleaved with training data acquired at the central 0° spoke every 8th readout. In the first half of the scan (pre-contrast), interleaved IR and T2prep-IR preparation pulses and two FLASH excitation angles are employed to generate T1 and T2 contrast and B1+ maps^{2,3}. The second half of the scan automatically switches to IR-only preparation immediately prior to Gd injection, allowing ECV mapping and PSIR-LGE (Fig. 1).

Image Model: We jointly reconstructed all images in the 20-min acquisition spanning pre- and post-contrast (10 mins “pre” + 10 mins “post”) using the Multitasking framework. The 10-min post-contrast acquisition was time-resolved to track the post-injection kinetics, with the last time point used for post-contrast measures such as ECV and LGE. Pre-contrast images were represented as a 6-way tensor with a combined spatial dimension and 5 time dimensions (T1 recovery, T2prep duration, flip angle, cardiac motion, and respiratory motion). Post-contrast images were a 5-way tensor with a combined spatial dimension and 4 time dimensions (T1 recovery, cardiac motion, respiratory motion, and DCE). The spatial basis is shared between pre- and post-contrast images for joint reconstruction.

Data Collection: N=10 human volunteers (2 males and 8 females, mean age 37.1±20.8) were imaged on a 3T scanner (MAGNETOM Vida, Siemens). One farm pig with reperfusion injury by LAD balloon dilation catheter was imaged on a 3T scanner (MAGNETOM mMR, Siemens).

Multitasking pulse sequence parameters were: TR/TE=3.6ms/1.7ms, recovery period=2.5s, 1.4x1.4x8.0mm³. Total scan time was 20:20min (9:29pre/10:51post) for all subjects. The Gd dose was 0.2mmol/kg. Reference pre- and post-contrast 2D T1 maps with MOLLI and pre-contrast 2D T2 maps with T2-prep FLASH at basal, mid, and apical slices, full short-axis stacks of 2D bSSFP cine scans (pre-contrast), and PSIR scans (post-contrast) were acquired.

Results and Discussion: T1/T2/ECV/PSIR-LGE results from the pig are shown in Fig. 2. Figs. 3 and 4 depict the summary statistics and Bland-Altman comparisons for segment-wise T1/T2/ECV values in humans. In humans, Multitasking-JR measured higher myocardial T1 values (1383±136.4ms) than MOLLI (1217±48.4ms), which is known to underestimate T1⁴. Multitasking-JR measured higher myocardial T2 values (43.9±9.0ms) than T2-prep FLASH (40.0±4.2ms), which is consistent with previous observations, and is still within the reported normal range⁵. Multitasking-JR ECV values (27.5±3.9%) were similar to MOLLI ECV (27.9±4.1%), and were all within the normal range⁶. The reported left ventricular ejection fraction (LVEF) values were 60.6%±6.3% for Multitasking-JR and 62.7%±6.0% for reference. LGE was not present in any of these healthy volunteers in either reference or Multitasking-JR acquisitions. Significant susceptibility issue is observed in the lateral wall of the myocardium in native T1/T2 of both Multitasking-JR and reference in the injured farm pig. The extent of Multitasking LGE matched reference LGE in the injured farm by visual estimation.

Conclusion: Joint reconstruction of pre- and post-contrast data is feasible with CMR Multitasking. This method is promising for producing T1/T2/Cine/ECV/LGE in one 20-min data acquisition. Future directions include shortening the pre-contrast scan time and including clinical patients for further validation. **References:** [1] Christodoulou, A.G. et al. Nature BME. 2018; [2] Mao, X. et al. Front Cardiovasc Med. 2022; [3] Serry, F. et al. MRM. 2021; [4] Kellman, P., & Hansen, M. S. JCMR. 2014; [5] Snel, G. J. H. et al. JCMR 2020; [6] Heidenreich, J. F., et al. BMC Med Imaging. 2019

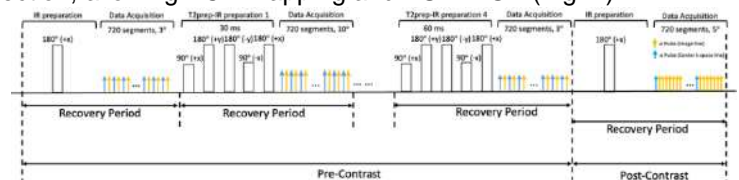


Figure 1. Schematic diagram of the proposed 3D CMR Multitasking sequence, where 5 different preparations (IR and T2prep-IR with 4 different preparation times, 30ms, 40ms, 50ms, 60ms) are repeated throughout the pre-contrast scan. The FLASH readouts are alternating between 3° and 10° for each pre-contrast recovery period. The IR and 5° FLASH readout are used for the post-contrast period.

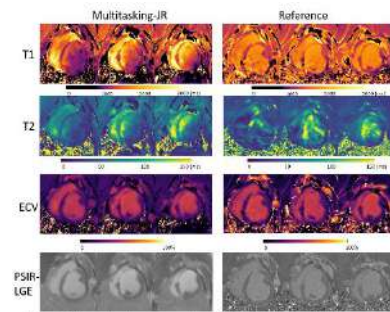


Figure 2. Three short-axis pre-contrast T1/T2, ECV, and PSIR-LGE images from the proposed 3D Multitasking-JR method and reference methods in the farm pig with reperfusion injury. Significant susceptibility issue occurred in the lateral wall of the myocardium in both Multitasking-JR and reference.

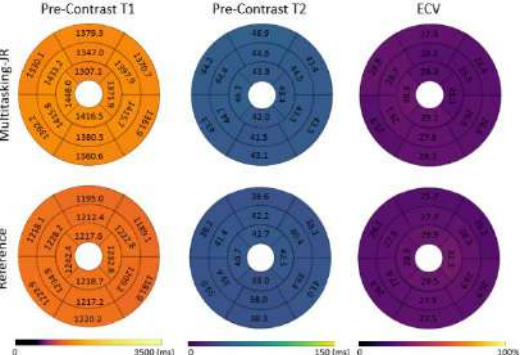


Figure 3. The 16-segment AHA model for the proposed multitasking T1/T2/ECV maps and the reference T1/T2/ECV maps in the myocardium in all 10 human subjects.

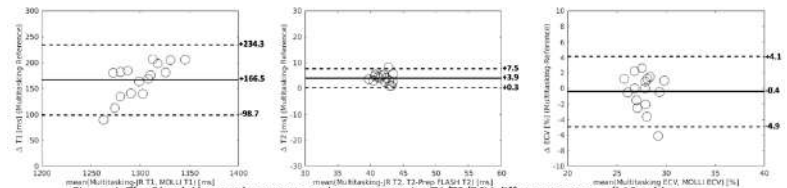


Figure 4. The Bland-Altman plot compares the segment-wise T1/T2/ECV differences across all 10 subjects.

Image Contrast and Left Atrial Fibrosis from Late Gadolinium Enhancement are influenced by the Balanced Steady-State Free Precession Flip Angle

Suvai Gunasekaran¹, KyungPyo Hong¹, Julia Hwang¹, Mohammed S.M. Elbaz¹, Rod Passman¹, Saman Nazarian², Eugene Kholmovski³, and Daniel Kim¹

¹Northwestern University, Feinberg School of Medicine, Chicago, IL, United States, ²Medicine, University of Pennsylvania, Perelman School of Medicine, Philadelphia, PA, United States, ³Radiology, University of Utah, School of Medicine, Salt Lake City, UT, United States

Purpose: Left atrial (LA) fibrosis as measured by late gadolinium enhancement (LGE) MRI has been shown to predict atrial fibrillation (AF) recurrence following AF ablation.[1] The image intensity ratio (IIR),[2] defined as LA signal divided by the mean blood pool signal, with established cutpoints (IIR = 1.2-1.32 as interstitial fibrosis; IIR > 1.32 as dense scarring) has been described as “standardized, reproducible late gadolinium-enhanced cardiac magnetic resonance thresholds.” [2] We have recently developed a self-calibrated, free-breathing 3D LA LGE sequence with XD-GRASP reconstruction. [3] This sequence uses a b-SSFP readout to achieve relatively higher signal-to-noise ratio compared to GRE readout. However, in inversion-recovery with b-SSFP, the level of T2 weighting (i.e. bright blood) depends on the flip angle (FA) and k-space ordering. The purpose of this study was to determine the sensitivity of said pulse sequence to FA for IIR (fibrosis) quantification. **Methods:** Subjects: 12 patients (age = 62 ± 12 years, 10 males, 7 with AF) were scanned on a 1.5 T scanner (Siemens, AERA or AVANTO) using a previously described 3D LA LGE with b-SSFP and stack-of-stars k-space sampling.[3] Each patient received a double dose of gadolinium and underwent back-to-back coronal 3D LA LGE using 20 degree FA (FA 20) and 40 degree FA (FA 40), where the pulse sequence order was randomized. The inversion time (TI) to null the left ventricular myocardium was determined using a TI scout sequence immediately before LGE imaging. Image reconstruction was performed offline using Matlab (Mathworks, Natick, MA) using XD-GRASP.[3] **Image analysis:** We were not able to calculate contrast-to-noise ratio because we did not have access to a signal-free region within the field of view to estimate noise. Instead, we calculated the relative signal difference (RSD) defined as the mitral valve (MV) signal minus LA blood pool (BP) signal, then divided by the MV signal, as shown in Figure 1. LA fibrosis was calculated with a standard protocol using ADAS 3D Software (Galgo Medical, Barcelona, Spain). [2] Briefly, first, LA wall contours were manually drawn in each axial plane, and then pulmonary veins and the mitral valve were excluded from segmentation to focus the analysis on LA tissue. The IIR density for each patient was plotted to demonstrate the IIR distributions (Figure 3), and an IIR cut point of 1.2 [2] was used for fibrosis quantification (Figure 4). **Results:** The mean LGE scan start time was 24 ± 6 minutes and 33 ± 6 minutes after contrast injection for the first and second LGE scans, respectively. The mean RSD was greater for FA 20 (0.38 ± 0.15) than that of FA 40 (0.28 ± 0.13). The mean IIR was greater for FA 20 (0.91 ± 0.08) than FA 40 (0.86 ± 0.08) (Figure 3), which resulted in higher fibrosis for FA 20 fibrosis (9.2 ± 8.9%) than FA 40 (4.5 ± 5.2%) (Figure 4). **Discussion:** 3D LA LGE was successfully run in 12 patients using FA 20 and FA 40. As shown in Figure 2, FA 40 produces brighter blood pool signal and higher SNR compared with FA 20. However, RSD between the LA wall and blood pool was higher for FA 20 than FA 40, which resulted in higher IIR (ultimately fibrosis) values for FA 20 compared to FA 40. LA fibrosis quantification using the IIR method is sensitive to the b-SSFP FA. In this study, FA 20 resulted in 25.7% higher signal contrast and 104% higher fibrosis quantification compared to FA 40; however, another study with a larger sample size is needed to derive statistical significance. This study demonstrates that the IIR method is sensitive to FA when using a 3D LGE pulse sequence that produces a mixture of T1 and T2 weighting (i.e. b-SSFP). **References:** 1. Marrouche, N.F., JAMA, 2014. 2. Benito, E.M., Europace, 2017. 3. Gunasekaran, S., Radiol Cardiothorac Imaging, 2020.

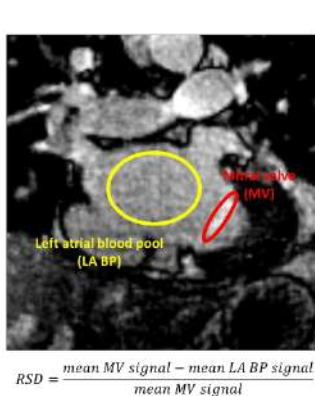


Figure 1. Computing relative signal difference (RSD). Example LGE MRI with ROI drawn around the enhanced mitral valve (MV) and the left atrial blood pool (LA BP) and equation for computing RSD.

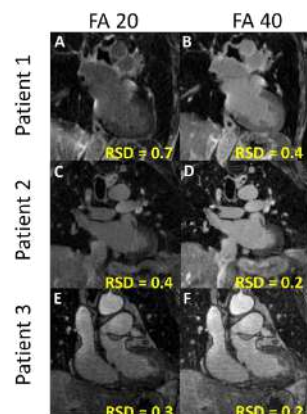


Figure 2. Representative LGE MRI examples and RSD calculations of three different patients with FA 20 imaging and FA 40.

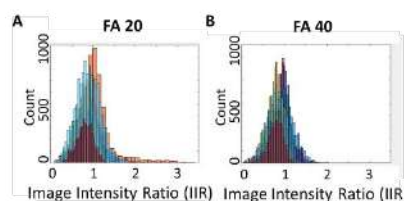


Figure 3. IIR distributions for FA 20 and FA 40.

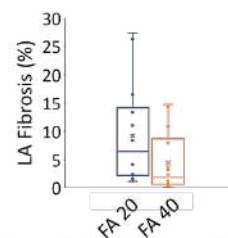


Figure 4. LA fibrosis quantification plot from FA 20 and FA 40 imaging.

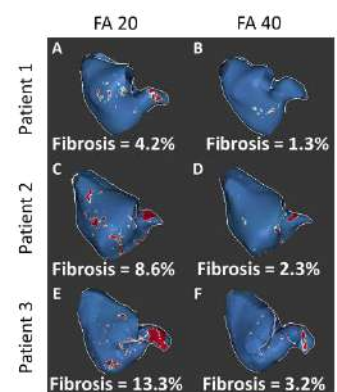


Figure 5. Representative fibrosis maps from three different patients with FA 20 and FA 40. Blue = Healthy myocardium, Red = fibrotic tissue

5D-GRASP whole-heart imaging with ferumoxytol detects variation of LVEF during respiration

Yitong Yang¹, Jackson Hair¹, Zahraw Shah¹, Jerome Yerly², Matthias Stuber², John Oshinski^{1,3}

¹Wallace H. Coulter Biomedical Engineering, Georgia Institute of Technology & Emory University, Atlanta, GA, USA

²Diagnostic and Interventional Radiology, Lausanne University Hospital, Lausanne, Switzerland

³Department of Radiology & Imaging Sciences, Emory University, Atlanta, GA, USA

Purpose: XD-GRASP (eXtra-Dimensional-Golden-angle-Radial Sparse Parallel)^{1,2} technique was developed to reconstruct the pseudo-randomly under-sampled multidimensional k-space data. Extending XD GRASP for cardiac and respiratory-resolved 3D whole-heart imaging in a free-running framework is termed 5D-GRASP³. Acquiring 3D whole-heart images in different respiratory and cardiac states enables the assessment of physiological interactions between the respiratory and cardiac function⁴. This work utilizes 5D-GRASP free running framework to study the modulation of left ventricle ejection fraction (LVEF) during respiration, specifically, the change in LVEF from end-expiration and end-inspiration. *We hypothesize that the LVEF is greater during end-expiration than during end-inspiration by assessing in 3D whole-heart volumes during end-diastole and end-systole in four respiratory states.*

Method: The study was performed on three healthy farm pigs on a 3T scanner (MAGNETOM Prisma^{fit}, Siemens Medical Systems) under an IACUC approved protocol. Prior to scanning, each pig was anesthetized with Propofol, intubated, and mechanically ventilated with a mixture of isoflurane and oxygen for the duration of the scan. Ferumoxytol (Fereheme, AMAG pharmaceutical) at a concentration of 4 Fe mg/kg was dissolved in 100 mL saline and infused into the auricular artery over 15 to 20 minutes, followed by a 100 mL saline flush. The pigs were then placed in the scanner head-first and supine. An 18-channel body coil was placed over the heart. Data were acquired with a prototype continuous, ungated, golden-angle radial spoiled-GRE sequence over a 192x192x192 mm³ FOV with an isotropic resolution of 1mm³. Excitation used a 15° flip angle and was preceded by 10 linearly increasing ramp-up pulses. A total of 129,000 radial lines were acquired with 22 segments per interleaf (TR/TE of 3/1.64ms, bandwidth of 1002Hz/px). The time required to sample all 5983 interleaves was 389 seconds. The raw data were exported offline for reconstruction. For all datasets, cardiac and respiratory motion signals were extracted from the raw data and subsequently binned³ using MATLAB (MathWorks). The raw data were binned into four respiratory states and a variable number of cardiac phases determined such that each phase

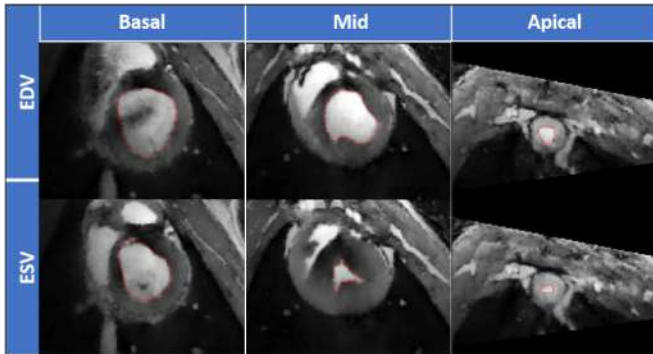


Figure 1. Example manual segmentations of LV endocardium at end-diastole (top) and end-systole (bottom) at basal, mid, and apical positions in one respiratory state. 2D cine movies are generated for 30 multiplanar reformatted short-axis slices covering LV from mitral annulus to apex of each respiratory states for segmentation in Segment Medviso.

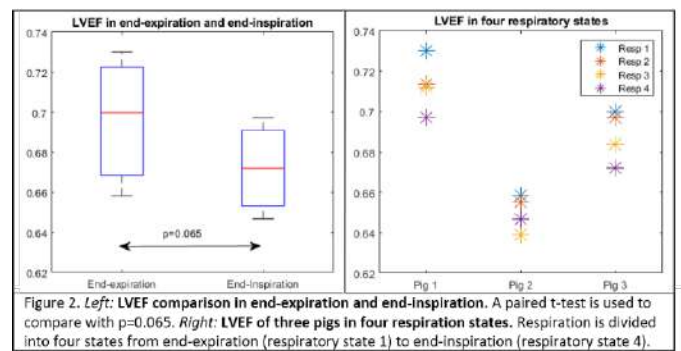
represented a 50 ms window. Alternating direction method of multipliers (ADMM) is used to solve the under-sampled reconstruction. Each reconstructed 3D (spatial) + 1D (respiratory) + 1D (cardiac) images are multiplanar reformatted into short-axis views and 30 slices covering LV from mitral-annulus to the apex are segmented on Segment Medviso to quantify LV volume (Fig.1 top row). A total of 8 volumes (four respiratory phases for end-diastolic volume (EDV) and end-systolic volume) are segmented for each pig and LVEF is computed as (EDV-ESV)/EDV. Example EDV (top) and ESV (bottom) segmentations in basal, mid, and apical positions shown in figure 1. Each of four respiratory phases represent one motion states from end-expiration (Resp 1) through end-

inspiration (Resp 4). End-expiration and end-inspiration LVEF were compared with a student paired t-test

Results: We found that LVEF is greater in end-expiration (0.70 ± 0.04) than end-inspiration (0.67 ± 0.03) with $p=0.065$ (Fig. 2 left). LVEF is greatest during end-expiration (respiratory position 1) for all pigs ($n=3$), and the lowest during end-inspiration (respiratory position 4) for two pigs and near end-inspiration (respiratory position 3) for one pig (Fig.1 right).

Conclusion: Use of 5D GRASP free-running framework enables comparison of LVEF at multiple respiratory states. This study showed that LVEF is modulated by respiration such that it is greater during end-expiration than end-inspiration.

References: ¹Feng L. et al., MRM 2014 ²Piccini D. et al., MRM 2017 ³Di S. L. et al., MRM 2018 ⁴Feng L. JMRI 2022



Fractional Myocardial Blood Volume Estimation using Ferumoxytol-Enhanced Magnetic Resonance Imaging: Early Findings in Healthy Human Subjects

Xinyi M. Li^{1,2}, Caroline M. Colbert^{1,2}, Arutyun Pogosyan^{2,3}, Zhengyang Ming^{1,2}, J. Paul Finn^{1,2}, Kim-Lien Nguyen^{1,2,3}

¹Physics and Biology in Medicine Graduate Program, University of California, Los Angeles, Los Angeles, CA; ²Diagnostic Cardiovascular Imaging Research Laboratory, David Geffen School of Medicine at UCLA, Los Angeles, California, USA; ³Division of Cardiology, David Geffen School of Medicine at UCLA and VA Greater Los Angeles Healthcare System, Los Angeles, California, USA

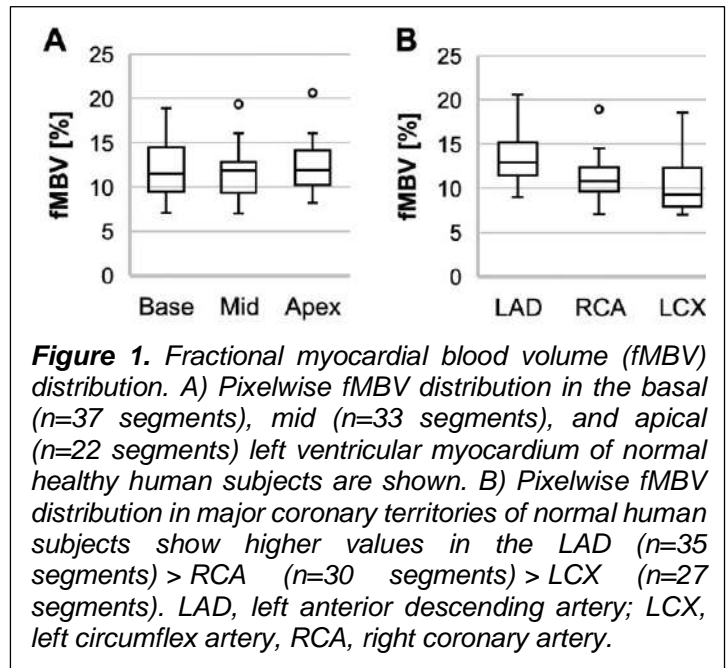
Purpose: Fractional myocardial blood volume (fMBV) derived from ferumoxytol-enhanced magnetic resonance imaging (FE-MRI) provides unique insight on the detection and quantification of myocardial tissue perfusion without reliance on gadolinium or pharmacologic stress agents. In diseased microvasculature, the fMBV is expected to be lower, whereas in ischemic epicardial coronary disease, the fMBV is expected to be higher relative to myocardial tissues.³ Researchers have recently proposed a two-compartment model for estimating fMBV from steady-state FE-MRI in healthy and ischemic swine.¹ However, fMBV based on FE-MRI has yet to be adapted for clinical testing and validation. In this work, we aim to investigate the feasibility of FE-MRI derived fMBV in a group of healthy human subjects and evaluate a two-compartment water exchange model based on FE-MRI to estimate fMBV in ischemic microvascular disease.

Methods: We recruited healthy human volunteers and one patient with known apical hypertrophic cardiomyopathy to undergo FE-MRI on a clinical 3.0T MRI scanner (Skyra®, Siemens Medical Solutions USA, Malvern, PA). Using the 5(3)3(3)3 Modified Look-Locker Inversion (MOLLI) recovery sequence with a balanced steady-state free precession (bSSFP) readout [TR/TE=2.4/1.33ms, pixel bandwidth=1085Hz, flip angle=35°, TI=100-1500ms, TI increment=80ms, in-plane resolution=0.9 x 0.9 x 8mm³], we acquired left ventricular short-axis T1 maps at the base, mid, and apex of the heart during contrast steady state. Ferumoxytol was infused over a cumulative dose of 4.0 mg/kg, in increments of 0.0, 0.125, 2.0, and 4.0 mg/kg. The Instantaneous Signal Loss simulation (InSiL) algorithm was used for T1 fitting to reduce the heart-rate dependence on T1 estimation.² An in-house two-compartment water exchange model was applied to generate pixel-wise fMBV maps,¹ which were segmented according to the American Heart Association 17-segment model.

Results: Eight human volunteers (age 34±8.4, 8 females) and one patient (male) with apical hypertrophic cardiomyopathy underwent FE-MRI for pixelwise fMBV mapping without adverse events. Figure 1 summarizes the fMBV distribution in the left ventricular myocardium and in three major coronary vessel territories (left anterior descending artery [LAD], right coronary artery [RCA], left circumflex artery [LCX]). In healthy volunteer females, we observed no significant differences (p=.68, Kruskal-Wallis test) in fMBV for the basal, mid-ventricular, and apical locations of the left ventricle, which had median fMBV values of 11.5 (IQR 4.8)%, 11.8 (IQR 3.2)%, and 11.9 (IQR 3.4)%, respectively. Among the coronary vessel territories, the LAD territory had the highest median fMBV of 12.9 (IQR 3.6)% while the LCX had the lowest fMBV of 9.3 (IQR 2.6)%. The RCA had a fMBV of 10.7 (IQR 4.1)%. Relative to healthy volunteers who had a global median fMBV of 11.8 (IQR 3.7)%, our patient with apical hypertrophic cardiomyopathy and microvascular disease had a global median fMBV of 8.3 (IQR 3.0)%.

Conclusion: Mapping of tissue blood volume distribution based on FE-MRI is feasible. Additional investigations are needed in a wider spectrum of healthy volunteers and patients with ischemic heart disease. If proven successful, FE-MRI derived fMBV based on a 2-compartment water exchange model has potential for providing additional insight about local tissue perfusion without the need for pharmacologic stress agents.

References: [1] Colbert, C. M. et. al *J Magn Reson Imaging*. 2021 [2] Shao J et. al *Magn Reson Med*. 2017 [3] Feher A. et. al *Circ Cardiovasc Imaging*. 2017



A MINIMAL CARDIAC MRI PROTOCOL FOR CATHETER ABLATION PLANNING IN PATIENTS WITH CARDIAC IMPLANTABLE ELECTRONIC DEVICES

Calder Sheagren¹, Terenz Escartin¹, Philippa Krahn¹, Judi Paulson¹, Melissa Larsen¹, Martin Janich², Idan Roifman¹, and Graham Wright¹

1. Sunnybrook Research Institute, Toronto ON Canada. 2. GE Healthcare, Munich BY Germany.

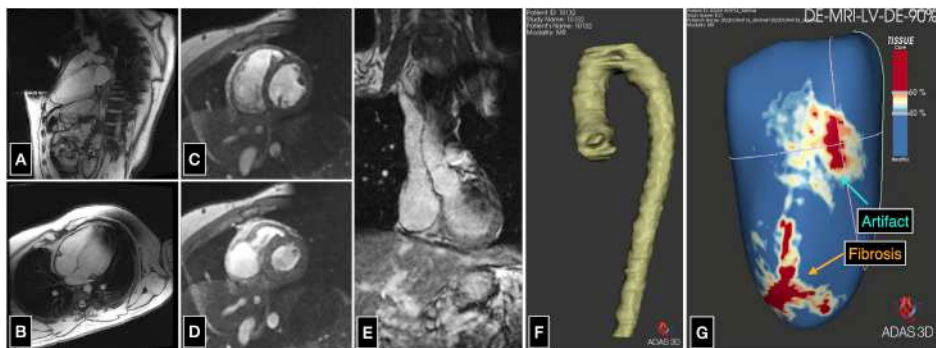


Figure 1. Example images from healthy volunteers and porcine subjects with externally positioned devices. **A-B:** spoiled gradient echo localizers. **C-D:** spoiled gradient echo cine. **E-F:** 3D aortic MRA and manual segmentation interpolated every five slices. **G:** Scar map in porcine subject with infarct and CIED. CIED-generated hyperintensity artifacts in LGE present as false positive regions of fibrosis.

Total Scan Time	FSPGR Localizers 3P, LAX, SAX, 4Ch, 3Ch, 2Ch, LVOT	FSPGR Cine SAX Stack	Perfusion 3 SAX slices	3D MRA Coronal Slab	3D Wideband LGE SAX Slab
39:32	8:11	9:09	1:27	6:30	14:15

Table 1. Proposed protocol and timing information. Gadolinium contrast agent is injected immediately before the GRE Perfusion scan. *3P:* 3-plane. *LAX:* long axis. *SAX:* short axis. *(4,3,2)Ch:* (4,3,2)-chamber. *LVOT:* left ventricle outflow tract.

Purpose

Propose a minimal cardiac MRI (CMR) protocol for assessing cardiac function and fibrosis content in patients with cardiac implantable electronic devices (CIEDs) to facilitate catheter ablation procedure planning.

Motivation

Late gadolinium enhancement (LGE) CMR can characterize arrhythmogenic tissue in patients with prior myocardial infarction being considered for a catheter ablation by delineating regions of heterogeneous fibrosis that cause ventricular arrhythmia [1]. However, 89% or more of patients receiving a catheter ablation procedure have a CIED, limiting clinical CMR adoption because of safety and image quality concerns [2]. Current guidance suggests that MR-conditional devices are safe to scan with a device technician present, and some MR-nonconditional devices are safe to scan with an additional advanced cardiovascular life support-trained health professional present [3]. In this work, we propose a minimal protocol to assess cardiac function and fibrosis in patients with CIEDs being considered for a catheter ablation.

Discussion

Imaging was conducted on 1.5 and 3 Tesla scanners (MR450w & MR750; GE Healthcare; Waukesha, Wisconsin) for healthy volunteers and porcine subjects, respectively. CIEDs were taped to subjects' chests at a representative location to simulate the artifacts generated by a patient's CIED. No evidence of thermal injury was observed in porcine subjects, and volunteers did not report any heating or adverse effects. Myocardial anatomy and function was assessed using fast spoiled gradient echo (FSPGR) cine images: slice thickness = 4mm (4mm spacing), readout bandwidth = 125 kHz [4]. The aortic arch aids in CMR and electroanatomical map registration, so we performed a T2-prepared saturation recovery gradient-echo (GRE) MR angiography (MRA) with diaphragmatic navigator gating (2mm isotropic resolution, ARC acceleration = 2). Conducting the MRA immediately after GRE perfusion reduces wait time and improves SNR because of the T1 contrast. 3D wideband GRE LGE (1.4mm isotropic resolution, ARC acceleration = 2) with diaphragmatic navigator gating (efficiency ~ 30%) was used to delineate regions of dense and heterogeneous fibrosis. 3D LGE provides detailed fibrosis information, although motion correction techniques are needed to reduce scan times [1, 5]. Scar maps created using ADAS 3D (Galgo Medical, Barcelona, Spain) can be exported into clinical electrophysiology software, but some manual corrections of scar maps may be needed to eliminate CIED-related artifacts.

In conclusion, we have proposed an efficient imaging protocol for pre-ablation procedure planning in patients with CIEDs.

References

1. Andreu et al, *EP Europace* (2015).
2. Soto-Iglesias et al. *JACC EP* (2020).
3. Paterson et al. *Can J Cardiol* (2021).
4. Vigen and Francois. *SIGNA Pulse of MR by GE Healthcare* (2019).
5. Zeilinger et al, *Eur. Radiol.* (2022).

Volumetric Multi-Contrast Dark Blood Cardiac MRI using Readout Balanced SSFP

Robert R Edelman, MD^{1,2}, Amit Pursnani, MD^{1,3}, Jianing Pang, PhD⁴, Ioannis Koktzoglou, PhD^{1,3}

¹Northshore University HealthSystem, Evanston, IL; ²Feinberg School of Medicine, Northwestern University, Chicago, IL; ³University of Chicago Pritzker School of Medicine, Chicago, IL; ⁴Siemens Medical Solutions USA, Chicago, IL

Introduction

With unbalanced steady-state free precession (SSFP) techniques, which include *SSFP-FID* (e.g., FISP, GRASS, FFE) and *SSFP-Echo* (e.g., PSIF, GRASS, T2-FFE), the slice-select and readout gradients each have a net non-zero area over each sequence repetition. These techniques have been used for dark blood imaging but are restricted by their extreme motion sensitivity to imaging of stationary regions [1,2]. An ECG-gated SSFP-FID technique which is unbalanced in the slice-select and readout directions has shown promise for dark blood imaging of the aorta [3] but remains too motion sensitive to be used reliably for the heart, particularly in patients with fast heart rates. To overcome these limitations, we implemented a prototype ECG-gated, multi-shot “readout balanced” 3D SSFP pulse sequence. We hypothesized that it would permit reliable multi-contrast dark blood imaging of the heart and tested it in healthy subjects and patients undergoing clinically indicated cardiac MRI scans.

Methods

This study was approved by the hospital institutional review board. Imaging was performed at 1.5 Tesla (MAGNETOM Avanto_{dot}, Siemens Healthcare, Erlangen, Germany). An SSFP-echo pulse sequence was used with a balanced readout gradient and unbalanced slice-select gradient. Scan parameters included: diastolic ECG gating, two shots, 10 dummy RF pulses, sampling bandwidth = 1184 Hz/pixel, reconstructed voxel = 1.1-mm x 1.1-mm x 1-mm to 3-mm, adjustable spoiler gradient applied along the slice-select direction, breath-holding or free-breathing with navigator gating. For T1-weighting, a non-selective inversion preparation was applied with the inversion time (TI) determined by a TI scout scan. For T2-weighting, a T2prep module was applied with T2prep time of 90 ms and gating to every second heartbeat.

Results

The readout balanced SSFP-Echo technique proved less sensitive to cardiac motion than our previously reported SSFP-FID technique [3]. Regions of late myocardial enhancement were well shown using an inversion preparation (Fig. 1). Navigator gating allowed volumetric imaging of the entire heart as well as T2-weighted dark blood imaging.

Discussion and Conclusion

Our initial results suggest that an ECG-gated readout balanced SSFP-Echo sequence shows promise for volumetric multi-contrast dark blood imaging of the heart, with less motion sensitivity than previously described unbalanced SSFP techniques. Further technical optimization and clinical validation are needed to assess its potential utility.

References

1. Langham, M.C., et al., Acad Radiol, 2016. 23(4): p. 457-67.
2. Yang, A., et al., Sci Rep, 2021. 11(1): p. 2255.
3. Edelman, R.R., et al., J Cardiovasc Magn Reson, 2021. 23(1): p. 127.

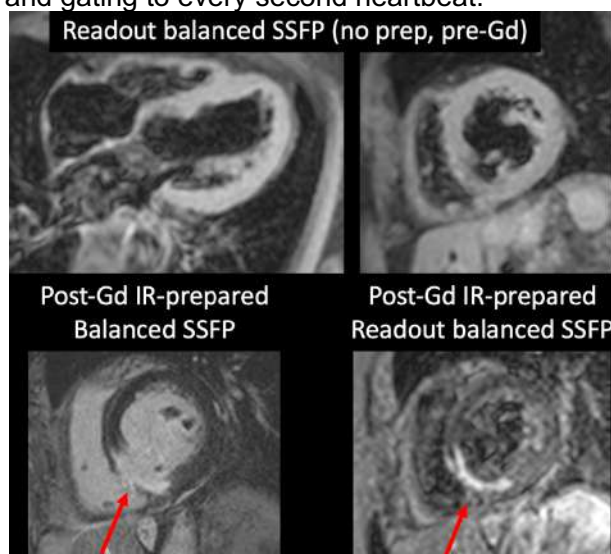


Fig.1. Patient with inferoseptal infarct.

Non-rigid Motion-compensated Whole-heart 18F-FDG PET and 3D T₂ mapping in a hybrid PET- MR system

Alina Schneider¹, Camila Munoz¹, Alina Hua¹, Sam Ellis¹, Sami Jeljeli³, Karl P Kunze², Radhouene Neji^{1,2}, Eliana Reyes¹, Tefik F Ismail¹, René M Botnar¹, Claudia Prieto¹

¹School of Biomedical Engineering and Imaging Sciences, King's College London, London, UK; ²MR Research Collaborations, Siemens Healthcare Limited, Frimley, UK; ³PET Centre, St Thomas' Hospital, King's College London & GSTT London, UK

Purpose: Current clinical guidelines for diagnosing cardiac sarcoidosis (CS) suggest combining several different investigations, including late gadolinium enhancement (LGE) CMR and 18F-fluorodeoxyglucose (18F-FDG) positron emission tomography (PET) in addition to histology¹. Simultaneously acquired 18F-FDG PET and quantitative 2D T₂-mapping has been suggested to improve diagnosis, however misalignments between the two modalities results in challenging clinical interpretations. A free-breathing motion-corrected 3D whole-heart T₂-mapping sequence acquired simultaneously with 18F-FDG PET at a 3T PET-MR system was proposed here. This approach enables the non-rigid motion-correction for both the 3D T₂-mapping and the PET data to the same respiratory position, resulting in aligned volumes for improved clinical interpretation. In this study, we tested this approach in two patients with suspected cardiac sarcoidosis.

Methods: The proposed PET-MR protocol includes a free-breathing 3D T₂-mapping sequence simultaneously acquired with list-mode PET data on a 3T PET-MR system (Biograph mMR, Siemens Healthcare, Erlangen, Germany). The 3D T₂-mapping data (T₂-prep duration = 0, 28 and 55 ms) are acquired using a 3-fold undersampled variable-density Cartesian trajectory². The sequence includes a saturation pulse at each heartbeat to render it heart-rate insensitive and a fat saturation pulse. Image navigators (iNAV)s³ are integrated in the sequence to enable 100% respiratory scan efficiency and predictable scan time. Beat-to-beat translational respiratory motion is estimated from 2D iNAVs (foot-head and right-left directions) and virtual 3D (v3D) iNAV based on autofocus^{4,5} (right-left and anterior-posterior direction). The estimated translational motion is used to correct and bin the MR data and produce respiratory-resolved multi-contrast 3D images. 3D non-rigid motion is then estimated and incorporated into a multi-contrast motion-corrected MR reconstruction⁶ with high-dimensional patch-based low-rank regularization⁷. T₂-maps are finally computed from the multi-contrast MR images using dictionary-matching⁸. The estimated translational respiratory motion is used to also bin the PET data into the same positions as the MR data. The μ -map is registered to the third 3D T₂-map contrast to improve alignment between the μ -map and PET image position. The third 3D T₂-map contrast is used together with the estimated non-rigid motion fields to perform MR-guided motion-corrected PET reconstruction⁹. At the end of this process, 3D MR and PET images are corrected to the same respiratory position, enabling direct fusion of both datasets for analysis and interpretation. We tested this approach in two patients with suspected cardiac sarcoidosis undergoing simultaneous PET-MR imaging. Relevant T₂-mapping parameters include coronal orientation, FOV = 336x336x156-160 mm³, 1.5 mm³ isotropic resolution, TR/TE = 3.45/1.57 ms, FA=15°, scan time ~ 12 min. The proposed technique was compared against conventional 2D T₂ mapping (Fig.1).

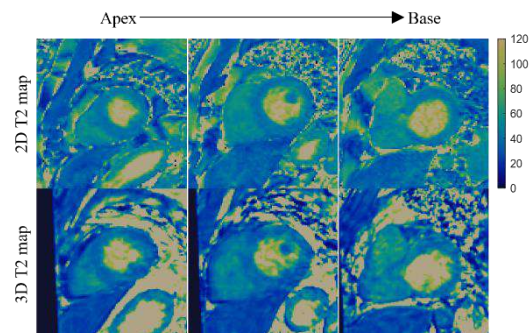


Figure 1 Comparison of the conventional 2D T₂ map and 3D T₂ map. No T₂ elevation were found in these patients.

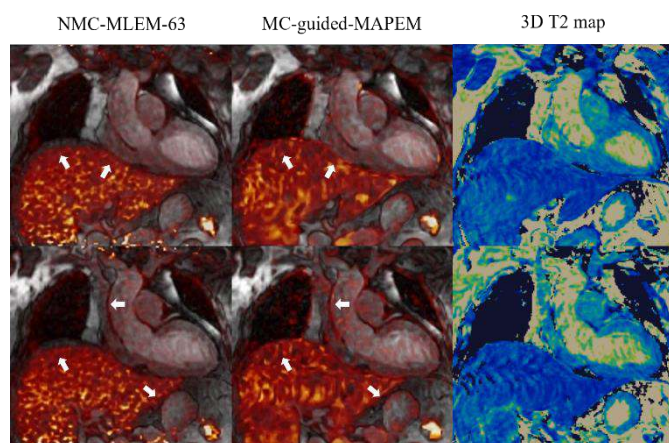


Figure 2 Fused PET-MR image, showing the conventional no motion correction maximum-likelihood expectation-maximization reconstruction and the proposed motion corrected MR-guided maximum a posteriori expectation maximisation. Third column shows the corresponding 3D T₂ maps. Improvements in the correspondence between PET and MR are highlighted with the white arrows.

Results: T₂ values of the proposed 3D T₂-mapping sequence were slightly underestimated compared with the conventional 2D T₂-mapping, however with the conventional 2D T₂ map only 3 slices are acquired, while for the 3D T₂ map 16-segment AHA evaluation ~100 slices at 1.5 isotropic resolution are analysed (Fig.1). Image quality in the PET data visually improved due to motion correction as well as it improved correspondence to the 3D MR data compared to conventional uncorrected PET reconstructions (white arrows on Fig.2). No T₂ elevation or 18F-FDG uptake was observed in these subjects.

Discussion: A novel approach for simultaneously acquired non-rigid motion corrected 18F-FDG PET and 3D T₂-mapping data was successfully evaluated in two patients with suspected cardiac sarcoidosis. 3D T₂ values were comparable with the conventional 2D T₂ values. Improved PET images due to motion correction and MR guidance call for future studies in more patients with cardiac sarcoidosis undergoing simultaneous PET-MR.

References: 1. Birnie, D. H. et al. JACC. 68, 411-421 (2016). 2. Prieto, C. et al. JMRI 41, 738-746 (2015). 3. Henningsson, M. et al. MRM. 67, 437-445 (2012). 4. Atkinson, D., et al. IPMI 1997. Lecture Notes in Computer Science, vol. 1230, 341-354. 5. Schneider, A et al. MRI (2022) 6. Batchelor, P. G. et al. MRM. 54, 1273-1280 (2005). 7. Bustin, A. et al. MRM. 81, 3705-3719 (2019). 8. Weigel, M. JMRI. 41, 266-2.95 (2015). 9. Munoz, C. et al. JNM (2021). 10. Munoz, C. et al. MRM. 79:339 (2018).

Bringing the Spotlight Back to Segmental Strain: Identifying Reproducible Segments for Left Ventricular Strain Evaluation

Siva Sreedhar¹, Chitiboi, Teodora², Maurice Pradella¹, Mohammed Elbaz¹

¹Department of Radiology, Feinberg School of Medicine, Northwestern University, Chicago, IL

²Digital Technology and Innovation, Siemens Healthineers, Princeton, NJ, USA

Purpose: In clinical practice, ejection fraction (EF) plays a significant role in monitoring cardiac (dys)function. Recently, left ventricular (LV) strain by cardiac MRI (CMR) feature tracking (FT) – a measure of cardiac wall deformation – has been rising in popularity as a biomarker for cardiac disease progression, providing additional prognostic value over EF alone¹. Strain is typically only reported globally due to the lower reproducibility of regional strain values. However, regional strain values can be vital in characterizing local changes associated with disease, such as areas of fibrosis. Previous CMR FT-based strain reproducibility studies have focused on an aggregate average of segmental strain reproducibility, with lack of data on individual segmental strain reproducibility². It remains unclear whether the lower average reproducibility for segmental strain is due to a consistently low individual reproducibility over all segments or whether there exist segments of high reproducibility. Therefore, the aims of this study were: 1) to assess the test-retest reproducibility of global and segmental LV FT strain, and 2) to identify segmental FT strain parameters that have comparable reproducibility to the current gold standard of global strain to help introduce a set of potential reproducible region-specific strain measurements.

Methods: With IRB-approval, 12 healthy volunteers [6 Male, age: 44.0±16.2 years] were prospectively acquired for a test-retest study. Each volunteer underwent two CMR scans, spaced two weeks apart, including a standard cine short-axis steady-state free precession MRI scan of the LV and 2-chamber (CH), 3-CH, and 4-CH views. TruFiStrain 2.0 (Siemens Healthineers) was used for automatic segmentation (manually checked by SS) of the LV and tissue-tracking-based strain calculations³. The measured strain parameters were global longitudinal strain (GLS), global circumferential strain (GCS), global radial strain (GRS), AHA 16 segmental radial strain values, AHA 16 segmental circumferential strain values, and 6 segmental longitudinal strain values, based on 2-CH, 3-CH, and 4-CH views. First, to assess test-retest reproducibility in global and segmental strain, the coefficient of variation (CV) and intraclass correlation coefficient (ICC) with a 95% confidence interval (CI) were calculated. Second, to determine which segmental strain values had a

reproducibility equivalent to the corresponding global strain reproducibility level, we assessed: 1) the absolute relative strain difference $|(Scan1-Scan2)/Scan1|$ between the first and second scan for the segmental and associated global strain values, and 2) the relative differences in per-segment strain versus global strain using a matched paired t-test or Wilcoxon signed-rank test (per normality). Comparable reproducibility of a segment's strain versus global strain was defined as a non-significant difference ($p>0.05$) in absolute relative difference between the segment's and corresponding global strain.

Results: The global strain values for Scan 1 were $-15.2\% \pm 0.9\%$ for GLS, $27.3\% \pm 5.1\%$ for GRS, and $-16.4\% \pm 1.7\%$ for GCS. The global strain parameters showed good reproducibility with GLS ICC = 0.76 (95% CI = 0.35, 0.92), GRS ICC = 0.77 (95% CI = 0.37, 0.93), and GCS ICC = 0.67 (95% CI = 0.19, 0.89). All global parameters had CV values < 10% (GLS = 3.89%, GRS = 9.98%, GCS = 5.62%). Circumferential strain showed 10 segments with reproducibility comparable to GCS. Radial strain showed 10 segments comparable to GRS (Fig. 1). Longitudinal strain showed 3 segments comparable to GLS: the apical anterior segment in both the 2-CH (CV = 10.95%), and the 3-CH (CV = 23.47%) views, and the apical lateral segment in the 4-CH view (CV = 21.04%). Table 1 shows results of the global and reproducible segmental strain test and retest scans.

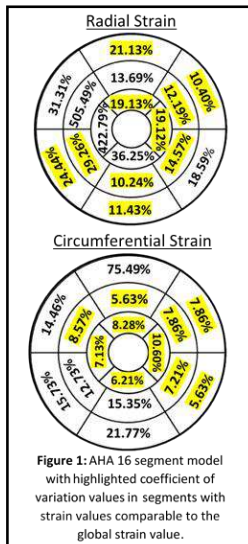
Discussion: This study quantified test-retest FT strain reproducibility of individual LV segments compared to global strain reproducibility. The results demonstrated variable reproducibility of segmental strain regions depending on the type of measured strain. Notably, the results revealed that there exist segments with similar reproducibility levels to the global strain. Circumferential strain and radial strain showed the largest number of reproducible segments. The circumferential strain at the basal inferolateral, mid anterior, and apical inferior segments showed the highest reproducibility. This is consistent with segmental reproducibility in echo data, which has found highest reproducibility for circumferential strain compared to longitudinal and radial⁴. In terms of regions, the apical layer for the circumferential and longitudinal strain contained the highest fraction of segments with equivalently reproducible strain to global strain. This may be important when monitoring diseases that affect the LV apex, such as Takotsubo cardiomyopathy and apical HCM⁵. Furthermore, the used automated segmentation mitigates variability, thus facilitating reproducibility. However, more investigation is required on the accuracy and generalization of this automated segmentation. Future work should assess the prognostic value of these segmental strain parameters.

References: [1] Eitel, I., et al. (2018), JACC. [2] Morais, P., et al. (2017), JCMR. [3] Chitiboi, T., et al, (2020), ISMRM. [4] Kleijn, S., et al. (2012), Eur. Heart J. [5] Cisneros, S., et al. (2011), Insights Imaging.

Table 1: Relative % difference between Scan 1 and Scan 2 for Global Strain and equivalently reproducible Segmental Strain.

	Region	% Diff.*	95% CI
G*	GLS	4.83%	[7.57%, 2.10%]
	GRS	11.61%	[5.04%, 18.17%]
	GCS	6.29%	[2.73%, 9.85%]
LS*	2C Apical Anterior	11.82%	[5.13%, 18.5%]
	3C Apical Anterior	27.55%	[11.96%, 43.14%]
	4C Apical Lateral	24.96%	[10.84%, 39.09%]
Radial Strain	Basal Anterior	27.05%	[11.74%, 42.35%]
	Basal Inferoseptal	32.20%	[13.98%, 50.41%]
	Basal Inferior	15.43%	[6.7%, 24.17%]
	Basal Anterolateral	13.62%	[5.91%, 21.32%]
	Mid Inferoseptal	30.93%	[13.43%, 48.42%]
	Mid Inferior	11.90%	[5.17%, 18.63%]
	Mid Inferolateral	17.28%	[7.5%, 27.06%]
	Mid Anterolateral	16.44%	[7.14%, 25.74%]
	Apical Anterior	21.28%	[9.24%, 33.32%]
	Apical Lateral	22.58%	[9.8%, 35.35%]
Circumferential Strain	Basal Inferolateral	6.45%	[2.8%, 10.1%]
	Basal Anterolateral	8.87%	[3.85%, 13.89%]
	Mid Anterior	6.41%	[2.78%, 10.03%]
	Mid Anteroseptal	9.25%	[4.02%, 14.48%]
	Mid Inferolateral	8.38%	[3.64%, 13.12%]
	Mid Anterolateral	8.18%	[3.55%, 12.81%]
	Apical Anterior	9.79%	[4.25%, 15.33%]
	Apical Septal	7.78%	[3.38%, 12.18%]
	Apical Inferior	7.68%	[3.34%, 12.03%]
	Apical Lateral	10.49%	[4.55%, 16.42%]

*% Diff. = $|(Scan 1 Strain - Scan 2 Strain)/(Scan 1 Strain)|$
G = global, LS = longitudinal strain



Improving reproducibility of cardiac ASL using T1 and flip angle corrected reconstruction

M. Božić-Iven^{1,2}, S. Rapacchi³, I. Pierce⁴, G. Thornton⁴, Q. Tao², L. Schad¹, T. Treibel⁴, S. Weingärtner²

¹Computer Assisted Clinical Medicine, Heidelberg University, Mannheim, Germany; ²Department of Imaging Physics, Delft University of Technology, Delft, The Netherlands; ³Faculté de Médecine, Université Aix-Marseille, Marseille, France; ⁴Barts Heart Centre, Barts Health NHS Trust, London, United Kingdom

Purpose: Myocardial Arterial Spin Labeling (myoASL) may offer a contrast agent free alternative to first pass myocardial perfusion. MyoASL has shown to be sensitive to changes in myocardial perfusion as induced by vasodilatory stress¹ and provides myocardial blood flow (MBF) values that are in agreement with positron emission tomography measurements². However, limited reproducibility and robustness have hampered more widespread clinical use so far. In this work, we sought to investigate how variations in physiological parameters such as the blood T1 time (T1B) and system parameters such as the acquisition flip angle (FA) influence myoASL based MBF. Further, we propose an improved acquisition and reconstruction approach for reproducible myoASL in vivo.

Methods: In previous studies, a fixed, literature-based T1B has been used to reconstruct myoASL-MBF from Buxton's general kinetic model³. However, T1B is known to vary with factors such as hematocrit levels⁴. Bloch simulations were performed to assess the effect of a mismatch in the actual and reconstruction T1B (-300 – 300 ms) on myoASL-MBF. Moreover, relative FA deviations (actual/prescribed FA) between 0.5 and 1.5 were simulated to assess myoASL-MBF variations due to a varying acquisition FA. A double ECG-triggered Flow-Alternating Inversion Recovery (FAIR) sequence⁵ was used in all simulations and measurements. Phantom measurements were performed in a NiCl₂-doped agarose phantom with relative FA deviations of 0.07-2.0. Six pairs of control and tag images were acquired with bSSFP and spoiled GRE (spGRE) readout. With bSSFP, two baseline images were acquired, while with spGRE one of the two was directly preceded by a WET saturation pulse ("saturated baseline", Sat-BL). All images were acquired with FA 70°/15° (bSSFP/spGRE), voxel size 2x2x8mm³. An additional MOLLI⁶ T1-map was acquired in phantom and in vivo. In-vivo images of 6 healthy subjects (6 male, 35±4 years) were obtained during mid-systole⁷ in 12-18s long breath-holds per image pair depending on the heart rate. Imaging was performed across two 3T scanners. After excluding image pairs with skipped heartbeats, all images were registered groupwise⁸. Individual T1B values from the T1 maps were used to reconstruct pixel- and segment-wise MBF. In order to alleviate the flip angle dependence in spGRE, the difference between the original and Sat-BL image was used for reconstruction instead of the original baseline signal. Thereby, the FA dependent magnetization transfer function is reproduced in the model.

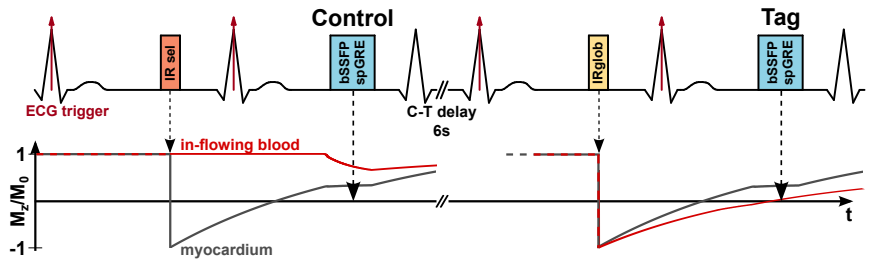


Figure 1: Diagram and magnetization dynamics during the double ECG-triggered Flow-Alternating Inversion Recovery myocardial ASL (FAIR-myocardial ASL) sequence. The effect of the snap-shot image readout on myoASL based perfusion is investigated in this work.

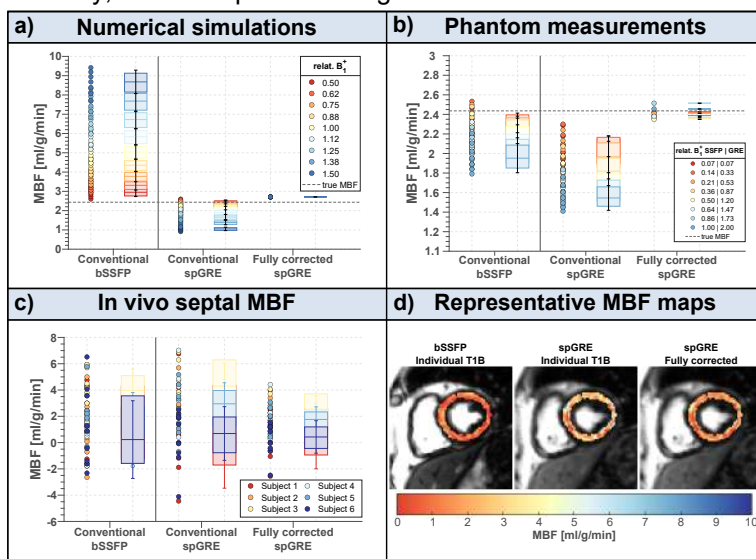


Figure 2: MBF values reconstructed with and without T1 and flip angle (FA) correction. **a)** Simulated and **b)** phantom MBF for varying blood T1 (T1B) and acquisition FA with bSSFP and spGRE readout. In vivo **c)** septal MBF and **d)** perfusion maps from bSSFP and spGRE for one representative subject.

Results: Simulation and phantom results show a coefficient of variability (CoV) up to 8.5 % and 8% across different blood T1 times, respectively (Fig. 2a,b). Variability in the acquisition FA leads to MBF variation of up to 37%/24% and 5%/12% (bSSFP/spGRE) in simulations and in phantom, respectively. If spGRE-based MBF is reconstructed with a correct T1B and including Sat-BL, the MBF variance is fully eliminated in simulations and the overall CoV is reduced by 83% in phantom measurements. In vivo mean septal MBF was 1.63±2.81/1.20±4.03 ml/g/min (bSSFP/spGRE) without correction and 0.74±2.35 ml/g/min for fully corrected spGRE (Fig. 2c). Using adaptive T1B and Sat-BL reduced septal MBF standard variation by 40% and CoV by 5.6%. **Discussion:** Our results demonstrate that parameters related to the physiology and the imaging readout lead to variations in MBF with conventional myoASL. If not accounted for, this might impair the reproducibility of FAIR-myocardial ASL. In case of spGRE, the MBF variation can be reduced by 83% in phantom and 5.6% in vivo if individual T1B and Sat-BL is used leading to more robust MBF reconstruction in FAIR-myocardial ASL.

References: 1) Zun, Z., et al., *JACC: Cardiovasc. Imaging* (2011). 2) Zun, Z., et al., *MRM* (2009). 3) Buxton, R.B., et al., *MRM* (1998). 4) Lu, H., et al., *MRM* (2004). 5) Do, H.P., et al., *MRM* (2017). 6) Messroghli, D. R., et al., *MRM* (2004). 7) Henningsson, M., et al., *NMR Biomed.* (2020). 8) Tao, Q., et al., *JMRI* (2018).

Intra and inter-rater agreement of LA fibrosis quantification derived from 3D LGE using b-SSFP readout and XD-GRASP reconstruction

Julia Hwang¹, Suvai Gunasekaran¹, Aggelos Katsaggelos¹, Rishi Arora¹, Mehri Mehrnia¹, Michael Markl¹, Saman Nazarian³, Daniel Lee¹, Mohammed Elbaz¹, Rod Passman¹, Eugene Kholmovski², Daniel Kim¹
¹Northwestern University, Feinberg School of Medicine, Chicago, IL, United States, ²Johns Hopkins University Baltimore, MD, United States, ³University of Pennsylvania, Philadelphia, PA, United States

Purpose: Left atrial (LA) fibrosis is known to be a substrate for atrial fibrillation (AF). 3D late gadolinium enhancement (LGE) is the most promising modality for quantification of LA fibrosis in AF patients [3]. Our lab has developed a 3D LA LGE sequence using b-SSFP readout and XD-GRASP reconstruction. The purpose of this study was to evaluate intra- and inter-rater agreement of LA fibrosis quantification in order to assess the reproducibility of our analysis methodology.

Methods: We randomly selected 20 patients (mean age = 62.8 ± 11 years, 19/1 males/females) with AF who had underwent 3D LA LGE using a 1.5T MRI scanner (Siemens, AERA, Avanto) before first-time ablation. The 3D LA LGE data were reconstructed using the XD-GRASP framework as previously described [2]. Relevant imaging parameters are summarized in Table 1. LA wall contours were manually drawn in each axial plane using ADAS 3D (Galgo Medical, Barcelona, Spain) independently by two different raters. The mitral valve and pulmonary veins were excluded to focus analysis on LA tissue. The image intensity ratio (IIR) cutoff used to calculate fibrosis was 1.2 as previously described [1].

Results: As summarized in Table 3, the intra-rater intraclass correlation coefficient (ICC) was excellent (ICC> 0.90) for all categories and good for fibrosis quantification (ICC = 0.75). Inter-rater ICC was excellent (ICC> 0.90) for surface area, blood pool intensity and volume, good for sphericity (ICC = 0.87) and moderate for fibrosis quantification (ICC = 0.56).

Discussion: This study shows that our image acquisition and analysis methods used to quantify LA fibrosis from processing 3D LA LGE produce moderate (inter-rater ICC) to good (intra-rater) reliability. The lower ICC's observed for fibrosis values can be explained by the limited spatial resolution (2.2 mm slice thickness), which makes it challenging to segment the LA wall accurately, and the subsequent thresholding-based fibrosis quantification with an IIR cutoff. Future studies include improving both the image quality and segmentation using deep learning.

References: [1] Benito E.M., et. al. EP Europace 2016 [2] Gunasekaran, S. et.al. Radiology: Cardiothoracic Imaging [3] Marrouche, N.F. et. al. JAMA 2014

Table 1. Relevant imaging parameters			
TE/TR	Scan time	Resolution	Flip angle
1.8/3.5 ms	5.9 min ± 1.3	1.5 x 1.5 x 2.2 mm ³	40

Table 2. Average LA parameters	
	Mean values
Fibrosis (%)	6.0 ± 1.9
Volume (mL)	108 ± 33
Sphericity (%)	76 ± 3

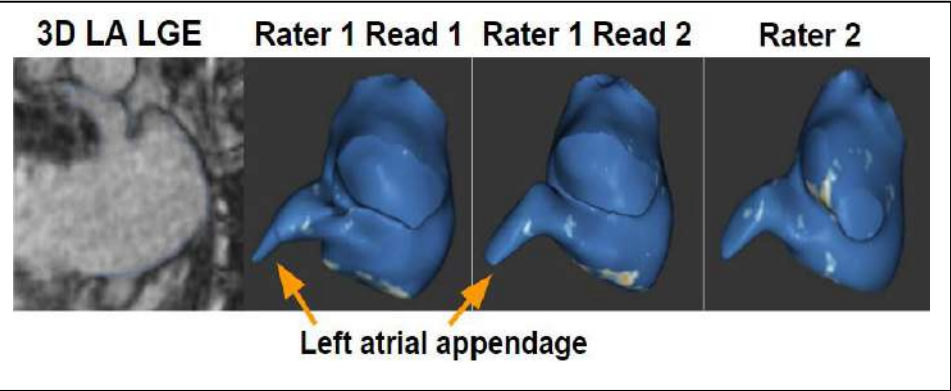


Table 3. ICC values		
	Intra ICC	Inter ICC
Surface Area	0.95	0.92
Fibrosis	0.75	0.56
Mean blood pool intensity	0.99	0.99
Sphericity	0.93	0.87
Volume	0.97	0.96

Figure 1

A randomized controlled trial of statins to reduce inflammation in unruptured cerebral aneurysms using high resolution vessel wall MRI

Chengcheng Zhu¹, Huibin Kang², De-Cai Tian³, Binbin Sui⁴, Mahmud Mossa-Basha¹, Michael R Levitt⁵, David Hasan⁶, Xinjian Yang², Yisen Zhang²

1. Radiology, University of Washington, USA 2. Neurosurgery, Tiantan Hospital, China 3. Neurology, Tiantan Hospital, 4. Radiology, Tiantan Hospital 5. Neurosurgery, University of Washington, USA 6. Neurosurgery, Duke University, USA.

Background: Intracranial aneurysm (IA) is a common disease with a prevalence of 3-5% in the general population. Inflammation and atherosclerotic changes play a critical role in the formation and rupture of IAs. Statins may reduce aneurysmal inflammation, but several clinical studies did not reach a consistent conclusion [1]. Aneurysm wall enhancement as shown on contrast-enhanced vessel wall magnetic resonance imaging (VW-MRI) is a surrogate and sensitive biomarker of aneurysm wall inflammation [2]. Our study aimed to evaluate if statins could decrease UIA wall enhancement, suggesting modulation of inflammation.

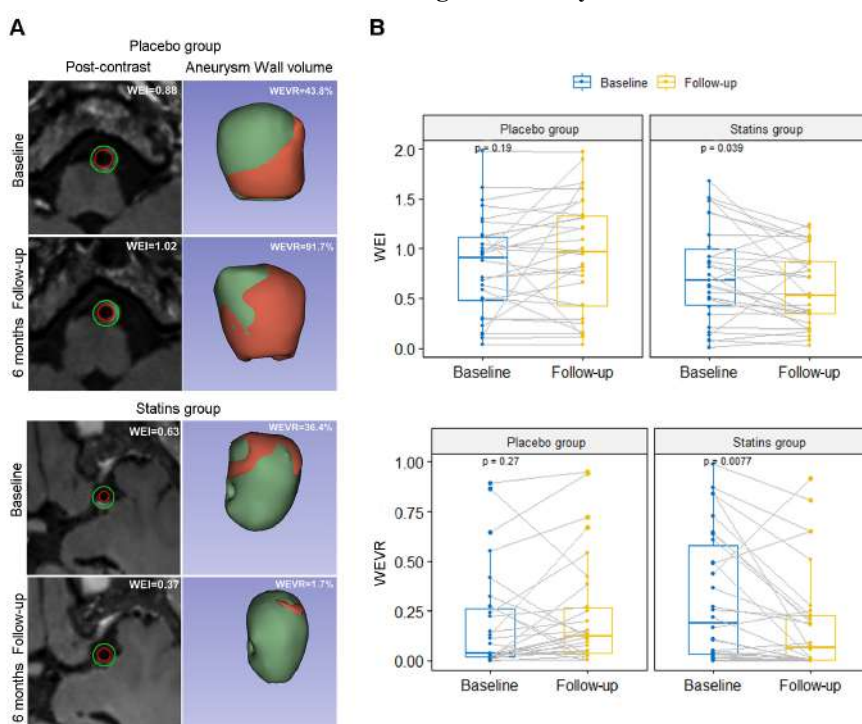
Materials and Methods: In this double-blind, randomized, placebo-controlled trial (RCT, registered with ClinicalTrials.gov, NCT04149483), 60 patients with UIAs were enrolled 2019-2021. They were randomized 1:1 to either atorvastatin 20mg daily or placebo. Subjects were imaged at baseline and at 6-month follow up with VW-MRI. MR imaging was performed at Siemens 3.0T (Prisma) with a 32-channel head coil. 3D T1-weighted turbo-spin-echo with variable flip angle (SPACE) was acquired in sagittal plane with whole head coverage and 0.7 mm isotropic resolution before and immediately after gadolinium contrast injection: TR/TE: 800/22ms, echo train length 52, scan time 5:30s. The primary endpoint was change in the quantitative wall enhancement index [2] ($WEI = SI_{WallPre} / SI_{WhitematterPre} - SI_{WallPost} / SI_{WhitematterPost} / (SI_{WallPre} / SI_{WhitematterPre})$) and three dimensional wall enhancement volume rate (WEVR): Aneurysm Enhancement Volume/Whole Aneurysm Volume x100%.

Results: In the atorvastatin group, the WEI and WEVR decreased significantly at 6-month follow-up compared to baseline ($P=0.039$ and $P=0.008$, respectively), but not in the placebo group ($P=0.188$ and $P=0.268$ respectively). Furthermore, circulating plasma levels of C-reactive protein, tumor necrosis factor- α and interleukin-6 in the atorvastatin group decreased significantly at 6 months compared to baseline ($p=0.033$, 0.049 and 0.023 , respectively). Aneurysm size did not change significantly in either group.

Conclusion/Discussion: In this RCT, we found that statins decreased wall enhancement of UIAs, a surrogate marker for aneurysm wall inflammation. The quantitative WEI and WEVR as well as several circulating inflammatory biomarkers decreased significantly after 6-month atorvastatin treatment. However, aneurysm size did not change in either group. **To the best of our knowledge, this is the first prospective randomized controlled trial on the effect of statins for changes in aneurysm wall enhancement as shown in VWI-MRI.**

The use of quantitative and three-dimensional enhancement characters was a unique advantage of our study. By using VWI-MRI, we are able to observe the inflammatory changes of the aneurysmal wall within a short period of 6 months, before any changes in size or shape of IAs. VWI-MRI has great potential in future image-guided clinical trials to investigate novel treatment of IAs. Our results should be validated with larger sample sized RCTs.

Reference: 1. Marbacher S, *Journal of Neurosurgery*. 2012 116: 638-642.; 2. Fu Q, *Stroke* 2021 52: 213-22



Noise Reduction in Magnetic Resonance Fluid Dynamics Using Deep Learning

Miku Nakashima¹⁾ Haruo Isoda^{2,1)} Yoshiyuki Hirano¹⁾

1. Nagoya University Graduate School of Medicine 2. Brain and Mind Research Center, Nagoya University

Purpose

Magnetic resonance fluid dynamics (MRFD) and computational fluid dynamics (CFD) are used to evaluate hemodynamics of intracranial aneurysms (IAs)¹⁾. CFD is believed to be highly accurate, but it takes time to analyze. On the other hand, MRFD is an analysis method that uses 4D flow MR imaging (MRI)²⁾ and 3D time of flight MR angiography (3D TOF MRA) data collected directly from humans in a short period of time³⁾. However, the MRFD contains noise derived from the 4D flow MRI, which reduces the accuracy of the 3D velocity vector field in the analysis result. The objective of this study was to use artificial intelligence (AI) with deep learning to reduce MRFD noise and convert it into results with accuracy comparable to CFD.

Methods

Our study was approved by our institutional review board. The subjects were 28 patients with IAs who underwent 4D Flow MRI and CFD at the university and two affiliated institutions. Of these, 23 cases were used as training data, and 5 cases were used to validate the accuracy of the deep learning model after training. Generating Training data : The training data consisted of 23 patients with IAs. 3D velocity data of CFD were used as the grand truth data. To add noise that mimics MRFD, phase and magnitude images were created from the 3D velocity data of the CFD (grand truth data) and transformed onto k-space using the Fast Fourier Transform. Then, an appropriate Gaussian distribution noise that mimics MRFD was added to k-space⁴⁾, and the inverse Fourier transform was used to convert the data back to 3D velocity data, which was used as the input data. Data augmentation was performed using inversion, creating a total of 9972 data sets as the training data. Network Architecture : Using the WIN5-RB⁵⁾ structure, a noise reduction model. Accuracy Validation : After the deep learning model was trained with the training data, qualitative and quantitative evaluations were conducted to examine the prediction accuracy using CFD and MRFD data from five patients who were not used in the training data. Angle Similarity Index (ASI)⁶⁾ and Magnitude Similarity Index (MSI)⁶⁾ of the 3D velocity data were used as quantitative evaluation indices, with CFD as the standard.

Result

3D velocity field of prediction result of deep learning model with MRFD as input data showed reduced noise in the velocity (Figure 1 (A)(B)) and well-connected streamlines within an IA (Figure 1 (C)(D)). The accuracy of ASI and MSI improved in the prediction results (Table 1).

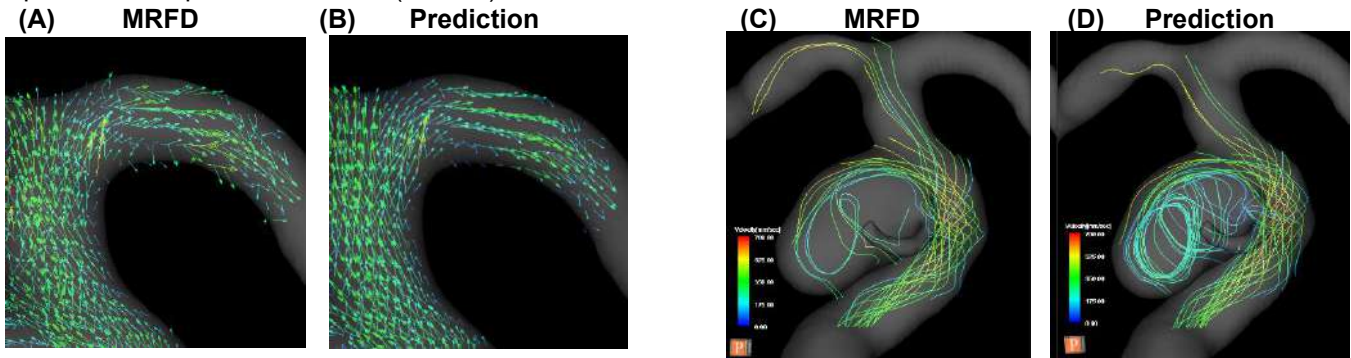


Figure 1. Qualitative evaluation before and after deep learning model prediction using MRFD in patient with an intracranial aneurysm

(A) 3D velocity field of MRFD (B) 3D velocity field of prediction result of deep learning model with MRFD as input data
(C) Streamline of MRFD (D) Streamline of prediction result of deep learning model with MRFD as input data

Table 1. Quantitative evaluation before and after deep learning model prediction using MRFD in patients with five intracranial aneurysms

		Case01	Case02	Case03	Case04	Case05
ASI	MRFD	0.71	0.80	0.82	0.71	0.73
	Predict	0.74	0.83	0.83	0.75	0.76
MSI	MRFD	0.85	0.88	0.83	0.85	0.84
	Predict	0.86	0.88	0.84	0.86	0.85

ASI, angle similarity index; MSI, intensity similarity index; MRFD, input data as magnetic resonance fluid dynamics, Prediction, prediction results of deep learning model with MRFD as input data

Discussion and Conclusion

By using a deep learning model trained with appropriate noise mimicking the MRFD in the k-space of the CFD 3D velocity data, the 3D velocity data of prediction result of deep learning model with MRFD as input data were qualitatively and quantitatively reduced in noise.

Reference

1)Isoda H, et al. Neuroradiology 2010; 52: 913-20. 2)Markl M, et al. J Magn Reson Imaging 2003; 17: 499-506.
3)Isoda H, et al. Neuroradiology 2010; 52: 921-8 4)Ferdian E, et al. Frontiers in Physics 2020; 8: 138
5)Liu P, et al. arXiv e-printsarXiv :1707.05414 (2017) 6)J Biomech Eng 2014; 136:4.

Deep-MyoSeg: Deep learning-based approach for myocardium segmentation in clinical T₁-MOLLI and T₂-bSSFP maps

R. Jakubicek^{1,2}, C. Velasco¹, A. Hua¹, A. Fotaki¹, C. Prieto¹, R. M. Botnar¹

¹School of Biomedical Engineering and Imaging Sciences, King's College London, London, UK

²Department of Biomedical Engineering, Brno University of Technology, Brno, CZ

Purpose: Accurate myocardium segmentation is an essential part of cardiac magnetic resonance (CMR) analysis, but it is a laborious and error-prone task for evaluators. Recently, several studies have shown that it can be performed automatically using machine learning-based methods¹. Nevertheless, obtaining a robust and generalized network that works on multiparametric data with a high success rate is challenging due to the diverse range of acquisition sequences, various image contrast, noise, artifacts, or high variability in determining the ground truth myocardial contours. In this work, we propose and implement a general approach to enable fine-tuning the neural network for multiparametric CMR myocardial segmentation and we present achieved results of the proposed Deep-MyoSeg on clinical T₁-MOLLI and T₂-bSSFP maps.

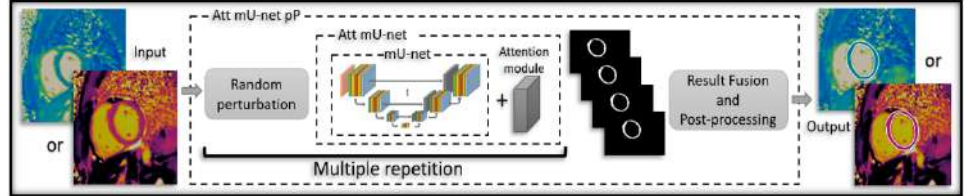


Fig.1. Block diagram of the proposed approach containing an U-net (mU-net) segmentation model, an Att U-net with attention modules, and a version containing the proposed post-processing block based on multiple repetition prediction with random perturbation.

Methods: We collected a mixed, relatively heterogenous dataset of T₁, T₂, LGE and CINE cardiac MR images containing a total of ~7000 2D annotated CMR images. This includes a novel multiparametric 3D joint T₁/T₂² mapping dataset, clinical reference 2D T₁-MOLLI and T₂-bSSFP maps and publicly available datasets such as ACDC³, MyoPS⁴ and Emidec⁵. The final dataset was split into training and test dataset in a 4:1 ratio. The proposed network architecture is based on the fully convolutional network type of U-net (called mU-net) including batch normalization and residual connections in each convolution blocks. Pixel size resampling into 1x1 mm² and image value standardization are also performed in the input layer. Each subsequent block contains two convolutional layers [3x3] with ReLU and at the end of each block there is a MaxPooling layer [2x2;2]. The encoder/decoder depth is designed as [1,32,64,128,256]. Special training approaches were implemented including pre-training on CINE data², training data augmentation (translation, rotation, scaling), consistency regularization using unlabelled data and hard data mining to avoid overfitting. Our proposed mU-net was further compared to two additional refined networks based on the first one: a) a mU-net including attention modules (Att mU-net) and b) an Att mU-net with further post-processing (Att mU-net pP) based on multiple predictions (in which the input image is perturbed with random geometric translation, rotation, and mirroring) and subsequent fusion of predictions via statistic median value (Fig.1). The employed loss function was defined as $\mathcal{L} = 1 - \text{dice}(g(x), f(x)) + \lambda \|w\|_2^2$ for all three-network version, where $g(x)$ is the predicted mask, $f(x)$ is the ground truth mask and w are network weights. This loss function was optimized by Adaptive stochastic gradient descent method (lr=0.0024) with L2 regularization ($\lambda=10^{-7}$). The hyperparameters were optimized by Bayes optimization.

Results and discussion: Three slices of 2D T₁ and T₂ maps (N=30 subjects) were annotated by a medical expert, and resulting segmentation was compared via Dice coefficient and Hausdorff distance (HD) against the networks' predictions. The Dice score improved for the networks with attention modules and post-processing. The predictions on T₂ maps more accurately match the manual segmentations than on T₁ maps and the best results are provided by Att mU-net pP. The higher HD value for the Att U-net variant (2.65) is due to smoother contours and greater distance between inner and outer myocardial contours (see Fig.2A). In the case of T₂ maps, the network provides a higher rate of false positive contours in similar anatomical structures increasing HD error. The proposed pP allows removing of the objects and thus significantly decreasing the HD error. For T₁ maps, the incidence of false positive predictions is minimal.

Conclusion: We designed and implemented a general deep learning-based approach for multiparametric myocardial segmentation and fine-tuned it for specific clinical T₁ and T₂ CMR myocardial segmentation. Based on the results, the network was shown to have high potential for segmentation generalization. Future validation studies of our proposed network on other multiparametric datasets (e.g., LGE, CINE, or other contrast-weighted images) are warranted.

References: ¹Ch. Chen et al, FICM, 2020, doi.org/10.3389/fcvm.2020.00025 ²G. Milotta et al, MRM, 2020. doi.org/10.1002/mrm.28039, ³O. Bernardo et al., IEEE TMI, 2018, doi:10.1109/TMI.2018.2837502, ⁴X. Zhuang, IEEE PAMI, 2019, doi:10.1109/TPAMI.2018.2869576, ⁵A. Lalande et al., Data, 2020.

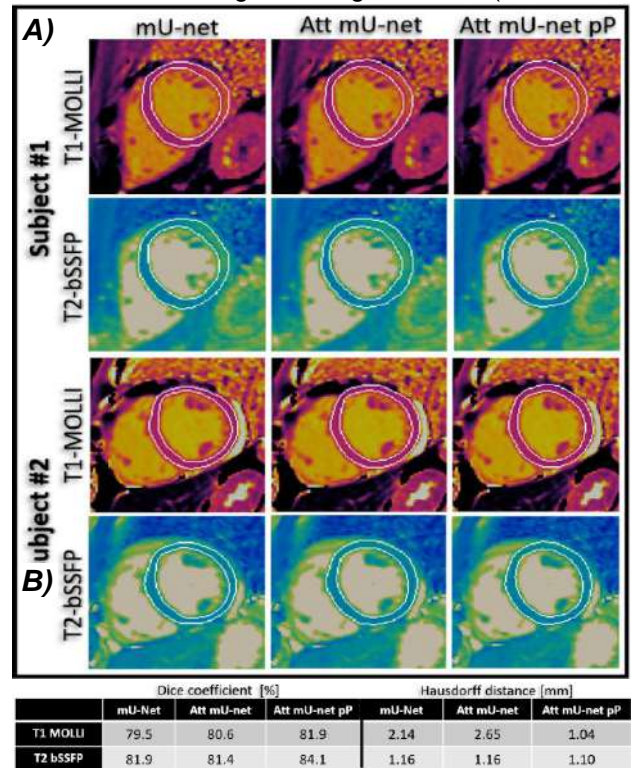


Fig.2. A) Examples of two-subject segmentation results for the three proposed approaches on T₁ and T₂ maps separately. **B)** Network evaluation table on the T₁ and T₂ clinical validation dataset.

Conditional Invertible Neural Network for Rapid Dictionary and Parameter Map Generation for Cardiac Magnetic Resonance Fingerprinting

Thomas Fletcher, Carlos Velasco, Gastao Cruz¹, Alina Schneider¹, René M Botnar¹, Claudia Prieto¹

¹School of Biomedical Engineering and Imaging Sciences, King's College London, UK

Purpose: Dictionary generation and pattern matching are significant bottlenecks for cardiac Magnetic Resonance Fingerprinting (MRF). Dictionaries depend on the subject's cardiac rhythm and must be generated for each new scan and the time taken for both dictionary generation and pattern matching grow exponentially with the number of parameters encoded. Separate neural networks have been proposed to speed up either dictionary generation¹ or parameter map generation² for cardiac MRF. Herein, we propose a conditional invertible neural network^{3,4} (cINN) capable of both rapidly generating dictionaries or quantitative maps from highly undersampled cardiac MRF images in 3.2 seconds for a T_1 , T_2 and $T_{1\rho}$ sequence⁵.

Methods: Training data was generated by using ground-truth maps derived from 20 separate scans using a T_1 , T_2 , $T_{1\rho}$ cardiac MRF sequence⁵. To encode the dependence of cardiac rhythm on the measured signals within the network, 1056 unique RR sequences were obtained from ECG data from patient scans. Dictionaries were generated using EPG⁶ simulations and these RR sequences so that from each of the 20 sets of ground truth maps undersampled MRF images could then be simulated according to different cardiac rhythms. In total, 1056 sets of undersampled MRF images and their corresponding ground-truth parameter maps were simulated and a 70:20:10 training, validation, test split was used.

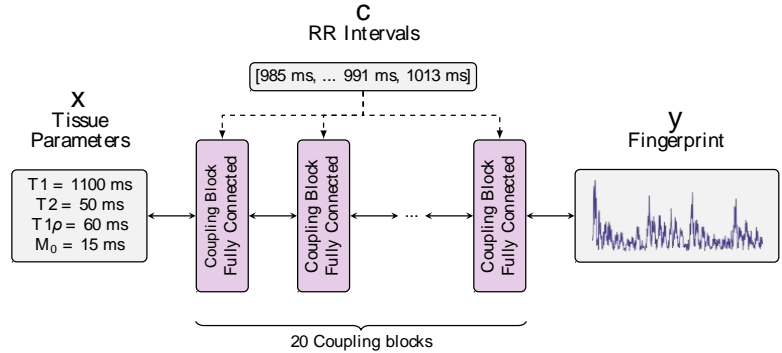


Fig 1: Network Architecture of the cINN-cMRF, consisting of 20 invertible coupling blocks containing fully connected networks and conditioned on the RR intervals. When run in the forwards direction, the network preforms dictionary generation, while in the backwards direction the network performs parameter estimation.

The conditional invertible neural network for cardiac MRF (cINN-cMRF) consists of 20 invertible affine GLOW⁷ coupling blocks, each followed by a random permutation layer and conditioned on the RR intervals. Each invertible block consists of a feedforward neural network with an input and output layer and 3 hidden layers of 480 neurons. The inputs to the cINN-cMRF are the T_1 , T_2 , $T_{1\rho}$, M_0 values and the RR intervals in the forwards direction (dictionary generation) or the 480-element complex vector of the fingerprint and the RR intervals in the backwards direction (map generation). The network is constructed using the FrEIA⁸ package and written in PyTorch.

Results: The proposed cINN-cMRF produces accurate parameter maps in 3.2 seconds without the need for a dictionary, as can be seen in Figure 2. The cINN-cMRF achieves low relative errors, particularly for myocardium and a SSIM>0.84 across the different parameter maps. In addition, the network is capable of accurate parameter estimation across a wide range of different cardiac rhythms. Training the same network on a dataset of fully sampled EPG-generated fingerprints enabled the network to accurately generate dictionaries with inner products >0.9993 when compared to the reference fingerprints.

Discussion: We have presented a conditional invertible neural network for cardiac MRF capable of rapid dictionary and map generation. The network can accurately estimate maps from simulated undersampled MRF images over a wide range of cardiac rhythms in 3.2 seconds for a T_1 , T_2 , $T_{1\rho}$ sequence. Future work will extend this network to *in-vivo* acquisitions and incorporate a learned latent space to determine full posterior parameter distributions for ambiguous cases.

References:

¹Hamilton, J et al. IEEE, 2019;108(1):69-85.

²Hamilton, J et al. MRM, 2021;85(4):2127-2135

³Ardizzone, L et al. arXiv, 2018;arXiv:1808.04730. ⁴Balsiger, F et al. MLMIR, 2020;60-69. ⁵Velasco, C et al. MRM, 2022;87(4):1992-2002. ⁶Weigel, M et al. MRI, 2015;41(2):266-295. ⁷Kingma, D et al. arXiv, 2018;arXiv:1807.03039

⁸Framework for Easily Invertible Architectures (FrEIA), <https://github.com/VLL-HD/FrEIA>

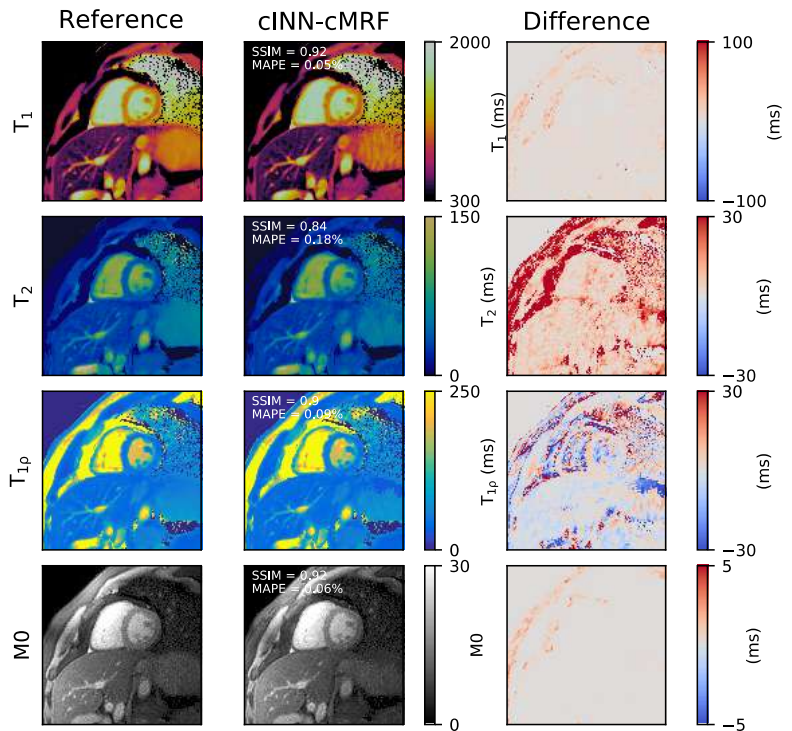


Fig 2: Parameter maps generated using the cINN-cMRF and simulated highly undersampled MRF images as input compared to reference maps using conventional dictionary matching. The cINN-cMRF accurately generates maps with low relative errors for myocardium.

In vitro Relaxometry Comparison of Three USPIO Agents for Magnetic Resonance Imaging at 3.0T

Zhengyang Ming,^{1,3} Caroline M. Colbert,^{1,2,3} Arutyun Pogosyan,² J. Paul Finn,^{1,3} Kim-Lien Nguyen^{1,2,3}

¹Physics and Biology in Medicine Graduate Program, David Geffen School of Medicine at UCLA

²Division of Cardiology, David Geffen School of Medicine at UCLA and VA Greater Los Angeles Healthcare System

³Diagnostic Cardiovascular Imaging Research Laboratory, Department of Radiological Sciences, David Geffen School of Medicine at UCLA

Purpose: Because of its long intravascular half-life and performance as a blood pool imaging agent, the ultrasmall, superparamagnetic iron oxide (USPIO) nanoparticle ferumoxytol (Feraheme) has unique applications in cardiac, vascular and body MRI^{1,2,3}. However, limited availability and high cost have hindered its clinical adoption. The recent clinical availability of generic ferumoxytol (Sandoz, Princeton, NJ), and the emergence of Molday ION (BioPal, Worcester, MA) as an alternative USPIO with similar properties as ferumoxytol, provide additional opportunities to expand the use of USPIO-enhanced MRI techniques. The purpose of this study is to compare ex-vivo (in vitro) relaxometry of Feraheme, generic ferumoxytol, and Molday ION at 3.0T.

Methods: We prepared phantoms composed of Feraheme, generic ferumoxytol, and MoldayION at concentrations of 1/2048 [0.26 mM], 1/1024 [0.52 mM], 1/512 [1.05 mM], and 1/256 [2.10 mM] in saline, plasma, and human blood. Using a clinical 3.0T scanner (Skyra®, Siemens Medical Solutions, Malvern, PA), we scanned the phantoms at ambient temperature, removed the phantoms from the scanner, and repeated our measurements to establish repeatability. An inversion-recovery spin echo sequence with 10 different inversion times (TIs) were used for R₁ measurement and a spin echo sequence with 18 different echo times (TEs) were used for R₂ measurement. Scanning parameters are outlined in Table 1. We used mono-exponential fitting to fit the signal curve and excluded the signal lower than the noise floor. We compared r₁ and r₂ relaxivity constants among MoldayION, Feraheme, and generic ferumoxytol using two-way analysis of covariance (ANCOVA).

Results: Figure 1 illustrates the R₁ and R₂ values of Feraheme, generic ferumoxytol, and MoldayION at varying concentrations in saline, plasma, and human blood at 3.0T. The r₁ relaxivity values for Feraheme, generic ferumoxytol, and MoldayION in saline (22°C) were 7.11±0.13mM⁻¹s⁻¹, 8.30±0.29mM⁻¹s⁻¹, 8.62±0.16mM⁻¹s⁻¹, and the r₂ relaxivity values were 111.74±3.76mM⁻¹s⁻¹, 105.07±2.20mM⁻¹s⁻¹, and 109.68±2.56mM⁻¹s⁻¹, respectively. We observed a highly linear correlation (R² > 0.99) between R₁ and contrast concentration for all three contrast agents in saline and in plasma. A two-way ANCOVA comparing the three USPIOs found a minor but statistically significant difference in the variance of r₁ (p<0.01). R₂ was also highly linear (R²>0.99) in all three media. Moreover, a two-way ANCOVA comparing the three USPIOs found a small but significant difference in r₂ among contrast agents (p<0.01). We found a coefficient of variation of 3.7% (95% CI 2.8 – 4.6%) for R₁ and 9.4% (95% CI 7.0 – 11.8%) for R₂ between two repeated acquisitions.

Table 1. MRI acquisition parameters for in vitro r ₁ and r ₂ relaxometry at 3.0T		
Parameters	Inversion-recovery spin echo	Spin echo
TI [ms]	50, 57, 65, 75, 119, 188, 300, 488, 669, 1000	N/A
TE [ms]	7.4	7.1,8,9,10,11,12,15,17, 20,26,31,41,47,55,64, 74,86,100
TR [ms]	2500	2500
Number of echoes	1	1
Flip angle [degrees]	180, 90	90,180
Bandwidth [Hz/pixel]	1530	1500
Resolution [mm]	1.98 x 1.98 x 10	2.97 x 2.97 x 10

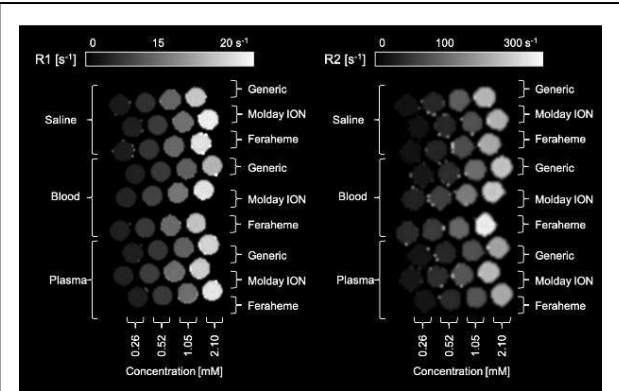


Figure 1. Grayscale pixelwise R₁ and R₂ maps of phantoms consisting of Feraheme, MoldayION and generic ferumoxytol in saline, whole blood, and plasma (3.0T, coronal view) across a contrast concentration range of 0.26 to 2.10 mM.

Discussion: R₁ and R₂ values are highly linear for Feraheme, generic ferumoxytol, and MoldayION contrast concentrations between 0.26mM to 2.10mM in saline, plasma, and human blood. The differences in r₁ and r₂ relaxivity values for Feraheme, generic ferumoxytol, and MoldayION are modest. These results suggest that relative to Feraheme, MoldayION and generic ferumoxytol likely produce very similar contrast enhancement effects in-vivo.

References: 1. Bashir MR, et al. Emerging applications for ferumoxytol as a contrast agent in MRI. J Magn Reson Imaging. 2015;41(4):884-898.
2. Finn JP, Nguyen KL, Han F, et al. Cardiovascular MRI with ferumoxytol. Clin Radiol. 2016;71(8):796-806.
3. Toth GB, Varallyay CG, Horvath A, et al. Current and potential imaging applications of ferumoxytol for magnetic resonance imaging. Kidney Int. 2017;92(1):47-66.

Differentiation of benign and malignant breast cancer lesions based on DCE-MRI voxel-by-voxel time-intensity curve profile ratios

Bingyu Yao^{1,2}, Zhou Liu³, Yumin Chen², Dong Liang¹, Xin Liu¹, Hairong Zheng¹, Na Zhang¹

¹College of Computer and Information Engineering, Xiamen University of Technology, Xiamen, China. ²Paul C. Lauterbur Research Center for Biomedical Imaging, Shenzhen Institute of Advanced Technology, Chinese Academy of Sciences, Shenzhen, China. ³Department of Radiology, National Cancer Center/National Clinical Research Center for Cancer/Cancer Hospital & Shenzhen Hospital, Chinese Academy of Medical Sciences and Peking Union Medical College, Shenzhen, China

Purpose: To Explore a novel approach to reflect hemodynamic heterogeneity within tumor lesions based on the percentage of voxel-by-voxel time-intensity curve (TIC) profiles ratios and validate its potential clinical value by differentiating between benign and malignant breast tumors.

METHODS: DCE-MRI data were retrospectively collected from 270 patients with 343 pathologically confirmed breast lesions who underwent breast MRI. The voxel-by-voxel TICs are classified into 19 different types based on the Wash-in slop, Wash-out slop, and stability of Wash-out slop. The percentage of each TIC type within the tumor lesion was calculated as a new feature (referred to as Type19) to assess the hemodynamic heterogeneity within the tumor. After extracting Type19 features, the dispersion of these features (or known as the degree of confusion) was quantified using Entropy, Gini Impurity, Variation Ratio, Interquartile range, Coefficient of variation, and Range. These calculated dispersion measures were compared between benign and malignant breast lesions. In addition, based on the Type19 features and dispersion metrics, several machine learning based models were used to explore the efficacy of these individual features and combination of several features in differentiating between benign and malignant breast lesions. Receiver operating characteristic(ROC) curve is used to assess the accuracy of these dispersion metrics and machine learning.

RESULTS: A representative color-coded map of Type19 features is shown in Figure 1. The mean and standard deviation (SD) of these six dispersion indicators and the corresponding p-value and area under curve (AUC) for distinguishing benign and malignant breast lesions are summerized in Table 1. After feature selection, Entropy and Interquartile range were selected for machine learning model building. The classification results of benign and malignant breast lesions based on machine learning are shown in Table 2.

Discussion: There are significant difference of all six indicators in distinguishing benign from malignant lesions (p-value<0.001), indicating the proposed Type19 features based method can reflect the hemodynamic heterogeneity within the tumor. Furthermore, in distinguishing between benign and malignant breast cancer lesions, the machine learning model based on Type19 features outperformed other models, including conventional semi-quantitative parameters-based model, ROI-based model, and three-time-point(3TP)-based model in the validation set.

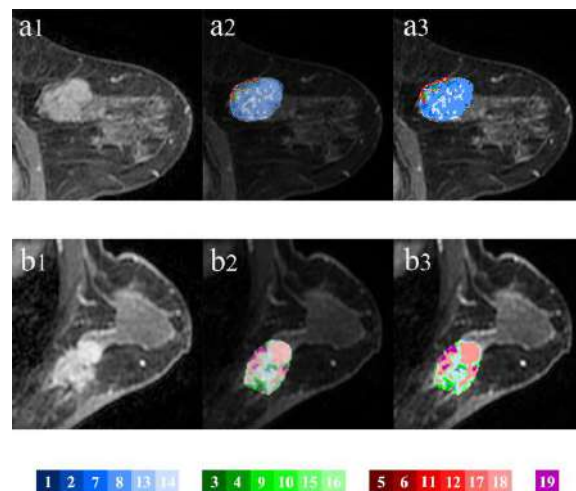


Figure 1. Schematic diagram in ROI of one lesion using Type19 classification results. (a) benign lesion ;(b) malignant lesion.

	Mean \pm SED		P-value	AUC
	benign	malignant		
Entropy	2.428 \pm 0.056	2.962 \pm 0.023	<0.001	0.770
Gini Impurity	0.721 \pm 0.013	0.819 \pm 0.005	<0.001	0.761
Variation Ratio	0.585 \pm 0.014	0.701 \pm 0.007	<0.001	0.733
Quartile Deviation	0.052 \pm 0.002	0.072 \pm 0.002	<0.001	0.715
Coefficient of Variation	1.982 \pm 0.054	1.510 \pm 0.027	<0.001	0.761
Range	0.415 \pm 0.015	0.299 \pm 0.007	<0.001	0.733

Table 1. The results of dispersion indicators for distinguishing benign from malignant breast lesions

		AUC	Accuracy	Sensitivity	Specificity
RandomForest Classifier	Semi-quantitative parameters	0.802	0.838	0.948	0.657
	ROI	0.845	0.849	0.862	0.828
	3TP	0.662	0.698	0.810	0.514
	Entropy & Quantile Difference	0.788	0.827	0.948	0.628
	Type19	1.000	1.000	1.000	1.000

Table 2. The results of mechine learning model for distinguishing benign form malignant breast lesions.

AI-Assisted Online Reconstruction for CMR Multitasking

Zihao Chen^{1,2}, Hsu-Lei Lee¹, Yibin Xie¹, Debiao Li^{1,2}, Anthony G. Christodoulou^{1,2}

¹Biomedical Imaging Research Institute, Cedars-Sinai Medical Center, Los Angeles, CA

²Department of Bioengineering, UCLA, Los Angeles, CA

Introduction: CMR multitasking (MT) is a promising approach for quantitative imaging without breath-holds or ECG monitoring [1], but slow iterative non-Cartesian reconstruction is a barrier to clinical adoption. Clinically feasible reconstruction time has been demonstrated using supervised artificial intelligence (AI) [2,3], but as with any supervised AI, generalizability and transparency are open questions, especially in a clinical setting. To retain the goal of fast, online image reconstruction without sacrificing generalizability or transparency, we explore an AI-Assisted Iterative (AAI) reconstruction method for CMR multitasking. The proposed method takes an AI reconstruction output as a “warm start” to a well-characterized iterative reconstruction algorithm with only 3 iterations, with the goal of producing better image quality than either pure AI or pure 3-iteration reconstruction.

Methods:

Reconstruction methods: To assess the performance of AI-assisted iterative reconstruction, we compare three different reconstruction methods (Fig. 1) for determining the spatial factor U in T1 CMR multitasking: a) Pure AI reconstruction U_{cnn} using a CNN block (U-Net [4]) with a zero-filled input U_0 ; b) Pure iterative wavelet reconstruction U_{iter3} from the initial guess U_0 (**3 iterations**); c) The proposed AI-assisted iterative reconstruction U_{AAI} from the initial guess U_{cnn} (**3 iterations**). All three methods are compared to the reference reconstruction U_{ref} that uses iterative wavelet reconstruction (**20 iterations**) from the initial guess U_0 . All iterative reconstruction was done using the alternating direction method of multipliers (ADMM) algorithm.

Dataset overview: A total of 120 T1 CMR MT datasets were collected from Siemens 3T scanners. We used 96 cases for training the U-Net, 12 cases for validation and 12 cases for testing. The matrix size of spatial subspaces is $320 \times 320 \times 32$.

Evaluation methods: The spatial factors reconstructed by the three methods (U_{cnn} , U_{iter3} and U_{AAI}) were compared against the reference U_{ref} using Normalized Root Mean Square Error (NRMSE) for the testing set. The reconstruction time of each method including the reference method was recorded.

Results and Discussion: Table 1 shows different methods' reconstruction time and their spatial factors' NRMSE compared to the reference method. The proposed method U_{AAI} has the best NRMSE with statistical significance ($p < 0.001$), and accelerates the reconstruction time by 10x compared to the reference method. Compared to the pure iterative method U_{iter3} , the proposed method uses similar reconstruction time to achieve much better reconstruction quality. Figure 2 shows T1 maps of one testing data reconstructed with different methods as well as their corresponding error maps. The proposed method has the best T1 map quality and the least T1 error compared to the reference.

Conclusion: In order to accelerate CMR multitasking reconstruction and improve the quality and robustness of AI reconstruction, we proposed an AI-Assisted iterative reconstruction method for CMR multitasking. The proposed method produces better image quality than other accelerated reconstruction methods, in less than 30 seconds.

References: [1] Christodoulou, A.G. et al. Nature BME. 2018; [2] Chen, Y. et al. MICCAI. 2019; [3] Chen, Z. et al. IEEE ISBI. 2022; [4] Ronneberger, O. et al. MICCAI. 2015.

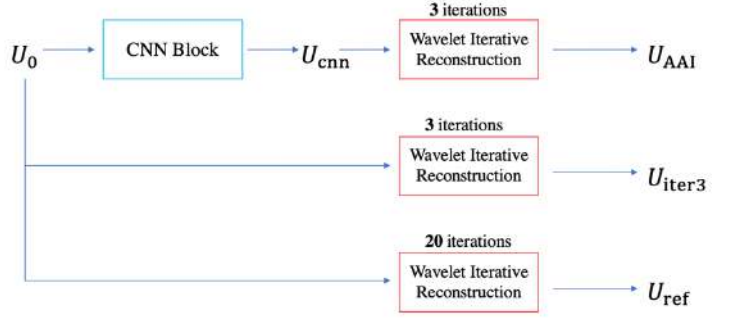


Fig. 1. An overview of different reconstruction methods. U_{AAI} is the proposed method.

Table 1. The performance of different reconstruction methods. The number in the bracket is the standard deviation. The method with the best NRMSE is bold.

	NRMSE compared to U_{ref}	Reconstruction time
U_{ref}	N/A	220 s
U_0	0.279 (0.096)	N/A
U_{iter3}	0.189 (0.085)	20 s
U_{cnn}	0.169 (0.052)	1.7 s
U_{AAI}	0.113 (0.045)	22 s

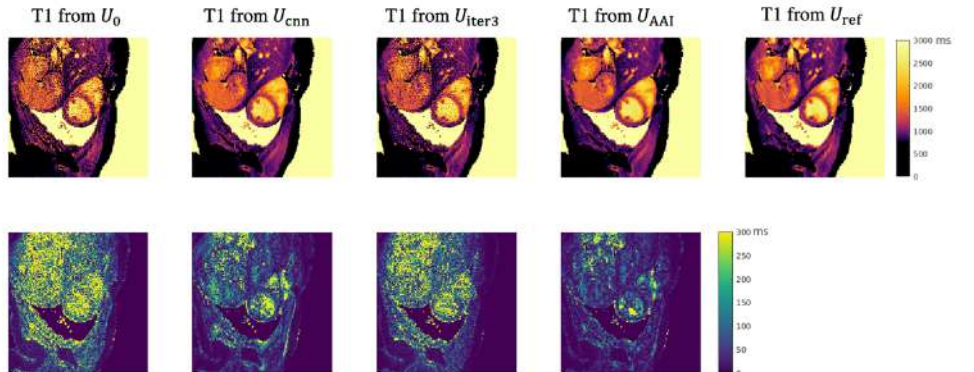


Fig. 2. T1 maps of one testing data reconstructed with different methods. The top row is the T1 maps, and the bottom row is the corresponding error maps against U_{ref} .

An interleaved 2D GRE MRA sequence to image utero-placental and fetal vasculature

Karthikeyan Subramanian^{1,2}, Pavan K. Jella^{1,2}, Feifei Qu¹, Ewart M. Haacke^{1,2}, Tinnakorn Chaiworapongsa^{3,4}

¹Department of Radiology, ²Department of Biomedical Engineering, ³Perinatology Research Branch, NICHD/NIH/DHHS, Bethesda, Maryland, and Detroit, Michigan, USA, ⁴Department of Obstetrics and Gynecology, Wayne State University, Detroit, Michigan, USA.

Purpose: To evaluate the feasibility of obtaining non-contrast enhanced magnetic resonance (MR) angiographic data along with quantitative T1 and R2* maps. Angiographic imaging in pregnancy can not only help in evaluating the normal developing vasculature of the human fetus and placenta but may also help in identifying abnormal development. In this study, we propose a technique for overcoming motion artifacts using an interleaved gradient echo sequence that allows us to acquire TOF like images, T2*, T1 and spin density maps.

Methods: To accomplish this, we used a 2D interleaved multi-echo GRE imaging that allows us to acquire a low (PD weighted) and high (T1 weighted with a TOF like effect) flip angle within the same sequence in roughly 5 seconds. This makes it possible to quantify tissue characteristics and help separate arteries from veins. Three pregnant women suspected of fetal growth restriction were scanned during their second and third trimester (24 – 37 weeks of gestation) using a 3.0T Siemens Verio scanner. A single interleaved multi-echo gradient echo sequence using two different flip angles [1] was acquired using the following imaging parameters: TR = 28 ms, TE = 7.8 / 14.44 - 20 ms, FAs = 6°/30°, voxel size = 1×1 mm² and slice thickness = 3 mm. In order to extract the vascular information, a Frangi vesselness filter [2] was applied to the data. The vesselness results were then manually cropped using SPIN-Research software and overlaid onto the original high flip angle data using MRlcron (v1.0.2, <https://www.nitrc.org/projects/mrlcron/>).

Results: The interleaved sequence provided images showing the usual TOF effect from the high FA interleaved images that were then compared with the conventional TOF sequences acquired with the same resolution. Due to the simultaneous acquisition of the multi-echo interleaved GRE data using two FA, we were able to create water content, T1 and R2* maps, that aids us in differentiating the veins from arteries. When MRA was acquired covering the entire abdomen of the mother, we were able to visualize the following vascular territories: blood supply of the mother's uterine arteries; the endometrial vessels feeding the placenta; the umbilical cords merging into the chorionic plate; and the fetal vessels including the heart, inferior vena cava, aortic arch, subclavian artery, carotid arteries, jugular veins and the ductus venosus (Fig 1).

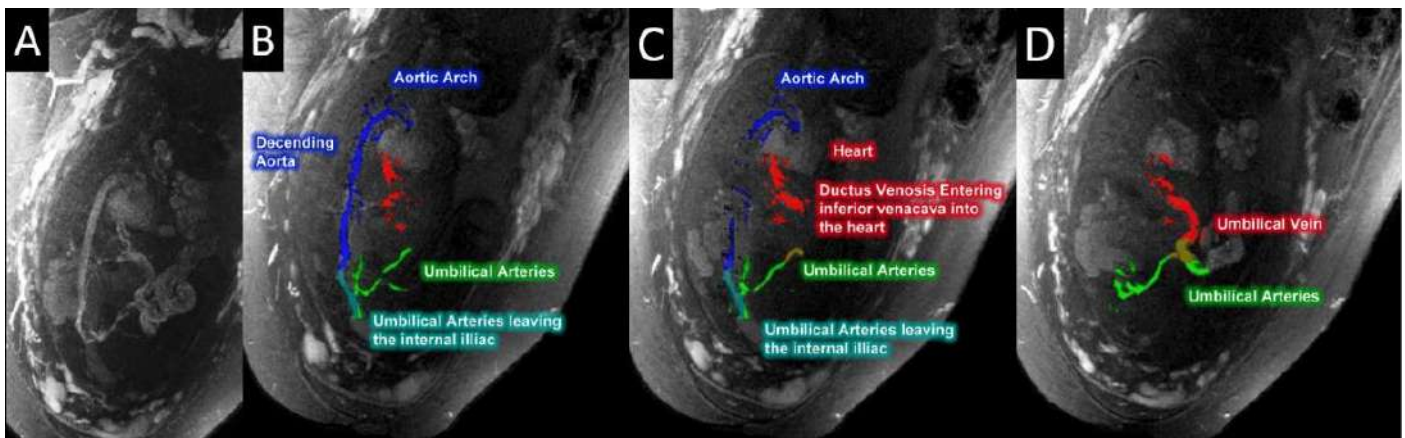


Figure 1 shows the overlay labeling the fetal circulation.

Discussion: In this study, we presented a non-invasive approach for acquiring and processing the interleaved multi-echo GRE data that helps in the visualization (high flip angle) and quantification of the placental-fetal vascular territory. Future applications include automated vessel extraction and mapping tissue properties, using phase data and susceptibility mapping to monitor oxygen saturation and T2* to monitor placental health and study intrauterine growth restriction that can be achieved all in one scan.

References:

1. Chen, Y., et al., *An interleaved sequence for simultaneous magnetic resonance angiography (MRA), susceptibility weighted imaging (SWI) and quantitative susceptibility mapping (QSM)*. Magnetic Resonance Imaging, 2018. **47**: p. 1-6.
2. Frangi, A.F., et al. *Multiscale vessel enhancement filtering*. in *Medical Image Computing and Computer-Assisted Intervention — MICCAI'98*. 1998. Berlin, Heidelberg: Springer Berlin Heidelberg.

Fully automated myocardial segmentation of 3D multiparametric T₁ and T₂ maps using an attention fully convolutional neural network

C. Velasco¹, R. Jakubicek^{1,2}, A. Fotaki¹, A. Hua¹, C. Munoz¹, C. Prieto¹, R. M. Botnar¹.

¹School of Biomedical Engineering and Imaging Sciences, King's College London, London, UK. ²Department of Biomedical Engineering, Brno University of Technology, Brno, CZ.

Purpose: Myocardial tissue characterization via T₁ and T₂ mapping plays an important role in the evaluation of many cardiovascular diseases¹. In the clinical setting, single parameter quantitative maps such as T₁ and T₂ are obtained from sequential 2D scans under separate breath-holds². In recent years, novel multiparametric approaches have shown the feasibility to produce co-registered 3D whole-heart T₁ and T₂ maps within a single free-breathing acquisition^{3,4}. These 3D whole-heart multiparametric approaches promise a richer assessment of myocardial tissue alterations, while simplifying scan planning and providing more patient comfort. Nevertheless, the higher amount of data obtained from a single 3D whole heart multiparametric scan (up to ~40 slices per parametric map) increases considerably the time required to segment and analyze the quantitative maps. Thus, an automated segmentation tool for these maps is

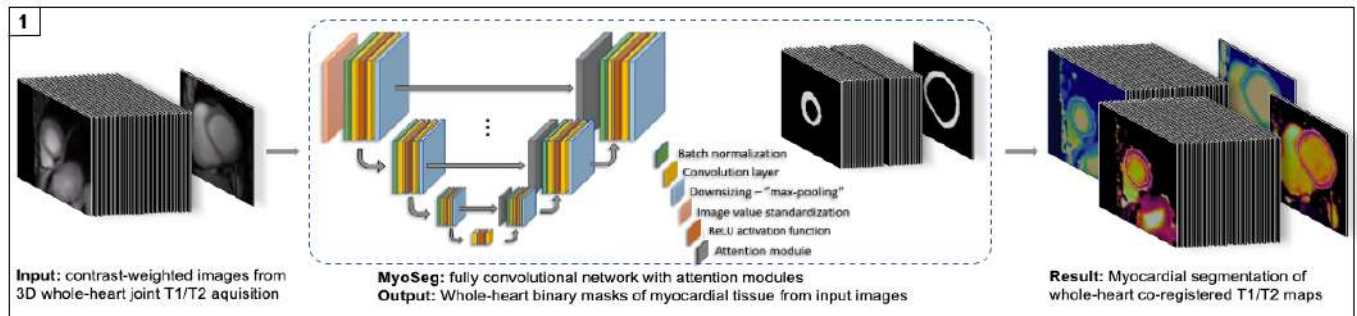


Fig. 1): Schematic drawing of the proposed workflow for fully automated estimation of myocardial masks on multiparametric whole heart maps.

desirable to perform this otherwise prohibitively laborious task. Here, we show the potential of an attention fully convolutional network to perform fast, automated segmentation of 3D whole-heart simultaneous T₁ and T₂ maps.

Methods: The proposed DL-approach (DL-MyoSeg) consists of a fully convolutional U-net based network with attention modules (Fig.1). Input images are normalized to 1x1mm² 2D slices of different nature (T₁, T₂ maps and T₁/T₂-weighted images). The network was pre-trained on 2D multi-slice CINE data and trained on a mixed manually annotated dataset consisting of a) ~1250 slices from multiparametric 1x1x2 mm³ 3D whole-heart joint T₁/T₂ maps and T₁/T₂ contrast-weighted images from N=34 subjects and b) ~500 1.6x1.6x8 mm³ slices from clinical T₁-MOLLI and T₂-bSSFP maps from subjects with suspected cardiovascular disease. To increase robustness, the training dataset was further enriched with annotated T₁ and T₂ maps from Emidec⁵ (N=700 slices) and MyoPS⁶ (N=100) publicly available datasets. Training and validation was performed in an 8:2 ratio. The testing dataset consisted of a total of 72 slices from 3D whole-heart joint T₁/T₂ mapping scans from 8 subjects, distributed in 3-3-3 in the apical, mid-ventricular and basal regions. Manual segmentations for these 72 slices were performed by an experienced clinical reader for comparison purposes. All scans included in datasets a) and b) were acquired on a 1.5T scanner (MAGNETOM Aera, Siemens Healthcare, Erlangen, Germany) and all segmentations for testing were performed on the 4th contrast (T₂ prepared) of the joint T₁/T₂ 3D mapping sequence. Dice scores and Hausdorff distance were computed on the testing dataset to compare manual segmentation vs. predicted masks. Bland-Altman plots comparing T₁ and T₂ values for predicted and reference masks were also calculated.

Results: The predicted masks produced an average Dice score of 0.788 (0.783, 0.784 and 0.798 for apical, mid and basal levels), while average Hausdorff distance was 1.16 pixels (1.11, 1.16 and 1.20 for apical, mid and basal levels). Bland-Altman plots comparing T₁ and T₂ values for predicted vs. manually delineated ROIs resulted in a bias of -14.7 ± 46.8ms and -3.0 ± 6.9ms respectively, both non-significantly different from 0 (Fig.2). Segmentation time was ~45s per slice for manual segmentation vs. ~0.5s per slice for the proposed DL-MyoSeg approach.

Discussion: We demonstrate the feasibility of an attention fully convolution neural network to perform automated myocardial segmentation on 3D joint T₁/T₂ maps, shortening the segmentation and analysis time by ~100x, compared to manual segmentation. Predicted masks were visually comparable to manual segmentation and results with regard to T₁ and T₂ quantification were not significantly different to those within manual segmentation.

References: ¹Kim, P.K. et al., Korean J. Radiol. 2017. ²Messroghli, D.R. et al., JCMR 2017. ³Milotta, G. et al., MRM 2020. ⁴Qi, H. et al., MRI 2019. ⁵Lalande, A. et al. Data 2020. ⁶Zhuang, X. IEEE PAMI 2019.

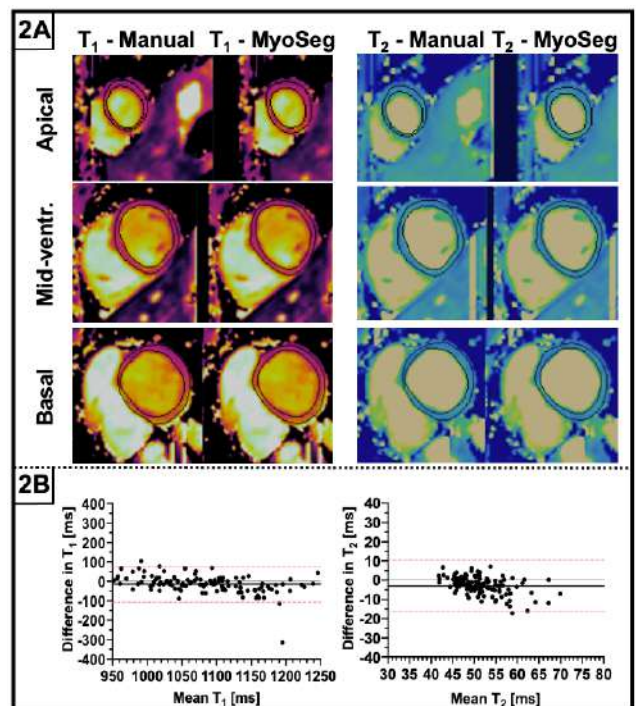


Fig. 2. A): Example manual vs. predicted masks for 3 slices at apical, mid-ventricular at basal levels. **B).** Bland-Altman plots of T₁ (left) and T₂ (right) quantification within manual vs. predicted masks for each AHA-segment.

T1 map estimation of carotid plaque with machine learning in clinical sequences

Jeff Snyder¹, Glen Jickling², Joseph Kamtchum², and Alan H. Wilman¹

University of Alberta, Biomedical Engineering¹ and Neurology², Edmonton, AB, Canada

INTRODUCTION: Quantitative MRI is a useful tool to assess properties of healthy and diseased tissues. T1 and T2 mapping techniques can provide valuable insight to characterize carotid plaques (1,2). However, gold standard T1 and T2 mapping methods (using fast spin echo (FSE) sequences) are time-consuming and often have low resolution making clinical translation difficult. Dedicated sequences such as GOAL-SNAP (3) and 3D FSE methods (4) can save time and improve resolution, although they are not widely adopted in clinical studies. As a proof of concept, we investigate the use of clinical sequences in conjunction with prior knowledge provided by machine learning (ML) to elucidate T1 maps in routine imaging studies without the need for specialized sequences.

METHODS: Data from seven previous healthy volunteer scans in the brain (encompassing a large range of T1 values, ~800 – 3000 ms (5)) at 3 T were used to train a MATLAB based regression learner. MPRAGE (1 mm³ resolution, TE/TI = 2.3/1800 ms) images and 2D B1⁺ maps (TE/TR = 2.24/4.6 ms, flip angle = 5°, 1.1 x 1.1 x 3 mm³ (6)) were used as ML inputs while gold standard T1 maps (2D IR FSE; TE/TR = 10/7000 ms, 7 TIs from 50 to 3000 ms, 0.9 x 0.9 x 3 mm³) were used as the expected output. After training, the ML was employed on data from patients giving informed consent with CTA-confirmed stenosis of carotid arteries. The clinical carotid protocol included MPRAGE (2 scans - brain and neck), FLAIR, TOF, B1⁺ mapping and DTI. MPRAGE levels were normalized first between head MPRAGE scans (previously acquired for ML training and current clinical), then the clinical head and neck scans.

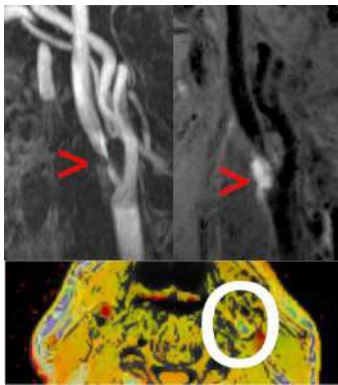


Figure 1: TOF (left) and MPRAGE (right) scans showing carotid stenosis in a patient before endarterectomy, with estimated T1 map (bottom).

RESULTS: Stenosis was visible (Figure 1, red arrows) in a patient prior to carotid endarterectomy as confirmed with TOF (left), with a concurrent hyperintense region in MPRAGE (right) indicating intraplaque hemorrhage (IPH) (7) – also seen on the calculated T1 map (bottom). Axial slices of resultant T1 maps centered on the carotid (Figure 2) show variations in plaque composition. In accordance with T1 literature values (2), several regions can be identified including loose matrix (red/orange), necrotic core (yellow/green) and IPH (blue), with average T1 values of 1184 ± 20 , 1070 ± 28 , and 864 ± 87 ms, respectively.

DISCUSSION: Estimated carotid plaque T1s agreed with literature within error, though values tended to be lower in loose matrix and necrotic core regions than previously reported. While a sufficient T1 range was used as ML input (from brain scans), further improvements can be made by using input and output data from the neck only, removing error from the normalization of MPRAGE images. In conclusion, T1 mapping using MPRAGE and B1⁺ as shown in this proof of concept does not require specialized or gold standard sequences and provides a simple T1 quantification method for carotid plaques.

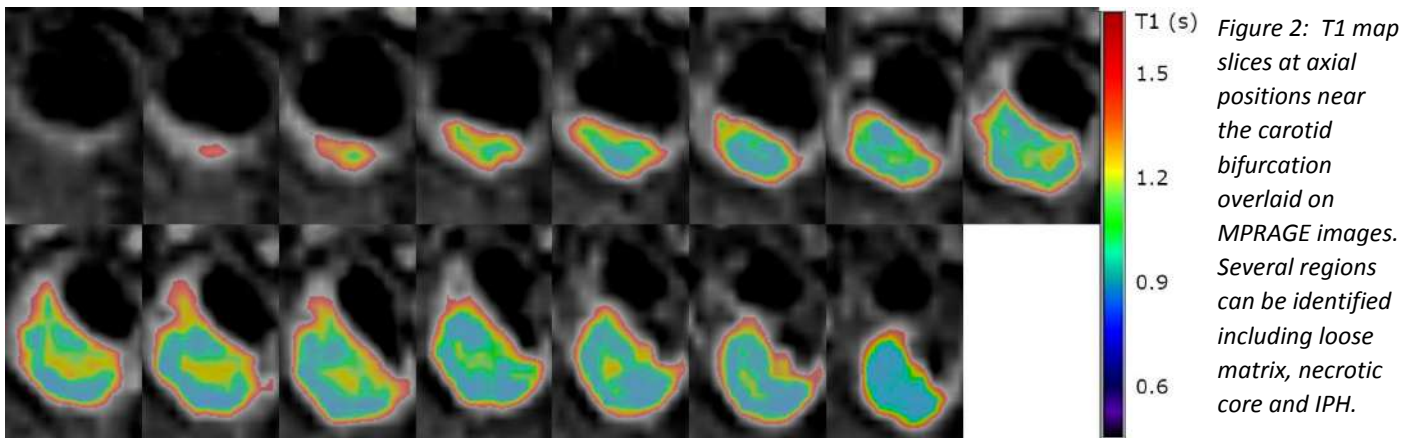


Figure 2: T1 map slices at axial positions near the carotid bifurcation overlaid on MPRAGE images. Several regions can be identified including loose matrix, necrotic core and IPH.

REFERENCES: 1. Biasioli L. J. Cardiovasc. Magn. Reson. 2013;15:1. 2. Qiao H. J. Cardiovasc. Magn. Reson. 2020;22. 3. Qi H. Radiology 2018;287:276–284. 4. Snyder J. Magn. Reson. Med. 2022;87:2145–2160. 5. Bojorquez JZ. Magn. Reson. Imaging 2017;35:69–80. 6. Sacolick LI. Magn. Reson. Med. 2010;63:1315–1322. 7. Saba L. Am. J. Neuroradiol. 2018;39:E9–E31.

Non-invasive Angiography Trends Across a Decade

R Burgul, G Roditi

NHS Forth Valley, NHS Greater Glasgow and Clyde, Scotland, UK

Purpose: Non-invasive angiography has transformed vascular imaging since the advent of MRA and CTA. We sought to evaluate the temporal and geographic trends in the performance of these studies across a decade of imaging. The purpose is to determine how the different modalities are being used for evaluation of different body regions across the whole health economy of Scotland and evaluate variation to inform the research community and aid in resource planning.

Methods: Governance permission was obtained for collation of anonymised data at national and local levels for all non-invasive angiographic studies performed by CT and MRI from 2009 to 2019 inclusive across Scotland. Data were collated from the Scottish National PACS archive regarding examination modality, examination type (body area), date and site of performance. More detailed data in regard to gender, age, patient type (in-patient versus out-patient versus ED etc.), time and day of performance was extracted from the local Radiology Information Systems (RIS) of two Health Boards representative of city/university teaching hospital versus district general hospital-based practise.

Results: Highlights of the results are -

- A 45% increase in district general hospital-based studies compared with a 72% increase in city/university teaching hospital practise over the decade as a whole.
 - Pulmonary angiography almost exclusively performed by CT accounted for up to 48% of all studies with rates having increased by up to 55% over the decade with up to 644 studies performed per 100,000 population in 2019.
 - Coronary studies (again almost exclusively performed with CT) increased up to threefold over the period.
 - The share of total studies (excluding pulmonary & coronary) performed with MRA has fallen from 40% to 33% in a city/university teaching hospital health board versus now only 25% share in a district general hospital-based health board.
 - Lower limb angiographic studies overall have grown modestly in number (around 20%) but peaked for MRA around 2016, declining since with CTA having grown from under 20% of the examination totals to outnumber MRA at just over 50% of studies in 2019 (figure 1).
 - Carotid studies overall increased up to sixfold over the period with CTA increasing consistently, outnumbering MRA in 2019 by a factor of 10:1 as absolute MRA numbers had fallen (figure 2).
- * MRA is rarely if ever performed out-of-hours or for ED patients in contrast to CTA studies where this has increased from 2% to 15% of the total CTA workload over the period.

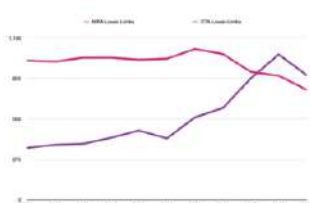


Figure 2

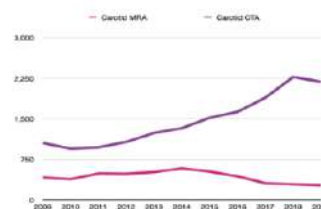


Figure 1

Discussion: Despite an overall growth in non-invasive angiographic imaging over the decade across Scotland MRA has shown a reduced use and share compared to increasing CTA activity.